



HAL
open science

Generation and Application of Attosecond Pulses

Zsolt Diveki

► **To cite this version:**

Zsolt Diveki. Generation and Application of Attosecond Pulses. Other [cond-mat.other]. Université Paris Sud - Paris XI, 2011. English. NNT : 2011PA112290 . tel-00722473

HAL Id: tel-00722473

<https://theses.hal.science/tel-00722473>

Submitted on 2 Aug 2012

HAL is a multi-disciplinary open access archive for the deposit and dissemination of scientific research documents, whether they are published or not. The documents may come from teaching and research institutions in France or abroad, or from public or private research centers.

L'archive ouverte pluridisciplinaire **HAL**, est destinée au dépôt et à la diffusion de documents scientifiques de niveau recherche, publiés ou non, émanant des établissements d'enseignement et de recherche français ou étrangers, des laboratoires publics ou privés.

THÈSE DE DOCTORAT DE L'UNIVERSITÉ PARIS-SUD
XI

Effectuée au Service des Photons, Atomes et Molécules, IRAMIS, DSM
Commissariat à l'Énergie Atomique, Saclay.

Spécialité: Lasers et Matière

GENERATION AND APPLICATION
OF ATTOSECOND PULSES

Présentée par

ZSOLT DIVEKI

pour obtenir le grade de
DOCTEUR EN SCIENCES DE L'UNIVERSITÉ PARIS-SUD XI.

Soutenue le 16 décembre 2011
devant le jury composé de :

Mme.	VALERIE BLANCHET	Rapporteur
M.	PIERRE AGOSTINI	Rapporteur
Mme.	DANIELLE DOWEK	
Mme.	KATALIN VARJÚ	
M.	MAURO NISOLI	
M.	PASCAL SALIÈRES	Directeur de thèse



UNIVERSITÉ
PARIS-SUD 11

GENERATION AND APPLICATION OF ATTOSECOND PULSES

© 2009 Zsolt Diveki
All rights reserved
Printed in Paris, 2011

Commissariat à l'Énergie Atomique
Direction Science de la Matière
Institut Rayonnement Matière Saclay
Service des Photons, Atomes et Molécules
Bâtiment 522
F-91191 Gif-sur-Yvette
France

<http://iramis.cea.fr/spam/MEC/>

This thesis was typeset with the L^AT_EX-system and the memoir class, using a model developed by Stefan Haessler and the smart people of the Atomfysik division at Lund University.

ABSTRACT

To capture electronic rearrangements inside a molecule or during chemical reactions, attosecond (as, $1 \text{ as} = 10^{-18} \text{ s}$) time resolution is needed. To create a light pulse with this duration, the central frequency has to be in the XUV range and cover several tens of eVs. Moreover, the frequency components have to be synchronized. The so called High Harmonic Generation (HHG) in gases well suits this task. During this process a high intensity laser pulse is focused in a gas jet, where its electric field bends the potential barrier of an atom allowing an electron wave packet (EWP) to tunnel ionize. Following the electric field of the laser the EWP gets accelerated, gaining a large kinetic energy that may be released as a high energy (XUV) photon in the event of a re-collision with the ionic core. These re-colliding EWP probe the structure and dynamics of the core in a self-probing scheme: the EWP, that is emitted by the molecule at a certain time, probes itself later. More precisely, this "self-probing" scheme gives access to the complex valued recombination dipole moment (RDM) of the molecule which is determined by both the nuclear and electronic structure. The recombination encodes these characteristics into the spectral amplitude, phase and polarization state of the harmonic radiation emitted by the dipole. Due to the coherent nature of HHG it is possible to measure all these three parameters. Moreover, it is in principle possible through a tomographic procedure to reconstruct the radiating orbital.

The objective of my thesis was two-fold. By implementing advanced characterization techniques of the harmonic amplitude, phase and polarization we studied i) the electronic structure of N_2 and laser induced multi-channel tunnel ionization; and ii) the reflectivity and dispersion of recently designed chirped XUV mirrors that can shape the temporal profile of attosecond pulses.

Study of molecular structure and dynamics induced by multi-channel ionization in N_2

Aligning a molecular gas with a laser we were able to probe the angular dependence of the RDM of the molecules in the laboratory frame. Molecular orbitals are usually close to each other energetically. Therefore, changing the generating conditions, as for instance increasing the intensity of the generating laser (I_L), we may induce simultaneous multi-channel ionization in molecules. In that case, the potential barrier is so bent that not only the highest occupied molecular orbital (HOMO) is contributing to harmonic generation, but lower lying orbitals such as HOMO-1 in N_2 , too. Therefore, the measured harmonic signal is given by the interference of the harmonic emission issued from both orbitals. In principle, it should result in a blurring of the image when reconstructing the molecular orbitals with tomography. However, analyzing the measured harmonic phases we showed that decreasing the I_L we could minimize the contribution coming from HOMO-1, creating good conditions to perform HOMO orbital reconstruction. Moreover, we showed that by properly choosing I_L we could disentangle the HOMO and HOMO-1 contributions into the imaginary and the real part of the measured dipole and reconstruct both orbital wavefunctions.

From theoretical considerations we demonstrated that the features of nuclear vibration dynamics are very specific to each orbital. While the tunnel ionization from HOMO barely induces nuclear dynamics, we showed that tunnel ionization from HOMO-1 creates a nuclear wavefunction which evolves on the attosecond time scale and its influence can be seen in the measured harmonic phase. This phenomenon provides a new way to control the properties of the generated harmonics through the laser intensity and wavelength.

Since molecular alignment is not perfect, the measured harmonic signal is a result of the averaging of the single molecule response over the alignment distribution. We showed that the non aligned molecular ensemble is not an ideal reference where structural signs are washed out. On the contrary, independently from the molecular alignment we evidenced a constant minimum in the spectral intensity of the harmonics'. In addition, we showed that the harmonic phase contains signs of multi-orbital contributions even after the molecular averaging. We shortly discussed how we could extract the single molecule response from the averaged macroscopic signal and what requirements have to be fulfilled to do so.

We showed that in molecules elliptically polarized harmonics can be generated using linearly polarized driving laser. This phenomenon can only be seen in molecules. The study of the polarization state of harmonics provides an additional parameter that may result in the determination of both molecular structures and induced intra-molecular electron dynamics. Our model showed that neither single nor multi-orbital contributions were sufficient to reproduce the experimental results suggesting the presence of additional ultra-fast effects like coupling between different orbitals.

Compression and shaping of as pulses

In the XUV spectral range, optical systems are much more difficult to design than in the visible range, in particular because of the absorption of materials. Several techniques were proposed to overcome the problem of as pulse control after the high harmonic source, for example using filters, plasmas or gas jets. Multilayer aperiodic chirped mirrors, which efficiently reflect XUV radiation, were recently proposed in order to manipulate such pulses. However, the possibility of phase control over large spectral bandwidths has not yet been demonstrated with these mirrors because of high technical demands. We designed and manufactured three plane aperiodic multilayer mirrors with optimized reflectivity and controlled spectral phase in the 35-55 eV range near 45° incidence. Their reflectivity was characterized on the Elettra Synchrotron and their spectral phase, on an attosecond pulse source at CEA SPAM, providing a full characterization of their spectral response. We reported on the characterization of these mirrors and showed how they control the temporal profile of the as pulses. Such pulses provided by the HHG process are intrinsically chirped. We demonstrated that they can be recompressed using our multilayer mirrors. We also proposed a more flexible way to shape the pulses giving relatively high intensities. A combination of two mirrors with an Al filter provides an active as pulse-shaper, allowing a phase control up to third-order dispersion. The pulse shaper allows the realization of some simple functions as tunable pulse compression, or shaping of single, double or multiple sub-100 as pulses, the properties of which can be set by simply turning the pulse-shaper.

SYNTHÈSE

En vue de la capture de réarrangements électroniques au sein d'une molécule ou au cours de réactions chimiques il est indispensable de développer un dispositif dont la résolution temporelle est attoseconde ($1 \text{ as} = 10^{-18} \text{ s}$). La voie naturelle est de rechercher des impulsions lumineuses dans cette gamme de durée. Leur fréquence centrale doit alors être dans la gamme UVX et couvrir plusieurs dizaines d'eVs. De plus, ses composantes fréquentielles doivent être synchronisées. Le processus de génération d'harmoniques d'ordre élevé (GHE) dans les gaz remplit ces exigences. Pendant ce processus, une impulsion laser de haute intensité est focalisée dans un jet de gaz, où son champ électrique courbe la barrière de potentiel d'un atome et permet l'ionisation tunnel d'un paquet d'ondes électronique (POE). Entraîné par le champ électrique du laser, le POE accélère et acquiert une énergie cinétique élevée. Dans le cas où il repasse au voisinage du cœur ionique cette énergie cinétique peut être émise sous la forme d'un photon UVX. Ces POE explorent la structure et la dynamique de l'ion dans un schéma d'auto-sonde: le POE émis à un instant donné revient lui même ultérieurement sonder l'ion. Plus précisément ce processus d'auto-sonde donne accès à la valeur complexe du dipôle de recombinaison moléculaire (DRM), lui-même déterminé par les structures nucléaire et électronique de l'ion. Le dipôle de recombinaison, en rayonnant des harmoniques, encode ces caractéristiques dans l'amplitude, la phase et l'état de polarisation de l'émission harmonique. Grâce à la nature cohérente de la GHE nous pouvons mesurer ces trois paramètres.

L'objectif de ma thèse de doctorat était double. En mettant en œuvre des techniques avancées de caractérisation de l'amplitude, de la phase et de la polarisation des harmoniques nous avons dans un premier temps étudié la structure électronique de N_2 et l'ionisation tunnel multi-canaux induite par le laser et dans un deuxième temps la réflectivité et la dispersion de miroirs UVX à compensation de dérive de fréquence, fabriqués sur mesure. Ces miroirs autorisent la mise en forme temporelle d'une impulsion attoseconde.

Étude de la structure de N_2 et de la dynamique moléculaire induite par ionisation multi-canaux

En alignant l'aide d'un laser des molécules en phase gazeuse, nous avons pu étudier la dépendance angulaire de leur DRM dans le référentiel du laboratoire. Les orbitales moléculaires sont en général relativement proches en énergie l'une de l'autre, à l'échelle de l'énergie crête des faisceaux laser utilisés. En changeant légèrement les conditions de génération, comme par exemple en augmentant l'intensité du laser de génération (I_L), il est donc possible d'induire simultanément l'ionisation via plusieurs canaux. Dans ce cas, la barrière de potentiel est tellement courbée que ce n'est plus seulement l'orbitale moléculaire la plus haute occupée (HOMO) qui contribue à la GHE mais les orbitales plus basses en énergie également, comme la HOMO-1 dans N_2 par exemple. Le signal d'harmoniques mesuré est alors donné par l'interférence des émissions harmoniques issues des deux orbitales. En principe, ceci pourrait brouiller l'image de l'orbitale moléculaire reconstruite par tomographie. Cependant, en analysant la phase spectral mesurée nous avons montré qu'en diminuant I_L la contribution de HOMO-1 pouvait être minimisée. Ainsi, nous avons pu créer les conditions appropriées pour reconstruire la HOMO seule. De plus, nous avons montré qu'en choisissant I_L avec soin, il nous a été possible de séparer les contributions de

HOMO et HOMO-1 respectivement dans les parties imaginaire et réelle du dipôle mesuré et ainsi reconstruire les fonctions d'onde des deux orbitales.

En nous basant sur des considérations théoriques nous avons montré que, selon qu'un électron est émis depuis l'une ou l'autre orbitale, les cœurs ioniques présentent des caractéristiques vibrationnelles spécifiques. Plus précisément, au contraire de l'ionisation tunnel de HOMO qui induit des dynamiques nucléaires d'amplitude très faibles, nous avons montré que l'ionisation tunnel de HOMO-1 crée une fonction d'onde nucléaire dont les caractéristiques évoluent significativement à l'échelle de temps attoseconde et dont l'influence peut être détectée dans la phase spectrale mesurée. Ce phénomène offre un nouveau contrôle sur les propriétés de la GHE par l'intensité ou la longueur d'onde du laser.

L'alignement moléculaire n'étant jamais parfait, le signal mesuré est donné par le moyennage de la réponse d'une molécule unique sur la distribution d'alignement. Nous avons montré que l'ensemble moléculaire non aligné n'est pas une référence idéale pour laquelle les caractéristiques propres à la structure moléculaire seraient supprimées. Au contraire, nous avons observé un minimum constant dans l'intensité spectrale des harmoniques indépendant de l'alignement moléculaire. De plus, nous avons montré que des caractéristiques spécifiques de contributions multi-orbitales persistent dans la phase des harmoniques, même après moyennage sur leur distribution angulaire. Nous discutons rapidement comment la réponse moléculaire unique peut néanmoins être extraite du signal macroscopique moyenné et quels critères doivent être respectés pour y parvenir.

Enfin, nous avons montré qu'un laser polarisé linéairement peut générer des harmoniques polarisées elliptiquement. Ce phénomène est réservé aux molécules. L'étude de l'état de polarisation des harmoniques ouvre donc une nouvelle voie pour accéder à la structure moléculaire et à la dynamique électronique ultra-rapide induite par le laser. Notre modèle montre que ni la contribution d'une orbitale unique, ni d'éventuelles contributions multi-orbitales ne sont suffisantes pour reproduire les résultats expérimentaux. Ceci suggère un rôle joué par des effets ultra-rapides additionnels comme par exemple le couplage entre orbitales.

Compression et façonnage d'impulsions attosecondes

Dans le domaine spectral UVX, les systèmes optiques sont beaucoup plus difficiles à concevoir que dans le domaine visible, notamment en raison de l'absorption des matériaux. Plusieurs techniques ont été proposées pour surmonter le problème du contrôle des impulsions attosecondes après la source harmonique, par exemple en utilisant des filtres, des plasmas ou des jets de gaz. Les miroirs multicouches aperiodiques ont récemment été proposés dans le but de manipuler ces impulsions, pour profiter notamment de leur réflectivité potentiellement élevée pour le rayonnement UVX. Mais leurs possibilités de contrôle de la phase sur une grande bande spectrale n'a pas encore été démontrée.

Nous avons conçu et fabriqué trois miroirs plans aperiodiques multicouches ayant des réflectivités optimisées et des phases spectrales contrôlées dans la gamme 35-55 eV au voisinage d'un angle d'incidence 45°. Leur réflectivité a été caractérisée sur le synchrotron Elettra et leur phase spectrale sur une source d'impulsions attosecondes au CEA SPAM, fournissant une caractérisation complète de leur réponse spectrale. Après avoir présenté ces résultats, nous montrons comment ils contrôlent le profil temporel des impulsions attoseconde. Les impulsions fournies par le processus de GHE présentent une dérive de fréquence intrinsèque. Nous démontrons qu'elles peuvent néanmoins être recomprimées en utilisant ces miroirs multicouches. Nous avons également proposé une approche plus flexible pour façonner des impulsions en conservant des intensités relativement élevées. Une combinaison de deux de ces miroirs avec un filtre d'aluminium fournit un "façonneur d'impulsions" actif à l'échelle as, permettant un contrôle de phase jusqu'au troisième ordre de dispersion. Ce "façonneur d'impulsions" permet la réalisation de certaines fonctions simples comme la compression d'impulsions accordables, ou le façonnage d'une impulsion de moins de 100 as, simple, double ou multiple. Ces propriétés peuvent être réglées simplement en tournant le façonneur.

LIST OF PUBLICATIONS

This thesis is based on the following papers, which will be referred to by their roman numerals in the text.

- I. **Attosecond imaging of molecular electronic wavepackets**
S. Haessler, J. Caillat, W. Boutu, C. Giovanetti-Teixeira, T. Ruchon, T. Auguste, Z. Diveki, P. Breger, A. Maquet, B. Carré, R. Taïeb and P. Salières
Nature Physics **6**, 200206 (2010).
- II. **Spectrally-resolved multi-channel contributions to the harmonic emission in N₂**
Z. Diveki, A. Camper, S. Haessler, T. Auguste, T. Ruchon, B. Carré, P. Salières
R. Guichard, J. Caillat, A. Maquet, R. Taïeb
Submitted (2011).
- III. **Theoretical and experimental studies of extreme broadband phase-controlled attosecond mirrors**
Z. Diveki, C. Bourassin-Bouchet, E. English, E. Meltchakov, O. Gobert, D. Guenot, B. Carré, P. Salières, and T. Ruchon S. de Rossi, F. Delmotte
Unpublished
- IV. **Control of the attosecond synchronization of XUV radiation with phase-optimized mirrors**
C. Bourassin-Bouchet, Z. Diveki, S. de Rossi, E. English, E. Meltchakov, O. Gobert, D. Guenot, B. Carré, F. Delmotte, P. Salières,² and T. Ruchon
Optics Express **19**, 4 (2010).

ABBREVIATIONS

APT	Attosecond Pulse Train
BO	Born-Oppenheimer
DME	Dipole Matrix Element
EWP	Electron Wave Packet
FFT	Fast Fourier Transform
FWHM	Full Width at Half Maximum
GTO	Gaussian-type orbitals
HF	Hartree-Fock
HHF	High Harmonic Frame
HOMO	Highest Occupied Molecular Orbital
HWP	Half Wave Plate
IR	Infra Red
LCAO	Linear Combination of Atomic Orbitals
LF	Laboratory Frame
MF	Molecular Frame
MIR	Mid-Infra Red
MO	Molecular Orbital
RABBIT	Reconstruction of Attosecond harmonic Beating by Interference of Two-photon Transitions
RDM	Recombination Dipole Moment
SFA	Strong Field Approximation
SMR	Single Molecule Response
STO	Slater-type orbital
TDSE	Time Dependent Schrödinger Equation
TISE	Time Independent Schrödinger Equation
XUV	eXtreme Ultra Violet

CONTENTS

Introduction	1
1 Theoretical Background	9
1.1 Wavepackets	10
1.1.1 Optical Wavepackets	10
1.1.2 Electron Wavepackets	13
1.2 Atomic Electronic States	14
1.2.1 Bound States	14
1.2.2 Continuum Electronic States	15
1.3 Molecular Orbitals	17
1.4 High Harmonic Generation	20
1.4.1 Tunnel Ionization	20
1.4.2 Theory of High Harmonic Generation	23
1.4.3 Recombination	28
1.4.4 Nuclear Wavepacket Dynamics in Molecules	32
1.4.5 Propagation Effects	32
2 Experimental Tools for Attosecond Physics	37
2.1 Experimental Tools for High Harmonic Generation	38
2.1.1 Molecular Alignment	40
2.2 Experimental Tools for Harmonic Characterization	45
2.2.1 Technique for the measurement of the harmonics' spectral intensity	46
2.2.2 Techniques for Phase Measurement	47
2.2.3 Principles of Polarization Measurements	54
3 Self-probing of Electrons in Molecules	59
3.1 Self-probing technique to measure the recombination dipole	60
3.2 Molecular Orbital Tomography	62
3.2.1 Length form RDM	62
3.2.2 Velocity form RDM	63
3.2.3 How reliable is the plane wave approximation?	64
3.2.4 Experimental Molecular orbital Tomography	65
3.2.5 Two-center interference	66
3.2.6 Multi-Orbital Contributions to HHG	66
PAPER I	69
3.3 Control of the Two Orbital Contributions	84
3.3.1 Experimental results	84
3.3.2 Model construction	88
PAPER II	93
3.4 Effect of the Molecular Distribution	99
3.4.1 Experimental results	100
3.4.2 Simple model	101
3.4.3 QRS like model	103
3.5 Study of the harmonic polarization	104
3.5.1 Origin of ellipticity and offset angle	105
3.5.2 Spectral amplitudes and phases measured for the parallel component	109
3.5.3 Vectorial Orbital Tomography (VOT)	110
3.6 Conclusion	111
4 Chirped XUV Multilayer Mirrors	113

PAPER III	115
PAPER IV	133
4.1 Conclusion	143
5 Conclusions and perspectives	145
A Atomic Units	149
B Symmetry properties of the Fourier transform	151
Acknowledgments	153
References	154

INTRODUCTION

“What then is time? If no one asks me, I know: if I wish to explain it to one that asketh, I know not.” (The Confessions of St. Augustine)

The question “What is time?” was always hard to answer. St. Augustine asked himself more than 1500 years ago, but even in the beginning of the 21st century we do not have a common unique answer. We meet with time in the *everyday* life, like asking: “What time is it?” or like lacking time to finish a PhD thesis. In the *society* and *economy* time is usually referred to be money. From the *philosophical* point of view there are several interpretations. Newton considers time as part of the universe, separated from space and both being absolute (Rynasiewicz [132]). Time is a dimension in which events occur in sequence. On the contrary, for Leibniz (Burnham [16]) and Kant (McCormick [102]), time is not an event nor a thing, it is rather an intellectual concept (*a priori*) that makes humans able to perceive and compare the sequence of events. In the last century Heidegger went even further relating time to the existence of the individual (Stanbaugh [151]).

Considering the *physical* point of view, time is what the clock measures. A sequence of events and we use time also to compare the length of events (duration). As before mentioned, Newton considered the time to be absolute, independent of the reference systems. But, the postulation of a constant and finite speed of light by (Einstein [25]), necessarily changed our understanding of space and time. They are not separated but build up the space-time continuum while both of them become dependent on the reference systems. This implies that two simultaneous events in one reference system are not necessarily simultaneous in another.

The postulation of constant and finite light speed was a fundamental change in physics, that based the time measurements on light. Later on we will see, that the extreme time interval measurements are all using techniques involving the light somehow. Hence, it is not surprising that the Bureau International des Poids et Mesures defines the basic unit of time, *second*¹ on light measurements: *The second is the duration of 9 192 631 770 periods of the radiation corresponding to the transition between the two hyperfine levels of the ground state of the caesium 133 atom* (BIP [1]).

From everyday life we also know that time passes from the past through the present towards the future. In physics numerous processes are symmetric (reversible) to time, but time is attributed with a direction by the Second Law of Thermodynamics (Srivastava and Jain [150]) implying that processes/events (time as well) have to follow the direction which leads to entropy increase.

Through the history of mankind, several ways were developed to measure the elapsed time. Usually we compare the length of the investigated sequence of events to a stable periodic reference process. At the beginning the time measurements aimed to make easier the everyday life, to measure seconds, minutes or hours with burning candles, sand or sun

¹Here is a list for some useful prefactors and corresponding values: ms = 10⁻³s, μ s = 10⁻⁶s, ns = 10⁻⁹s, ps = 10⁻¹²s, fs = 10⁻¹⁵s, as = 10⁻¹⁸s, zs = 10⁻²¹s.

Target types	ΔL	v	t
Gallop horse	few cm	≈ 10 m/s	few ms
Flying bullet	few mm	≈ 500 m/s	μ s
Flowing red blood cells	sub μ m	≈ 10 m/s	few ns
Slow conformation changes in proteins	sub-nm	≈ 10 m/s	few 10 ps
Vibration of molecules	sub-nm	≈ 1 km/s	≈ 100 fs
Intra-atomic electron motion	sub-nm	$\approx 10^6$ m/s	≈ 100 as

Table 0.1: List of different targets/processes and of the corresponding time resolutions. More detailed description can be found in (Zewail [182]).

watches or the modern quartz arm watches. Observation of the periodic motion of the star constellations led to the definition of the year and seasons, aiming to improve the agriculture. As the technology developed scientists could see even farther in the past by using telescopes to study stars similar (and not similar) to the Sun and foresee the future of our solar system on the time scale of billion years. Scientists could even determine the age of the Universe, possibly the most largest observable time period, studying the cosmic microwave background radiation and obtaining 13.75 billion ($\times 10^9$) years (Jarosik *et al.* [57]). The exploration of the shorter time scales was also led by practical reasons, maybe not serving as noble purposes like agriculture, but by deciding whether all four of a horse's hooves are off the ground at the same time during a gallop (Leslie [91]). Eadweard Muybridge came up with the wonderful idea and also managed technically to solve this question, namely to take pictures one after the other using a fast shutter to decrease the exposure time. This idea opened up the route to image fast motions. By zooming in matter, the constructing elements become smaller, thus the resolution has to be better and the shutter faster. To have a clear (not blurred) image of the target, the target should move less than its own size while the shutter opens and closes. Assuming that v is the target (or process) velocity and ΔL is the maximum allowed displacement of the target in order to get a clear image, the exposure time t can be estimated with a simple calculation: $t = \frac{\Delta L}{v}$. Table 0.1 presents the time resolutions needed to observe different phenomena. There is a theoretical lower limit for measurable/detectable time intervals foreseen by quantum gravity. It is called Planck time, $t_P \sim 10^{-44}$ s, and on this scale space and time are supposed to become fuzzy, leading to the ultimate time resolution (Ng *et al.* [116]).

Electronic motion induced effects inside atomic, molecular or nano structures are the basic phenomena in biology, chemistry and physics (Krausz and Ivanov [74]). Charge transfer in these systems is responsible for bioinformation and initiates conformation changes in biomolecules, bond breaks in chemistry, nanoscale current effects in physics, etc. All these phenomena take place on sub-fs time scale. Control over electronic dynamics on this micro level could result in steering electrons in a chemical bond. In order to get a simple image of the properties of quantum dynamics, let us consider a particle in the superposition of two states with ΔE energy difference. The time dependent expectation value of an observable for this superposition of states will oscillate with $T_{osc} = 2\pi\hbar/\Delta E$. To do one oscillation between two different energy states on a sub-fs timescale, $\Delta E \geq 3$ eV energy difference is needed. If charge transfer accompanies this oscillation between two states, electromagnetic radiation is created through dipole oscillation, having the same T_{osc} oscillation period and ΔE spectrum. Thus, XUV radiation is an ideal tool to induce and investigate attosecond quantum dynamics. The process, called High Harmonic Generation (HHG) bears all the characteristics to create pulses with as duration.

High Harmonic Generation

The first realization of laser emission (Maiman [97]) launched a new era in light-matter interaction. The exploitation of the non linear behavior of matter was discovered soon after, by (Franken *et al.* [35]), i.e. second harmonic generation. Frequency up/down conversion became possible when sending light field in crystals with nonlinear dielectric polarization response.

Due to enormous efforts put in laser development, at the end of the 20th century Titanium:Sapphire (Ti:Sap) based laser systems could reach sub-10 fs pulses with energies on the order of microjoules (see a very good review by (Brabec and Krausz [15])). When focusing such pulses, the intensity in the focal spot reach peak intensity higher than $\geq 10^{15}$ W/cm². The electric field of the laser light at these intensities becomes comparable with the static Coulomb field experienced by an outer-shell electron in an atom. Therefore it may distort the atomic potential barrier, leading to highly nonlinear effects. Frequency up-conversion from the visible to the XUV domain was first achieved by focusing strong laser light to atomic gas jets by research groups in Chicago (Mcpherson *et al.* [105]) and in Saclay (Ferry *et al.* [33]). The result surprised everyone, since the spectrum gave a very characteristic form (see Fig. 0.1), namely a plateau region with constant amplitudes and a sudden cut-off with exponential decrease. This phenomena is known as High Harmonic Generation. Describing HHG as a sequence of three separate steps provides a simple phys-

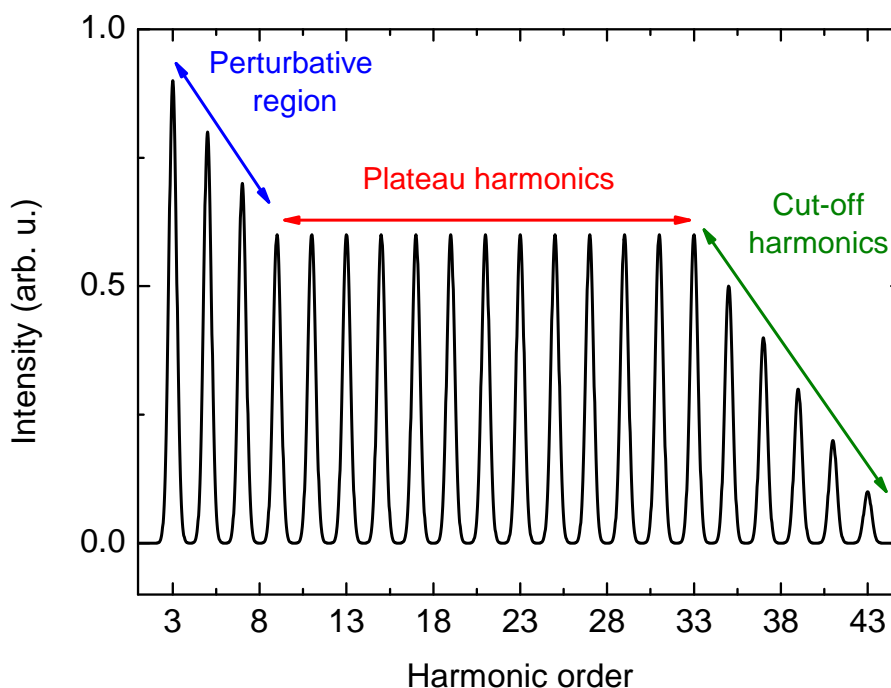


Figure 0.1: Schematic visualization of a high order harmonic spectrum.

ical picture (Corkum [21], Lewenstein *et al.* [93], Schafer *et al.* [138]). In the first step (i), as already mentioned, the strong electric field of the laser distorts the potential barrier, until an electron is able to tunnel out. When liberated (ii), it gets steered and accelerated by the laser field. As the sign of the electric field changes, the electron might be driven back to the ionic core where it can recombine (iii) and emit XUV photon covering a spectral range of several tens or hundreds of eVs. This process can be repeated each half cycle of the laser oscillation producing a train of pulses. The process is triggered by the laser's electric field, hence all the emitted harmonics are coherent.

The XUV radiation obtained with HHG has several advantages with respect to other sources in this spectral range: a) Spectral coherence - It was foreseen by (Farkas and Toth [29]) that the sequence of these coherent harmonics can form an attosecond pulse in the time domain. This characteristic was confirmed in 2001 for Attosecond Pulse Train (APT) by (Paul et al. [122]) and for single attosecond pulses (SAP) by (Hentschel et al. [47]); b) High brilliance and ultrafast spectroscopy - These pulses are promising tools to do XUV-pump, XUV-probe measurements (Tzallas et al. [162]), non-linear XUV processes (Papadogiannis et al. [118]) or to control and steer electron dynamics (Drescher et al. [23], Hockett et al. [51], Shiner et al. [145]); c) Spatial coherence - The short wavelength of the XUV radiation in the sub-Ångström (Å) region allows the coherent lensless diffraction imaging of nano-size structures with only few tens of nm spatial resolution (Gauthier et al. [37], Morlens et al. [109], Ravasio et al. [127], Sandberg et al. [135]). It was also shown, that the Free Electron Lasers, producing intense but not coherent XUV synchrotron radiation, can be seeded by the harmonics generated from gas targets, leading to better temporal coherence and possibly allowing applications with fs temporal resolution (Lambert et al. [77, 78]).

Molecular Structure and Electron Dynamics Study Using HHG

Right after the discovery of HHG, people realized its importance. But unfortunately the laser to XUV emission conversion efficiency is very low. During the '90s the experiments were focusing on maximizing the harmonic signal from gas phase medium and it was found that atoms give higher signal than molecules. Thus, molecules were put aside. But as the laser technology developed and new theoretical simulations were appearing, concerning the study of molecular structures, the attosecond community slowly turned back to molecules. Since HHG in molecules/atoms requires the tunnel ionization of an electron and its re-collision, this electron can be used as a tool to provide structural and dynamical information (Lein [87]). Especially, the new advances on mid-infrared (MIR) lasers, allow to generate higher energy electrons (see the discussions in 1.4) providing larger range of spatial and temporal resolution.

Three substantial methods exist to extract structural or dynamical information from the re-collision process. Two of them are based on electron (possibly ion) detection. In one case the returning electron scatters elastically or inelastically on the Coulomb potential of the molecule. Either way the angularly resolved electron distribution pattern bears information on the size of the molecule or even on induced charge rearrangement dynamics. Elastic scattering is studied via electron diffraction imaging (Meckel et al. [106], Spanner et al. [149]), while the inelastic process by non-sequential double ionization (Kling et al. [70], Niikura et al. [117], Rudenko et al. [131]), when two electrons are removed from the molecule. The other case is when the molecule is exposed to the XUV radiation generated through HHG. The absorption of one XUV photon directly ionizes (see Molecular Frame Photoionization (Holmegaard et al. [52], Lebeck et al. [83, 84])) or excites (pumps) and a second XUV or IR pulse probes the molecule (Caillat et al. [17], Drescher et al. [23], Haessler et al. [42], Tzallas et al. [162]), creating an electron that is detected.

We concentrate on the third method here, since it provides the basis of this thesis and it is mainly discussed in Chapter 3. In this scheme, referred as *self-probing*, one detects and characterizes the high harmonic emission created during the interference between the unbound re-colliding electron wavepacket (EWP) and its bound part. An important breakthrough was the theoretical description and experimental observation of high degree optical molecular alignment can be achieved in field free conditions (Rosca-Pruna and Vrakking [129], Seideman [141], Stapelfeldt and Seideman [152]). The intensity of the generated harmonics is controlled by the alignment beam's time delay (Velotta et al. [169]) and gives a hint on the symmetry of molecular orbitals (Lein et al. [89]).

The possibility of molecular alignment plus the characterization of the harmonic emission in amplitude and phase in the self-probing scheme gives access to the complex valued angularly resolved transition matrix elements of the recombination. This is a great advantage with respect to the studies done with synchrotron radiation, since there the phase is not accessible. Manfred Lein and the group at Imperial College in London paved the way for molecular structure studies via the self-probing scheme (Lein et al. [88, 89]). Their simulation revealed that if approximating the molecule as a two center emitter, interference pattern appears in the harmonic spectra as a function of the molecule's alignment with respect to the laser. Alignment dependent *structural minima* may appear when the harmonics, emitted from the two centers, interfere destructively, providing information on the separation of the atoms inside the molecule. It was investigated experimentally mainly in CO₂ by several groups (Boutu et al. [13], Kanai et al. [63], Vozzi et al. [171]). The only, but very clear, problem was that each experiment found different atomic separations. This contradiction was solved by the proposition of multiple orbitals contributing to HHG by (Smirnova et al. [147, 148]) and first observed experimentally by (McFarland et al. [103]). In molecules the bound states are energetically close to each other and lower lying orbitals like HOMO-1, HOMO-2 etc. may contribute to tunnel ionization, inducing laser intensity (I_L) dependent electron dynamics, leading to intensity minima in the harmonic spectrum, called *dynamical minima*. Multi-orbital contributions provide a tool to control the evolution of intra-molecular electron dynamics on as time-scale by controlling the I_L or the molecular alignment (see PAPER I and (Torres et al. [159], Wörner *et al.* [179])).

The group of NRC at Ottawa proposed a revolutionary approach to study molecular structures, notably to reconstruct molecular orbital wavefunctions (Itatani et al. [54]) based on the self-probing scheme. They measured the harmonic signal from aligned molecules and applied the principle of tomography to probe the molecule from different angles. With clever assumptions they retrieved the Recombination Dipole Moment (RDM) in the molecular frame and applied a mathematical trick to access the Highest Occupied Molecular Orbital (HOMO). This idea led to buzzing discussions in the attosecond community (Le et al. [81], Schwarz [140], van der Zwan et al. [166], Walters et al. [176], Zwan and Lein [186]). The investigation of the validity and applicability of the principle and the extraction of additional information from phase measurements provided the main motivation for this thesis (see PAPER I). Recent results of (Vozzi et al. [172]) raised molecular tomography to even higher level of study and meanwhile initiated new discussion concerning the assumptions made and the determination of RDM's phase.

Tunnel ionization of an electron may lead to bond weakening, especially in molecules containing light atoms, inducing nuclear vibration on the as time-scale. A technique, called *Probing Attosecond Dynamics by Chirp Encoded Recollision* (PACER), was proposed and tested by the group of Imperial College, to evidence nuclear motion by measuring the intensity of the emitted harmonics (Baker et al. [7, 9], Lein [86]). Later on, (Kanai et al. [65]) and (Haessler *et al.* [44]) made a heroic try to study the spectral phase of high harmonic emission as an observable to probe the nuclear dynamics, but the predicted phase variation seemed to be too small to be observed. Parts of this thesis pushed the idea a bit further, foreseeing new ways of sub-fs molecular dynamics studies.

Better understanding of structural and dynamical information encoded in the HH signal requires the detection and analysis of many observables. Apart from the spectral intensity and phase, the measurement of harmonic's ellipticity and offset angle was also realized using XUV polarimetry (Lee et al. [85], Levesque et al. [92], Mairesse et al. [101], Zhou et al. [184]). Despite the linear polarization of the generating laser light, when the symmetry of the aligned molecular ensemble with respect to the generating laser is broken, elliptically polarized harmonics can be generated. Several theoretical attempts exist to explain the

origin of the (sometimes quite high) harmonic ellipticities, starting from one contributing orbital (Le *et al.* [82], Ramakrishna *et al.* [126], Sherratt *et al.* [144], Zimmermann *et al.* [185]) or from multiple orbital contributions with coupling between ionization channels (Mairesse *et al.* [101]). Even in a plane wave based theory, (small) ellipticity can be obtained, assuming that the active electron is ionized at one atomic center within the molecule and recombined at the other (Etches *et al.* [27]). The symmetry of molecular orbitals is related to specific characteristics in polarization (Hijano *et al.* [50], Levesque *et al.* [92]). Measurements resolved in polarimetry may bring additional indication on two-center type structural minima (van der Zwan and Lein [165]) and may provide more precise molecular orbital tomographic reconstruction (Gibson and Biegert [38]).

The holy-grail for all these techniques would be the time-resolved measurement of chemical reactions. Especially, it is attractive for tomography, since it could follow the ongoing changes in the molecular wave function (Le *et al.* [81]). A major difficulty for following photo-excited reactions with HHG spectroscopy is that only $\approx 10\%$ of the target molecules will be excited so that their HHG signal will be lost among that of the unexcited molecules. A promising approach has appeared, based on transient grating technique to initiate dissociation of molecules (Wörner *et al.* [178]). By detecting the interference between the harmonic emission between the excited/unexcited molecules, the harmonic intensity and phase from the excited molecules is retrieved which are related to structural changes as a function of time with as resolution.

Self-probing scheme still hides great possibilities to study molecules. Control over the continuum EWP is still in infancy and new ideas come up day after day. Adding a low intensity second order harmonic frequency, perpendicularly polarized with respect to the generating laser, with a controllable delay, has already provided examples to determine atomic orbital symmetry (Shafir *et al.* [142]) and the instant when the EWP is tunnel ionized. Possible future application may be to induce controlled charge rearrangement during the excursion of the EWP and probe it at the instant of recombination.

Motivation and Outline of the Thesis

This work has started in the end of 2008 in the continuation of the work of Stefan Haessler, the previous PhD student of Dr. Pascal Salières. His work included the first truly experimental tomographic molecular orbital reconstruction, while the author of this thesis was involved in the interpretation and analysis of the results. The gathered knowledge, during that period and the suddenly raised and not answered questions gave the first push and determined the main direction of this thesis. The second subject was motivated by the need of high flux, compressed attosecond pulses with the possibility of pulse shaping for applications.

Chapter 1 is dedicated to the description of the theoretical background of HHG. It starts with the definition and short presentation of helpful physical principles and mathematical tools that are inevitable when explaining the HHG process. We detail all the theoretical approximations and ideas that provide the basis for tools used in the experiments and in the main work; thus reading Chapter 1 is highly advised.

Chapter 2 is the technical part of the thesis. It shortly presents the experimental setups, parameters and conditions used during the work. It details the principle of non-adiabatic molecular alignment, different spectral phase measurement techniques and describes the basis of harmonic polarimetry for determining the ellipticity and the offset angle of harmonics generated from molecules.

Chapters 3 and 4 are presenting the experimental results obtained during the period of the thesis. The Chapters may consist of larger sub-parts, standing as individual islands but related to other parts of the Chapters. Each sub-part consist of experimental results and the

related theoretical simulations and they are finished with the related article (if it exists). We tried not to repeat the content of articles, but rather to enforce their scientific message with missing information (due to length limitation) and present unpublished results.

Chapter 3 is the largest part of the thesis. The theoretical support for this section was provided by the group from the Université Pierre et Marie Curie, Paris consisting of Richard Taïeb, Alfred Maquet, Jérémie Caillat, Roland Guichard and Cecilia Giovanetti-Teixeira. It is focused on the tomographic reconstruction of molecular orbitals. All the experiments and studies were performed on N_2 .

The first part is related to the results presented in Paper I, where the first truly experimentally based reconstruction of molecular wave functions was performed. We lay down the basics of molecular orbital tomography. Then, by studying the angular dependence of the measured spectral phase, we uncover harmonic contributions from HOMO-1, especially enhanced when molecules are aligned perpendicular to the generating laser polarization. Finally, we present a way to image the dynamics of the electron hole density that is created through simultaneous ionization of HOMO and HOMO-1.

The second part is the continuation of the previous work with the three-fold aim presented in Paper II. By applying our phase measurement technique, we investigate how the multi-orbital contributions can be controlled by changing the I_L . We will show that the spectral phase is much more sensitive to structural or dynamical minima. Simulating the measured phase behavior, we also show evidence of switching from major HOMO contribution to multi-orbital contributions by finely tuning the I_L . Furthermore, from theoretical considerations, we identify the nuclear wave packet motion in the HOMO-1 ionization channel, initiating a new kind of experimental approach to investigate as electronic and nuclear dynamics.

The third part focuses on the understanding of the spectral phases measured from different molecular alignment ensembles. In contrast to many earlier studies, we emphasize the importance of the averaging over the alignment distribution. Up to now, tomography was performed with macroscopic harmonic intensity and phase, while the single-orientation molecular response may contain sudden phase jumps, that are washed out by the averaging over the alignment.

In the last part of Chapter 3 we present our results on the most complete harmonic characterization performed up to now, when besides the spectral amplitude and phase, the ellipticity and the offset angle of the polarization ellipse, is also measured. These observables give access to parallel and perpendicular components of the harmonic field with respect to the laser polarization. We reconstruct the molecular orbitals from both of the components and attempt to clarify the origin of ellipticity.

Chapter 4 studies the possibility of compressing and shaping as pulses, based on the Papers III and PAPER IV. The group of Franck Delmotte, Sébastien de Rossi and Charles Bourassin-Bouchet from Laboratoire Charles Fabry, Institut d'Optique, provided specially designed aperiodic multilayer mirrors for the XUV spectral domain to compensate the so called attochirp of the XUV emission from HHG. Our group at Saclay tested the mirrors by measuring the spectral phase after reflection. Three different spectral responses were demonstrated for three mirrors resulting in three different temporal profiles for the reflected as pulses. Driven by the need of versatile XUV pulse shaper, we proposed a novel way to induce changes in the temporal profile of the as pulses.

THEORETICAL BACKGROUND

In the beginning of the theoretical part we present some useful mathematical and physical tools that give aid when describing HHG and the phenomena observed in attosecond physics. Later on HHG itself is presented. All 3 steps of HHG, tunnel ionization, continuum acceleration and recombination will be examined in details and all the techniques used later in the main part will be clarified.

RÉSUMÉ DU CHAPITRE

Dans ce chapitre, nous présentons et détaillons les outils mathématiques et principes utiles à la physique attoseconde. La nature de toute impulsion de courte durée est liée à son spectre large. Tout d'abord, nous définissons un outil mathématique appelé paquet d'ondes qui permet de décrire à la fois les impulsions lumineuses et les électrons. Nous établissons le lien entre profil temporel et profil spectral et nous présentons certaines de leurs caractéristiques, comme le retard de groupe, dérive de fréquence, etc... La plupart des principes définis ici seront largement utilisés au chapitre 4.

Un électron piégé dans un puits de potentiel occupe des états électroniques bien définis énergétiquement. C'est le cas dans les atomes ou petites molécules par exemple. Nous présentons dans ces deux cas les caractéristiques de ces états, leur allure et la technique utilisée pour leur calcul. Un électron peut aussi librement se propager dans le voisinage d'un puits de potentiel. Nous rappelons quelques-uns des modèles décrivant de tels électrons, comme l'approximation d'ondes planes ou la théorie de la diffusion.

Les impulsions attosecondes sont le résultat de l'interaction ultra-rapide entre des impulsions laser de haute intensité et des cibles gazeuses. Ce processus s'appelle la génération d'harmoniques d'ordres élevés. Nous présentons et détaillons un modèle simple qui rend compte du phénomène: le modèle à trois étapes. Celui-ci isole le moment où (i) le champ électrique intense et rapidement oscillant du laser abaisse la barrière de potentiel de l'atome ou de la molécule et libère un électron par effet tunnel, puis (ii) cet électron est accéléré dans le champ du laser et redirigé vers son ion parent où (iii) il se recombine produisant des impulsions attosecondes. Nous discutons les différents modèles de l'ionisation tunnel, les conséquences de l'excursion de l'électron dans le continuum et les différentes méthodes pour décrire la recombinaison. Nous présentons également l'évolution possible de la fonction d'onde nucléaire de l'ion parent, pendant que l'électron en est éloigné. Enfin, nous présentons comment l'émission UVX macroscopique se construit à partir d'un ensemble de cibles en phase gazeuse.

Les principes définis dans le modèle en trois étapes donnent par ailleurs la base du schéma d'auto-sonde décrit dans le chapitre 3.

1.1 Wavepackets

In attosecond science we often meet with the dynamical evolution of light and charged particles which are treated with the Maxwell- and Schrödinger equations, respectively. Their solutions are waves with well defined energies. Experimentally we are able to measure their energies, but we never obtain a Dirac peak at a given energy. Therefore it is better to describe the solutions of the previous equations as the superposition of wave solutions that correspond to different energies. Such kind of superposition is called a *wavepacket*. With other words, the wavepacket has a non-negligible amplitude in a restricted range of space and time and close to zero elsewhere (Atkins and Friedman [5]). If the time dependent solutions of the motion equation corresponding to different energies are labeled as $\Psi_\omega(x, t)$ ¹, where ω is the so called angular frequency, related to the energy of the particle, x is the spatial coordinate and t is time then the wavepacket in general can be written as:

$$\Psi(x, t) = \int g(\omega)\Psi_\omega(x, t)d\omega, \quad (1.1)$$

where $g(\omega)$ is the shape function. To examine the characteristics of wavepackets, $\Psi_\omega(x, t)$ has to be derived. From now on we will study the special cases of optical wavepackets and electron wavepackets (EWP).

1.1.1 Optical Wavepackets

Let us consider the temporal and spatial evolution of the electric field $E(x, t)$ of a propagating light in a non-magnetic medium along the x axes, that is determined by the sourceless Helmholtz equation:

$$\frac{\varepsilon}{c^2} \frac{\partial^2}{\partial t^2} E(x, t) = \frac{\partial^2}{\partial x^2} E(x, t), \quad (1.2)$$

where ε is the dielectric constant and c is the speed of light in vacuum. The solution of 1.2, $E(x, t)$, gives the vectors of the electric field whose superposition construct an optical wave packet and the solution is given in the form:

$$E(x, t) = A e^{i[k(\omega) \cdot x - \omega t]} \hat{e}_z, \quad (1.3)$$

where A is the amplitude of the electric field (but we are not interested in it, for the moment), \hat{e}_z is the unit vector in the z direction and $k(\omega)$ is the frequency dependent wavenumber, defined through the so called dispersion relation:

$$k(\omega) = \frac{n(\omega)\omega}{c}, \quad (1.4)$$

where $n(\omega) = \sqrt{\varepsilon(\omega)}$ is the refractive index. The behavior of the refractive index is related to the medium of propagation. In vacuum $n(\omega) = 1$, thus the wavenumber is a linear function of the frequency. The air, crystals or other optical elements can introduce non-linear dispersion relation through $n(\omega)$ leading to pulse distortions. These effects are going to be discussed in the following.

Let us construct an optical wavepacket by substituting 1.3 to 1.1 and by using a gaussian form as the shape function, that is centered around ω_0 and has a width of σ :

$$g(\omega) = \frac{1}{\sqrt{2\pi}\sigma} e^{-\frac{(\omega-\omega_0)^2}{2\sigma^2}} \quad (1.5)$$

$$E(x, t) = \hat{e}_z \int g(\omega) A e^{i[k(\omega)x - \omega t]} d\omega. \quad (1.6)$$

¹For the sake of simplicity we consider only one spatial dimension

In an optical wavepacket, defined like in 1.6, the spectral amplitude is important only around ω_0 . To study the dispersion effects caused by the medium, we expand $k(\omega)$ as a Taylor-series around ω_0 and discard the derivatives with higher order than three:

$$k(\omega) = k(\omega_0) + (\omega - \omega_0) \left. \frac{\partial k}{\partial \omega} \right|_{\omega_0} + \frac{1}{2} (\omega - \omega_0)^2 \left. \frac{\partial^2 k}{\partial \omega^2} \right|_{\omega_0} + \frac{1}{6} (\omega - \omega_0)^3 \left. \frac{\partial^3 k}{\partial \omega^3} \right|_{\omega_0} + \dots \quad (1.7)$$

When multiplying the wavenumber with the spatial coordinate x , one gets the angular frequency dependent *spectral phase* $\phi(\omega)$. We introduce new parameters as the product of each term in 1.7 and x , in order to visualize their effect on the wavepacket:

$$\text{Zeroth order spectral phase [rad]} : \varphi_0(\omega) = k(\omega_0)x \quad (1.8)$$

$$\text{Group delay [s]} : \mathbf{GD} = x \left. \frac{\partial k}{\partial \omega} \right|_{\omega_0} = \left. \frac{\partial \varphi(\omega)}{\partial \omega} \right|_{\omega_0}$$

$$\text{Group delay dispersion [s}^2\text{]} : \mathbf{GDD} = x \left. \frac{\partial^2 k}{\partial \omega^2} \right|_{\omega_0} = \left. \frac{\partial^2 \varphi(\omega)}{\partial \omega^2} \right|_{\omega_0}$$

$$\text{Third order dispersion [s}^3\text{]} : \mathbf{TOD} = x \left. \frac{\partial^3 k}{\partial \omega^3} \right|_{\omega_0} = \left. \frac{\partial^3 \varphi(\omega)}{\partial \omega^3} \right|_{\omega_0}$$

Each of these terms introduce different changes on the temporal shape of the wavepacket and on its electric field. We investigate them separately:

- Substituting only the first term, $k(\omega) = k(\omega_0)$ into 1.6 one obtains a gaussian shaped pulse in time at a given x coordinate:

$$\mathbf{E}(x, t) = e^{-\frac{t^2 \sigma^2}{2}} e^{ik(\omega_0)(x-v_p t)} \hat{\mathbf{e}}_z, \quad (1.9)$$

where $v_p = \frac{\omega_0}{k(\omega_0)}$ is the *phase velocity* of the central frequency component. The pulse shape and duration are not affected by the propagation, only shift of the spectral phase, $\varphi_0(\omega) = k(\omega_0)x$, is added to the oscillation of the electric field under the pulse shape (see Fig. 1.1 a, e, when $\varphi_0(\omega) = 0$ and $\varphi_0(\omega) = k(\omega_0)L$). The characteristics of a light pulse are defined on the intensity profile (that is proportional to the modulus square of $\mathbf{E}(x, t)$). The spectral bandwidth ($\Delta\omega$) and the pulse duration (τ_0) at full width of half maximum (FWHM) are:

$$\Delta\omega = 2\sigma\sqrt{\ln 2} \quad (1.10)$$

$$\tau_0 = 2 \frac{\sqrt{\ln 2}}{\sigma}. \quad (1.11)$$

The pulse durations characterized by eq. 1.11 are the smallest duration that can be related to a given spectral bandwidth. These pulses are called Fourier limited and these are the unique pulses which fulfill the equality in the following general formula, that relates the spectral and the temporal domain:

$$\Delta\omega\tau \geq 2.77. \quad (1.12)$$

- The group delay \mathbf{GD} results a linear spectral phase, which is responsible for a temporal shift, while the temporal pulse shape remains unchanged just as the pulse duration:

$$\mathbf{E}(x, t) = \hat{\mathbf{e}}_z e^{-\frac{(\mathbf{GD}-t)^2 \sigma^2}{2}} e^{ik(\omega_0)(x-v_p t)}. \quad (1.13)$$

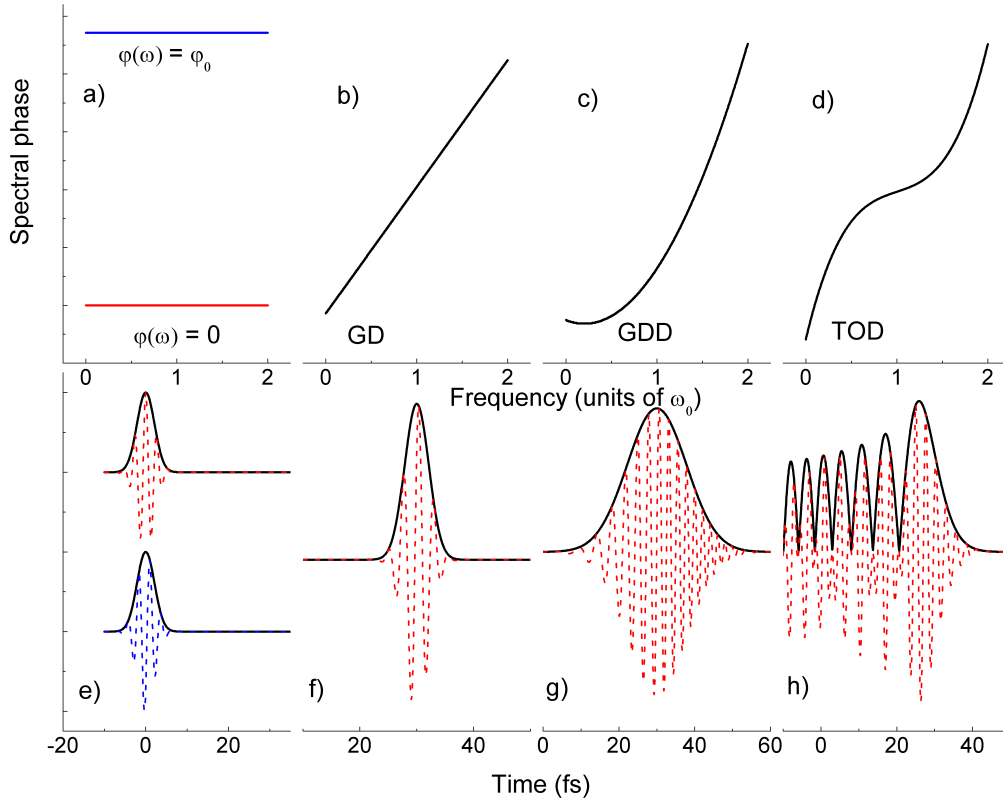


Figure 1.1: Influence of the different spectral phase terms on the temporal envelope and electric field profile. a-d present the spectral phase as a function of frequency given in the units of the angular frequency of an 800 nm wavelength. e-h show the corresponding envelope (black line) and electric field (red and blue dashed lines) as a function of time in fs units.

An example is presented in Fig. 1.1 b, f, where the group delay corresponds to 30 fs shift in the time domain. The **GD** is directly related to the *group velocity* $v_g = \frac{\partial \omega}{\partial k}$, that determines the velocity of the envelope of the pulse.

- When group delay dispersion (**GDD**) is present, the different spectral "slices" propagate with different group velocities leading to pulse broadening. In this case both the envelope and the phase of the wavepacket are distorted:

$$E(x, t) = \hat{e}_z \frac{1}{\sqrt{\gamma}} e^{-\frac{(GD-t)^2 \sigma^2}{2\gamma^2}} e^{i[k(\omega_0)(x-v_p t) + \frac{1}{2} \arctan(GDD\sigma^2) - \frac{(GD-t)^2 GDD\sigma^4}{2\gamma^2}]}, \quad (1.14)$$

where $\gamma = \sqrt{1 + GDD^2 \sigma^4}$. The spectral phase takes a quadratic shape shown in Fig. 1.1 c, the amplitude of the pulse, in the time domain, decreases by $\sqrt{\gamma}$ and the pulse duration (τ) increases with respect to the previous Fourier limited pulse durations (τ_0):

$$\tau = \tau_0 \sqrt{1 + \frac{(2 \ln 2)^4 GDD^2}{\tau_0^4}}. \quad (1.15)$$

The temporal phase $\varphi(t)$ is modulated quadratically due to the presence of the group delay dispersion. This modulation can be quantified with the derivative of the phase with respect to time, called *instantaneous frequency*: $\omega(t) = -\frac{\partial \varphi(t)}{\partial t}$, and the second derivative, named *chirp*: $\alpha(t) = -\frac{\partial^2 \varphi(t)}{\partial t^2}$. From equation 1.14 it is evident, that there

is a constant phase term, which only shifts the electric field under the envelope; that $\omega(t)$ is centered at ω_0 and varies linearly around it due to *GDD*. In Fig. 1.1 g, positive *GDD* was applied resulting in a red shifted instantaneous frequency on the leading edge and blue shifted on the falling edge. The effect of negative *GDD* is inverse. There is a simple connection between the spectral and temporal domain concerning the group delay dispersion and the chirp:

$$\alpha(t) = \frac{GDD \sigma^4}{1 + GDD^2 \sigma^4}. \quad (1.16)$$

Usually materials found in nature possess positive group delay dispersion, thus if a Fourier limited pulse passes through the material, it becomes stretched with red component on the leading edge and blue on the falling edge. A plasma medium may induce high order dispersion terms and chirp the traversing laser pulse. The compensation of the *GDD* (or chirp) of a pulse is an essential procedure in laser science.

- When the spectral phase is a cubic function of the frequency, third order dispersion (TOD) becomes observable. In the temporal domain it introduces Airy oscillations:

$$\Psi(x, t) = 2\pi e^{ia[\frac{2a^2}{3} - b]} Ai(b - a^2), \quad (1.17)$$

where $a = -\left(\frac{2}{TOD}\right)^{\frac{2}{3}}\left(\frac{1}{i2\sigma^2} - \frac{GDD}{2}\right)$, $b = \left(\frac{2}{TOD}\right)^{\frac{1}{3}}(GD - t)$ and *Ai* is the Airy function, that can be expressed with the modified Bessel functions (Abramowitz and Stegun [2]). Fig. 1.1 d presents the spectral phase and 1.1 h shows how the shape of the pulse is distorted. The main big peak is preceded by slowly decaying smaller peaks. For an opposite value of TOD, these distortions occur on the falling edge. In mode locked laser pulse generation, the appearance of third order dispersion is very probable, which destroys the quality of the laser beam.

In general, heading towards the generation of short pulses, the appearance of the above listed dispersions and pulse shape distortions is inevitable. When talking about attosecond pulses all these dispersions have to be compensated over a huge spectral bandwidth in order to obtain Fourier limited pulses. These problems are addressed in Chapter 4.

1.1.2 Electron Wavepackets

The quantum mechanical properties of electrons are described by the solutions of the Time Dependent Schrödinger Equation (TDSE). To familiarize with the basic behavior of an electron, we construct an EWP from *free electron* wavefunctions, that means, no external force (potential) is affecting the dynamics of the electron. In this case the TDSE takes the following form, considering only one spatial dimension:

$$i\hbar \frac{\partial}{\partial t} \psi(x, t) = -\frac{\hbar^2}{2m_e} \frac{\partial^2}{\partial x^2} \psi(x, t), \quad (1.18)$$

where \hbar is the reduced Planck constant and m_e is the electron mass. The harmonic solution in 1.3 is also appropriate to resolve the TDSE for free electrons, just with a different dispersion relation:

$$\psi(x, t) = e^{i[k(\omega)x - \omega t]}, \quad (1.19)$$

$$k(\omega) = \sqrt{\frac{2m_e\omega}{\hbar}}. \quad (1.20)$$

Expanding $k(\omega)$ or $\omega(k)$ in their Taylor series, one may obtain characteristics in spatial or temporal domain, respectively. In both cases, the relation between the wavenumber and

the frequency is non-linear, thus the wavefunction of the free electron will spread spatially and temporally during its propagation, even in vacuum. Each of the ω components will propagate with a group velocity $v_g = \frac{\hbar k}{m_e}$, thus the higher energy components travel faster than the lower energy ones, leading to spatial spreading. Conversely, each k component acquires a group delay $GD(\omega) = x\sqrt{\frac{m_e}{2\hbar\omega}}$ showing how much time it needs to get to the point x . These properties play an essential role in HHG as we will see in section 1.4.

1.2 Atomic Electronic States

1.2.1 Bound States

After study of the dynamics of the free electron, the aim of this section is to collect some knowledge on the characteristics of bound electron wavefunctions. The stationary electronic states in systems with potential barrier $V(\mathbf{r})$ are referred to as *bound states*, since the particles are trapped inside the potential. They possess discrete negative energies that are eigenvalues of the time independent Hamiltonian (\mathcal{H}): $\mathcal{H} = -\frac{1}{2}\nabla^2 + V(\mathbf{r})$. From now on, in the equations atomic units will be used, except stated otherwise. See Appendix A for the translation into SI system. Since in this case there is no time dependent force affecting the dynamics of electrons, their wavefunctions can be factorized as: $\psi(\mathbf{r}, t) = e^{-iEt}\phi_E(\mathbf{r})$ resulting in the following time independent Schrödinger equation (TISE):

$$E\phi_E(\mathbf{r}) = \left(-\frac{1}{2}\nabla^2 + V(\mathbf{r})\right)\phi_E(\mathbf{r}). \quad (1.21)$$

First we investigate the eigenfunctions $\phi_E(\mathbf{r})$ and corresponding eigenvalues (E) of a Hamiltonian constructed in atoms and then we turn to molecules.

In hydrogenic type atoms the bound electrons are trapped by the Coulomb potential $V(\mathbf{r}) = -Z/r$ of the point like nucleus with charge Z . The TISE with this potential has analytical solutions that can be found in text books like (Cohen-Tannoudji et al. [20]). When solving the TISE the eigenfunction $\phi_E(\mathbf{r})$ is further factorized to radial and angular functions, this way introducing a new effective potential:

$$V_{eff}(r) = -\frac{Z}{r} + \frac{l(l+1)}{2r^2}, \quad (1.22)$$

where l is the angular momentum. The second term in 1.22 is a repulsive potential and it competes with the attractive Coulomb potential to prevent the electron of falling in the nucleus. But the repulsive potential tends to 0 faster ($\sim \frac{1}{r^2}$) than the Coulomb potential ($\sim \frac{1}{r}$), thus far from the nucleus it is mainly the Coulomb potential that steers the electrons (this becomes important later for the scattering states, see 1.2.2).

The eigenfunction of the Hamiltonian is characterized by 3 quantum numbers: n – main quantum number, l – angular momentum and m_l – magnetic quantum number, and it takes the following form:

$$\phi_{nlm}(\mathbf{r}) = R_{nl}(r)Y_{lm}(\theta, \varphi). \quad (1.23)$$

The radial part of equation 1.23 is $R_{nl}(r) \propto e^{-r/n}(2r/n)^l L_{n-l-1}^{2l+1}(2r/n)$, where the $L_{n-l-1}^{2l+1}(2r/n)$ are the associated Laguerre polynomials. The angular part, $Y_{lm}(\theta, \varphi) \propto P_l^m(\cos\theta)e^{im\varphi}$, corresponds to spherical harmonic and $P_l^m(\cos\theta)$ are the associated Legendre polynomials. The associated energy eigenvalues are: $E_n = -Z^2/n^2$. A one-electron wavefunction defined by the three principle quantum numbers is called an *atomic orbital* (AO):

- $n \in \mathbb{N}^+$ being the main quantum number, determining the total number of energy levels of the electron (E_n) and the total number of radial and angular nodes $n - 1$.

- $l = 0, 1, 2, 3, \dots, n - 1$ specifies the orbital angular momentum, and these numbers are also associated with the letters s, p, d, f, ... There are l angular nodes in the wavefunction and thus $n - l - 1$ radial nodes.
- $m_l = -l, \dots, l$, thus there are $2l + 1$ different states for each l value. It means that an E_n energy level is n^2 times degenerate. This is characteristic for the hydrogen like atoms, but this degeneracy is lost when considering multiple electrons. It also specifies the component of the angular momentum, for example if $l = 1$, then $m_l = 0$ refers to p_z orbital.

In many electron systems the repulsive effect between the electrons has to be taken into account. The effective potential of the nucleus felt by an electron will not be symmetric and Coulomb like, but will be distorted by the surrounding electrons. Thus the Hamiltonian should contain a sum of repulsive Coulomb like potential over all the electron pairs: $\sum_{i < j} 1/r_{ij}$, but such kind of approach to solve the TISE is very time and power consuming. Instead approximations are made that in general provide acceptable solutions.

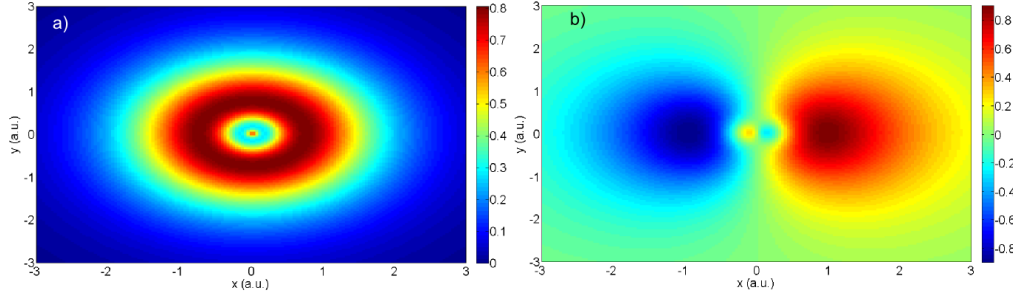
One approach is to assume an *effective nuclear charge* Z_{eff} , where $Z_{eff} < Z$ and it is not necessarily integer. This is due to the shielding of other electrons. Each atomic orbital is characterized by different effective charge, and for example an ns -electron feels a less shielded potential than does an np -electron. This l dependent shielding is the cause of not having degenerate states anymore in multi-electron systems. The construction of the so called *Slater type orbitals* (STOs) are expressed with the help of the effective charges. These orbitals serve for more sophisticated numerical simulations as initial wavefunctions.

Pseudo-potentials are very clever tools for imitating artificially the characteristics of the atomic potential (Muller [110], Wörner et al. [177]). This is an l dependent analytic formula including fitting parameters. The pseudo-potential is considered well behaving when the solutions of the TISE can give back the experimentally observed characteristics of the atom, like the Cooper-minimum in argon (for a comparison of different pseudo-potentials, see (Le et al. [79])).

A powerful numerical procedure is the *Hartree-Fock* (HF) approximation or with another name, the method of *self-consistent fields*. Several computational packages are based on this procedure and we used the GAMESS code (Schmidt et al. [139]) to calculate the atomic orbitals of argon in Chapter 3. Such orbitals are presented in figure 1.2. The main assumption behind HF is that each electron moves in an average potential created by the other electrons and the nucleus and that can be expressed as a single charge centered on the nucleus. This approach also assumes that all the electron wavefunctions are known, except the one we are looking for, in order to calculate the averaged potential. Slater type of orbitals or even equation 1.23 can be used as initial wavefunctions. Then by solving the TISE we obtain a new wavefunction. This new result is used to recalculate the average potential, and the whole procedure starts again with a new electron. These steps are repeated until the previous wavefunctions do not differ much from the new ones. The n -electron wavefunction is expressed as the antisymmetrized product of n one-electron wavefunctions.

1.2.2 Continuum Electronic States

When an unbound electron is propagating in the vicinity of a nucleus, like the electron before recombination during the HHG, its state cannot be described by the solutions of the free particle (see section 1.1.2). The electron may interact with the potential of the nucleus and scatter on it, hence such kind of electronic states are called *scattering* or *continuum* states. Scattering is affected by the energy and the direction of the incoming electron. Hence, TISE


 Figure 1.2: Hartree-Fock electron wave function for Ar: a) 3s b) $3p_x$ state.

takes the following form:

$$E\psi_k(\mathbf{r}) = \left(-\frac{1}{2}\nabla^2 + V(\mathbf{r}) \right) \psi_k(\mathbf{r}), \quad (1.24)$$

where $V(\mathbf{r})$ is the potential of the nucleus as a function of $\mathbf{r} = (r, \theta, \varphi)$, $\psi_k(\mathbf{r})$ is the continuum electronic state, where k refers to the energy dependence. Although, $V(\mathbf{r})$ may be complicated near the nucleus, due to the many-electron interaction inside an atom/molecule, at infinity the energy is asymptotically approaching the energy of the free electron $E = \frac{k^2}{2}$, thus it is positive and continuous. $\psi_k(\mathbf{r})$ alone is not square integrable, but by constructing wavepackets as presented in section 1.1, they become square integrable. Hence, a continuum electron is always in a superposition of states that are solutions of equation 1.24.

The usual approach to solve equation 1.24 is to divide the potential into short range $U(\mathbf{r})$ and long range $V^l(\mathbf{r})$ potentials. The short range potential tends to zero much faster than the long range as $r \rightarrow \infty$. Then, one solves the Schrödinger equation with each potential and connects them and their first derivative continuously at the edge of the defined potentials. There is a very important form of the calculated wavefunctions, called *asymptotic form*, obtained by assuming $V(\mathbf{r}) \xrightarrow{r \rightarrow \infty} 0$. This is the form of the electron when it is far way from the atom and it contains the imprints of the potential, from where the electron re-scattered.

The solution of $\psi_k(\mathbf{r})$ can be expanded in terms of spherical harmonics (see detailed derivation in (Messiah [107])). One may separate the variables into radial and angular terms:

$$\psi_{klm}(\mathbf{r}) = R_{kl}(r)Y_{lm}(\theta, \varphi), \quad (1.25)$$

where $l \in \mathbb{N}^+$, and $m = -l \dots, l$ are being still the angular and magnetic quantum numbers. By assuming that the potential does not vary with φ , $\psi_k(\mathbf{r})$ becomes independent of φ , hence $m = 0$ and the spherical function reduces simply to the Legendre polynomials $Y_{l0}(\theta) = P_l(\cos\theta)$. $R_{kl}(r)$ is describing the radial dependence of the scattering.

If we consider a Coulomb-like potential as the long range potential, $V^l(\mathbf{r}) = -\frac{Z}{r}$, the radial function takes the following form:

$$R_{kl}(r) = \frac{\Gamma(l+1+i\gamma)}{(2l+1)!} e^{-\frac{\pi\gamma}{2}} e^{ikr} (2kr)^l {}_1F_1(l+1+i\gamma; 2l+2; -2ikr), \quad (1.26)$$

where $\gamma = \frac{Z}{k}$ and ${}_1F_1(a; b; c)$ is the confluent hypergeometric function. When dealing with large distances the radial function 1.26 takes the $R_{kl}(r) \xrightarrow{r \rightarrow \infty} \sin(kr - \frac{\pi}{2}l - \gamma \ln 2kr + \sigma_l)$ asymptotic form, with $\sigma_l = \arg \Gamma(l+1+i\gamma)$ called the *Coulomb phase shift* (sometimes it is referred to as scattering phase shift, as in PAPER I, but here we use this name for another parameter). σ_l corresponds to a phase delay between plane waves and continuum waves.

If we use the short range potentials $U(\mathbf{r})$, the solution of continuum states will change but the asymptotic form can be written like this:

$$\psi_k(\mathbf{r}) \xrightarrow{r \rightarrow \infty} \frac{1}{2kr} \sum_l (2l+1) i^{l+1} \left[e^{-i(kr - \gamma \ln 2kr - \frac{l\pi}{2})} - e^{2i\delta_l} e^{2i\sigma_l} e^{i(kr - \gamma \ln 2kr - \frac{l\pi}{2})} \right], \quad (1.27)$$

where δ_l is the so called *scattering phase shift* and it corresponds to an additional phase delay as compared to the previous case. It is energy dependent and it is completely determined by the form of the short-range potential. $\delta_l = 0$ if $U(\mathbf{r}) = 0$ or if $l \rightarrow \infty$, meaning that the continuum electronic state gains back its form of the Coulomb potential. Furthermore, in the high energy particle regime, σ_l and δ_l tend to 0.

These phase shifts play a crucial role in the physics of scattering since they are related to the exact form of atomic/molecular multi-electron potential, thus to the structure of the target. In particular, they will appear in the phase of the recombination dipole matrix element between the continuum and the bound state in HHG (see section 1.4.3). Calculation of exact scattering states is a complicated task. Due to its complexity, only few studies were performed, mainly investigating the so called Cooper-minimum in Ar (Farrell et al. [32], Higuete *et al.* [49], Jin et al. [59], Wörner et al. [177]).

1.3 Molecular Orbitals

Now we shall concentrate on the understanding of why atomic arrangements in molecules are changing in certain conditions, namely in chemical reactions. Molecules consist of multiple nuclei and electrons that are correlated through the attractive and repulsive potentials, thus there is no hope for solving the Schrödinger equation analytically, and even numerically it is a great problem. The only investigated molecule is N_2 in this thesis, so in the following we derive the equations for diatomic molecules.

First the Hamiltonian has to be built up for a diatomic molecule with n electrons positioned at \mathbf{r}_i and two nuclei placed at \mathbf{R}_1 and \mathbf{R}_2 :

$$\begin{aligned} \mathcal{H} &= \sum_{\alpha=1}^2 -\frac{1}{2M_{\alpha}} \nabla_{\alpha}^2 + \sum_{i=1}^n -\frac{1}{2} \nabla_i^2 + \sum_{i<j} \frac{1}{r_{ij}} + \sum_{\alpha<\beta} \frac{Z_{\alpha}Z_{\beta}}{r_{\alpha\beta}} - \sum_{i,\alpha} \frac{Z_{\alpha}}{r_{i\alpha}} \\ &= T_N + T_e + V_{ee}(\mathbf{r}) + V_{NN}(\mathbf{R}) + V_{Ne}(\mathbf{r}, \mathbf{R}), \end{aligned} \quad (1.28)$$

where $\mathbf{r} \equiv \mathbf{r}_1, \dots, \mathbf{r}_n$, $\mathbf{R} \equiv \mathbf{R}_1, \mathbf{R}_2$ and for convenience we introduced T_N and T_e that represent the nuclear and electron kinetic energy operators and $V_{ee}(\mathbf{r})$, $V_{NN}(\mathbf{R})$, $V_{Ne}(\mathbf{r}, \mathbf{R})$ representing the electron-electron, nuclear-nuclear and electron-nuclear interaction potential operators, respectively. Then the TISE looks like the following:

$$[T_N + T_e + V_{ee}(\mathbf{r}) + V_{NN}(\mathbf{R}) + V_{Ne}(\mathbf{r}, \mathbf{R})]\Psi(\mathbf{r}, \mathbf{R}) = E\Psi(\mathbf{r}, \mathbf{R}), \quad (1.29)$$

with $\Psi(\mathbf{r}, \mathbf{R})$ being the n -electron wavefunction of the molecule. There is a difference of several orders of magnitude in the timescale of motion between electrons and nuclei, hence we use the *Born-Oppenheimer* (BO) approximation to separate the contributions of electrons $\phi(\mathbf{r}; \mathbf{R})$ parametrically depending on the nuclear position, and the contributions of the nuclei $\chi(\mathbf{R})$: $\Psi(\mathbf{r}, \mathbf{R}) = \phi(\mathbf{r}; \mathbf{R})\chi(\mathbf{R})$. This assumption has two major consequences:

- a) Nuclear motion is much slower than the motion of electrons, hence the latter can immediately/adiabatically accommodate to the new nuclear positions.
- b) Due to their larger mass, the nuclear wavefunctions are better localized, meaning that they rise more steeply than the electron wavefunctions, resulting in: $\nabla_{\alpha}\chi(\mathbf{R}) \gg \nabla_{\alpha}\phi(\mathbf{r}; \mathbf{R})$

By using the BO approximation one succeeds to describe the electronic and nuclear wavefunctions separately. The electronic states and energies are first calculated for "frozen" nuclei and will thus be parametrized by the nuclear distances \mathbf{R} :

$$\mathcal{H}_e(\mathbf{R})\phi(\mathbf{r}; \mathbf{R}) = [T_e + V_{ee}(\mathbf{r}) + V_{Ne}(\mathbf{r}, \mathbf{R}) + V_{NN}(\mathbf{R})]\phi(\mathbf{r}; \mathbf{R}) = \epsilon(\mathbf{R})\phi(\mathbf{r}; \mathbf{R}). \quad (1.30)$$

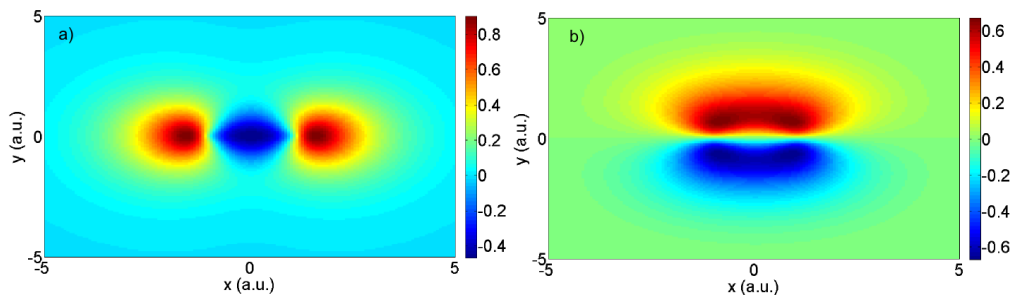


Figure 1.3: Hartree-Fock electron wave functions for N_2 : a) HOMO $3\sigma_g$ b) HOMO-1 $3\pi_u$ orbitals.

This electronic eigenvalue equation results in a set of normalized eigenfunctions $\phi_n(\mathbf{r}; \mathbf{R})$ with the corresponding eigenvalues $\epsilon_n(\mathbf{R})$ that have to be calculated for each nuclear separation. They determine an electronic potential, the so called *Born-Oppenheimer potential* $V_{BO}(\mathbf{R})$. This BO potential enters the hamiltonian for the nuclear part:

$$\mathcal{H}_N \chi(\mathbf{R}) = [T_N + V_{BO}(\mathbf{R})] \chi(\mathbf{R}) = E \chi(\mathbf{R}). \quad (1.31)$$

This procedure helps to find the equilibrium state of the molecule and to understand vibrational dynamics. These things will be more detailed in section 1.4.4.

Having separated the nuclear and electronic part, the next task is to calculate the molecular single-electron wavefunctions, molecular orbitals (MOs). In the previous section, 1.2.1 we have already seen that the Hartree-Fock method can provide us the $\phi(\mathbf{r}_i; \mathbf{R})$ state for the i th electron. In equation 1.30 $V_{ee}(\mathbf{r})$ has to be replaced with an average potential, created by the other electrons. An initial basis set has to be chosen, that may vary in different numerical packages. In an ideal case infinite number of basis functions are available, but numerically it could not be handled. A traditional choice is a finite number of Slater-type orbitals (STOs), with their $e^{-\zeta r}$ radial part. With this exponential term, the evaluation of two-electron integrals becomes complicated and time consuming (especially when there are many of them). Instead, *Gaussian-type orbitals* (GTOs) were suggested (Boys [14]) i.e. $\propto r^l e^{-\alpha r^2}$, since the integral of the product of Gaussian functions is also a Gaussian function. Although, this approach is faster to resolve the two-electron integrals, it needs a larger basis set to reach the same precision as with STOs. In Chapter 3 GTO approach was used to calculate MOs of N_2 . They are presented in fig. 1.3.

Besides these complicated numerical calculations, let us investigate less precise approaches to describe the electronic states in molecules, hoping to obtain some applicable general ideas that reflect some features of those states. The *linear combination of atomic orbitals* is such an approach established by (Lennard-Jones [90]). The principle idea is to construct MOs as a linear combination of a given basis set of atomic orbitals $\psi_i(\mathbf{r})$. Technically only finite number of basis orbitals can be included. This method is going to be detailed for the case of N_2 , linear diatomic homonuclear molecule. In a first approximation, only occupied atomic orbitals of the same symmetry are combined: $\phi(\mathbf{r}) = c_A \psi(\mathbf{r} + \hat{x}R/2) + c_B \psi(\mathbf{r} - \hat{x}R/2)$, where $\psi(\mathbf{r} \pm \hat{x}R/2)$ means that the atomic orbitals are centered on each atomic component and the atoms are bonded along the \hat{x} direction. Due to symmetry reasons in N_2 , $c_A = \pm c_B$ (their exact value will not be relevant to our conclusions). The sign of the coefficients is related to the corresponding MO energy level. The lower energy orbital is a *bonding orbital* while the higher energy orbital is the *antibonding orbital*. These MOs can be classified according to their symmetry properties under the inversion of the electron coordinates. If the molecular wavefunction does not change sign then it has a *gerade*, 'even', symmetry and is denoted g, otherwise it is *ungerade*, 'even' denoted with u.

We need selection rules to choose, for example in N_2 which orbitals should be paired when having the following atomic orbitals at hand: $(1s)^2$, $(2s)^2$, $(2p)_x$, $(2p)_y$, $(2p)_z$. First, the constructing atomic orbitals should be neither too diffuse nor too compact, in order to have strong enough constructive or destructive overlap to build up the bonding. Hence, mainly valence orbitals will play important role in bonding. Second, the energy difference of orbitals should be small. This way the energy of the constructed MOs may be considerably different from the energy of the AOs. As a consequence mainly those orbitals will be paired which have the same n and l quantum numbers, although AOs with the same n but with different l are not so much separated in energy, so they should not be excluded. This is the case for the $N_2 3\sigma_g$ orbital that is a mixture of $2p$ and $2s$ atomic orbitals.

As in the case of AOs, when building up MOs, one fills up with electrons the lower energy orbitals, implementing the Pauli principle as well. If several orbitals have the same energy, then first each orbital is filled up with electrons to decrease the electron-electron repulsion and also to benefit from spin correlation with the same spins. With the aid of all these principles now we are able to construct the MOs of N_2 (without normalization factors):

$$\phi_{1\sigma_g} = \psi_{1s} + \psi_{1s}, \quad (1.32)$$

$$\phi_{1\sigma_u} = \psi_{1s} - \psi_{1s}, \quad (1.33)$$

$$\phi_{2\sigma_g} = \psi_{2s} + \psi_{2s}, \quad (1.34)$$

$$\phi_{2\sigma_u} = \psi_{2s} - \psi_{2s}, \quad (1.35)$$

$$\phi_{1\pi_u} = \psi_{2p_{y/z}} + \psi_{2p_{y/z}}, \quad (1.36)$$

$$\phi_{3\sigma_g} = \alpha(\psi_{2p_x} - \psi_{2p_x}) - \beta(\psi_{2s} + \psi_{2s}), \quad (1.37)$$

where α and β corresponds to the weight of contributing to the construction of the MO. Here, σ and π refers to the cylindrical symmetry of the orbital around the internuclear axis, the former being invariant against the rotation while the latter is anti-symmetric against the rotation by 180° . The angular momentum of MOs is constructed by summing the AO's angular momenta. Thus, a σ orbital does not possess angular momentum, while the π orbitals may have depending on the number of electrons and on their state of spin. The lowest energy level occupied by electrons, here $\phi_{3\sigma_g}$, is called *highest occupied molecular orbital* (HOMO), while the states lying beneath it are referred to as HOMO-1, HOMO-2 etc. respectively. In HHG from molecules these molecular orbitals are playing a crucial role, as it will be shown in Chapter 3.

In the previous section we gave a short introduction to the description of atomic scattering states. Implementing all those principles in molecules is even harder, due to the complexity of the electronic structure. The group of C. D. Lin is pushing the theoretical study of scattering phenomena in HHG with their quantitative re-scattering theory (QRS) (Le et al. [79]) based on the calculations of R. Lucchese (Lucchese et al. [96]). M. Ivanov and O. Smirnova developed a model called eikonal-Volkov approximation (EVA) strictly coupled with strong field phenomena, where they introduce correcting terms to the Volkov function to take into account the atomic/molecular potential (Smirnova et al. [146]).

In chapter 3 we try to recover the molecular structure of N_2 by characterizing indirectly the recombination dipole moment. In this method the continuum states are approximated with plane waves, thus the scattering phase shifts are neglected. There will be a short discussion about the validity of this method.

1.4 High Harmonic Generation

The production of attosecond pulses relies on the processes happening during HHG, that is the result of interaction between an ultrashort high intensity laser pulse and a gas phase medium, as it was shortly presented in the Introduction. Hence, the electrons in the target media are exposed to time dependent potential changes:

$$i\frac{\partial}{\partial t}\psi(\mathbf{r}, t) = \left[-\frac{1}{2}\nabla^2 + V(\mathbf{r}, t) \right] \psi(\mathbf{r}, t), \quad (1.38)$$

where $V(\mathbf{r}, t) = V(\mathbf{r}) + \mathcal{W}(\mathbf{r}, t)$, $\mathcal{W}(\mathbf{r}, t)$ being the term for describing the laser-matter interaction. The strength of the laser field is comparable with the intra-atomic/molecular electric field, therefore its influence cannot be treated as a perturbation. The numerical solution of equation 1.38 for multi-electron systems would be extremely complicated, hence at this early stage, the *single active electron* (SAE) approximation is used. That means, only one electron (usually from the highest occupied orbital) is exposed to the rapidly varying laser field. There are attempts to solve the problem in many electron systems (Patchkovskii et al. [120, 121], Santra and Gordon [137]).

There are two commonly used gauges to describe the laser-matter interactions (Han and Madsen [45]): the length gauge $\mathcal{W}_L(\mathbf{r}, t) = \mathbf{r}E(t)$ and the velocity gauge $\mathcal{W}_V(\mathbf{r}, t) = -i\mathbf{A}(t)\nabla$, where $E(t) = -\partial_t A(t)$ and $A(t)$ is the corresponding vector potential. Quantum mechanics is in principle gauge invariant, hence both of them should give the same result. However, performing approximate theoretical assumptions may give deviations between the two gauges (see section 1.4.3).

A more descriptive way to understand HHG, besides the solution of the TDSE, is the 3 step model. As we already know, it relies on the tunnel ionization, electron acceleration and recombination. The result of these subsequent processes is the burst of XUV emission that is repeated each optical half-cycle (with $T_0/2$ periodicity) of a multi-cycle laser pulse. As the sign of the electric field changes each $T_0/2$, the dipole created in symmetric atoms/molecules is also changing sign: $\mathbf{d}(t + \frac{T_0}{2}) = -\mathbf{d}(t)$. This implies that the emitted harmonic orders are the odd multiples of the fundamental laser frequency. In this thesis we apply multi-cycle laser pulses. Applying near-single cycle pulses, one would end up with a continuum XUV emission. Using asymmetric molecules or asymmetric laser field (e.g. by mixing the laser with its second harmonic) would result in the appearance of even order harmonics.

From now on we will concentrate on describing each of the 3 steps in more details to understand the fundamentals and the basic characteristics of HHG.

1.4.1 Tunnel Ionization

Tunnel ionization is the very heart of HHG and attophysics. This process is responsible for the high non-linearity of harmonic scaling. To build up a descriptive picture of the importance of tunnel ionization we use classical ideas to introduce basic principles.

Let us assume that the electric field of the laser pulse is linearly polarized along the \hat{z} direction, $E = \hat{z}E$, and its intensity is strong enough to distort a Coulomb potential $V_0(z)$ created by a nucleus with an effective charge Z_{eff} . Then, in the length gauge, the total potential felt by the single active electron is:

$$V(z) = V_0(z) + zE, \quad (1.39)$$

where $V_0(z) = -Z_{eff}/|z|$. Figure 1.4 shows the resulting potential (equivalent to the energy of the system in atomic units), for different strengths of the field. When the external electric

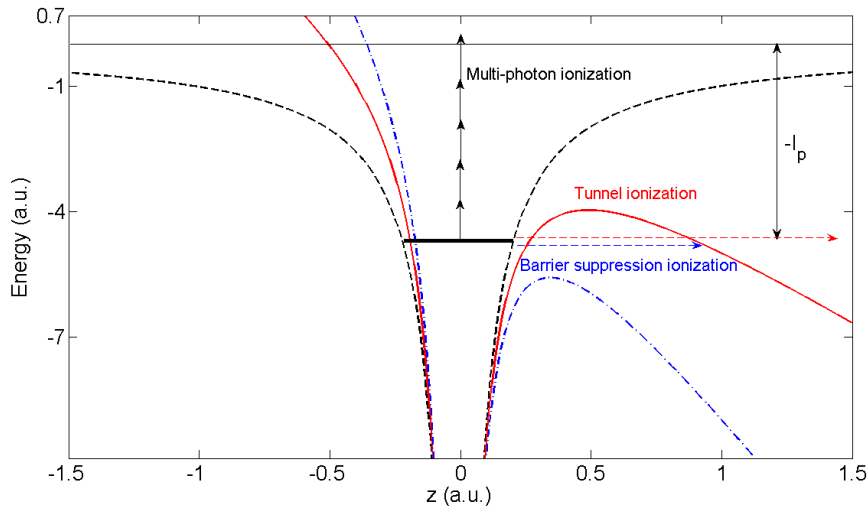


Figure 1.4: Schematic picture of the various ionization processes. Black dashed line represents the Coulomb potential of an atom which has a bound electron on the energy level of $-I_p$, presented by a thick black line. The vertical black arrows show the multi-photon ionization, when the strength of the laser is weak. The red curve represents the distorted potential barrier that allows the horizontal escape of the electron, namely tunnel ionization. When the electric field is strong enough to lower the potential below the ground state of the atom, barrier suppression ionization occurs, see blue dashed line.

field is negligible ($E = 0$), the electron is confined between the potential walls (see the dotted line in figure 1.4). As the strength of the field is increasing, the potential barrier starts to bend (solid line in figure 1.4), creating a potential barrier. At this point tunnel ionization may occur. There is a non-zero probability for the bound electron wavepacket, to propagate under the barrier, while its amplitude is exponentially decreasing. The amplitude of the tunneled EWP will depend on the thickness and height of the potential barrier. By increasing further the electric field until $E = E_{BS}$, the potential barrier decreases below the energy level of HOMO ($V(z_0) = -I_p$, where I_p is the ionization potential), the electron becomes free. This is called *barrier suppression ionization*. The maximum laser intensity (referred to as *saturation intensity* $I_{BS} = E_{BS}^2/(8\pi)$), that can be applied before reaching the barrier suppression ionization can be found by determining the position (z_0) of the inflection point on the potential barrier. By deriving the equation 1.39 with respect to the position, one finds that $z_0 = \sqrt{\frac{Z_{eff}}{E_{BS}}}$. The saturation intensity is found by substituting the z_0 back to eq. 1.39:

$$E_{BS} = \frac{I_p^2}{4Z_{eff}}, \quad I_{BS} = \frac{I_p^4}{128\pi Z_{eff}^2}, \quad I_{BS}[\text{W}/\text{cm}^2] = 4 \times 10^9 \frac{I_p^4[\text{eV}]}{Z_{eff}^2}. \quad (1.40)$$

For the rare gases argon and neon, which $Z_{eff} = 1$, this implies $I_{BS}^{Ar} = 2.5 \times 10^{14} \text{ W}/\text{cm}^2$ and $I_{BS}^{Ne} = 8.6 \times 10^{14} \text{ W}/\text{cm}^2$. These results already foresee the magnitude of the laser intensities that should be applied when generating harmonics.

The potential barrier of atoms and molecules that are exposed to an oscillating laser field, $E(t) = \hat{z}E_0 \cos(\omega_0 t)$, is not static. The tunneling rate of electrons, defined by the transition from the bound to the unbound states, is strong when the electric field reaches its maximum. Due to the fast oscillation, only a small portion of time is available for tunneling. (Keldysh [67]) defined a parameter, γ , that helps to categorize the different ionization regimes. γ is the ratio between the "time" that would need the electron to propagate

through the potential barrier, and the period of the oscillation, $T_0 = 2\pi/\omega_0$. Assuming that the width of the potential barrier is given by I_p/E_0 and that the mean velocity of the electron under the barrier is $\kappa = \sqrt{2I_p}$, γ takes the following form:

$$\gamma \sqrt{\frac{I_p}{2U_p}}, \quad (1.41)$$

where $U_p = E_0^2/4\omega_0^2$ is the ponderomotive potential, i.e. the mean quiver energy of a free electron in the laser field. Tunnel ionization is efficient if the electron has time to get through the potential barrier, i.e. $\gamma \ll 1$. It means that lasers with high intensity and long wavelengths, like IR or MIR, are good candidates. Also, $\omega < I_p$ has to be true, otherwise single-photon ionization takes place. If the intensity is not high enough, $\gamma \gg 1$ then *multi-photon ionization* is the dominant process.

Based on the *strong field approximation* (SFA), namely assuming that the influence of the binding potential on the detached electron can be neglected with respect to the strong external laser field, Keldysh succeeded to deduce a simple expression for the tunnel ionization rate:

$$\Gamma = \frac{(6\pi)^{1/2}}{4} I_p \left(\frac{E_0}{I_p^{3/2}} \right)^{1/2} \exp\left(-\frac{2(\sqrt{2I_p})^3}{3E_0}\right). \quad (1.42)$$

Equation 1.42 is the base of many sophisticated models for tunneling. The exponential term represents the leading factor stating the strong dependence of the tunneling rate on both E_0 and I_p . The pre-factors in front of the exponential become important when $E_0 \gg I_p$ makes the exponential term tend towards 0.

Equation 1.42 is very simple and already includes the very basic characteristics of tunnel ionization. It does not include however the multi-electron effects nor the structure and symmetry of molecular orbitals. For this aim we introduce a new formula for the tunnel ionization rates, that can summarize the various sophisticated models:

$$\Gamma = \Gamma_a R(\theta). \quad (1.43)$$

For the tunnel ionization from atoms $R(\theta) = 1$. We discuss two models below:

Keldysh-Faisal-Reiss (KFR) model (Reiss [128]): This method is essentially based on the Keldysh approach, but using velocity gauge, that results in less assumptions and easier handling of the analytic equations. Based on the SFA the released electron is described with the Volkov states. The model works correctly for the hydrogenlike molecules and for helium, but for more complex atoms, like rare gases, it gives incorrect results.

Ammosov-Delone-Krainov (ADK) model: The model is based on the ionization rate of hydrogenlike atom in a static electric field. The effect of the electronic structure on the tunnel ionization is brought in through the coefficients C_{n^*l} and $f(l, m)$ that contain the effective principle quantum number (n^*), the angular (l) and magnetic (m) quantum numbers (Ammosov et al. [3]):

$$\Gamma = \Gamma_a = C_{n^*l}^2 f(l, m) I_p \left(\frac{3E(t)}{\pi\kappa^3} \right)^{1/2} \left[\frac{2\kappa^3}{E(t)} \right]^{2n^* - |m| - 1} \exp\left(-\frac{2\kappa^3}{3E_0}\right), \quad (1.44)$$

where $C_{n^*l} = \left(\frac{2}{n^*}\right)^{n^*}$, with $l \ll n^*$ and $f(l, m) = \frac{(2l+1)(l+|m|)!}{2^{|m|}|m|!(l-|m|)!}$. The exponential factor of the Keldysh-rate is present, giving the main contribution, but the quantum number dependent factors take care of the orbital specific result. This approach is very convenient and gives reliable rates in some specific conditions, but it is not applicable to molecules.

The calculations of Γ rates for molecules are usually very demanding tasks. Based on the simple approximations used in the atomic case, new methods were developed to include the dependence on the geometry of the molecules. Such models are obtained by the introduction of $R(\theta)$ correcting term, that involves the molecular structure:

Molecular SFA (MO-SFA) model: It is based on the KFR model, but for describing the molecular orbitals, they use the LCAO approach. First it was formulated in the velocity gauge (Muth-Böhm et al. [114]), leading to an orbital symmetry dependency of the tunneling rate. $R(\theta)$ appears as an interference term between the waves that are ionized from the different atomic centers. This explains the ionization suppression observed for the O_2 molecule whose HOMO has a π_g symmetry. The destructive interference between the two O atomic centers leads to a decreased probability of finding the electron on the axis of the molecule, leading to the suppression of tunnel ionization in that direction. This theory was further investigated and details can be found in the following references: (Kjeldsen and Madsen [69], Milošević [108]). One big limitation of MO-SFA is the gauge non-invariance.

Molecular ADK (MO-ADK) model: The model aims to generalize the principles introduced in the atomic ADK model. MO-ADK has the same atomic tunneling rates Γ_a as the equation 1.44. To include molecular characteristics, the molecular electronic wavefunctions in the asymptotic region are expressed in terms of summations of spherical harmonics expanded in one-center (Shan et al. [143], Tong et al. [156]). The coefficients of the expansion are dependent on the angular momentum and magnetic quantum numbers implying alignment dependency $R(\theta)$, with respect to the laser field. Therefore, the orbital symmetry and geometry are inherently involved in $R(\theta)$. The limitation of this approach comes from the single-center expansion of the wavefunctions, that would be problematic for complex, multi-center large molecules.

PYMOLION: In this method, developed by R. Murray et al. (Murray [111], Murray et al. [112, 113]), the electronic wavefunction is described as the sum of basis functions expanded on multi-centers including the coulombic and higher order potential terms as well. Then this electron is propagated with the Wentzel-Kramers-Brillouin (WKB) method through the potential barrier. These considerations lead to a tunneling rate form as equation 1.43, with Γ_a being the tunneling rate for an s atomic orbital obtained with ADK and $R(\theta)$ containing both characteristics of molecular orbital symmetry and interference of the tunneling currents coming from the different lobes of the orbital. In contrast to the other models, this model predicts a laser intensity dependent angular position of the tunnel ionization peak in CO_2 that was confirmed by experiments. Another advantage is that the model contains both the characteristics of MO-ADK and MO-SFA. Hence, PYMOLION is used throughout this thesis to describe the tunneling rates.

1.4.2 Theory of High Harmonic Generation

After tunnel ionization the electron is exposed to the strong external laser field. To describe the behavior of the continuum electron, at this point, we rely on the strong field approximation where the influence of the binding potential is neglected. The electron motion can then be treated classically. As announced in the Introduction this is the 2nd step of the 3 step model first described by P. Corkum (Corkum [21]) and Schafer et al. (Schafer et al. [138]).

Semi-Classical approach

At a certain moment t_i the potential barrier is enough bended for an electron to tunnel ionize (first step), with an initial velocity $\dot{z}(t_i) = 0$. For the sake of simplicity we assume that the position of the electron at t_i corresponds to the position of the atom, $z(t_i) = 0$. It is

considered to be an acceptable approximation, since as we will see below, the length of the trajectory on which the electron is steered until it comes back to the vicinity of the atom, is much larger than the exit point of the tunnel ionization. The Newton equation for the electron motion and its solution take the following form:

$$\ddot{z}(t) = -E_0 \cos(\omega_0 t) \quad (1.45)$$

$$\dot{z}(t) = -\frac{E_0}{\omega_0} [\sin(\omega_0 t) - \sin(\omega_0 t_i)] , \quad (1.46)$$

$$z(t) = \frac{E_0}{\omega_0^2} [\cos(\omega_0 t) - \cos(\omega_0 t_i)] + \frac{E_0}{\omega_0} \sin(\omega_0 t_i)(t - t_i) . \quad (1.47)$$

Several conclusions can be made from these solutions. First, not all the electrons have closed trajectories, meaning not all of them return to the core (see brown line in figure 1.5 a). This is the case for $T_0/4 < t_i < T_0/2$, where T_0 is the period of the field oscillation. Second, the trajectories originating at $0 < t_i < T_0/4$ do return to the core. Some of them may recombine with the core ion, giving XUV emission, while some others may re-scatter resulting in the so called *above threshold ionization* (ATI) electrons. Finally, some of the electrons may return and recombine at a later instant. This shows, that multiple recombination instants t_r may exist for one t_i , although the re-collisions occurring at $t_r > T$ are not contributing to HHG in a detectable manner, since these EWPs are too much spread in space (see the notes in section 1.1.2). Phase matching effects (see section 1.4.5) also decrease their contributions to the macroscopic signal (Antoine et al. [4]).

From now on, we consider only those (t_i, t_r) pairs where t_r corresponds to the first return. Figure 1.5 b presents the re-collision energy, $\dot{z}(t_r)^2/2$ of the trajectories starting from different ionization instants. The first surprising observation is that each energy is related to two different (t_i, t_r) pairs. To make a difference between the rising side of the energy curve in figure 1.5 b (blue squares) and the dropping side (red dots), we refer to them as *short* and *long* trajectories, respectively. Both of them are "born" when $t < T_0/4$, but short trajectories recombine before $\approx 3T_0/4$ while the long ones recombine after $\approx 3T_0/4$. This particular recombination instant corresponds to near zero laser field and gives the most energetic (and unique) electrons, that is the second surprising observation. The re-combining electrons lead to emission of the XUV photons with an energy: $\dot{z}(t_r)^2/2 + I_p$. The most energetic photons (q_{\max} th order) have an energy given by the, so called *cut-off* law: $q_{\max}\omega_0 = I_p + 3.2U_p$, that was first observed in "numerical experiments" by Krause et al. (Krause et al. [73]). In figure 1.5 b, the cut-off is indicated with a dashed line.

The simple cut-off law is already able to predict some useful information concerning HHG. On one hand, the I_p dependence shows that the maximum order of the emitted harmonics varies with the target atom/molecule. On the other hand, $U_p \propto I_L \lambda^2$. Hence, one can achieve higher harmonic order emission either by increasing the intensity of the laser, I_L , but I_p determines an upper applicable limit (see section 1.4.1), or by increasing the laser's wavelength, λ towards the MIR domain. The latter parameter gives more flexibility, but the price to pay is the drop of the HHG efficiency. By increasing λ the excursion time $\tau = t_r - t_i$ of the EWP increases, leading to enhanced spreading that causes low XUV emission signal during the recombination. The exact scaling of the efficiency is not clear yet, but depending on the theory (experiment) it may be $\propto \lambda^{-6-9}$ (Popmintchev et al. [123], Tate et al. [154]). With good phase matching conditions one may shift this rate back towards $\propto \lambda^{-2}$ dependence (Popmintchev et al. [124]).

Assuming that the instant of recombination, t_r corresponds to the instant of emission of harmonic radiation t_e , from figure 1.5 b it comes that the emitted harmonic components are delayed in time from each other. Around the center of the leading and the falling edges, t_e is a linear function of the harmonic energy. This corresponds to a constant GDD, or chirp in

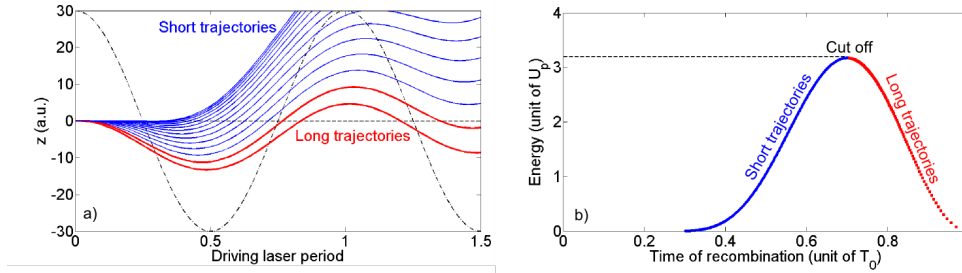


Figure 1.5: Oscillatory motion of the continuum electrons driven by the laser field a). Short and long trajectories are represented by the blue and red lines, respectively. The dashed black line shows the laser field oscillation in arbitrary units. b) presents the kinetic energy at the instant of recombination expressed in units of U_P . Blue dots and red squares correspond to short and long trajectories, respectively. The dashed line indicates the result of the cut-off law, see the text for more details.

the temporal domain. This GDD is called the *attochirp* (Δt_e). Short trajectories have positive, while long trajectories have negative chirp. Therefore, the attosecond pulse constructed by the emitted harmonics is intrinsically not Fourier limited. Furthermore, from the cut-off law one may already suspect, that $\Delta t_e \propto 1/I_L$. The reason for this is that the instant of recombination is always confined to the same part of the laser period, while increasing I_L results in higher energy photons, leading to an increase of the absolute value of the slope of the curve shown in figure 1.5 b). These observations will be justified more clearly when discussing the quantum interpretation of HHG.

From the equations 1.45, 1.46 and 1.47 it is also clear that efficient harmonic generation can be obtained only when using linearly polarized laser field. A small perpendicular component of the field would drive the electrons sideways, so that they miss the core at return. However, because of the spreading of the EWP in the direction perpendicular to the propagation, one may measure harmonic emission up to some degree of ellipticity ($\epsilon \approx 0.2$) of the generating laser field. The recombination probability is higher for molecules than for atoms, because of their spatial extent (Flettner et al. [34]).

Quantum mechanical approach

Lewenstein et al. (Lewenstein et al. [93]) formulated a very descriptive analytic quantum mechanical theory of HHG. They solve the TDSE (equation 1.38) in the length gauge:

$$i \frac{\partial}{\partial t} \psi(\mathbf{r}, t) = \left[-\frac{1}{2} \nabla^2 + V_0(\mathbf{r}) + \mathbf{r} \cdot \mathbf{E}(t) \right] \psi(\mathbf{r}, t), \quad (1.48)$$

where $V_0(\mathbf{r})$ is the Coulomb potential. It is assumed that the system is initially in its ground state ψ_0 . To derive an analytical solution they assume the following:

- (i) Concerning the bound states only the energetically highest occupied orbital (with energy $-I_p$) is contributing to the evolution of the system.
- (ii) Sufficiently energetic electrons in the continuum are only affected by the laser field. They do not experience the Coulombic potential of the ionic core (SFA).

A low frequency field with high enough intensity interacting with a rare gas atom fulfills these requirements, which also corresponds to the conditions for tunneling. The fact that the electron returning to the core, is in fact affected by the coulombic potential, may be included in various ways (Le et al. [79], Smirnova et al. [146]). We return to this question in section 1.4.3.

For the sake of simplicity, the depletion of the ground state is also neglected. To solve the equation 1.48 the wavefunction of the system is written as a superposition of the ground state $\psi_0(\mathbf{r})$ and continuum states $|\mathbf{k}\rangle = e^{i\mathbf{k}\cdot\mathbf{r}}$:

$$\psi(\mathbf{r}, t) = e^{iI_p t} \left[\psi_0(\mathbf{r}) + \int \frac{d^3k}{(2\pi)^3} a(\mathbf{k}, t) e^{i\mathbf{k}\cdot\mathbf{r}} \right], \quad (1.49)$$

where $a(\mathbf{k}, t)$ represents the time dependent amplitude and phase of the corresponding states. The phase of $a(\mathbf{k}, t)$ is defined with respect to the ground state. Substituting Eq. 1.49 into Eq. 1.48 and projecting the result to the space spanned by $\psi_0(\mathbf{r})$ and $|\mathbf{k}\rangle$ one finds a solution for the time dependent amplitudes of the continuum states. Hence, the wavefunction of the system $\psi(\mathbf{r})$ becomes accessible.

The harmonic dipole $d(\omega)$ from an atom/molecule can be obtained by Fourier transforming the time dependent expectation value of the dipole:

$$d(\omega) = \mathcal{F}_{t \rightarrow \omega} [d(t)] \quad (1.50)$$

$$d(t) = \langle \psi(\mathbf{r}, t) | \hat{\mathbf{d}} | \psi(\mathbf{r}, t) \rangle \quad (1.51)$$

Substituting Eq. 1.49 into Eq. 1.51 and neglecting continuum-continuum transitions, since they do not contribute to the harmonic emission, one finds:

$$d(t) = -i \int_0^t dt_i \int d^3\mathbf{p} \mathbf{d}^*(\mathbf{p} + \mathbf{A}(t)) e^{iS(\mathbf{p}, t_i, t)} \mathbf{E}(t_i) \cdot \mathbf{d}_L(\mathbf{p} + \mathbf{A}(t_i)), \quad (1.52)$$

where $\mathbf{p} = \mathbf{k} - \mathbf{A}(t_i)$ is the canonical momentum and

$$S(\mathbf{p}, t_i, t) = - \int_{t_i}^t dt'' \left[\frac{[\mathbf{p} + \mathbf{A}(t'')]^2}{2} + I_p \right], \quad (1.53)$$

is the quasi-classical action of the continuum electron.

Equation 1.52 reflects the 3 step approach of the classical description. (i) Tunnel ionization is given by the $\mathbf{E}(t_i) \cdot \mathbf{d}_L(\mathbf{p} + \mathbf{A}(t_i))$ transition amplitude: it means that at the instant t_i , a part of the bound electron wavefunction tunnel ionizes to the continuum state with \mathbf{p} canonical momentum. The transition dipole matrix element (DME), $\mathbf{d}_L(\mathbf{p} + \mathbf{A}(t_i)) = \langle \mathbf{p} + \mathbf{A}(t_i) | \mathbf{r} | \psi_0 \rangle$ is given in the length form, since it is determined by our choice of gauge made in equation 1.48. (ii) The propagation of the EWP in the continuum with a constant canonical momentum induces a phase given by eq. 1.53: this action depends also on the I_p of the system and not just on the laser itself. This is due to the phase accumulated by the ion. (iii) The recombination is described with the transition from the continuum to the bound state with the recombination dipole matrix elements $\mathbf{d}^*(\mathbf{p} + \mathbf{A}(t)) = \langle \psi_0(\mathbf{r}) | \hat{\mathbf{d}} | \mathbf{p} + \mathbf{A}(t) \rangle$ at the instant t . The spectrum of the XUV emission is given by the Fourier transform of the dipole and by substituting 1.52 into 1.50, one gets:

$$d(\omega) = -i \int dt \int_0^t dt_i \int d^3\mathbf{p} \mathbf{b}(\mathbf{p}, t_i, t) e^{i\varphi_{\text{XUV}}(\mathbf{p}, t_i, t)}, \quad (1.54)$$

where

$$\varphi_{\text{XUV}}(\mathbf{p}, t_i, t) = \omega t + S(\mathbf{p}, t_i, t), \quad (1.55)$$

and $\mathbf{b}(\mathbf{p}, t_i, t) = \mathbf{d}^*(\mathbf{p} + \mathbf{A}(t)) \mathbf{E}(t_i) \cdot \mathbf{d}_L(\mathbf{p} + \mathbf{A}(t_i))$.

In the equations 1.54 and 1.55 each triplet of (\mathbf{p}, t_i, t) determines a quantum path (orbit). The harmonic dipole comes from the integration over the infinite number of quantum paths, which makes the evaluation quite difficult.

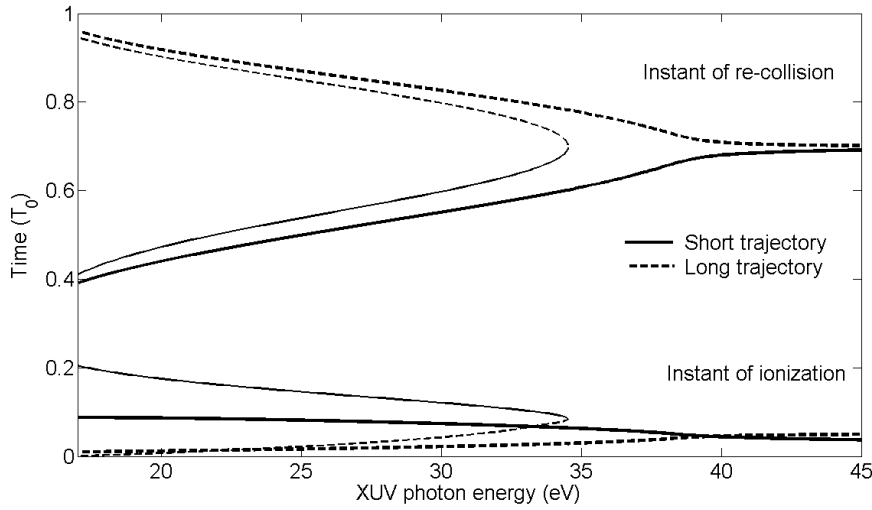


Figure 1.6: Ionization and recombination times as a function of photon energy. Thick and thin lines correspond to quantum and classical calculations respectively. Full lines represent the short while the dashed lines represent the long trajectories. The calculations were done for an argon like atom, with an $I_p = 15.58$. The electric field of the generating laser has a cosine oscillation at 800 nm with $I_L = 1 \times 10^{14}$ W/cm².

Saddle-point approximation

Further simplifications can be performed over the equation 1.54. One may realize that the fastest variation in eq. 1.54 is given by the total phase $\varphi_{\text{XUV}}(\mathbf{p}, t_i, t)$. This rapidly varying phase term (eq. 1.55) will lead to a destructive interference of the contributions of most quantum orbits and only those corresponding to a stationary phase with respect to the triplets (\mathbf{p}, t_i, t) , will give significant contributions to the dipole. (Lewenstein et al. [93], Salières et al. [134], Sansone et al. [136]). Stationary phases φ_{XUV}^s can be retrieved by equating to zero the derivatives of the action, with respect to the canonical momentum \mathbf{p} , instant of ionization t_i and the instant of recombination $t = t_r$:

$$\nabla_{\mathbf{p}} \varphi_{\text{XUV}}(\mathbf{p}, t_i, t) = \int_{t_i}^{t_r} [\mathbf{p} + \mathbf{A}(t')] dt' = \mathbf{r}(t_r) - \mathbf{r}(t_i) = 0 \quad (1.56)$$

$$\frac{\partial \varphi_{\text{XUV}}(\mathbf{p}, t_i, t)}{\partial t_i} = \frac{[\mathbf{p} + \mathbf{A}(t_i)]^2}{2} + I_p = 0 \quad (1.57)$$

$$\frac{\partial \varphi_{\text{XUV}}(\mathbf{p}, t_i, t)}{\partial t_r} = \omega - \frac{[\mathbf{p} + \mathbf{A}(t_r)]^2}{2} - I_p = 0. \quad (1.58)$$

Each of the three above equations reflects one of the assumptions made in the classical description of HHG, proving that the classical approach gives good qualitative description. Eq. 1.56 states that those trajectories are contributing the most which have a closed path i.e. the electrons are returning to the vicinity of the core. This also refers to the conservation of the momentum. Eq. 1.57 implies that the tunneling electron has a negative kinetic energy at the instant of ionization t_i . It means that the real part of the electron's velocity is zero, as it is foreseen by the classical description. This imaginary-valued velocity can be obtained if t_i is complex, that leads us back to the idea of the tunneling time (see section 1.4.1). This has important consequences since all quantities will then be complex. In particular, the imaginary part of the action will give the well known Keldysh exponential factor characteristics of tunnel ionization. Finally, eq. 1.58 means that the kinetic energy of the electron at return plus the binding energy are transferred to the XUV photon during the recombination t_r .

This simply corresponds to the energy conservation law.

By solving the coupled stationary equations one finds the main quantum paths that contribute to the XUV emission, described by the stationary triplets $(\mathbf{p}^s, t_i^s, t_r^s)$, where s represents the order of the stationary trajectories. These stationary triplets are ordered with the magnitude of the excursion time $\tau_s = \text{Re}(t_r^s - t_i^s)$, where the first two of these τ_1 and τ_2 correspond to the already known short and long quantum orbitals, respectively. Figure 1.6 shows a comparison between the classical and quantum trajectories (calculated by Thierry Augustine). For the latter the real parts of (t_i, t_r) are shown. In the plateau region the classical simulation shows good agreement with the quantum calculations, although there are considerable differences in t_i . The biggest difference is in the cut-off region, where the short and long trajectories converge. The quantum calculation leads to the generation of higher harmonic orders than the classical simulation.

Resolving the integrals in eq. 1.54 with the saddle-point method, the harmonic dipole becomes a sum over the stationary trajectories:

$$\begin{aligned} d(\omega, I_L) &= \sum_s \mathbf{b}_s(\omega, I_L) \exp[i\varphi_{XUV}^s(\omega, I_L)] \\ &= \sum_s \frac{i2\pi}{\sqrt{\det(S'')}} \left[\frac{\pi}{i\tau_s/2} \right]^{3/2} \mathbf{d}^*(\mathbf{p}_s + \mathbf{A}(t_r^s)) e^{iS(\mathbf{p}_s, t_i^s, t_r^s) + i\omega t_r^s} \mathbf{E}(t_i^s) \cdot \mathbf{d}_L(\mathbf{p}_s + \mathbf{A}(t_i^s)) \end{aligned} \quad (1.59)$$

where $\det(S'')$ is a 2×2 matrix with the second derivatives of $\varphi_{XUV}(\mathbf{p}_s, t_i, t_r)$ with respect to t_i and t_r . The second term in eq. 1.59 is proportional to $\tau_s^{-3/2}$ is a consequence of the spreading of the EWP during the excursion. As we increase s , τ_s becomes larger as well, hence the spreading is getting more important. That is one of the reasons why only the short and long trajectories are contributing efficiently to a harmonic emission.

1.4.3 Recombination

The choice of the dipole operator in equation 1.51 determines the way of calculating the recombination DMEs. The source term in the Maxwell equations for the emitted XUV field is the acceleration of the dipole moment. Thus in principle, one should use the expectation value of the dipole acceleration operator $\hat{\mathbf{a}}$, although via the Ehrenfest theorem the acceleration dipole operator can be replaced by the velocity $\hat{\mathbf{p}}$ and the dipole $\hat{\mathbf{r}}$ operator. The latter two cases are referred to as the velocity and the length form. Then the harmonic spectrum can be expressed as follows:

$$\epsilon_{XUV}^{\hat{\mathbf{a}}}(\omega) = \mathcal{F}_{t \rightarrow \omega} [\langle \psi(\mathbf{r}, t) | \hat{\mathbf{a}} | \psi(\mathbf{r}, t) \rangle] \quad (1.60)$$

$$\epsilon_{XUV}^{\hat{\mathbf{p}}}(\omega) = \mathcal{F}_{t \rightarrow \omega} \left[\frac{d}{dt} \langle \psi(\mathbf{r}, t) | \hat{\mathbf{p}} | \psi(\mathbf{r}, t) \rangle \right] = i\omega \mathcal{F}_{t \rightarrow \omega} [\langle \psi(\mathbf{r}, t) | \hat{\mathbf{p}} | \psi(\mathbf{r}, t) \rangle] \quad (1.61)$$

$$\epsilon_{XUV}^{\hat{\mathbf{r}}}(\omega) = \mathcal{F}_{t \rightarrow \omega} \left[\frac{d^2}{dt^2} \langle \psi(\mathbf{r}, t) | \hat{\mathbf{r}} | \psi(\mathbf{r}, t) \rangle \right] = -\omega^2 \mathcal{F}_{t \rightarrow \omega} [\langle \psi(\mathbf{r}, t) | \hat{\mathbf{r}} | \psi(\mathbf{r}, t) \rangle] \quad (1.62)$$

There are numerous theoretical studies investigating which combination of the gauge and dipole form is the best, both in precision and in efficiency (Bandrauk et al. [11], Han and Madsen [45]). When calculating the exact $\psi(\mathbf{r}, t)$ wavefunction, the three forms should lead to the same result. However, due to the different approximations made, in particular the SFA, they are in general not equivalent. The question of which form should be used has become especially important for molecules, since the determination of the exact electronic wave functions is even harder in this case. The group of Gordon and Kärtner (Gordon and Kärtner [39]) claims that the acceleration form is the best choice, while Chirilă and Lein (Chirilă and Lein [19]) are supporting the velocity form. Concerning the comparison with the macroscopic harmonic field a very recent study of the group of Madsen (Baggesen and Madsen [6]) states that the velocity form should be the reference.

In this thesis we will use mainly the length form of the dipole combined with the length gauge, unless stated otherwise. The \mathbf{r} dipole operator can be decomposed into parallel \mathbf{r}_{\parallel} and perpendicular \mathbf{r}_{\perp} components with respect to the driving laser polarization (they are written with bold characters to sign their operator role). These features will become important in sections 2.1.1 and 3.5 discussing molecular alignment and harmonic ellipticity. For the moment, we treat the dipole operator generally, without decomposition. In order to generalize it to multi-electron systems and in particular to molecules, we rewrite the recombination dipole moment and neglect the notations concerning the order of the trajectories (since the DMEs do not depend on them):

$$\mathbf{d}_{rec}(\omega, \theta) = \mathbf{d}^*(\mathbf{p} + \mathbf{A}(t_r)) = \langle \psi_i(\mathbf{r}, \mathbf{R}) | \mathbf{r} | \psi_f(\mathbf{r}, \mathbf{R}) \rangle, \quad (1.63)$$

where $\psi_i(\mathbf{r}, \mathbf{R}_i) = \chi_i(\mathbf{R})\phi(\mathbf{r}_1, \dots, \mathbf{r}_j, \dots, \mathbf{r}_N)$ and $\psi_f(\mathbf{r}, \mathbf{R}) = \chi_f(\mathbf{R})\phi^+(\mathbf{r}_1, \dots, \mathbf{r}_{j-1}, \mathbf{r}_{j+1}, \dots, \mathbf{r}_N)\psi_c(\mathbf{r}_j)$ is the initial and final states of the HHG process. The initial state is the product of the nuclear wavefunction $\chi_i(\mathbf{R})$ and of the N electron orbital wavefunction $\phi(\mathbf{r}_1, \dots, \mathbf{r}_j, \dots, \mathbf{r}_N)$. The final state is also decomposed into a nuclear part $\chi_f(\mathbf{R})$, a one electron continuum part $\psi_c(\mathbf{r}_j)$ and to the wavefunction of the $N - 1$ electron ionic core $\phi^+(\mathbf{r}_1, \dots, \mathbf{r}_{j-1}, \mathbf{r}_{j+1}, \dots, \mathbf{r}_N)$. θ is the angle between the laser polarization and the molecular axis. In the case of atoms the above description is valid without the nuclear parts and the angular dependence. The dipole operator does not affect the nuclear wave function, hence their product can be factorized out $\langle \chi_i(\mathbf{R}) | \chi_f(\mathbf{R}) \rangle$, which is called the *nuclear autocorrelation function*. For the moment we assume that the initial and final nuclear wavefunctions are the same, thus $\langle \chi_i(\mathbf{R}) | \chi_f(\mathbf{R}) \rangle = 1$. The role of the autocorrelation function will be discussed in section 1.4.4.

For a correct treatment of the recombination dipole multi-electron effects should be taken into account (Patchkovskii et al. [120, 121], Santra and Gordon [137]), but the work done in this thesis is based on the single active electron approximation, hence we assume that from the N electrons, only the j th one is affected by the laser:

$$\mathbf{d}_{rec}(\omega, \theta) = \langle \phi(\mathbf{r}_1, \dots, \mathbf{r}_j, \dots, \mathbf{r}_N) | \mathbf{r}_j | \phi^+(\mathbf{r}_1, \dots, \mathbf{r}_{j-1}, \mathbf{r}_{j+1}, \dots, \mathbf{r}_N)\psi_c(\mathbf{r}_j) \rangle. \quad (1.64)$$

The \mathbf{r}_j dipole operator acts only on the continuum electron, hence the ionic core can be projected on the neutral molecule, resulting in the so called *Dyson-orbital*: $\psi^D(\mathbf{r}_j) \propto \langle \phi(\mathbf{r}_1, \dots, \mathbf{r}_j, \dots, \mathbf{r}_N) | \phi^+(\mathbf{r}_1, \dots, \mathbf{r}_{j-1}, \mathbf{r}_{j+1}, \dots, \mathbf{r}_N) \rangle$. This projection can be interpreted as the visualization of the created positive electronic hole in the molecular cloud (Smirnova et al. [148]).

More visual picture can be retrieved by further assuming that (i) the multi-electronic states are constructed from Hartree-Fock orbitals, meaning that $\phi(\mathbf{r}_1, \dots, \mathbf{r}_j, \dots, \mathbf{r}_N)$ and $\phi^+(\mathbf{r}_1, \dots, \mathbf{r}_{j-1}, \mathbf{r}_{j+1}, \dots, \mathbf{r}_N)$ are the anti-symmetrized products of single-electron orbitals (see section 1.3); (ii) there is no electronic relaxation in the ion after tunnel ionization, so the remaining occupied electronic states in the ion are identical to the corresponding neutral electronic states, this is the Koopmans approximation (Koopmans [72]). These assumptions results in the fact that the Dyson-orbital simplifies into the orbital from which the electron was removed. That is usually the HOMO orbital. Now, the recombination dipole takes the following simple form:

$$\mathbf{d}_{rec}(\omega, \theta) = \langle \phi(\mathbf{r}_j) | \mathbf{r}_j | \psi_c(\mathbf{r}_j) \rangle = \langle \phi_0(\mathbf{r}) | \mathbf{r} | \psi_c(\mathbf{r}) \rangle, \quad (1.65)$$

where we exchanged \mathbf{r}_j into \mathbf{r} and denoted the active orbital as $\phi_0(\mathbf{r})$.

In this thesis, the atomic/molecular orbitals will be calculated with the Hartree-Fock method, as presented in section 1.3, giving real orbital functions, while for the continuum states of the electron we will use two approaches: plane wave approximation in section 3.1

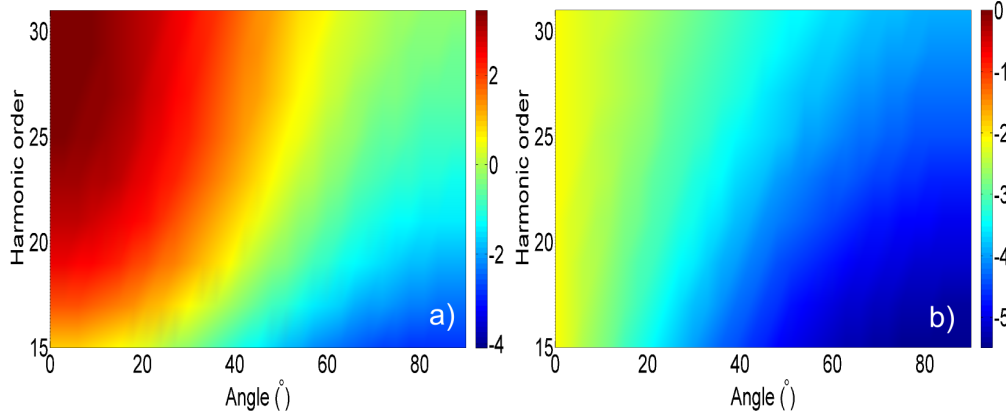


Figure 1.7: Amplitude of the plane wave recombination dipoles for the HOMO and HOMO-1 orbitals in N_2 as a function of angle and harmonic order (with respect to the frequency of an 800 nm laser). The color codes are not the same in the two plots.

and scattering states in sections 3.4 and 3.5. Plane wave approximation neglects the effect of the atomic/molecular potential on the continuum states exploiting the strong field approximation. It is easy to calculate the corresponding dipoles and this leads to comprehensive physical pictures, at the basis of molecular orbital tomography in section 3.2. In this thesis we will consider the HOMO and HOMO-1 orbitals of N_2 with σ_g and π_u symmetry, respectively. In the length form, the plane wave recombination dipoles for the two orbitals, take the following form:

$$\mathbf{d}_{rec}^{HOMO}(\omega, \theta) = \left\langle \phi_{HOMO}(\mathbf{r}) | \mathbf{r} | e^{i\mathbf{k}(\omega) \cdot \mathbf{r}} \right\rangle = \int \phi_{HOMO}(\mathbf{r}) \mathbf{r} e^{i\mathbf{k}(\omega) \cdot \mathbf{r}} d\mathbf{r} \quad (1.66)$$

$$\mathbf{d}_{rec}^{HOMO-1}(\omega, \theta) = \left\langle \phi_{HOMO-1}(\mathbf{r}) | \mathbf{r} | e^{i\mathbf{k}(\omega) \cdot \mathbf{r}} \right\rangle = \int \phi_{HOMO-1}(\mathbf{r}) \mathbf{r} e^{i\mathbf{k}(\omega) \cdot \mathbf{r}} d\mathbf{r} \quad (1.67)$$

where $\mathbf{k}(\omega)$ is the wavenumber of the continuum electron obtained from the canonical momentum. Equations 1.66 and 1.67 are nothing else than a simple spatial Fourier transform of $\phi_x(\mathbf{r}) \mathbf{r}$, where $x = HOMO, HOMO - 1$. Due to symmetry considerations of the Fourier transform, the HOMO recombination dipole is purely imaginary while the HOMO-1 dipole is purely real. This results in a constant $\Delta\varphi_{rec} = \pi/2$ phase difference between the two dipoles. The amplitude of these dipoles is visualized in figure 1.7. The HOMO dipole has a π phase jump in the presented spectral range in the 40-60° angular range, while the dipole of HOMO-1 is rather structureless.

More exact dipoles can be obtained by using the scattering continuum states. For molecules it is very demanding to calculate them, so we had the support from Robert Lucchese (Department of Chemistry Texas AM University) (Lucchese et al. [96]), who provided us with the exact photoionization transition dipoles, both for HOMO and HOMO-1. The detailed balanced principle states that radiative photorecombination is just the inverse process of single-photon ionization. C.D. Lin built up his Quantitative re-scattering theory (QRS) (Le et al. [79]) on this principle, to describe HHG. Up to now, the theoretical simulations obtained with QRS, seem to be in good agreement with experimental results, but there was no direct experimental proof or disproof concerning this assumption. However, the intuition would suggest that in HHG this principle should not apply because of two main reasons: a) The detailed balance is true for the field free equilibrium states. During HHG the high intensity laser field is present, therefore the recombination is not field free. However, the harmonics with the highest energy are recombining near to the instant when the electric field of the laser is near to zero. In this case, the conditions may be near to conditions of the detailed balance. b) HHG is an attosecond time scale coherent process creating a

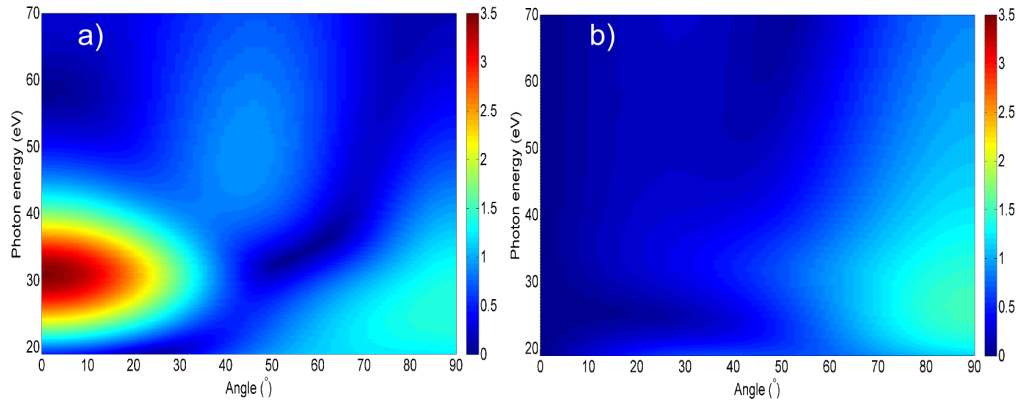


Figure 1.8: Parallel component (with respect to the polarization of the driving laser) of the amplitude of the scattering wave photoionization transition dipoles with respect to the driving field, in a.u., of the HOMO a) and HOMO-1 b) orbitals in N_2 as a function of angle and photon energy.

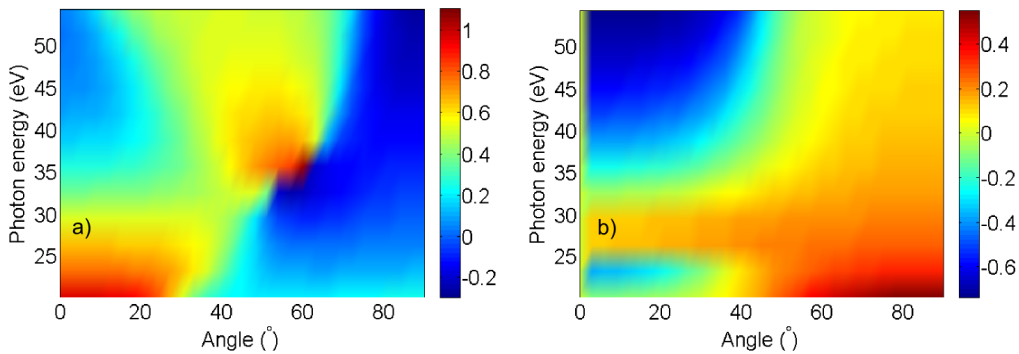


Figure 1.9: Parallel component (with respect to the polarization of the driving laser) of the phase of the scattering wave photoionization transition dipoles with respect to the driving field, in π radians, of the HOMO a) and HOMO-1 b) orbitals in N_2 as a function of angle and photon energy.

temporal filter in the recombination. If there are resonant states with long lifetime, the contribution of their recombination will not add up constructively, because of their incoherent nature. Therefore, long lived resonant states should not be present in the emitted harmonic signal. Nevertheless, the equality between the photoionization and the photorecombination dipole moments during HHG is still an open question.

We implemented also the photoionization dipoles in our calculations. These are complex quantities and figures 1.8 (a, b) and 1.9 (a, b) show the amplitude and phase, respectively of the photoionization dipole (for HOMO and HOMO-1). In contrast to the plane wave dipole, a strong shape resonance is present in the HOMO dipole at low angles between 20 and 40 eV. However, there is no experimental HHG measurement that could observe this shape resonance up to now. Interestingly, in figure 1.9 a, a phase jump around $45-65^\circ$ is present, similarly to the one observed in the plane wave dipoles in figure 1.7 a. The dipole of HOMO-1 does not have resonance structures, but in contrast to HOMO its amplitude is larger at higher angles than at small angles, figure 1.8 b.

1.4.4 Nuclear Wavepacket Dynamics in Molecules

When removing an electron from a bonding orbital the molecule is less tightly bound. During HHG, by the removal of an electron at t_i , the ground state nuclear wavefunction $\chi_0(\mathbf{R})$ is projected onto the ionic nuclear vibrational states. This occurs via a vertical transition, Franck-Condon transition, since it happens on an ultrashort time scale and the nuclei do not have time to move. It may happen that the potential curve of the ionic state is shifted horizontally compared to the one of the neutral state, so that, the new equilibrium distance is larger than that of the neutral molecule, see figure 1.10 a. The vertical transition will then favor the coherent population of many excited nuclear states forming a fast nuclear wavepacket. At the instant of recombination t_r^s for the short trajectory, the evolved nuclear wavepacket $\chi(\mathbf{R}, \tau_s)$ is projected back to the initial ground state, since HHG is a coherent process, see figure 1.10 b. Hence XUV emission efficiency may be decreased if the autocorrelation function

$$C(\tau_s) = \langle \chi_0(\mathbf{R}) | \chi(\mathbf{R}, \tau_s) \rangle = \int \chi_0^*(\mathbf{R}) \chi(\mathbf{R}, \tau_s) d\mathbf{R} \quad (1.68)$$

deviates from 1, i.e. the two nuclear wavepackets only partially overlap after τ_s , as it is presented in the inset of figure 1.10 b.

The effect of autocorrelation is pronounced especially in the case of light molecules like H_2 , where the nuclei can move quickly on the fs time scale. (Lein [86]) showed that in H_2 the autocorrelation function evolves significantly on the sub-femtosecond time scale. Later on (Baker et al. [7, 8, 9]) succeeded to observe this phenomenon both in H_2/D_2 and CH_4/CD_4 pairs, with their PACER technique (Probing Attosecond dynamics by Chirp-Encoded Recollision). PACER relies on the fact, that the recombination times of different harmonics are shifted in time (attochirp), hence each harmonic order probes the ionic core at different nuclear separation. Calibrating the harmonic signal with the heavier isotope, the electronic response can be eliminated, since the electronic structure of the isotopes are similar. The remaining part will correspond to the different nuclear dynamics, allowing the reconstruction of the nuclear separation at each instant of recombination.

Based on the PACER technique, (Kanai et al. [65]) and (Haessler *et al.* [44]) tried to observe the effect of nuclear vibration on the harmonic phase in H_2/D_2 , using mixed gas and RABBIT technique, respectively (both techniques are detailed in section 2.2.2). Both of them investigated the short trajectories. Neither of the experiments could present clear changes in the harmonic phase related to the vibration. Haessler et al. showed theoretically that the phase change is too small for short trajectories but should be measurable for the long trajectories.

(Patchkovskii [119]) performed simulations to investigate the influence of the autocorrelation function on HHG in various (mainly heavy) molecules. Surprisingly, he found a significant influence in many molecules such as O_2 , NO , NO_2 even using an 800 nm laser. In N_2 the effect is found to be negligible. In contrast, in section 3.3 we will show that heavier molecules may also show strong vibrational sub-femtosecond dynamics can be observed in HHG from N_2 when the lower lying orbitals, like HOMO-1 are contributing. We will examine both the intensity and the phase of the harmonics. A recent study done by Farrell et al. (Farrell et al. [31]) come to similar conclusions, analyzing only the intensity of the harmonics generated from water molecules.

1.4.5 Propagation Effects

The XUV radiation detected by the experimentalist is not the direct single atom/molecule response (eq. 1.59), but the macroscopic harmonic field. In this thesis HHG was performed in a supersonic gas jet, where the density of the emitters $n(r)$ is given by the number of

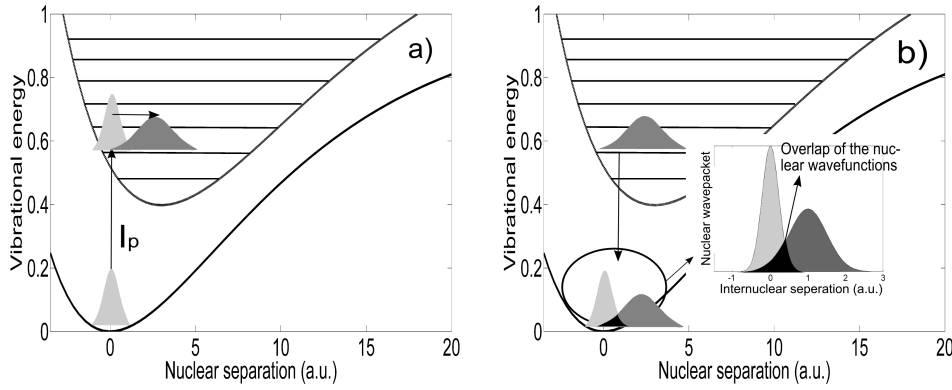


Figure 1.10: a) and b) show the neutral (full curve) and the ionic (dashed curve) potentials. The horizontal lines on the ionic potential curve represent the different vibrational states. In a) the ground state nuclear wave function (light gray) is projected via Franck-Condon transition to the ionic vibrational states. The resulting nuclear wavepacket evolves during the electron excursion in the continuum (dark gray). b) shows the recombination process, where the overlap of the neutral and ionic nuclear wavefunctions is enlarged.

atoms/molecules that interact with the spatial distribution $I(\mathbf{r})$ of the laser beam. The macroscopic harmonic field $E_{XUV}(\omega)$ constructs from the coherent sum of the fields created by the single emitters. It can be obtained from the solution of the Maxwell wave equation with a polarization source $\propto n(\mathbf{r})\epsilon_{XUV}(\omega, I(\mathbf{r}))$. So, the detected harmonic field is given by (L'Huillier et al. [94]):

$$E_{XUV}(\omega, \mathbf{r}') \propto \sum_s \int \frac{e^{ik(\omega)|\mathbf{r}'-\mathbf{r}|}}{|\mathbf{r}'-\mathbf{r}|} n(\mathbf{r}) \mathbf{b}_s[\omega, I(\mathbf{r})] \exp[i\varphi_{XUV}^s[\omega, I(\mathbf{r})]] d^3\mathbf{r}. \quad (1.69)$$

Constructive interference can be obtained in the far field if the phase front of the newly generated local field $\epsilon_{XUV}(\omega, I(\mathbf{r}))$ does not differ much from the propagated field $E_{XUV}(\omega, \mathbf{r})$. This requires good phase matching conditions:

$$\mathbf{k}_q = q\mathbf{k}_L + \vec{\nabla}\varphi_{XUV}^s(q, I(\mathbf{r})), \quad (1.70)$$

where q is the harmonic order, \mathbf{k}_q and \mathbf{k}_L are the wavenumber vectors of the harmonic and laser field, respectively (Balcou et al. [10], Salières et al. [133]), while the last term represents the spatial variation of the phase of the harmonic dipole response and can be approximated as: $\vec{\nabla}\varphi_{XUV}^s(q, I(\mathbf{r})) = -\alpha_q^s \vec{\nabla}I(\mathbf{r})$. α_q^s is a trajectory dependent coefficient, that becomes larger as s increases. Apart from the dipole phase, there are additional factors playing a role in determining both the harmonic and laser wavenumber vectors, like atomic/molecular dispersion, free electron dispersion, geometric dispersion (the Gouy phase shift).

Good phase matching can be achieved if these factors are in equilibrium with the single atom dipole phase variation. For trajectories with $s > 2$ the dipole phase variation is too fast, prohibiting good phase matching conditions. That is the second reason together with the wavepacket spreading, why only the short and long trajectories are considered in the macroscopic signal:

$$E_{XUV}(\omega, \mathbf{r}') = E_{XUV}^{short}(\omega, \mathbf{r}') + E_{XUV}^{long}(\omega, \mathbf{r}'). \quad (1.71)$$

By playing with the experimental conditions, like the positioning of the gas jet along the propagation axis, one can further control the number of contributing trajectories. On axis phase matching can be achieved when the laser is focused before the gas jet. In this case the direction and magnitude of $-\alpha_q^{short} \vec{\nabla}I(\mathbf{r})$ can compensate the phase mismatch caused by

the free-electron dispersion and the Gouy phase, resulting in a macroscopic signal coming from short trajectories. In contrast, when focusing after the gas jet, the long trajectories can be phase matched, but never on axis. It means that the divergence of the long trajectories is higher than the divergence for the short trajectories. When the focus is positioned in the gas jet, both trajectories may contribute. In the far field spatial profile of the harmonic beam, a central spot of short trajectories is then surrounded by annular shaped long trajectories. There is an intermediate region where both of them can be present, interfering with each other, giving rise to the so called *Quantum Path Interferences* (QPIs).

The macroscopic signal is thus the coherent sum of electric fields coming from spatially de-localized emitters which may be shifted in phase. Finally, absorption of the XUV radiation by the medium also modify both the amplitude and phase of the macroscopic field (Ruchon et al. [130]). However, by using a short jet (≈ 1 mm) a low pressure (few 10 Torr) and good phase matching conditions ($I \ll I_{BS}$, jet after laser focus, far field diaphragm) the macroscopic field does not differ much from the microscopic one, restricted to the short trajectories. This is supported by numerous experimental harmonic phase measurements, at least for the short trajectories (Dudovich et al. [24], Mairesse et al. [99], Varjú et al. [168]). These are the experimental conditions used throughout this thesis.

Attochirp and the Harmonic Spectral Profile

Based on the previous discussions from now on we consider that the measured macroscopic harmonic signal is well approximated by the microscopic response for the short trajectories, i.e. $\frac{\partial}{\partial \omega} \arg b_s(\omega, I) \approx 0$ in eq. 1.59. In the case of atoms, where the phase of the recombination dipole moment does not vary rapidly, the group delay related to the measured harmonic phase is determined by $\frac{\partial \varphi_{XUV}}{\partial \omega}$ and therefore, by the instant of recombination t_r (Mairesse et al. [99]). Indeed, deriving equation 1.55 with respect to ω and using equations 1.56, 1.57 and 1.58 one gets:

$$\frac{d\varphi_{XUV}}{d\omega} = \underbrace{\frac{\partial \varphi_{XUV}}{\partial \omega}}_{=t_r} + \underbrace{\frac{\partial \varphi_{XUV}}{\partial t_i}}_{=0} \frac{\partial t_i}{\partial \omega} + \underbrace{\nabla_{\mathbf{p}} \varphi_{XUV}}_{=0} \frac{\partial \mathbf{p}}{\partial \omega} + \underbrace{\frac{\partial \varphi_{XUV}}{\partial t_r}}_{=0} \frac{\partial t_r}{\partial \omega} = t_r. \quad (1.72)$$

The different timing of the recombining electrons is thus included in the quantum mechanical description of HHG as well. Like in the semi-classical model the instant of the recombination corresponds to the "instant" of the XUV emission, hence the real part of the recombination time is sometimes referred as *emission time* (t_e). Since the stationary triplets (\mathbf{p}, t_i, t_r) are varying with the laser intensity, the group delay is also a function of it, as it is presented in figure 1.11 a. This is also true for the spectrum of the harmonic emission figure 1.11 b, where the well known plateau and cut-off region appears. Supported by the cut-off law, by increasing the laser intensity higher order harmonics are generated.

There is no direct way to measure the laser intensity inside the gas jet: it is usually calculated from the measured values of the laser energy, duration and focal spot size. (Mairesse et al. [99]) proposed a technique to retrieve the effective intensity based on the emission time measurements. In certain conditions they show theoretically and measure experimentally that the slope Δt_e retrieved from the plateau region of the emission time curves (thus the group delay dispersion) is inversely proportional to the laser intensity. Their findings are plotted in figure 1.12, for Δt_e , the difference in emission times of two consecutive order. The result in figure 1.12 show that the macroscopic response follows the fixed intensity theoretical response with an effective intensity slightly smaller than the peak intensity. Thus the Δt_e is slightly larger than expected. Throughout this thesis we rely on these findings and use the data in figure 1.12 to determine the laser intensity in our experiments.

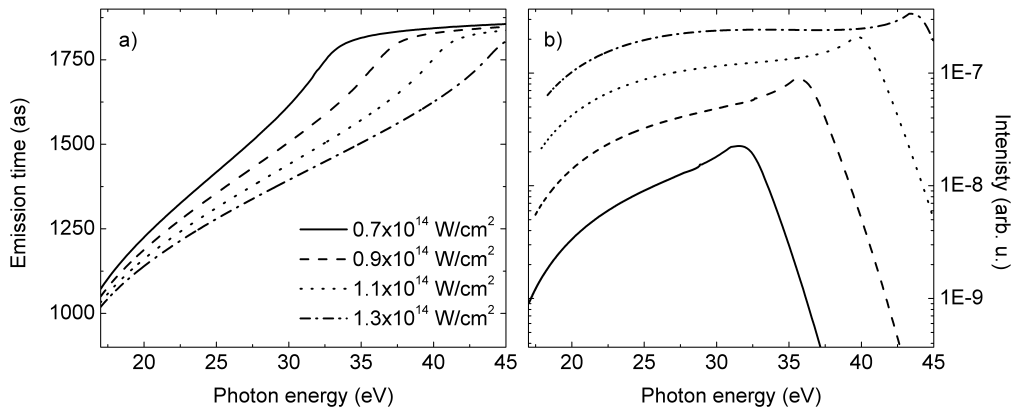


Figure 1.11: Short trajectory emission times (or group delays) a) and harmonic intensity b) as a function of photon energy for different laser intensities. The parameters used for the calculations are the same as in figure 1.6.

Figure 1.12: Difference in emission times of two consecutive orders in the plateau region as a function of generating laser intensity. The figure is taken from (Mairesse et al. [99]) Fig. 1.B (because of copyright reasons we do not present this figure). Theoretical calculation for a fixed intensity is the black line while the experimental measurements correspond to xenon (red triangle), argon (green squares) and neon (blue pentagrams).

In the experiments, the intensity variation in the envelope results in amplitude and phase changes in the XUV bursts at each half cycle of the laser, when I_L is high enough (Varjú et al. [168]). The measurements are an average over these changes.

EXPERIMENTAL TOOLS FOR ATTOSECOND PHYSICS

HHG is a non-linear process. It requires a medium that gives a non-linear response to an excitation. In HHG the excitation is induced by an ultra-short high intensity laser pulse. The exposed medium can be a solid-, gas-, plasma targets, nanoparticles etc. This thesis is exclusively concentrating on laser-matter interaction in gas jets.

Two principal experimental setups can be imagined for the application of high order harmonics:

- (i) In-situ: It is assumed, that during the recombination the accumulated difference between the ground and the continuum states is transferred to the XUV radiation without changes. It means that the amplitude, phase and polarization characteristics of the harmonics are directly related to structural or dynamical features of the target atom/molecule. These informations are traced back by observing and characterizing the harmonic emission. Chapter 3 exploits this approach that is also referred as *self probing scheme*.
- (ii) Ex-situ: Here the harmonic emission is already characterized and is used to induce (*pump*) some dynamical processes in a target medium or *probe* the time dependent dynamic state of an already induced process. This is also referred as pump-probe experiment and requires at least two beams that can be delayed with respect to each other. The third version of this type is when these characterized harmonics are used to determine a specific property of the target, like reflectivity, dispersion etc. The results presented in Chapter 4 are relying on the latter approach.

The experiments presented in Chapter 3 and 4 were performed in CEA-Saclay, on the *Laser Ultra-Court Accordable* (LUCA). This is a laser facility serving several experimental needs. It is run by devoted and high quality experts working in the *Saclay Laser-matter Interaction Center* (SLIC). The laser itself is centered at 795 nm and provides 40 mJ pulse energy in 55 fs duration. Its' repetition rate is 20 Hz.

In this Chapter we detail the experimental tools used during our work. We start by presenting the experimental setup used in Chapter 3 and detail each stage step-by-step. The fundamentals of molecular alignment will also be presented since Chapter 3 applies this technique. Considering the characterization of harmonics several phase measurement schemes are presented that are required for getting a full phase map. Subsequently, the experimental setup and realization of polarization measurements in the XUV domain are discussed.

RÉSUMÉ DU CHAPITRE

Ce chapitre présente les dispositifs expérimentaux et techniques associées utilisés au cours de cette thèse. La génération d'harmoniques élevées et la détection d'impulsions attosecondes peut être divisé en trois étapes qui nécessitent respectivement :

- (i) Des lasers de haute puissance, atteignant des intensités de 10^{14} W/cm² au foyer,
- (ii) une source de gaz sous vide (puisqu'il est absorbé dans l'air)
- (iii) un appareil qui puisse détecter des durées d'impulsions lumineuses avec une précision attoseconde.

Plus précisément, le faisceau laser initial est divisé en trois parties par deux interféromètres de type Mach-Zender: la première partie est utilisée pour aligner les molécules, la deuxième pour générer les harmoniques et la troisième pour caractériser la phase spectrale des harmoniques. Chaque interféromètre comporte une platine de translation nécessaire pour d'une part contrôler la distribution d'alignement des molécules, et d'autre part mesurer la phase spectrale des harmoniques. Pour effectuer des mesures de polarisation, nous avons par ailleurs installé un polariseur à la sortie de la chambre de génération et une lame demi-onde à son entrée afin de faire tourner conjointement la polarisation de l'ensemble des trois faisceaux laser.

La source de gaz est un jet pulsé synchronisé au laser. En le positionnant après le foyer du laser, nous privilégions la contribution des trajectoires courtes, ce qui est une étape cruciale dans nos expériences. La densité et la température est maintenue assez basse pour fournir une bonne qualité d'alignement des molécules. Le paragraphe 2.1.1 décrit le mécanisme d'alignement moléculaire optique.

Les impulsions émises doivent être caractérisées dans le domaine spectral, car il n'y a pas de processus assez rapide pour détecter les dynamiques attosecondes. Nous utilisons un spectromètre électronique à temps de vol à bouteille magnétique pour mesurer à la fois l'intensité spectrale et l'état de polarisation des harmoniques par ionisation à un photon, et la phase spectrale par ionisation à deux photons et deux couleurs, grâce à la technique du RABBIT. Les techniques de mesure de la phase spectrale et de la polarisation des harmoniques sont présentés dans les sections 2.2.2 et 2.2.3.

2.1 Experimental Tools for High Harmonic Generation

The setup of each HHG experiment can be divided into 3 main stages: (i) optical table, where the laser beam is prepared for the focusing into the gas jet; (ii) the generation chamber, where the harmonics are created; (iii) the detection area, where the XUV emission is captured. Figure 2.1 shows the experimental setup that was mostly used in this thesis.

Optical Ingredients

Harmonic generation has become nowadays a relatively simple task, provided a powerful laser is available with a peak intensity of several 10^{14} W/cm² when being focused. But if there is need for both phase characterization and angular resolved molecular studies, 3 laser beams are required.

Our setup consists of two intricate Mach-Zender like interferometers (figure 2.1). The incoming laser beam, that is linearly s-polarized, comes from the upper left side and is split in two. The reflected part is further separated in an outer (*generating*) and inner (*dressing*)

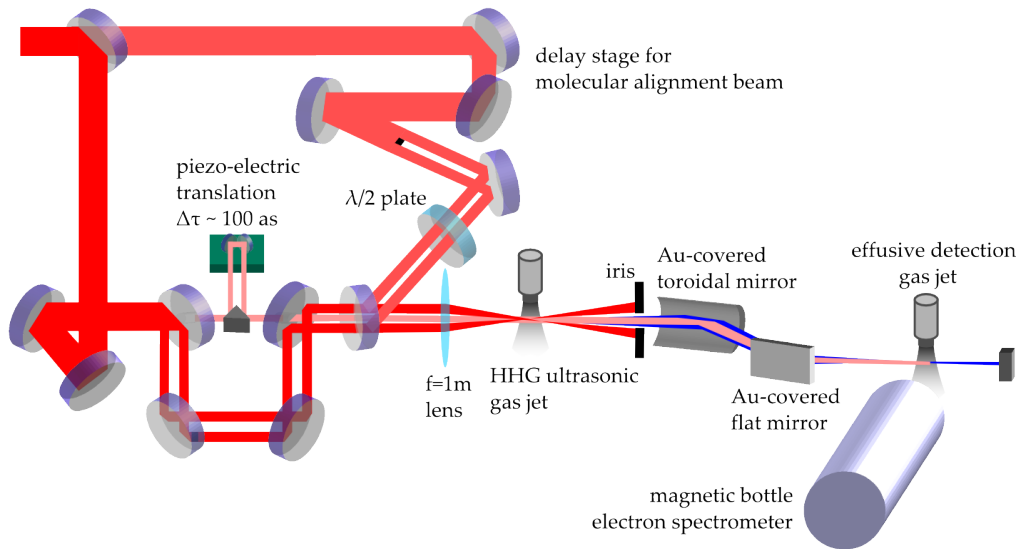


Figure 2.1: Experimental setup used in the experiments presented in Chapter 3 sections 3.2, 3.3 and 3.4.

beam with a drilled mirror. The size of the annular generating beam is approximately 18 mm. It is the most energetic and serves to generate harmonics. The inner part goes through a delay stage and is recombined with the annular part thanks to another drilled mirror. It is used downstream to achieve a cross correlation with the harmonic field and retrieve its spectral phase. The delay between this “dressing beam” and the “generating beam” should be well controlled. That is provided by a piezo-electric translation stage allowing ≈ 100 as precision. As we have seen earlier, the dressing beam has to be fairly weak ($\approx 10^{12}$ W/cm²), so that, first, it does not affect the HHG process and second it keeps the phase characterization in the perturbation regime. The beam, that was transmitted at the first beam splitter goes through a nanosecond precision delay stage and is brought together with the other two beams before the lens, by a second beam splitter. This is the *alignment beam* and serves for molecular alignment. In order to control the direction of the alignment in the laboratory frame, a half-wave plate (HWP) is inserted in this path, after the delay stage. The size of this beam is set to be smaller than the size of the generating beam, in order to align molecules in a larger volume than the volume of harmonic generation. The beam delivers a “moderate” intensity $\approx 0.5 \times 10^{14}$ W/cm², that is not enough to generate harmonics. A 4 cm thick glass block was also inserted in the beam path, in order to stretch the pulse to ≈ 120 fs. Therefore, we could put more energy in the pulse while keeping the same intensity, which provided a better degree of alignment. Finally, all three beams are focused in the generating medium by the same 1 m focal length lens.

In the XUV range that we target, the absorption is important, therefore the system is put under vacuum, from the generation chamber on, where the gas jet is and the optical table is decoupled from the rest of the setup, to keep the as interferometric stability.

The Medium of Harmonic Generation

The pulsed gas jet consists of a piezo-electric valve that is synchronized with the generating laser beam. The opening duration, thus the density of the gas in the jet, is optimized in order to have the highest harmonic signal. Considering the degree of molecular alignment, the molecules are better aligned when the jet is cooler. This is reached by choosing an hole size of 0.5 mm and by keeping a relatively large distance between the exit of the orifice and the

laser beam. This is a compromise between the level of harmonic signal and the rotational temperature T_{rot} .

In Chapter 3, Ar and N₂ gases were used one after the other, in order to maintain the same generating conditions for both of them. Independently from the target gas, we put 2.5 bar backing pressure on the valve and the pressure inside the generating chamber was kept at 7.5×10^{-4} mbar. The atomic/molecular density reached by these settings kept the macroscopic phase mismatching effects low. To secure the generation of mainly the short trajectories, we focus the laser beams before the gas jet (see section 1.4.5).

The generated XUV emission is less divergent than the generating laser beam, thus in order to prevent the latter to penetrate in the detection chamber an iris was put approximately 80 cm downstream from the gas jet. Although it is open enough to let through the XUV emission and the smaller dressing beam. Another feature of the iris is that it blocks the long trajectories' contributions, since they are more divergent than the short ones, reducing again their weight in the detector.

2.1.1 Molecular Alignment

Many chemical reactions depends on the relative orientation of the participating elements and this is especially true for photochemical reactions (Stapelfeldt and Seideman [152]). In the latter case it is the angle between the molecular axis and the polarization of the laser light that is related to symmetry selection rules, determining the outcome of the interaction. The theoretical work of (Seideman [141]) launched a huge interest of molecular alignment in the attosecond community because they showed that high degree of molecular alignment can be achieved in field free conditions. (Rosca-Pruna and Vrakking [129]) were the first who tested it experimentally.

The results presented in Chapter 3 are based on angle resolved molecular studies. In the case of symmetric molecules it is important to control the angle between the main molecular axis and a reference laboratory axis (in our case that is the polarization of the generating laser beam) and this control is referred as *alignment* of the molecules. If the molecules are turned perpendicular to the laser polarization then they are *anti-aligned*. In the case of asymmetric molecules one may set head-up or head-down *orientations*, further increasing the precision of angular studies. Nevertheless, in this thesis N₂ is mainly studied, that is a linear symmetric diatomic molecule, hence only alignment is discussed here. In the followings we will determine the optically induced rotational states of a molecule. First, we discuss how to construct the time dependent Hamiltonian. Second, we define the degree of alignment of a molecular ensemble and compare it with experimental results. At last, we determine the angular distribution in certain alignment conditions that leads us to the probability of finding a molecule at an angle θ with respect to the aligning laser.

The angular part of the nuclear wavefunction $\psi(\theta, \phi, t)$ can be expanded on basis of spherical harmonics: $\psi(\theta, \phi, t) = \sum_J \sum_M c_{J,M}(t) Y_{JM}(\theta, \phi)$, where $J = 0, 1, 2, \dots$ is the orbital momentum quantum number and $M = -J, -(J-1), \dots, J-1, J$ is the projection of J onto the direction of the laser polarization. In a field free rotation, the rotational operator and the corresponding eigenvalues are $\mathcal{H}_0 = B_0 J^2$ and $E_J = B_0 J(J+1)$, respectively, where B_0 is a rotational constant of the molecule.

When molecules are injected in the generating chamber, their axes are randomly aligned and they occupy different rotational and vibrational states. The electric field of a laser beam $\mathbf{E}(t)$, if strong enough, might apply a torque on the molecule and turn it towards the polarization of the light. The induced dipole is proportional to the electric field: $\mathcal{D} = \alpha \cdot \mathbf{E}$, where α is the polarizability tensor. Then the potential energy of the molecule is $U = -\mathcal{D} \cdot \mathbf{E} = -(\alpha \cdot \mathbf{E}) \cdot \mathbf{E}$. The molecule can be turned only if the polarizability is not isotropic, which is the case in linear molecules, $\Delta\alpha = \alpha_{||} - \alpha_{\perp} > 0$. The IR laser used in our experiment

is non-resonant with the rotational transitions. The oscillation of the electric field is too fast to follow for the heavy nuclei, rather they are affected by the envelope of the laser field. Therefore, they feel an average potential over one laser cycle, so the time dependent potential energy looks (Friedrich and Herschbach [36]):

$$U(\theta, t) = -(\alpha_{\perp} + \Delta\alpha \cos^2 \theta) E_0^2 f(t) = -U_0(t) \cos^2 \theta - \alpha_{\perp} E_0^2 f(t), \quad (2.1)$$

where E_0 is the amplitude of the field and $f(t)$ corresponds to the slowly varying envelope of the pulse integrated over one optical cycle, $U_0(t) = \Delta\alpha E_0^2 f(t)$ and θ is the angle between the molecular axis and the polarization of the laser. The lowest energy state of a linear molecule in an external field described by eq. 2.1 is when they aligned parallel $\theta = 0$. The last term in eq. 2.1 is just a constant energy shift as a function of angle, hence it does not affect the angular distribution.

We neglect vibrational excitation because the spectral bandwidth of an aligning laser pulse is small like $\Delta E \approx 14$ meV), while the vibrational states are separated by $\Delta E_{vib} \approx 100$ meV. In the presence of the external laser field, the TDSE for the rotational states are given by:

$$i \frac{\partial}{\partial t} \psi(\theta, \phi, t) = [B_0 J^2 - U_0(t) \cos^2 \theta] \psi(\theta, \phi, t). \quad (2.2)$$

In a non-resonant irradiation, the molecule is excited through inelastic scattering, through Raman-transitions. Selection rules imply that transition between two rotational states may exist when (i) $\Delta M = 0$, since molecules with the same ϕ coordinate are degenerate; (ii) $\Delta J = \pm 2$ referring to be a two photon transition process. In reality, the molecules are not rigid rotors, the chemical bond between the nuclei stretches with the rotation. Therefore, we introduce a correction term into the energy of the rotational states: $E_J = B_0 J(J+1) - D_0 [J(J+1)]$. The correction plays a role just at large J values, since $D_0 \sim 10^{-6} B_0$.

The initial conditions to solve equation 2.2 are defined by the distribution of the rotational states when the molecules are expanding freely from the orifice. We assume that the expanding molecules are in a thermodynamical equilibrium characterized by T_{rot} . The weight of each rotational states are thus given by the Boltzmann statistics:

$$P_J = \frac{1}{Z} g_J (2J+1) e^{-E_J/k_B T_{rot}}, \quad (2.3)$$

where k_B is the Boltzmann-constant, Z is a normalization constant and g_J controls the weight between the even and odd valued J states, due to nuclear spin effects. By decreasing the rotational temperature, we decrease the number of J states that were initially incoherently prepared. To solve eq. 2.2, we use a program written by Sébastien Weber that solves the equation numerically with the fourth order Runge-Kutta-method over the duration of the laser pulse τ_p , with the following N_2 molecular properties: $B_0 = 1.9896$ cm⁻¹; $D_0 = 5.67 \times 10^{-6}$ cm⁻¹; $\Delta\alpha = 1.0$ Å³; $g_{\text{even}} = 2$; $g_{\text{odd}} = 1$.

Depending on the duration of the aligning pulse, difference can be made between *adiabatic* and *non-adiabatic* alignment. We talk about adiabatic alignment if the different J states are filled slowly, following the evolution of the aligning pulse's envelope. This implies that the alignment will disappear as the pulse goes away. In HHG one would prefer that the molecules are aligned without being dressed up with an additional laser field. In non-adiabatic alignment, when τ_p much more smaller than the rotational period, the short laser pulse gives a sudden 'kick' to the molecules, by coherently populating many rotational J states, creating a rotational wavepacket. Therefore the molecular ensemble is well aligned right after the passage of the laser pulse. Subsequently, the rotational wavepacket evolves freely in time $\psi(\theta, \phi, t) = \sum_J c_{J,M} Y_{JM}(\theta, \phi) \exp[iE_J t]$, with $c_{J,M} = \langle Y_{JM} | \psi(\theta, \phi, t = \tau_p) \rangle$. The rotational states re-phase periodically after a certain time, called *revival time*, $T_{rev} = \frac{\pi}{B_0}$. In the case of N_2 , $T_{rev}(N_2) = 8.2$ ps. Non-adiabatic alignment suits well the needs of HHG, since it allows to perform experiments in a field free align molecular ensemble.

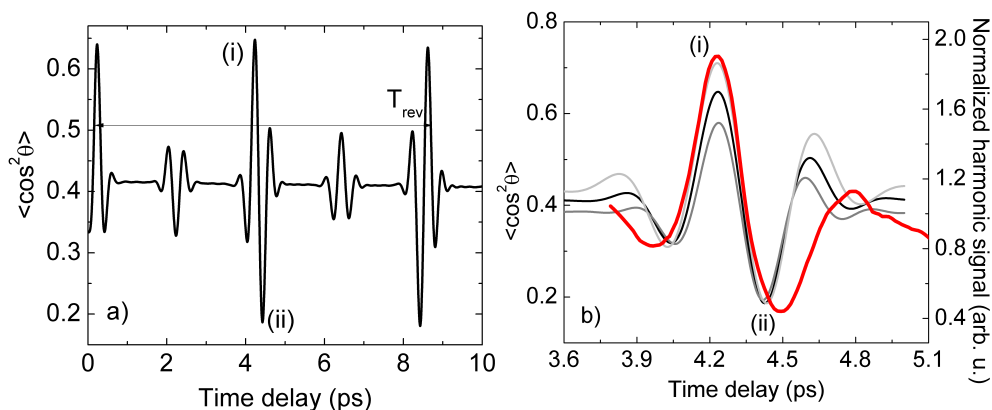


Figure 2.2: Simulation of the expected degree of alignment of N_2 in a) as the function of time passed after the aligning beam has gone. The simulation is done for an aligning laser intensity of $I_{align} = 0.5 \times 10^{14} \text{ W/cm}^2$, $\tau_p = 120 \text{ fs}$, $T_{rot} = 90 \text{ K}$ and $J_0 = 0, \dots, 15$ states were assumed to be occupied initially. T_{rev} denotes a full period of rotational re-phasing. (i) and (ii) signs the position of alignment and anti-alignment during the half-revival, respectively. In figure b) the zone of half-revival is zoomed in and the measured smoothed total harmonic signal (red curve) is compared with the expected degree of alignment, having the same input parameters except for the rotational temperature: $T_{rot} = 50 \text{ K}$ (light gray curve), $T_{rot} = 90 \text{ K}$ (black curve), $T_{rot} = 150 \text{ K}$ (dark gray curve).

The Degree of Molecular Alignment

The degree of alignment is expressed by the statistical average of the expectation value of the angle dependent part of the potential energy:

$$\langle \langle \cos^2 \theta \rangle \rangle_{stat} = \frac{1}{Z} \sum_{J_0, M_0} g_J (2J+1) e^{-E_J/k_B T_{rot}} \langle \psi(\theta, \phi, t) | \cos^2 \theta | \psi(\theta, \phi, t) \rangle, \quad (2.4)$$

where J_0 and M_0 are referring to the initial alignment distribution. To make life easier, from now on, the degree of alignment is going to be denoted by $\langle \cos^2 \theta \rangle$. Figure 2.2 a) shows the expected and statistical degree of alignment for N_2 . The aligning pulse interacts with the molecules at zero time delay, when the molecules are randomly aligned, $\langle \cos^2 \theta \rangle = 0.33$. Perfect alignment would correspond to $\langle \cos^2 \theta \rangle = 1$ while complete anti-alignment, when all the molecules are perpendicular to the polarization of the aligning laser, corresponds to $\langle \cos^2 \theta \rangle = 0$. The pulse is long gone while the molecules are still rotating and from time to time they regain their high degree of alignment. (Ramakrishna and Seideman [125]) pointed out, that there is a correspondence between the expected degree of alignment and the intensity of the emitted XUV radiation. In figure 2.2 b) we zoomed on the half-revival zone and compared the simulations for different T_{rot} with our experimentally measured total harmonic signal (red dashed curve). This comparison provides us the rotational temperature of the molecules, showing that our experimental conditions correspond to $T_{rot} = 50 \text{ K}$ (light gray curve). The molecular orbital symmetry also contributes to the measured harmonic signal over the alignment scan. N_2 has a σ_g orbital and the ionization along its' molecular axis is thus favored. The highest harmonic signal is expected when the molecules are aligned parallel to the laser (Itatani et al. [55]).

Knowing how to calculate the degree of alignment one can estimate the optimal pulse duration of the aligning beam. In figure 2.3 we present our simulation, while keeping the laser intensity, the rotational temperature and the number of the initially excited states con-

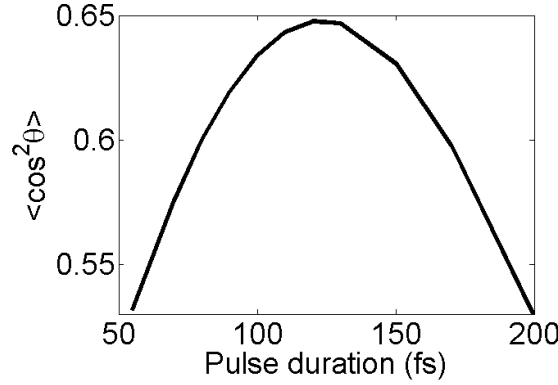


Figure 2.3: Degree of the molecular alignment at the half-revival point with respect to the pulse duration of the aligning laser beam.

stant, as it is given in the caption of figure 2.2. 120 fs seemed to be the optimum duration, that is why we stretched our aligning pulse with a glass block. Shorter pulses are passing too fast through the gas jet having not enough time to excite many rotational states. Meanwhile, longer pulses tend to have more and more adiabatic alignment aspect, high alignment right after the pulse passed or during its presence and low degree or no revival alignment.

Angular Distribution

The emitted XUV radiation after HHG shows angular dependent features due to the angular dependent tunnel ionization and recombination dipole moment. Therefore, the subtle structural signs of the molecule can be resolved, if they are preferentially aligned in one direction. The angular distribution of molecules at a given time delay is the statistically averaged probability function of finding a molecule in a given $\psi_{J,M}(\theta, \phi, t)$ state:

$$P(\theta, t) = \langle \langle \psi | \psi \rangle \rangle_{\text{stat}} = \frac{\sum_{J,M} g_J e^{-E_J/k_B T_{\text{rot}}} \langle \psi_{J,M} | \psi_{J,M} \rangle (\theta, \phi, t)}{\sum_J P_J}. \quad (2.5)$$

Since $\psi_{J,M}(\theta, \phi, t)$ is degenerate in ϕ (see the selection rules: $\Delta M = 0$), the angular distribution is independent of it. Figure 2.4 shows four examples of the shape of $P(\theta, \phi, t)$ calculated for N_2 at $T_{\text{rot}} = 90 \text{ K}$, $\tau_p = 120 \text{ fs}$, $I_{\text{align}} = 0.5 \times 10^{14} \text{ W/cm}^2$. $P(\theta, \phi, t)$ is represented in a Cartesian coordinate system where z indicates the direction of the aligning laser's polarization, y is the direction of laser propagation and x is orthogonal to both of them. The probability of finding a molecule aligned at θ and ϕ is given by the radial distance between the point of $r = P(\theta, \phi, t)$ and zero. Therefore, the Cartesian coordinates are: $x = P(\theta, \phi, t) \sin \theta \cos \phi$, $y = P(\theta, \phi, t) \sin \theta \sin \phi$, $z = P(\theta, \phi, t) \cos \theta$. When the molecules are aligned randomly (a), each angle is equally distributed. At half-revival (b), the molecules are aligning along the laser polarization creating a cone of $\approx 30^\circ$ around it. In the anti-alignment distribution (c), the molecules are preferentially aligned perpendicular to the laser polarization. Figure 2.4 d) represents a distribution which occurs between the half-revival and anti-alignment.

It was already mentioned that a HWP, installed in the path of the aligning laser beam, controls the angle ϑ between the polarizations of the aligning and the generating beam. The coordinates of the molecular alignment with respect to the aligning laser beam polarization are (r', θ', ϕ') , while with respect to the driving laser polarization they are (r, θ, ϕ) and $r' = r$, see figure 2.5 a) and b), respectively. The latter coordinate system is referred to as *laboratory frame* (LF), too. The transition between the two coordinate systems is given by a simple

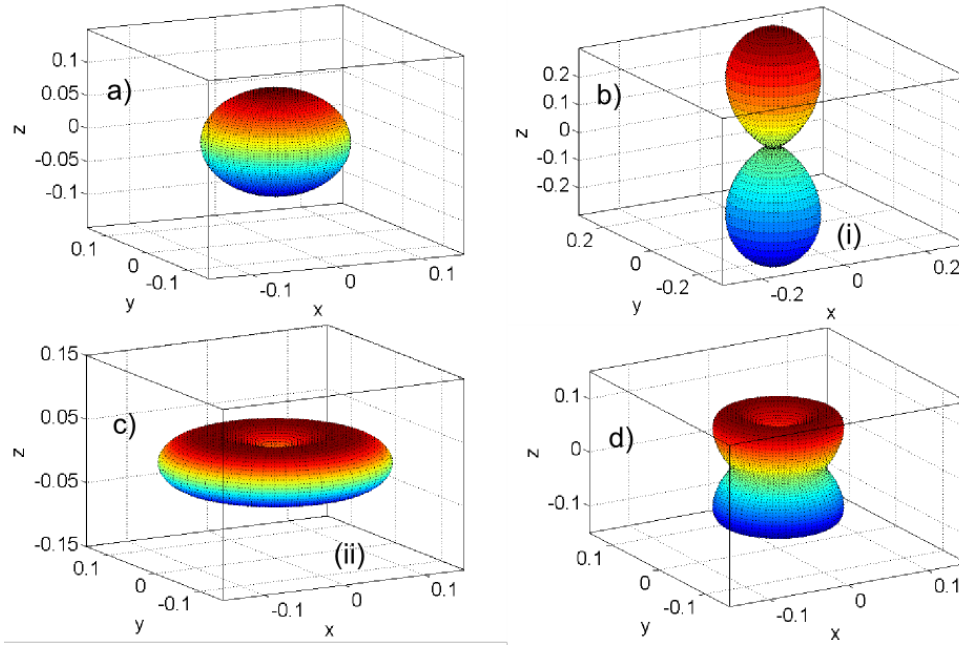


Figure 2.4: Three dimensional presentation of the molecular angular distributions at a) $t = 0$ ps that is a random distribution, b) $t = 4.235$ ps that is the half-revival, c) $t = 4.425$ ps that is the anti-revival, d) $t = 4.335$ ps that is an instant between the half-revival and anti-alignment. (i) and (ii) in figure b) and c), respectively, refers back to notations in figure 2.2.

rotation around the $y=y'$ axis:

$$\cos \theta = -\sin \theta' \cos \phi' \sin \vartheta + \cos \theta' \cos \vartheta \quad (2.6)$$

$$\tan \phi = \frac{\sin \theta' \sin \phi'}{\sin \theta' \cos \phi' \cos \vartheta + \cos \theta' \sin \vartheta} \quad (2.7)$$

Therefore, the angular distribution with respect to the driving laser beam polarization is given by $P(\theta(\theta', \phi', \vartheta), \phi(\theta', \phi', \vartheta), t, \vartheta)$, when the two beams are delayed by t in time and the angle between their polarization is ϑ . To obtain the probability $d\sigma(\theta, t, \vartheta)$, of finding the molecules between θ and $\theta + \Delta\theta$ at a given time delay t , one has to integrate over the azimuthal angle ϕ . If $\vartheta = 0^\circ$ then the two coordinate systems presented in figure 2.5 a and b become identical. Therefore, the distribution is cylindrically symmetric with respect to the polarization of the driving laser (see figure 2.4 a,b,c with respect to z), leading to $d\sigma(\theta, t, \vartheta = 0) = 2\pi P(\theta = \theta', \phi = \phi', t, \vartheta = 0) \sin \theta d\theta$. If $\vartheta \neq 0^\circ$ then the cylindrical symmetry remains with respect to axis z' , but not with respect to z axis, so $d\sigma(\theta, t, \vartheta) = \int_0^{2\pi} P(\theta(\theta', \phi', \vartheta), \phi(\theta', \phi', \vartheta), t, \vartheta) \sin \theta d\phi d\theta$. Figure 2.6 shows the result of such kind of calculations performed for $t = 4.235$ ps (half-revival) and for $\vartheta = 0^\circ$ (full), $\vartheta = 50^\circ$ (dashed) and $\vartheta = 90^\circ$ (dash-dot). The curves show that the alignment is not perfect and at $\vartheta = 0^\circ$ the majority of the molecules is aligned about $\theta = 25^\circ$. This is very important, since in this case the detected harmonic emission should show the molecular characteristics at 25° and not at 0° . When $\vartheta = 90^\circ$, most of the molecules are well aligned perpendicularly to the polarization of the generating laser.

The macroscopic harmonic signal is constructed from the coherent sum of the electric fields emitted from molecules aligned in a characteristic distribution (ϑ) at the instant t . When saying macroscopic, we do not include here the averaging due to the propagation effects. Care has to be taken when averaging over the distribution. The different compo-

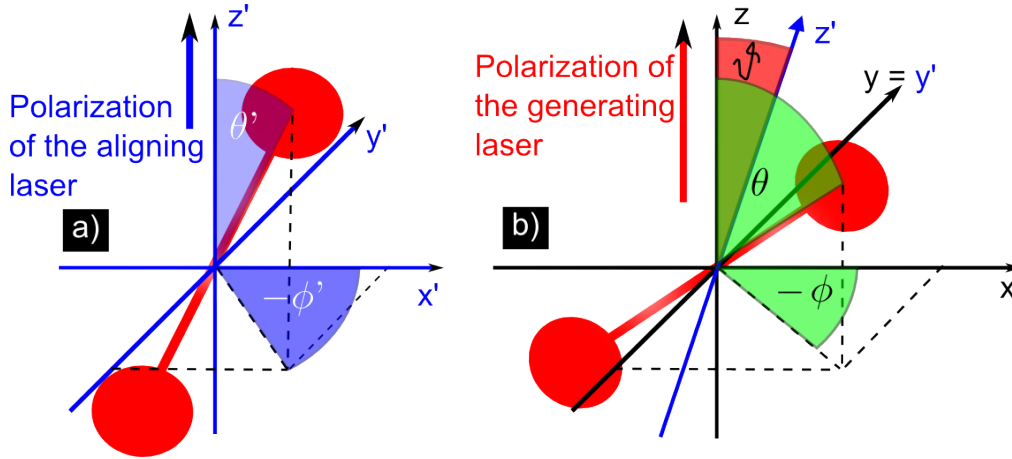


Figure 2.5: Schematic representation of the coordinates of the molecular alignment with respect to the polarization of the aligning laser z' (a) and the driving laser z (b). The two coordinate systems are rotated by ϑ around $y = y'$ axis, that denotes the propagation direction of both laser beams.

nents (\parallel, \perp) of the emitted harmonic field (see the discussions concerning the length form in section 1.4.3) are not summed in the same way. Experimentally we can measure the electric field of the harmonics along the z (\parallel) and x (\perp) axis. The parallel components ($E_{XUV}^{\parallel}(q\omega)$) are just simply summed up over θ and ϕ , while the perpendicular components ($E_{XUV}^{\perp}(q\omega)$) have to be projected on the x axis (Kajumba et al. [62]):

$$E_{XUV}^{\parallel,L}(q\omega, \vartheta) = \int_{\theta=0}^{\pi} \int_{\phi=0}^{2\pi} P(\theta(\theta', \phi', \vartheta), \phi(\theta', \phi', \vartheta), t, \vartheta) E_{XUV}^{\parallel,m}(q\omega, \theta) \sin \theta \, d\phi \, d\theta \quad (2.8)$$

$$E_{XUV}^{\perp,L}(q\omega, \vartheta) = \int_{\theta=0}^{\pi} \int_{\phi=0}^{2\pi} P(\theta(\theta', \phi', \vartheta), \phi(\theta', \phi', \vartheta), t, \vartheta) E_{XUV}^{\perp,m}(q\omega, \theta) \sin \theta \cos \phi \, d\phi \, d\theta, \quad (2.9)$$

where the electric field is complex valued for both the parallel and perpendicular components of the angle dependent single molecule response E_{XUV}^m and for the macroscopic response E_{XUV}^L .

Averaging the harmonic signal over the distribution may clear out characteristics about the recombination dipole moment, if the degree of alignment is not high enough. Hence, good degree of alignment is essential in the study of molecular structures. Sections 3.3, 3.4 and 3.5 apply the averaging over the alignment distribution and tries to understand its' consequences.

2.2 Experimental Tools for Harmonic Characterization

The properties like spectral amplitude, phase and polarization of high order harmonics have to be determined in order to extract structural or dynamical features of molecules. Up to now, mainly two approaches were used. First, one can directly measure the number of emitted photons with XUV photon sensitive electronic devices like, photo-multipliers and micro channel plates (MCP). Second, one can count the photoionized electrons after the absorption of the XUV radiation by a target gas, using electron spectrometers. In this thesis we apply the second approach that provides a relatively easy access to both the spectral amplitude and phase for one given distribution.

There are several types of spectrometers to detect the electron replica of the XUV photon. Depending on the needs one may use the Cold Target Recoil Ion Momentum Spectroscopy

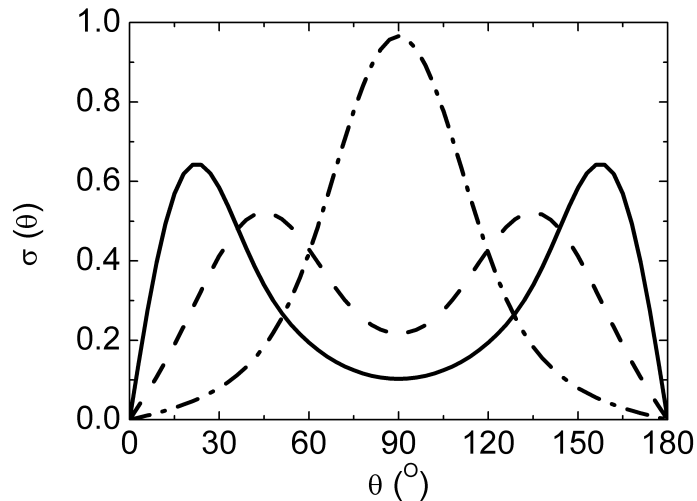


Figure 2.6: The probability of finding the molecules between θ and $\theta + \Delta\theta$ at the time delay corresponding to the half-revival $t = 4.235$ ps. The curves correspond to different alignment angle: $\vartheta = 0^\circ$ (full), $\vartheta = 50^\circ$ (dashed) and $\vartheta = 90^\circ$ (dash-dot).

(COLTRIMS) (Ullrich et al. [163]) that allows one to measure the vectorial momenta of several ions and electrons resulting from atomic or molecular fragmentation; Velocity Map Imaging Spectrometer (VMIS) (Eppink and Parker [26]) where all particles with the same initial velocity vector are mapped onto the same point on the detector giving a 2D image on the electrons velocity distribution; Magnetic Bottle Electron Spectrometer (MBES) (Kruit and Read [75]) that collects electrons (ions) by using strong static magnetic fields while conserving their initial velocity, giving an image of the modulus of their initial momenta.

2.2.1 Technique for the measurement of the harmonics' spectral intensity

Magnetic Bottle Electron Spectrometer and the Time of Flight Tube

We characterize the harmonic emission by using the latter spectrometer combined with a time of flight tube (TOF), because this gives the highest signal within fairly short acquisition time. As already mentioned, the IR beams are blocked by an iris after the generation (except for the dressing beam), not to influence the characterization of the harmonics. The generated XUV emission is focused into the detection chamber by a 1 m focal length toroidal mirror along with the dressing beam, as shown in figure 2.1. The toroidal mirror is set at an angle of incidence of 11.5° and with the help of a grating in zero order diffraction, all radiation is reflected into the detection chamber of the MBES. Through a thin needle, neon/argon gas is injected between the two poles of a strong static magnetic field $B \approx 1$ T. The direction of this magnetic field is set to collect the photoionized electrons in 2π steradian and guide them into an $L = 1.5$ m long TOF. The magnetic field is gradually decreased from the point of gas injection to the TOF, where it is kept constant $B \approx 10^{-3}$ T. This field is parallel to the tube and introduces a spiral motion to the electrons around the field lines, while keeping a constant electron velocity component along the TOF. An MCP detector is counting the number of impinging electrons and transfers their signal to an oscilloscope. The injection of the neon gas in the MBES was restricted to keep the pressure lower than 10^{-5} mbar in the TOF, because the operation of an MCP requires fairly high vacuum and it prevents spatial charge effects along the TOF tube.

The role of the TOF is to transform the kinetic energy of the XUV photons E_{kin} into the

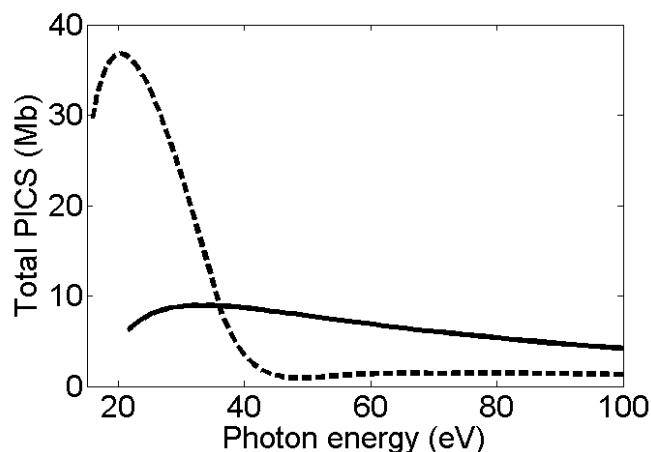


Figure 2.7: The total photoionization cross-section of neon (full curve) and argon (dashed curve) expressed in Mb as a function of photon energy.

time t_{TOF} , that is needed to fly along the tube (in SI units):

$$E_{\text{kin}} = \hbar\omega - I_{\text{p}} = \frac{m_e}{2} \frac{L^2}{(t_{\text{TOF}} - t_0)^2} + C, \quad (2.10)$$

where m_e is the mass of the electron. The HHG system is triggered by a signal coming from the laser oscillator and not from the instant of photoionization, t_0 takes into account all the electronics and light propagation delays. C is responsible for correcting any charge accumulation of the TOF which may accelerate or decelerate the electrons.

The spectral intensity of the harmonics within a small spectral range ($I(E)dE$) is equal to the measured time-dependent voltage within the temporal resolution of the oscilloscope ($I(t)dt$). Although, the temporal resolution is discrete ($dt = 1$ ns), the non-linear mapping between the electron energy and the time of flight leads to the stretching of the harmonics' spectral intensity $I(E) \propto I(t)t^3/L^2$ and to the decrease of the spectral resolution $dE/E = 2dt/t \propto E^{3/2}/L$. This results a resolution of 0.8 meV and 25 meV at electron energies of 1 eV and 10 eV respectively.

The type of the detection gas is determined by the spectral range that we want to observe. The ionization potential of Ar is lower than that of Ne, thus lower harmonic orders can be detected. Furthermore, the photoionization cross-section (PICS) that determines the number of the detectable photons is different for different gases, as shown in figure 2.7 for Ne (full line) and Ar (dashed line). Argon is more appropriate if more contrast is needed in the lower harmonic range, while Ne gives a relatively constant response over a larger spectral range. When presenting the intensity of the measured harmonics in our experiments, the contribution of the PICS was removed based on the values shown in figure 2.7.

2.2.2 Techniques for Phase Measurement

Generation of a large spectra, that may result attosecond pulses, is now quite straightforward. But measuring such short durations is not at all so direct. Already the femtosecond pulses are characterized in the spectral domain (Walmsley and Dorrer [174]). Techniques like, autocorrelation, Frequency Resolved Optical Gating (FROG) (Trebino [160]) and Spectral-Phase Interferometry for Direct Field Reconstruction (SPIDER) (Iaconis and Walmsley [53]) require non-linear processes¹ that is extremely difficult in the XUV spectral

¹Autocorrelation was shown to be feasible, but only for a low order harmonics in a restricted spectral range.

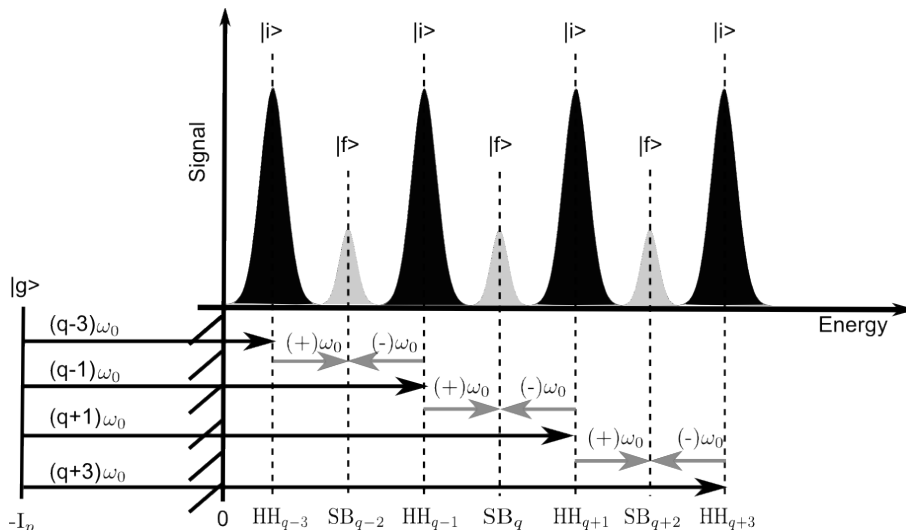


Figure 2.8: Schematic of the two photon two color transition from the ground state $|g\rangle$ through an intermediate state $|i\rangle$ to the final state $|f\rangle$, that corresponds to the sidebands (SB) of the neighboring harmonics (HH).

range. The biggest obstacles in HHG are the large spectral bandwidths, the low number of XUV photons and of the high absorption of XUV radiation by those materials.

New techniques were developed to characterize the spectral properties of HHG mainly based on photoionization and detection of the created electrons. In some cases, high intensity APTs can be obtained with low harmonic orders allowing to induce non-linear processes. This is exploited in the second order intensity volume autocorrelation (2-IVAC) (Nabekawa et al. [115], Tzallas et al. [161]). The APTs with moderate intensities and single attosecond pulses, are usually accompanied with a dressing IR field which acts on the XUV created photoelectron as a phase modulator. This approach is used in the Reconstruction of Attosecond Beating By Interference of Two-photon transition (RABBIT) (Paul et al. [122], Vénierd et al. [170]), in the FROG for Complete Reconstruction of Attosecond Bursts (FROG-CRAB) (Kim et al. [68], Mairesse and Quéré [98]) and in the attosecond streaking camera (Goulielmakis et al. [40], Hentschel et al. [47]).

RABBIT

In this thesis the harmonic spectral phase was characterized by the RABBIT technique. It is based on the measurement of the photoelectron signal created by the two photon, two color ionization (XUV+IR). During this process an electron in the ground state $|g\rangle$ may absorb an XUV photon arriving to the intermediate state $|i\rangle$ and then absorb (+) or emit (-) an IR photon (ω_0) ending on the final state $|f\rangle$. Having a multi-cycle generating IR pulse, the harmonics (HH) are odd multiples of ω_0 , hence the result of the described process is the appearance of even ordered sidebands (SB), as shown in figure 2.8. The intensity of the dressing IR laser pulse has to be kept low, otherwise multiple IR photon absorption can occur re-distributing the photoelectrons into both even and odd multiples of the fundamental photon energy (Swoboda et al. [153]).

Let us assume that the q th order SB comes from the absorption of the $(q-1)$ th ordered harmonic plus an IR photon (we denote this path as A_{abs}) and on the other quantum path it comes from the absorption of $(q+1)$ th harmonic and the emission of an IR photon (A_{em}). We define the electric field of the harmonics as: $E_{XUV}(q, t) = E_q^0 \exp(-iq\omega_0 t - \varphi_q)$ and the IR as: $E_{IR}(t) = E^0 \exp(-i\omega_0 t)$, where E_q^0 and E^0 are the amplitude of the harmonics' and IR's

field, respectively and φ_q is the phase of the q th ordered harmonic. When the two beams are delayed from each other by τ , the SB signal is given by the two photon transition described in the frame of the second order perturbation theory (Toma and Muller [155], Varjú et al. [167], Véliard et al. [170]):

$$S(q, \tau) \propto \left| \int_{-\infty}^{+\infty} (A_{abs}(t) + A_{em}(t)) dt \right|^2 \quad (2.11)$$

with

$$A_{abs}(t) = \sum_i \frac{\langle f|r|i\rangle \langle i|r|g\rangle}{\epsilon_i - \epsilon_g - (q-1)\omega_0} E_{IR}(t-\tau) E_{XUV}(q-1, t) e^{iI_p t} \quad (2.12)$$

$$A_{em}(t) = \sum_i \frac{\langle f|r|i\rangle \langle i|r|g\rangle}{\epsilon_i - \epsilon_g - (q+1)\omega_0} E_{IR}^*(t-\tau) E_{XUV}(q+1, t) e^{iI_p t}, \quad (2.13)$$

where ϵ_i, ϵ_g are the energies of the intermediate and ground state, respectively and I_p is the ionization potential, and E_{IR}^* is the complex conjugate of the IR field, referring to the emission of one photon. The term of summation becomes important only for the intermediate states corresponding to: $\epsilon_i = \epsilon_g + (q \pm 1)\omega_0$. We introduce the simplified notation of these sums by attributing an amplitude and phase term to them:

$$\mathcal{A}_{abs}^{q-1} e^{i\varphi_{abs}^{q-1}} = \sum_i \frac{\langle f|r|i\rangle \langle i|r|g\rangle}{\epsilon_i - \epsilon_g - (q-1)\omega_0} \quad (2.14)$$

$$\mathcal{A}_{em}^{q+1} e^{i\varphi_{em}^{q+1}} = \sum_i \frac{\langle f|r|i\rangle \langle i|r|g\rangle}{\epsilon_i - \epsilon_g - (q+1)\omega_0}. \quad (2.15)$$

The consecutive harmonics (especially in the plateau region) have comparable intensities $E_{q-1}^0 \approx E_{q+1}^0 \approx E_q^0$. Moreover we shall neglect the phase variations inside the harmonics and attribute φ_{q-1} and φ_{q+1} to the average of that variation. Substituting equations 2.14 and 2.15 into eq. 2.12 and 2.13, respectively and substituting the result into eq. 2.11 one finds the following expression for the side band signal:

$$S(q, \tau) \propto M \left| \int_{-\infty}^{+\infty} E_{IR}^0 E_q^0 e^{-iq\omega_0 t + iI_p t} dt \right|^2, \quad (2.16)$$

where

$$M = \left| \mathcal{A}_{abs}^{q-1} \exp(i\varphi_{abs}^{q-1} - i\varphi_{q-1} + i\omega_0 \tau) + \mathcal{A}_{em}^{q+1} \exp(i\varphi_{em}^{q+1} - i\varphi_{q+1} - i\omega_0 \tau) \right|^2. \quad (2.17)$$

Introducing the following notations: $S_0 = \left| \mathcal{A}_{abs}^{q-1} \right|^2 + \left| \mathcal{A}_{em}^{q+1} \right|^2$ and $S_1 = 2\sqrt{\mathcal{A}_{abs}^{q-1} \mathcal{A}_{em}^{q+1}}$ we find that the side band signal is proportional to:

$$S(q, \tau) \propto S_0 + S_1 \cos(\Delta\varphi_q^{at} + \Delta\varphi_q + 2\omega_0 \tau), \quad (2.18)$$

where $\Delta\varphi_q^{at} = \varphi_{em}^{q+1} - \varphi_{abs}^{q-1}$ is the so called atomic phase, $\Delta\varphi_q = \varphi_{q+1} - \varphi_{q-1}$ is the phase difference of the consecutive harmonics. By controlling the delay τ between the dressing and the XUV beam with a piezo-crystal, one introduces the cosine like oscillation of the side band signal with $2\omega_0$ frequency. The phase difference of the consecutive harmonics can be retrieved from this oscillation if the atomic phase is known.

The atomic phase can be understood as the phase gathered by the electron during the transition from the bound to the continuum state. As a first approximation, the atomic phase difference $\Delta\varphi_q^{at}$ is related to the one photon dipole transition. Theoretical calculations show that for atoms like argon and neon this phase is small, therefore we neglect them in our RABBIT technique. However in some special cases, the one photon transition is not eligible to explain the results. (Klünder et al. [71]) showed that XUV photoionization

in Ar from different shells in the presence of an IR field has to be discussed as a two photon process. They theoretically attributed two phase shifts to the two photon transitions. By examining the molecular phase instead of the atomic, (Haessler et al. [42]) showed experimentally that the intermediate state may corresponded to a resonant state (near to the threshold) that causes deviation from the one photon transition (Caillat et al. [17]). Nevertheless, with the increase of the photon energy, the difference between the single photon and two photon transition phases is decreasing. Despite the recent results, this is still a buzzing subject of the atomic and molecular physics.

From the obtained phase differences in eq. 2.18 one can express the emission time (or group delay) of the harmonics:

$$t_e(q\omega_0) := \left. \frac{\partial \varphi}{\partial \omega} \right|_{q\omega_0} \approx \tau_0 + \frac{\varphi_{q+1} - \varphi_{q-1}}{2\omega_0}. \quad (2.19)$$

The emission time defined here corresponds to the emission time defined by eq. 1.72. It represents a delay in the emission of the different harmonic components leading to the attochirp. However, in our experimental setup, the generating and the dressing beam are collinear. Although, the intensity of the dressing beam is weak, it modulates the intensity of the generating laser beam in the generating medium, inducing an additional ω_0 oscillation of the side band signal as the function of $\tau = \tau_0 + \tau'$, where τ_0 is the initial time delay between the two pulses while τ' is the delay controlled by the piezo-crystal. τ_0 is also called the *absolute timing* and it can be retrieved from the ω_0 oscillation of the side bands. The absolute timing appears in eq. 2.18 as $2\omega_0\tau = 2\omega_0\tau_0 + 2\omega_0\tau'$, therefore the measured emission times in eq. 2.19 are shifted vertically by τ_0 . This is translated to the spectral phase of the harmonics as a linear function of the harmonic order. Integrating eq. 2.19 while taking into account the absolute timing, the spectral phase is given by:

$$\varphi(q\omega_0) = \varphi_0 - q\omega_0\tau_0 + q\omega_0 t_e(q\omega_0), \quad (2.20)$$

where φ_0 is the integration constant, called the *absolute phase*. It does not affect the temporal profile of the attosecond pulse in contrast to τ_0 which shifts the envelope of the pulse along the time axes. Nevertheless, in aligned molecules the absolute phase may be angle dependent $\varphi_0(\theta)$ and the RABBIT technique does not relate angularly the measured spectral phase differences.

In our experiments τ_0 showed 200 as uncertainty within the same experimental conditions during one day. Therefore in Chapter 3 we arbitrarily set τ_0 for a fixed value. Such an act adds or removes a linear phase from $\varphi(q\omega_0)$ and does not make disappear any higher order phase behavior. These latter terms are usually related to molecular structural or dynamical signs transferred into the harmonic phase. In figure 2.9 we plot a measured RABBIT scan where the white line indicates the delay between the different ordered SB maximums. This delay is the emission time.

The reliability of RABBIT has been verified several times. However, (Kruse et al. [76]) compared the attosecond pulse durations measured by 2-IVAC and RABBIT in the same experimental conditions. They used long focal length to generate harmonics, that increases the presence of long trajectories in all experimental conditions. RABBIT does not make difference between the different trajectories, it measures an average phase in one harmonic order. They found that RABBIT underestimates the pulse durations in all conditions because of the presence of both long and short trajectories in their experiments. In our experiments the focal length is shorter creating more divergent long trajectories and we have two filtering stages to prevent long trajectories to get in the detection chamber. Moreover even when positioning our gas jet to favor the long trajectories we have never observed emission times with negative slope. This confirms that the contribution from the long trajectories in our case can be neglected.

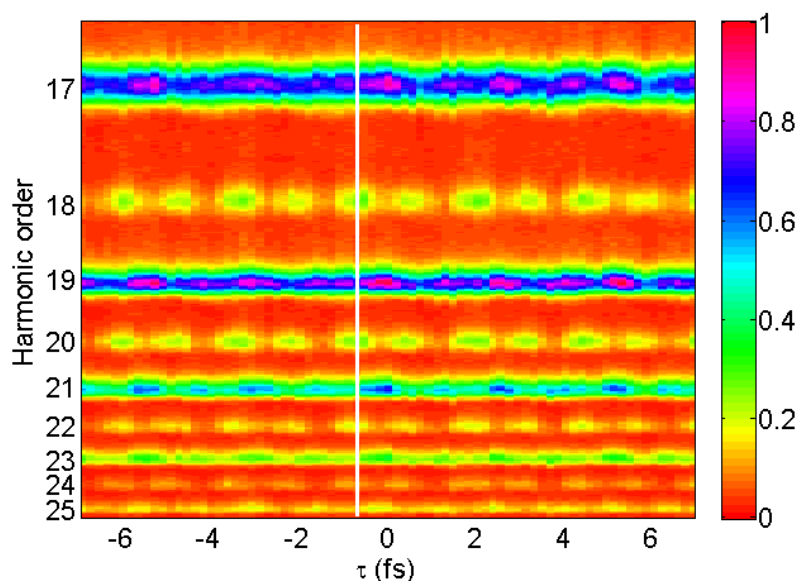


Figure 2.9: Experimental RABBIT scan done in N_2 aligned parallel to the laser polarization with $I_L = 1.1 \times 10^{14} \text{ W/cm}^2$. The gas of detection is neon. 100 shots were averaged for each delay. The white vertical line is centered on a SB maximum at SB18 and intends to show the delay of the SB maxima between different harmonics, i.e. the emission time.

To overcome the problem of the missing absolute phase two phase measurement techniques were developed: (i) harmonic generation in gas mixtures; (ii) two sources interferometry of the XUV emission. They are detailed right below.

Mixed Gases

The harmonic signal bears the characteristics of I_p , RDM, tunnel ionization etc., of the target medium. When mixing two different gases in the gas jet during HHG, both species will appear as an XUV emitter. The measured intensity $I_{mix}(q)$ of the q th harmonic order of the gas mixture is the interference of the electric fields of the q th harmonic generated from both type of emitters. The interference gives access to the phase difference of the two harmonic field, that is related to the phase differences in each step of the harmonic generation. It is assumed, that the tunnel ionization does not import any phases. The phase difference of the continuum acceleration step is given by $\Delta\phi_{con}(q) = \Delta I_p \tau_q$, ΔI_p and τ_q being the difference of the ionization potentials between the two species and the excursion time, respectively. The difference in the recombination comes from the structural construction of both RDMs. (Kanai et al. [64]) were the first to use this principle to extract the excursion time for a given harmonic order, knowing the ionization potentials of the investigated rare gas atoms. The technique opened up a new way to study the as dynamics of the acceleration step. The use of a mixture of atoms and molecules of the same I_p would result an interference, where the tunnel ionization and the acceleration step would be the same. Therefore this technique can be used to study the phase of the recombination dipole moment of molecules with respect to known atoms as a function of angle, like it was done in CO_2 and Kr (Kanai et al. [66], Wagner et al. [173]) or in N_2 and Ar (Farrell et al. [30], McFarland et al. [104]).

One severe requirement to perform such an experiment is to have very precise control partial pressure of each species inside the region of harmonic generation. Another restriction is to be in such phase matching conditions in which the resulted electric field is simply

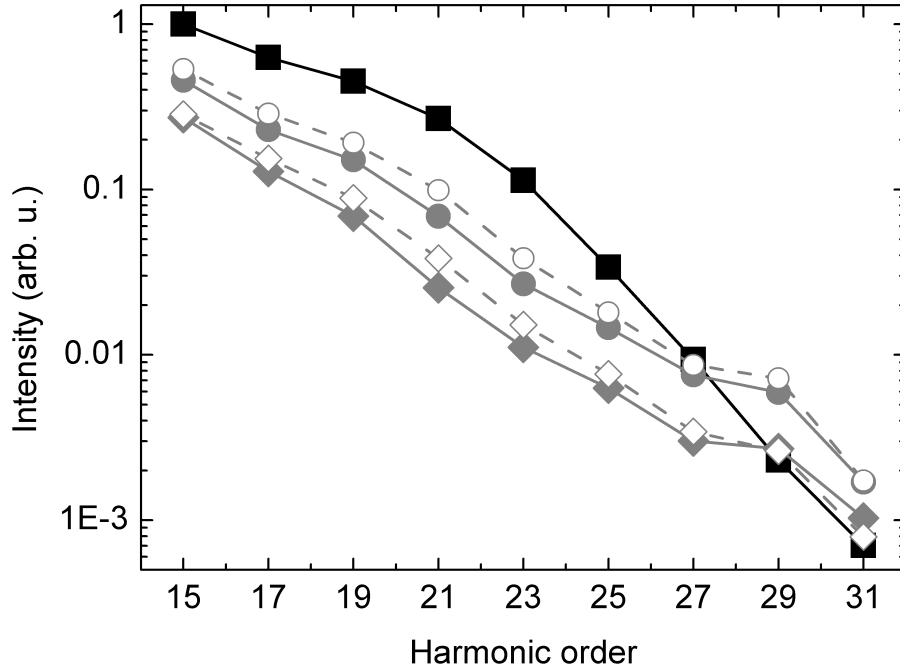


Figure 2.10: Measured Ar (black squares), N₂ (gray full symbols) and gas mixture (gray open symbols) harmonic intensities generated with $I_L = 1.3 \times 10^{14}$ W/cm² with $\lambda_0 = 800$ nm. In the latter case we used a bottle filled with the mixture Ar and N₂ in 1:9 ratio. The circle and diamond symbols refer to molecular alignment distribution at half-revival parallel and perpendicular, respectively, to the generating laser.

the superposition of the two fields, otherwise the overall knowledge of the phase matching condition is needed.

Let us assume, that we have a gas mixture of N₂ $I_p(N_2) = 15.6$ eV and Ar $I_p(Ar) = 15.8$ eV and that their proportion in the gas jet is ρ_{Ar} and $\rho_{N_2} = 1 - \rho_{Ar}$. The harmonic field of pure Ar and pure N₂ is given by $E_{Ar}(q) \exp(i\varphi_{Ar}(q))$ and $E_{N_2}(q, \theta) \exp(i\varphi_{N_2}(q, \theta))$ respectively, where θ shows the angular dependency of the molecular response in aligned ensembles. Therefore, the measured harmonic signal given by the mixture is:

$$I_{mix}(q, \theta) = \left| \rho_{Ar} E_{Ar}(q) e^{i\varphi_{Ar}(q)} + \rho_{N_2} E_{N_2}(q, \theta) e^{i\varphi_{N_2}(q, \theta)} \right|^2 \\ = \rho_{Ar}^2 I_{Ar}(q) + \rho_{N_2}^2 I_{N_2}(q, \theta) + 2\rho_{Ar}\rho_{N_2} \sqrt{I_{Ar}(q)I_{N_2}(q, \theta)} \cos \Delta\varphi(q, \theta), \quad (2.21)$$

where $I_x(q) = |E_x(q) \exp(i\varphi_x(q))|^2$ with $x = Ar, N_2$ represents the harmonic intensity coming from each emitter and $\Delta\varphi(q, \theta) = \varphi_{N_2}(q, \theta) - \varphi_{Ar}(q)$ is the phase difference.

Experimentally one has to perform three measurements, in the same conditions, to determine $I_{mix}(q, \theta)$, $I_{Ar}(q)$ and $I_{N_2}(q, \theta)$ precisely and express $\Delta\varphi(q, \theta)$. It should be noted that this relative phase can take both plus and minus sign (because of the cos function). Assuming the exact knowledge of $\varphi_{Ar}(q)$ (from theoretical calculations) one may explore the full phase map (spectral and angular) of the N₂ recombination dipole moment. This is an advantage with respect to the RABBIT.

In figure 2.10 we present our experimental results on the harmonic intensity measurements by the MBES-TOF system. The generating conditions were kept the same in all three gases. Unfortunately the calculated cosine of the phase differences do not fit between the +1 and -1 range. It suggests that either our experimental conditions changed somehow or the proportion of the gases in the mixture was wrongly estimated. What is clearly visible is

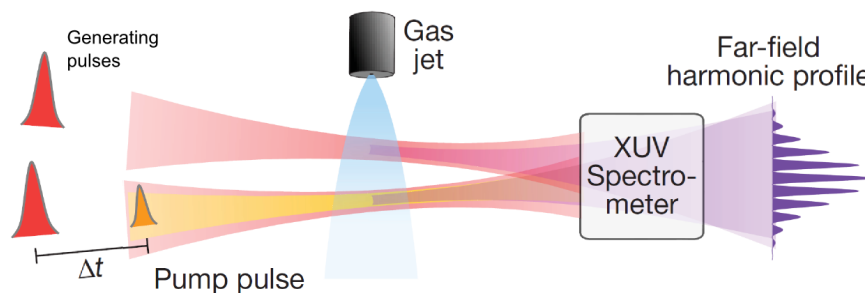


Figure 2.11: Experimental setup scheme of the interferometric phase measurement taken from (Smirnova et al. [147]). Two separated generating beams are focused into the gas jet (red pulses) creating two independent harmonic source. The aligning laser pulse is superimposed with the generating pulse on the lower source and it is delayed in time in order to create an aligned ensemble of the molecules when the generating beam arrives. An XUV spectrometer disperses the spectrum in the end.

that the intensities obtained from the mixture are very close to the intensities measured in N_2 . It means that the electric fields generated from Ar and N_2 are not equally intense in the mixture, decreasing the contrast of the interference.

The great disadvantage of the gas mixture technique is the generally poor and inaccurate control over the density of the elements in the gas jet. The two source interferometry technique overcomes this problem by basing its principles on fully optical interferometry.

Two Source Interferometry

Zerne et al. (Zerne et al. [181]) demonstrated that by splitting the generating laser beam into two spatially separated beams in the gas jet one obtains two independent, but phase locked harmonic source. The XUV radiation coming from both sources may interfere in the far field creating fringe patterns that encodes the relative phase behavior between the two sources. The technique requires high relative temporal stability of the beams, not to blur the fringes pattern.

The fringe pattern in the far field is determined by the relative position of the two sources at the generation and also by the phase difference existing between the two sources for a given harmonic. The phase evolution of a given harmonic can be investigated by inducing phase changes in one source while keeping the other as a reference. It was also demonstrated that by varying the generating laser intensity only in one arm, the total dipole phase of an atom can be retrieved (Corsi et al. [22]). In molecular targets, one source can be aligned and the angular phase variation $\partial\varphi(\theta)/\partial\theta$, with respect to the not aligned source can be investigated. A possible experimental setup is presented for this purpose in figure 2.11. The JILA-Colorado group (Lock et al. [95], Zhou et al. [183]) varied the time delay between the aligning beam and the generating beam in one source, passing through several alignment distributions, while the NRC-Canada group (Smirnova et al. [147]) aligned the molecules along the generating laser pulse and with a HWP they turned the main axes of the alignment by $\theta = -90^\circ, \dots, 90^\circ$. Having high degree of molecular alignment, these experiments can resolve the angular dependence of the RDM and induced as charge rearrangements from the HHG in molecular system.

The two source interferometry in aligned molecules gives the absolute angular phase variation for a given harmonic, but it does not connect the different spectral components. To obtain full phase mapping one has to combine it either with RABBIT or gas mixing techniques. The full characterization of the spectral and angular phase leads to completely

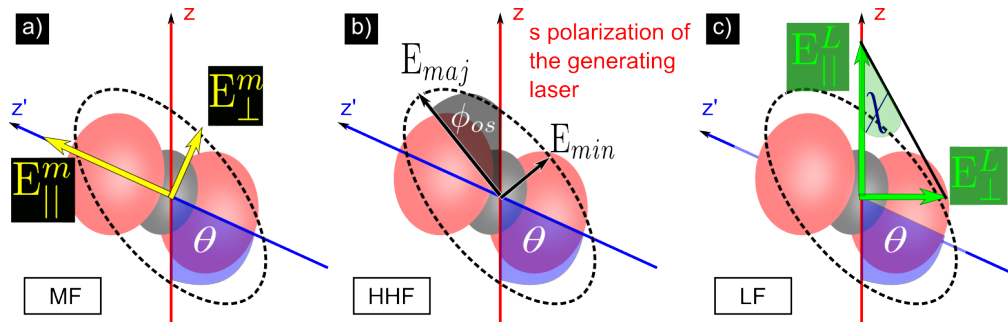


Figure 2.12: Scheme of the different frames used in connection of harmonic polarization. a) shows the molecular frame (MF) that is turned by θ from the z axis and the harmonic electric fields are defined parallel (E_{\parallel}^m) and perpendicular (E_{\perp}^m) to the main axis of the molecule. b) shows the polarization ellipse and we call it high harmonic frame (HHF). ϕ_{os} is called the offset angle and shows the orientation of the polarization ellipse with respect to the generating laser (z axis). c) is in the laboratory frame (LF), the electric fields are defined parallel (E_{\parallel}^L) and perpendicular (E_{\perp}^L) to the generating laser polarization.

describe the recombination dipole moments along one direction, providing better understanding of the molecular structure or induced electronic dynamics.

However, the recombination dipole moment of a molecule consists in general of two components: one along the main molecular axis and one perpendicular to it. None of the techniques presented above measures the polarization of the dipole. One way to go is to measure the polarization of the XUV field, since the properties of the dipole are transferred to the harmonic emission.

2.2.3 Principles of Polarization Measurements

The generating laser induces dipole oscillation in molecules. In linear molecules, like N_2 , the dipole may oscillate along the molecular axis (z') and perpendicularly (x') to it, as already mentioned in section 1.4.3. The coordinate system defined by the molecular axes is called *molecular frame* (MF). In this MF, the parallel $E_{\parallel}^m(q) \exp(i\varphi_{\parallel}^m(q))$ and the perpendicular $E_{\perp}^m(q) \exp(i\varphi_{\perp}^m(q))$ field oscillations may be shifted by $\delta^m(q) = \varphi_{\perp}^m(q) - \varphi_{\parallel}^m(q)$ in phase, giving rise to elliptically polarized light, see figure 2.12 a. Nevertheless, due to symmetry reasons, the distribution of the molecular ensemble has to break the cylindrical symmetry with respect to the polarization of the generating field in order to keep the ellipticity of the XUV radiation. If the emitted XUV radiation is elliptically polarized, then the major and the minor axes of the polarization ellipse defines a coordinate system, called the *high harmonic frame* (HHF), in which the phase difference between the two components of the electric field is $\pi/2$. In HHF the major component is denoted as $E_{maj}(q)$ and the minor as $E_{min}(q)$, see figure 2.12 b. The orientation of the major axis is given by the offset angle $\phi_{os}(q)$. The ellipticity of the field is defined as: $\epsilon(q) = E_{min}/E_{maj}$. The latter two observables can be measured experimentally. Furthermore, as already introduced before, there is the laboratory frame, figure 2.12 c. The main axis is defined with respect to the polarization of the generating laser. The molecule is turned by θ with respect to it. We denote the parallel harmonic field as $E_{\parallel}^L(q) \exp(i\varphi_{\parallel}^L(q))$ and the perpendicular as $E_{\perp}^L(q) \exp(i\varphi_{\perp}^L(q))$ and define the phase shift between them as $\delta^L(q) = \varphi_{\perp}^L(q) - \varphi_{\parallel}^L(q)$.

The experiments are all related to the LF, therefore we derive the transition between the

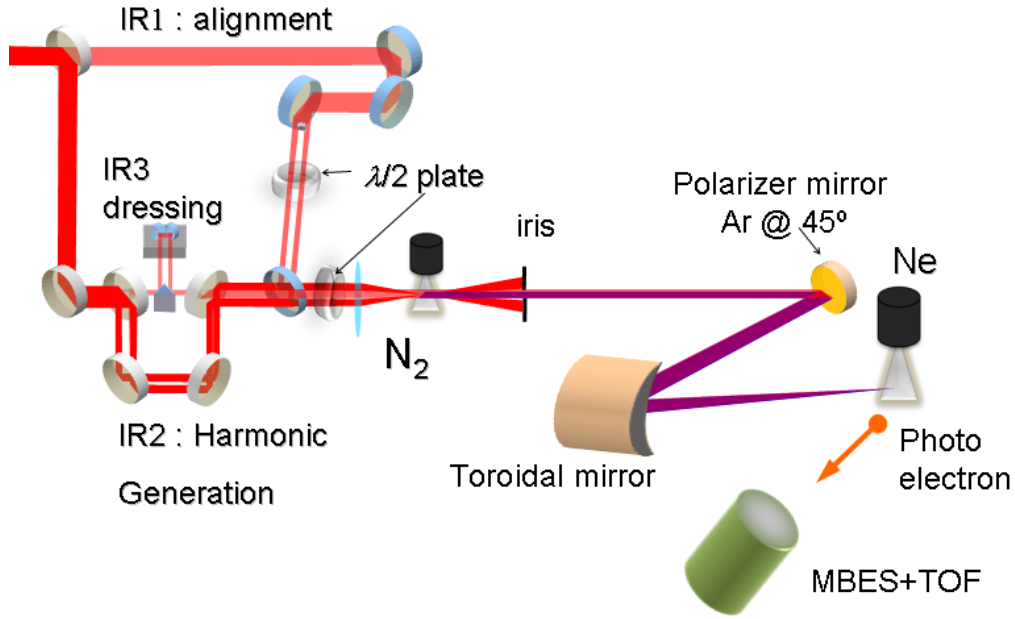


Figure 2.13: Scheme of the experimental setup used to determine the polarization of the harmonics. The setup is mainly the same as in figure 2.1 except that the grating is exchanged by an XUV polarizer (silver mirror set to 45°) and that an additional HWP is installed right before the focusing lens.

HHF and LF. It is given by the rotation of the coordinate system of HHF by ϕ_{os} :

$$E_{\parallel}^L(q)e^{i\phi_{\parallel}^L(q)} = E_{maj}(q) \cos \phi_{os}(q) + iE_{min}(q) \sin \phi_{os}(q) \quad (2.22)$$

$$E_{\perp}^L(q)e^{i\phi_{\perp}^L(q)} = -E_{maj}(q) \sin \phi_{os}(q) + iE_{min}(q) \cos \phi_{os}(q) \quad (2.23)$$

By dividing the perpendicular component with the parallel, one may express the field ratios $E_{\perp}^L(q)/E_{\parallel}^L(q)$ and phase shifts in the LF by equating the real and imaginary parts, respectively on both sides. After applying several trigonometrical equalities and introducing $\chi = \arctan \frac{E_{min}}{E_{maj}}$ (Born et al. [12]), one finds two simple expressions for the intensity ratios and phase differences in LF:

$$\tan \delta^L = \frac{\tan 2\chi}{\sin 2\phi_{os}} \quad (2.24)$$

$$\frac{I_{\perp}^L}{I_{\parallel}^L} = \left(\frac{E_{\perp}^L}{E_{\parallel}^L} \right)^2 = \frac{\tan^2 \phi_{os} + \tan^2 \chi}{1 + \tan^2 \phi_{os} \tan^2 \chi}, \quad (2.25)$$

where we dropped the dependence on q for simplicity. Now we shall see how all these parameters are measured and retrieved.

In traditional optics, the polarization characteristics of the light is measured by polarizers and half- and quarter waveplates. In the XUV domain, especially when a large spectral range is to be covered, it is very hard to find proper tools. (Levesque et al. [92]) proposed a simple way to adapt the techniques of the visible spectral domain to the XUV domain. Our version of the setup is shown in figure 2.13. The polarization profile of the harmonics is measured with a pair of a HWP and an XUV polarizer. The formers are set just in front of the focusing lens while the latter is installed after the harmonics are generated and spatially filtered. These tools are needed to measure the so called *Stokes parameters* (S_0, S_1, S_2, S_3) (Hecht [46]) that describes the polarization states. In the following we express them in

the LF:

$$S_0 = \left| E_{\parallel}^L e^{i\varphi_{\parallel}^L} \right|^2 + \left| E_{\perp}^L e^{i\varphi_{\perp}^L} \right|^2 \quad (2.26)$$

$$S_1 = \left| E_{\parallel}^L e^{i\varphi_{\parallel}^L} \right|^2 - \left| E_{\perp}^L e^{i\varphi_{\perp}^L} \right|^2 \quad (2.27)$$

$$S_2 = 2E_{\parallel}^L E_{\perp}^L \cos(\varphi_{\parallel}^L - \varphi_{\perp}^L) \quad (2.28)$$

$$S_3 = 2E_{\parallel}^L E_{\perp}^L \sin(\varphi_{\parallel}^L - \varphi_{\perp}^L). \quad (2.29)$$

The first Stokes parameter S_0 describes the total intensity of the light; the second parameter S_1 describes the preponderance of being linearly polarized in the horizontal or the vertical direction; the third parameter S_2 describes whether the polarization axes of the linearly polarized light is turned with an angle $\pm\phi_{os}$ and, finally, S_3 describes whether the parallel and perpendicular components are shifted in phase, resulting elliptically (circularly) polarized light. Our setup gives only an upper estimate of the ellipticity, since a quarter wave plate is needed, to make difference between elliptic and partially elliptically polarized lights.

The polarizer is a silver mirror set at 45° angle of incidence. Although, it is not a perfect polarizer, the ratio between the reflectivity of s- and p polarization (R_s perpendicular and R_p parallel, respectively, to the incidence plane) may reach even a factor of 10, see the dashed line in figure 2.14 a). A difficulty of this experiment lies in the low overall value of reflectivity ($\approx 10\%$). In figure 2.14 b) the black line with circle symbols shows our reflectivity measurement on the silver mirror for s polarization, performed in an independent experiment (detailed in Chapter 4). The experimental values are way below than the one retrieved from the database (black full line), possibly due to a pollution on the reflecting surface. The result is that our observable spectral range with the MBES+TOF system decreases to 21-45 eV (where the lowest limit is given by the ionization potential of Ne). Nevertheless, the toroidal mirror set at grazing incidence angle also preferentially reflects the s polarized light with respect to the p polarization, by a factor of 2. Therefore, our polarization filtering is even more increased.

To secure the symmetry break of the molecular distribution with respect to the generating beam, they are aligned at the half-revival and turned by ϑ . The principle of the XUV polarization measurement is based on the Malus oscillation. By using a HWP just before the focusing lens, the polarization of all participating beams can be turned with an angle $\rho=0^\circ, \dots, 180^\circ$ with respect to the s polarization, while keeping the relative alignment of each IR beam i.e. keeping the ϑ angle between the generating laser and the aligning beam. Since the XUV polarizer is not perfect, we describe the reflected intensity as the incoherent sum of the reflected parallel and perpendicular intensity:

$$I = R_s \left| E_{\parallel}^L e^{i\varphi_{\parallel}^L} \right|^2 + R_p \left| E_{\perp}^L e^{i\varphi_{\perp}^L} \right|^2. \quad (2.30)$$

The photoelectrons created by the parallel and perpendicular components of the XUV field are temporally delayed from each other (Kruit and Read [75]) and only a small portion of them is interfering. Therefore, as a first approximation we assume that the incoherent sum in eq. 2.30 is correct. By performing the transition from LF to HHF (while, we still disregard the dependence on q), i.e. substituting eqs. 2.22 and 2.23 into eq. 2.30 the measured intensity in the Malus oscillation is:

$$\begin{aligned} I &= \left[R_s I_{min} + R_p I_{maj} + \frac{(R_s - R_p)(I_{maj} - I_{min})}{2} \right] + \frac{(R_s - R_p)(I_{maj} - I_{min})}{2} \cos 2\rho \\ &= a + b \cos 2\rho, \end{aligned} \quad (2.31)$$

where $a = R_s I_{min} + R_p I_{maj} + \frac{(R_s - R_p)(I_{maj} - I_{min})}{2}$ is the offset of the oscillation while $b = \frac{(R_s - R_p)(I_{maj} - I_{min})}{2}$ is the amplitude and $I_{maj(min)} = E_{maj(min)}^2$. Figure 2.15 presents such an

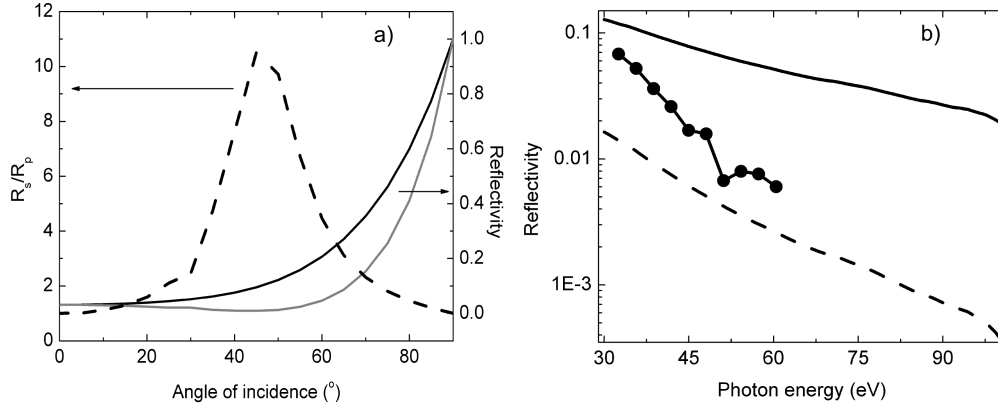


Figure 2.14: Reflectivity characteristics of the XUV polarizer. Black and gray line in a) shows the reflectivity properties in s- and p polarization, respectively as the function of incidence angle (with respect to the normal of the surface). The values are retrieved from the on-line CXRO database. The plot is done for 39 eV photon energy that corresponds to the 25th harmonic of an 800 nm wavelength laser. The dashed line indicates the ratio between the s- and p polarization. Full and dashed lines in b) shows the reflectivities for s- and p polarization, respectively as the function of photon energy. The curve with the circle symbol is the experimentally measured reflectivity.

oscillation (blue circles) and the calculated cosine fit (black curve) for the 23rd harmonic of an 800 nm laser, measured in N_2 at $\vartheta = 50^\circ$. The meaning of a and b are signed in the figure. Usually the maximum of the oscillation is not at $2\rho = 0^\circ$ but it is rather shifted. It means that the major axis of the polarization ellipse is not parallel to the s polarization axis but it is tilted. This tilt corresponds exactly to ϕ_{os} as marked in the figure.

The reflectivities in both s- and in p polarization are unknown parameters. Their ratio $C = R_p/R_s$ was determined by measuring the Malus oscillation in a linearly polarized reference system. Such radiation can be created in atoms like Ar, when generating with linearly polarized laser light and in aligned or unaligned molecules when they are cylindrically distributed with respect to the generating laser. This is the case when N_2 is aligned parallel ($\vartheta = 0^\circ$) and perpendicular ($\vartheta = 90^\circ$) at the half-revival. Following the route presented by eqs. 2.30 and 2.31 with linearly polarized light ($I_{min} = 0$), one obtains $a_{ref} = R_p I_{maj} + \frac{(R_s - R_p) I_{maj}}{2}$ and $b_{ref} = \frac{(R_s - R_p) I_{maj}}{2}$. The reflectivity ratio is expressed with the help of $\Gamma_{ref} = b_{ref}/a_{ref}$ as: $C = \frac{1 - \Gamma_{ref}}{1 + \Gamma_{ref}}$.

The ellipticity can be obtained by calculating the ratio of $b(\vartheta)$ and $a(\vartheta)$ from eq. 2.31, substituting the already introduced notations of ellipticity and reflectivity ratio:

$$\Gamma(\vartheta) = \frac{b(\vartheta)}{a(\vartheta)} = \frac{(1 - C)(1 - \epsilon^2(\vartheta))}{(1 + C)(1 + \epsilon^2(\vartheta))}, \quad (2.32)$$

where $\vartheta \neq 0^\circ, 90^\circ$ denotes the alignment distribution. After some reordering in the calculation and substituting Γ_{ref} , one can find that the ellipticity is:

$$\epsilon(\vartheta) = \sqrt{\frac{\Gamma_{ref} - \Gamma(\vartheta)}{\Gamma_{ref} + \Gamma(\vartheta)}}, \quad (2.33)$$

RABBIT, combined with a polarization characterization, results a complete spectral characterization of the recombination dipole moment. Approaching the most complete harmonic characterization provides unprecedented richness of information that encodes the complex structural and dynamical changes of the electronic construction of a molecule.

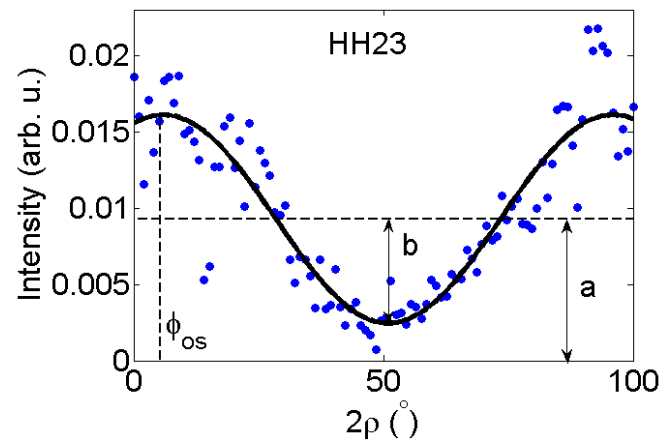


Figure 2.15: Malus oscillation of the HH23 intensity when $\theta = 50^\circ$. Blue dots are experimental values, black curve is the fitted function defining the a , b and ϕ_{os} parameters.

Advanced theoretical treatment is required to understand the physical background of the measured processes. This will be the subject of section 3.5.

SELF-PROBING OF ELECTRONS IN MOLECULES

Several schemes already exist to study atomic or molecular structures. Using light fields or high-energy electron impact (Chan et al. [18]) one may induce dipole transitions from the ground state to excited bound- and continuum states (photoionization) or vice versa (photorecombination). According to the detailed balance principle these quantities are the complex conjugate of each other. Both processes give access to information on the induced dipole, e.g. the photoionization dipole \mathbf{d}_{ion} or on the photorecombination dipole moment \mathbf{d}_{rec} . These are usually complex quantities, possibly with two orthogonal components. So far the existing techniques are based on non-coherent processes, like photoionization by synchrotron radiation and electron scattering, that give only the amplitude of the transition dipole and in special cases also the ellipticity.

The process of HHG encodes coherently the structure and dynamical charge rearrangement of atoms/molecules in the XUV radiation. Thanks to great techniques like optical molecular alignment, angle-resolved measurements can be done. Since HHG is a more complex process than a simple one-photon ionization, we explain in section 3.1 how the molecular recombination dipole moment in amplitude and phase can be retrieved by using the self-probing technique. For the sake of simplicity, in the beginning we assume perfect molecular alignment and do not take into account the perpendicular component of the RDM.

We present in section 3.3 the possibility of looking beyond the recombination dipole moment and extract (reconstruct) static molecular orbitals, based on the proposition of (Itatani et al. [54]). It will be shown that in certain experimental conditions multiple orbitals (HOMO and HOMO-1 in N_2) may contribute to the HHG and both of them may be reconstructed with certain assumptions. The results of our early studies are summarized in PAPER I. In section 3.3, by changing the intensity of the generating laser, we follow the evolution of the interference induced by the two orbitals, imprinted in the spectral intensity and phase of the harmonics. We uncover the so far hidden importance of the orbital-dependent nuclear vibration. Furthermore, we highlight that this interference can be "controlled" with experimental parameters. PAPER II gives a summary of these results. In section 3.4, the XUV emission obtained for different alignment distributions was characterized. The measurements are simulated by including averaging over the alignment distribution using different theoretical models. We remark few techniques which help to deconvolve the single molecule response from the averaged macroscopic signal. Finally, in section 3.5, we present XUV polarimetry measurements giving access to the two perpendic-

ular components of the RDM. By studying different models we try to reveal the origin of the measured ellipticities. Thanks to our sophisticated characterization technique, the first Vectorial Orbital Tomography (VOT) is also presented.

RÉSUMÉ DU CHAPITRE

Plusieurs approches existent pour étudier les structures atomiques et moléculaires. En utilisant des champs lumineux ou des collisions avec des électrons d'énergie élevée, il est possible d'induire des transitions de l'état fondamental vers des états liés excités et des états du continuum (photoionisation) ou vice versa (photorecombinaison). Ceux procurent des informations sur le dipôle induit, comme par exemple le dipôle de photoionisation \mathbf{d}_{ion} ou le dipôle de photorecombinaison \mathbf{d}_{rec} . Ces sont en général une grandeur vectorielle complexe. Jusqu'à présent, les techniques existantes pour la mesurer se basent sur des processus non cohérents, comme la photoionisation par radiation synchrotron ou la diffusion électronique. Elles ne donnent cependant que l'amplitude du dipôle de transition et, dans des cas particuliers, son ellipticité.

Le processus de GHE encode de façon cohérente dans le rayonnement UVX la structure et le ré-arrangement des charges dynamiques des atomes ou molécules. Grâce à des techniques comme l'alignement moléculaire optique, des mesures résolues en angle peuvent être effectuées. Comme la GHE est beaucoup plus complexe que l'ionisation à un photon, dans ce chapitre, nous expliquons comment le moment du dipôle de recombinaison d'une molécule, qui est un vecteur a priori complexe, peut être retrouvé en utilisant la technique d'auto-sonde. Cependant, pour simplifier, nous considérons initialement un alignement moléculaire parfait et l'on ne tient pas compte de la composante perpendiculaire du DRM.

Nous consacrons le paragraphe 3.3 à évaluer la possibilité de regarder au-delà du dipôle et d'extraire (reconstruire) les orbitales moléculaires statiques, en nous basant sur la proposition de (Itatani et al. [54]). Nous démontrons que, sous certaines conditions expérimentales, les orbitales multiples (HOMO et HOMO-1 dans N_2) peuvent contribuer à la GHE et que les deux peuvent être reconstruites simultanément moyennant certaines hypothèses. Les résultats de nos premières études sont résumés dans l'ARTICLE I. Dans le paragraphe 3.3, en changeant l'intensité du laser de génération et en observant l'intensité et la phase spectrale des harmoniques, nous suivons l'évolution de l'interférence du signal provenant des deux orbitales. Nous mettons en évidence l'importance de l'évolution – jusqu'à présent ignorée, de vibrations nucléaires dépendantes de l'orbitale étudiée. De plus, nous soulignons que cette interférence peut être contrôlée par les paramètres expérimentaux. L'ARTICLE II donne un résumé de ces résultats. Dans le paragraphe 3.4, l'émission UVX générée dans des distributions d'alignement différentes sont caractérisées. Les mesures sont simulées au moyen de différents modèles en incluant le moyennage sur les distributions d'alignement. Dans le cadre de ces études, nous soulignons l'importance de la phase spectrale au moment du moyennage. Enfin, dans le paragraphe 3.5, les résultats expérimentaux sont présentés et permettent de décomposer le DRM en deux composantes perpendiculaires. En étudiant différents modèles nous essayons de mettre en évidence l'origine de l'ellipticité mesurée. Grâce à notre technique de caractérisation sophistiquée, la première Tomographie Vectorielle de l'Orbitale (TVO) est présentée.

3.1 Self-probing technique to measure the recombination dipole

To see the relation between the harmonic signal and the recombination dipole moment, we recall the calculations presented in sections 1.4.2 and 1.4.3. As it was shown, by apply-

ing the saddle point method one can analytically factorize the harmonic dipole into three main terms: tunnel ionization, continuum acceleration and recombination, see eq. 1.59. The complex harmonic spectrum is obtained from the Fourier transform of the harmonic acceleration dipole. This can be calculated in three different dipole forms. Depending on the choice, eqs. 1.60, 1.61 and 1.62, one has different frequency dependent pre-factors (we denote them as η_f , f being the chosen form: $\hat{\mathbf{a}}, \hat{\mathbf{p}}, \hat{\mathbf{r}}$). It is also noted that the choice of the form affects only the dipole operator $\hat{\mathbf{d}}^f$ in the recombination dipole moment. By restricting the HHG to short trajectory contributions we reorder the components obtained after the Fourier transform and collect the variables into three parameters (similarly to (Ivanov et al. [56])) to calculate the harmonic spectrum:

$$\epsilon_{\text{XUV}}^f(\mathbf{k}, I_L, \theta) = \eta_f \gamma(\mathbf{k}, I_L, \theta) a(\mathbf{k}, I_L) \langle \psi_0(\mathbf{r}) | \hat{\mathbf{d}}^f | \psi_c(\mathbf{r}) \rangle, \quad (3.1)$$

where, γ is the square root of the tunnel ionization rate for molecules defined by eq. 1.43, a is a complex number including the gathered phase and the spreading during the excursion of the EWP, θ is the angle between the molecule and the polarization of the driving laser field and $\mathbf{k} = \mathbf{p} + \mathbf{A}(t_r)$ is the asymptotic wavenumber vector of the continuum electron and $\mathbf{k} = (0, 0, k)$ is parallel to the driving laser polarization. By rewriting eq. 1.58, including $\omega = q\omega_0$, one gets the following dispersion relation:

$$q\omega_0 = \frac{k^2}{2} + I_p, \quad (3.2)$$

where I_p is the ionization potential. More rigorous derivation of these result can be found in the great thesis of van der Zwan [164].

Eq. 3.1 shows that the emitted harmonic signal is proportional to the recombination dipole moment, that is characteristic of the target gas, with the given dispersion relation. The idea to retrieve the RDM is to remove the first two terms by calibration with an appropriate atom. The calibration also removes η_f . a is considered to be independent of the target and is defined by the intensity of the generating laser. γ consists of two parts. The first term (Γ_a) can be considered the same for atoms and molecules if the ionization potential and the laser intensity are the same. The second term $R(\theta)$ encodes the geometry of the molecular structure. Therefore, apart from $R(\theta)$ the tunnel ionization and the continuum process of HHG can be eliminated by calibrating the molecular signal with its correspondent atom under the same experimental conditions while assuming that the RDM of the atom can be calculated or is known from other experiments (Le et al. [79]).

The measured harmonic signal is constructed from the superposition of the harmonic field emitted by single atoms/molecules over the generating medium. (Jin et al. [58, 59, 60, 61]) investigated how macroscopic effects are modifying the single atomic/molecular response. They concluded, that in special experimental conditions like low gas density, not too high laser intensity and short gas medium, the atomic/molecular RDM can be still factorized from the other terms determining the macroscopic response, in particular from phase matching. Therefore, if the factors like absorption and free-electron are similar in the molecule and in the partner atom media, the calibration may be still performed and the molecular RDM can be still recovered.

Assuming that the measured complex harmonic field emitted by a molecule is $\epsilon_{\text{XUV}}(\mathbf{k}, I_L, \theta) = A(\mathbf{k}, I_L, \theta) \exp(i\varphi(\mathbf{k}, I_L, \theta))$ and by the reference atom is $\epsilon_{\text{XUV}}^{\text{ref}}(\mathbf{k}, I_L) = A_{\text{ref}}(\mathbf{k}, I_L) \exp(i\varphi_{\text{ref}}(\mathbf{k}, I_L))$, the RDM of the molecule takes the following form:

$$\begin{aligned} \mathbf{d}^f(\mathbf{k}, \theta) &= \langle \psi_0(\mathbf{r}) | \hat{\mathbf{d}}^f | \psi_c(\mathbf{r}) \rangle = \\ &= \frac{1}{\sqrt{R(\theta)}} \frac{A(\mathbf{k}, I_L, \theta)}{A_{\text{ref}}(\mathbf{k}, I_L)} e^{i[\varphi(\mathbf{k}, I_L, \theta) - \varphi_{\text{ref}}(\mathbf{k}, I_L)]} \langle \psi_{\text{ref}}(\mathbf{r}) | \hat{\mathbf{d}}^f | \psi_c(\mathbf{r}) \rangle. \end{aligned} \quad (3.3)$$

The listed requirements are quite well fulfilled in the case of N₂ and Ar. The recombination matrix elements of Ar can be easily calculated by quantum chemistry codes or using pseudo-potentials. The harmonics' spectral amplitude and phase from aligned N₂ and Ar are measured by using the MBES+TOF and the RABBIT technique while keeping the same experimental conditions for both gases.

3.2 Molecular Orbital Tomography

Using the plane wave approximation to describe the RDM, (Itatani et al. [54]) pointed out that the molecular orbital itself can be expressed from the RDM by performing an inverse spatial Fourier transform. The different aspects of molecular orbital tomography are well detailed in (Haessler et al. [43]). From now on we investigate the concept of molecular orbital tomography using both length ($f = \hat{r}$) and velocity ($f = \hat{p}$) form to describe the RDM $d^{f,\zeta}$ both in the molecular ($\zeta = m$) and the laboratory ($\zeta = L$) frame.

In general, the harmonic characterization is performed in the laboratory frame. For the moment we assume that both the parallel (\parallel) and the perpendicular (\perp) component of the RDM can be retrieved, with respect to the polarization of the driving laser. We define θ as the angle between the main molecular axis and the polarization of the driving laser. By the rotation of LF with θ we can express the RDM in the molecular frame (x', y', z'):

$$d_{z'}^{f,m} = d_{\parallel}^{f,L} \cos \theta - d_{\perp}^{f,L} \sin \theta \quad (3.4)$$

$$d_{x'}^{f,m} = d_{\parallel}^{f,L} \sin \theta + d_{\perp}^{f,L} \cos \theta. \quad (3.5)$$

The y' axis shows the propagation direction of the laser pulse, hence in that direction there is no induced dipole oscillation. Therefore, we define the 2 dimensional molecular orbital form, that contributes to the RDM, as the projection onto the plane perpendicular to the propagation of the laser: $\psi_0(x', z') = \int \psi_0(x', y', z') dy'$. This implies that an orbital with an odd symmetry in y' will not contribute to the dipole.

3.2.1 Length form RDM

In length form, the dipole operator is $\hat{\mathbf{d}}^{\hat{r}} = \mathbf{r}$ and we assume that the molecular orbital is real valued. Then the u -component ($u = x', z'$) of the dipole matrix element in the molecular frame writes as:

$$d_{u'}^{\hat{r},m}(\mathbf{k}) = \langle \psi_0(\mathbf{r}') | u | e^{i\mathbf{k} \cdot \mathbf{r}'} \rangle = \iint u \psi_0(x', z') e^{i(k_{x'} x' + k_{z'} z')} dx' dz'. \quad (3.6)$$

Now by performing an inverse Fourier transform of the recombination dipole moment, one can easily express the molecular orbital:

$$\psi_0^u(x', z') = \frac{\mathcal{F}_{\mathbf{k} \rightarrow \mathbf{r}}[d_{u'}^{\hat{r},m}(k_{x'}, k_{z'})]}{u}. \quad (3.7)$$

In PAPER I and sections 3.3 and 3.4 the complex recombination dipole moment was experimentally characterized only in the parallel direction with respect to the driving laser polarization. Relying on the fact that, the perpendicular RDM component is smaller than the parallel (see (Le et al. [80]) and figures 1.8, 3.13), as a first approximation we assumed that $d_{\perp}^{\hat{r},L} = 0$. Therefore, the dipole components in the molecular frame are obtained by the projections:

$$d_{x'}^{\hat{r},m} = d_{\parallel}^{\hat{r},L} \sin \theta \quad (3.8)$$

$$d_{z'}^{\hat{r},m} = d_{\parallel}^{\hat{r},L} \cos \theta. \quad (3.9)$$

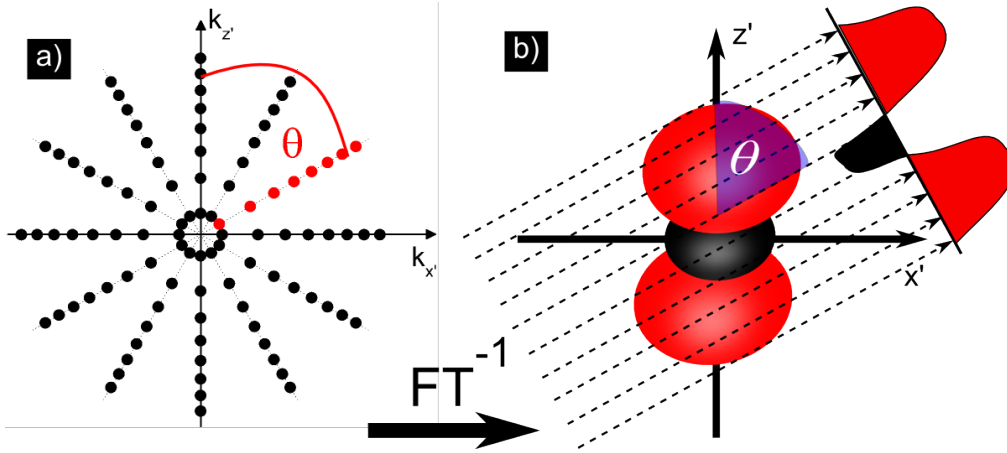


Figure 3.1: Figure (a) shows the discretized Fourier space of the object $q\psi_0(x', z')$. Red dots correspond to harmonic intensity and phase measurements along one molecular alignment θ . Figure (b) presents the real space coordinates with the schematic molecular orbital of N_2 HOMO aligned along z' . The inverse Fourier transform of the measured k space gives the 2-D projection of the orbital to the perpendicular plane in the direction shown by θ . This is also referred to as Radon transformation.

These projections provide points in the Fourier space, located at the positions $(k_{x'}, k_{z'})$ defined by i) the energy conservation law, eq. 3.2, where $k^2 = k_{x'}^2 + k_{z'}^2$; ii) the recollision angle θ . For a given θ , the harmonic spectrum gives access to a slice in one quadrant of the Fourier space, see figure 3.1 a. The sampling is discretized since our spectrum contains only the odd multiples of ω_0 . The inverse spatial Fourier transform of such a slice corresponds to a 2D projection of the molecular orbital onto the perpendicular plane with respect to the direction given by θ , figure 3.1 b. By exploring the whole Fourier space, i.e. changing the re-collision angle θ from 0 to 2π , the orbital is probed from all directions, allowing the reconstruction of the 2D orbital in real space.

Since the 2D reconstructions are performed on the same orbital using the dipoles along x' and z' axes, $\psi_0^{x'}(x', z')$ and $\psi_0^{z'}(x', z')$ should be equal, in principle. Although, due to the discrete sampling of the Fourier space and to the errors imported by the assumptions, this is not the case generally. Therefore, we define the *reconstructed molecular orbital* as the average of the two components:

$$\psi_0(x', z') = \frac{1}{2} \left(\psi_0^{x'}(x', z') + \psi_0^{z'}(x', z') \right). \quad (3.10)$$

3.2.2 Velocity form RDM

In velocity form, the dipole operator is $\hat{\mathbf{d}}^{\hat{\mathbf{p}}} = -i\nabla_{\mathbf{r}'}$, therefore the RDM is expressed in the MF as:

$$d_u^{\hat{\mathbf{p}}, m}(\mathbf{k}) = -i \langle \psi_0(\mathbf{r}') | \frac{\partial}{\partial u} | e^{i\mathbf{k}\cdot\mathbf{r}'} \rangle = k_u \iint \psi_0(x', z') e^{i(k_{x'}x' + k_{z'}z')} dx' dz'. \quad (3.11)$$

There is a clear difference in the dipole written in the velocity form with respect to the length form. Instead of the spatial coordinates we have wavenumbers. In the LF the velocity form RDM vector is parallel to \mathbf{k} and thus to the laser polarization. Therefore, this form does not have perpendicular component in LF and the rotation procedure in eqs. 3.8 and 3.9 can be directly applied. The orbital reconstruction is obtained by eq. 3.10 after calculating:

$$\psi_0^u(x', z') = \mathcal{F}_{\mathbf{k} \rightarrow \mathbf{r}} \left[\frac{d_u^{\hat{\mathbf{p}}, m}(k_{x'}, k_{z'})}{k_u} \right]. \quad (3.12)$$

Due to the different approximations and in particular the SFA, the two forms are not equivalent (see discussion in section 1.4.3). While there is no consensus on which reconstruction gives more precise orbital reconstruction, there may be technical reasons to prefer one or the other: if ψ_0 has a nodal plane containing the x' or z' axis, one will run into numerical problem when dividing by x' and z' in eq 3.7. This problem is not present in the velocity form, since one divides by k_u .

3.2.3 How reliable is the plane wave approximation?

From sections 1.3 and 1.4.3 we already know that the PW approximated dipole does not reproduce all the properties of the scattering dipole. In particular, resonances and phase terms like Coulomb and scattering phase shifts. Furthermore, HHG acts as a temporal filter on the recombination dipole. For example, the electrons that are "trapped" during HHG in a metastable state with longer lifetime than half optical cycle (like shape resonances) will have a contribution to the harmonic signal, but out of phase. Therefore, their contribution adds up destructively in the macroscopic signal, hence their influence may be filtered out.

In figures 3 b and c of PAPER I we compared the PW dipole phase with Coulomb wave (CW) dipole phases for the N_2 HOMO orbital at alignment angles of $\theta=0^\circ, 45^\circ, 90^\circ$. The CW dipole phase $\varphi_{CW}(\omega) = \sigma(\omega) \pm \pi/2$ deviates from the PW dipole phase due to the influence of the Coulomb potential. Two main deviations are observed: i) a vertical phase shift $\delta\phi_r$ that decays smoothly as k increases and ii) a translation δk of the phase jump. As a function of electron momentum the difference δk in position of the phase jumps corresponds to a shift in photon energy of $\sim I_p$. Therefore, the PW dipoles gives qualitatively good results (and better reconstructed orbitals) if one uses the heuristic dispersion relation $k^2/2 = \omega$, instead of the relation defined by eq. 3.2. The heuristic dispersion relation compensates for the acceleration given by the ionic core that is missing in the PWA. By compensating for the k -translation and the averaged phase shift, the PW dipole becomes a good approximation of the CW dipole. More generally one could say that although some effects of the exact potential well of the molecule may be lost by using PWA, a global structure form can be still described qualitatively.

Recently, a group in Milano found a clever way to get one step closer to the exact continuum states. Although, these new results presented by (Vozzi et al. [172]) are too recent to be applied in this thesis, they show that there are still things that can be done to improve the tomographic procedure. They presented a new experimental approach and a more developed theoretical treatment of orbital tomography. Instead of measuring the spectral phase, they apply an iterative code with some assumptions to retrieve it. Concerning the principles of tomography, they include first order corrections to the PWA, by expressing the continuum electron as:

$$\psi_c(\mathbf{r}) = e^{ikz} \left[1 - \frac{i}{k} \int V(\mathbf{r}, \theta) dz \right]. \quad (3.13)$$

$V(\mathbf{r}, \theta)$ corresponds to the molecular potential. Note that the equation is expressed in the LF. Recalling from the Schrödinger equation of a bound electron that $\mathcal{F}_{r \rightarrow k}[V(\mathbf{r}, \theta)\psi_0(\mathbf{r})] = -\left(I_p + \frac{k^2}{2}\right) \mathcal{F}_{r \rightarrow k}[\psi_0(\mathbf{r})]$ and substituting it along with eq. 3.13 into the expression of the velocity form dipole 3.11 (expressed in LF), one finds:

$$d_{\parallel}^{\dot{\mathbf{p}}, L}(\mathbf{k}) \propto \left(\frac{3k}{2} + \frac{I_p}{k} \right) \mathcal{F}_{r \rightarrow k}[\psi_0(\mathbf{r})] - i \mathcal{F}_{r \rightarrow k}[C(\mathbf{r}, \theta)\psi_0(\mathbf{r})]. \quad (3.14)$$

Here, $\mathcal{F}_{r \rightarrow k}$ indicates spatial Fourier transform and $C(\mathbf{r}, \theta) = \int V(\mathbf{r}, \theta) dz$ is rather an unknown function, since the exact shape of the potential is not known. Therefore, the authors neglect the contribution of the second term in eq. 3.14. Since the procedure of orbital tomography applies to the MF and to compare the so achieved reconstructed orbital with eq

3.12 we express the parameters in 3.14 in the MF:

$$\psi_0^u(x', z') = \mathcal{F}_{k \rightarrow r'} \left[\frac{d_{\parallel}^{\hat{p}, m}(k_{x'}, k_{z'})}{\frac{3k_{\parallel}}{2} + \frac{I_p}{k_{\parallel}}} \right]. \quad (3.15)$$

An additional term appears in the denominator as compared to eq. 3.12 that adds a correction to the PWA due to the influence of the ion field. This additional term, proportional to I_p , has similar effect on the reconstruction as the heuristic conservation law. Namely, it accounts for the acceleration by the molecular potential, although mathematically and physically in a more exact way.

It seems that the first correction to the PWA is really related to the acceleration effect of the Coulomb potential. How to include the effects of short-range potentials still needs investigation.

3.2.4 Experimental Molecular orbital Tomography

Partial experimental measurements were provided in the first article on molecular tomography (Itatani et al. [54]). Only the dipole amplitude was measured, while the phase and the polarization were assumed by theoretical considerations. They included an overall π phase jump for harmonic 25 for all angles ($\lambda_0 = 800$ nm). They did so because the dipole amplitude presented an angle independent minimum at that harmonic order.

With the RABBIT technique we were able to measure both the spectral amplitude and phase for the parallel dipole component, presented in figures 2 a and b, respectively in PAPER I. More details on the phase retrieval can be found in the Supplementary Information. The measurements were performed in the half-revival and the alignment laser polarization was turned from $\theta = 0^\circ$ to 90° with 10° steps. Turning the alignment further would not provide any additional information for symmetric molecules having only a linearly polarized driving laser. Their RDM is invariant for the transformations: $d_{\parallel}^{f, L}(-\theta) = d_{\parallel}^{f, L}(\theta) = d_{\parallel}^{f, L}(\theta + \pi)$. By controlling the trajectory of the re-colliding electron, hence the angle of the re-collision, for example with an additional perpendicularly polarized laser field, it would be possible to retrieve the symmetry characteristics of the molecule. Such an experiment was already done for atoms by (Shafir et al. [142]).

Because of these considerations, when performing an experimental tomographic reconstruction of a molecular orbital, we assume first that somehow, the orbital symmetry is already known. In the case of N_2 HOMO, it has a σ_g symmetry. It means, that the molecular orbital is even in both x' and z' . Calculating the dipole in the length form with eq. 3.6 gives that $d_{x'}^{\hat{r}, m}(k_{x'}, k_{z'})$ is odd in $k_{x'}$ and even in $k_{z'}$, while $d_{x'}^{\hat{p}, m}(k_{x'}, k_{z'})$ is even in $k_{x'}$ and odd in $k_{z'}$. Appendix B gives an overview on the parity features of the Fourier transform what we exploited here. Then it is enough to explore the first quadrant of the Fourier space $(k_{x'}, k_{z'})$ and by imposing the the parity of the wavenumber vector, the other quadrants can be extrapolated. Otherwise, if one deals with an unknown symmetric molecule, the determination of its HOMO symmetry is inevitable to do tomographic orbital reconstructions. When working with asymmetric molecules, besides of alignment they have to be oriented too. Since, the molecule is asymmetric, HHG on the top part and the bottom part of the molecular orbital is not equal, therefore their characteristics is blurred when using a simple multi-cycle IR beam. Therefore, in addition they require specially prepared driving laser pulses in order to probe only one side of the molecule during their interaction.

The reconstruction of the N_2 HOMO orbital from experimental measurements and imposing the symmetry is presented in PAPER I in figure 4 a, for a filtered Fourier space range (from harmonic 17 to 31). The corresponding theoretically obtained orbital is presented in figure 4 c (filtered in the experimental range) and in figure 4 e (complete HF orbital).

3.2.5 Two-center interference

The RDM is a "fingerprint" of the active orbital that is encoded in the XUV radiation of HHG. Molecular orbital tomography is quite demanding experimentally, hence we search for theoretical models with clearer relation between the RDM and the harmonic signal. We still stick to the PWA as it was introduced earlier, since that is the easiest way to describe the RDM. Considering the molecular orbital, let us imagine that it is an anti-symmetric combination of two atomic orbitals: $\psi_0(\theta) = \phi_0(\mathbf{r} - \frac{\mathbf{R}}{2}) - \phi_0(\mathbf{r} + \frac{\mathbf{R}}{2})$, with \mathbf{R} being the internuclear distance vector that makes an angle θ with the polarization of the generating laser field. Therefore, the expressed RDM in the velocity form and in LF $\hat{\mathbf{d}}^{\hat{\mathbf{p}},L} = -i\nabla_r$, is the following:

$$\langle \psi_0(\theta) | \hat{\mathbf{d}}^{\hat{\mathbf{p}},L} | e^{ik \cdot r} \rangle = 2ik \sin\left(\frac{kR}{2} \cos\theta\right) \langle \phi_0(\mathbf{r}) | e^{ik \cdot r} \rangle. \quad (3.16)$$

Besides the features of $\phi_0(\mathbf{r})$, such a dipole construction involves an alignment angle dependent dipole amplitude. The sign of the dipole changes when the alignment and the internuclear distance obeys the following relation:

$$R \cos\theta = n\lambda_e, \quad (3.17)$$

where n is an integer and $\lambda_e = \frac{2\pi}{k}$ is the de Broglie wavelength. This simple relation shows that the internuclear distance can be mapped by the re-colliding electrons. The same can be calculated with symmetric combination of atomic orbitals: $\psi_0(\theta) = \phi_0(\mathbf{r} - \frac{\mathbf{R}}{2}) + \phi_0(\mathbf{r} + \frac{\mathbf{R}}{2})$ resulting in the following destructive criteria:

$$R \cos\theta = \left(n - \frac{1}{2}\right) \lambda_e. \quad (3.18)$$

The same principles can be applied in the length form as well, resulting in slightly different criteria for the destructive interference (because of PWA). Through the dispersion relation, the destructive interference is mapped into the yield of the emitted harmonics, resulting in minima in the spectra, called *structural minima* and corresponding π phase jumps. This was first foreseen by (Lein et al. [88]).

The two criteria also predict that the position of this minimum in photon energy should vary with the molecular alignment. That was found experimentally by several groups, in CO₂ (Boutu et al. [13], Kanai et al. [63], Vozzi et al. [171]). However, it turned out that the position of the structural minimum, when CO₂ was aligned parallel to the driving laser polarization, disagreed between the different groups. It is clear that if a single orbital contributes to the emission, a variation of I_L only affects the prefactors of the RDM in the harmonic dipole, but not the RDM itself: the structural minimum should not move. (Smirnova et al. [147]) attributed this observation to several ionization channel contributing to the emission and interfering differently depending on the experimental conditions, namely the different I_L . Independently (McFarland et al. [103]) reported the observation of multi-channel contributions to the harmonic signal when investigating different alignment distributions of N₂. They saw double peaked structure in the scan of the half-revival (instead of the usual maximum at 4.2 ps and minimum at 4.4 ps, see figure 2.2 b) mostly at the cut-off harmonics. Since HOMO-1 has a π_u symmetry, it may largely contribute to the harmonic generation, when the N₂ molecules are perpendicularly aligned to the driving laser. That is why they could observe a maximum at 4.4 ps. The presence of HOMO-1 in the harmonic signal is clearer in the cut-off harmonics since its cut-off is more extended than the cut-off of HOMO.

3.2.6 Multi-Orbital Contributions to HHG

If the spectral minimum in the harmonic yield shifts with the intensity of the driving laser, we talk about *dynamical minimum*. In contrast to atoms, in molecules the separation of the highest occupied energy levels may be reduced to few eVs, like in N₂ $\Delta I_p =$

$I_p(\text{Homo}) - I_p(\text{Homo} - 1) \approx 1.4 \text{ eV}$. When such a molecule is exposed to high laser intensities, its potential barrier can be bent so much that tunnel ionization may occur from different orbitals simultaneously creating different ionization channels. The channel that connects the neutral ground state to the ionic ground state (the X state obtained by ionizing from HOMO) is called *X channel* while the channel that leads to the first excited ionic state (the A state obtained by ionizing from HOMO-1 in the Koopmans approximation) is called *A channel*. Therefore, the tunnel ionized electron leaves its parent ion in the superposition of two states. As a first approximation, to describe the HHG from a multi-channel system we neglect the coupling, relaxation or excitation between the channels. Therefore, the harmonic field for N_2 writes in the length form and LF as:

$$\epsilon_{\text{XUV}}^{\hat{i}L}(q, I_L, \theta) = \sum_i \gamma_i(q, I_L, \theta) a_i(q, I_L) \langle \psi_i(\mathbf{r}) | \mathbf{r} | \psi_c(\mathbf{r}) \rangle, \quad (3.19)$$

where $i = X, A$. The weight of each channel is given by the product of the tunnel ionization (γ_i) and the continuum acceleration (a_i). The higher ionization potential of HOMO-1 results in γ_A smaller than γ_X (in general). However, the electrons tunnel ionize more easily in the direction where their probability function is larger. Therefore, the difference in the geometry of the two orbitals will play a big role through $R(\theta)$ in eq. 1.43 (see figure 1.3). HOMO has a maximum possibility to ionize when the molecule is aligned parallel to the driving laser field and a minimum in the perpendicular case. HOMO-1 presents more important contribution with an inverse behavior at perpendicular alignment. Moreover, the cut-off law suggests that the highest order harmonics are completely generated by the HOMO-1, due to its larger ionization potential, as already mentioned. That increases the continuum amplitude a_A .

As already clarified, the structural minimum in molecules should be accompanied by a sudden π phase jump at a certain alignment angle. In figure 2b of PAPER I such jump is not visible. In fact, the phase shows a complex behavior as the molecule is rotated from parallel to perpendicular alignment. Two phase jumps seem to appear: a negative one around H23 which has a maximum at 90° and a positive one around H29-31 for all angles that may be truncated by the measured spectral range upper limit. A single plane wave recombination dipole does not explain such an evolution as a function of angle. Therefore, relying on the findings of (McFarland et al. [103]), we include both HOMO and HOMO-1 orbitals into our simulations.

The questions that now arise are: (a) How do these two orbital contributions affect the total harmonic phase?; and more interestingly (b) how do they manifest in the tomographic reconstruction? In our procedure of dipole extraction (see eq. 3.3), we calibrated the measured N_2 harmonic signal with the measured Ar signal to remove the tunnel ionization and the continuum acceleration factors. But, this calibration is not valid for the HOMO-1 since its ionization potential is not equal to the one of Ar. To clarify this let us investigate the phase difference between the HOMO-1 and the HOMO contributions in eq. 3.19: $\Delta\varphi_{\text{tot}}(q) = \Delta\varphi_{\text{ion}}(q) + \Delta\varphi_{\text{con}}(q) + \Delta\varphi_{\text{rec}}(q)$.

None of the tunnel ionization models detailed in section 1.4.1 contains phase terms, hence we assume that $\Delta\varphi_{\text{ion}}(q) = 0$. However, recent studies, like (Mairesse et al. [101]) and (Walters and Smirnova [175]) are discussing some sort of tunnel ionization phase, but mostly in the context of coupled ionization channels.

The electrons in the continuum are mainly governed by the driving laser. The only difference is coming from the fact that they are liberated from orbitals with different ionization potentials. As it was demonstrated by (Kanai et al. [64]) and as it is derived in the Supplementary Materials of PAPER I: $\Delta\varphi_{\text{con}}(q) \approx -\Delta I_p \tau_q$, where τ_q is the average excursion time of the trajectory corresponding to the emission of harmonic q (see section 1.4.2). Figure 3a in PAPER I shows the evolution of this term as a function of harmonic order for $I_L = 1.2 \times 10^{14}$

W/cm^2 . For the 25th harmonic order it is: $\Delta\varphi_{con}(25) \approx -\pi$ and it varies slowly by $\pm 0.2\pi$ in our spectral range.

As it was explained in section 1.4.3, due to the symmetry properties of the orbitals, the HOMO PW dipole is purely imaginary $\varphi_{rec}^{Ho}(q) = \pi/2$, while the HOMO-1 PW dipole is purely real $\varphi_{rec}^{Ho-1}(q) = \pi$, hence the two are shifted in phase by $\Delta\varphi_{rec}(q) = \pi/2$. Coulomb wave calculations showed that the HOMO and HOMO-1 dipole phases were shifted by the same amount $\delta\phi_r$ with respect to the PW calculations, corresponding to the Coulomb phase shift. One thus gets $\Delta\varphi_{rec}^{CW}(q) \approx \pi/2$.

Therefore, the answer to question (a) is that in total $\Delta\varphi_{tot} = -\frac{\pi}{2}$ for harmonic 25 and slightly varies around it. This clearly corresponds to the experimental results, showing the importance of the HOMO-1 contribution at $\theta = 90^\circ$. At parallel alignment HOMO-1 does not give contribution to the harmonic generation, while by increasing θ , the weight of HOMO-1 becomes larger and larger. This could explain the slow decrease of the minimum in the phase with increasing θ .

To answer question (b), we reconsider the discussion on the two recombination dipole moments. In principle, due to their symmetries and provided a $-\delta\phi_r$ rotation in the complex plane, their contributions should be disentangled into the real and imaginary parts of the measured dipole, if we do not take into account the tunnel ionization and acceleration steps. Therefore, the HOMO orbital could be reconstructed from the imaginary part, while the HOMO-1 from the real part of the measured recombination dipole moment. As seen above, $\Delta\varphi_{tot} \approx -\frac{\pi}{2}$ in our spectral range, preserving the disentanglement of the two orbitals. Figures 4 b,d,f in PAPER I show the experimental reconstruction, the filtered theoretical reconstruction and the exact HF HOMO-1 orbital, respectively.

Both for the HOMO and HOMO-1 reconstructions, the main distortions are coming from our restricted experimental spectral range. It is also worth noting that the reconstructions are sensitive for the dipole form we are using. As explained in the Supplementary Materials of PAPER I, the length form seems to fit better than the velocity form. Unfortunately, there are no exact criteria to decide which form is better.

Intramolecular Hole dynamics

Up to now, the measured harmonic signal was used to reconstruct static orbitals. But the superposition of the two orbitals is nothing else than the electronic hole that is left in the ion (Smirnova et al. [147]). The hole evolves in time, as it is defined by the sum of the two ionization channels: $\psi_{hole}(\mathbf{r}, t) = \alpha_X \psi_X(\mathbf{r}) + \beta_A \psi_A(\mathbf{r}) \exp(i\Delta I_p t)$. When the electron comes back to the ion, it probes the ion at the instant of recombination. Therefore, the evolved electronic hole is probed about $t = 1.5$ fs after its creation. The emitted harmonics thus encode a snapshot of the hole averaged over $\tau \approx 600$ as, given by the attochirp in the spectral range of our experiment. Theoretically, we can set t to zero and calculate the position of the electronic hole at the ionization instant. In figure 5 of PAPER I, we can see that the probability density of the electronic hole flipped from one side of the molecule to the other as the time passed.

PAPER I

Attosecond imaging of molecular electronic wavepackets

S. Haessler, J. Caillat, W. Boutu, C. Giovanetti-Teixeira, T. Ruchon, T. Auguste, Z. Diveki, P. Breger, A. Maquet, B. Carré, R. Taïeb and P. Salières
Nature Physics **6**, 200206 (2010).

Attosecond imaging of molecular electronic wave-packets

S. Haessler¹, J. Caillat^{2,3}, W. Boutu¹, C. Giovanetti-Teixeira^{2,3}, T. Ruchon¹, T. Auguste¹, Z. Diveki¹, P. Breger¹, A. Maquet^{2,3}, B. Carré¹, R. Taïeb^{2,3}, P. Salières¹

¹ CEA-Saclay, IRAMIS, Service des Photons, Atomes et Molécules, 91191 Gif-sur-Yvette, France.

² UPMC Univ. Paris 06, UMR 7614, Laboratoire de Chimie Physique-Matière et Rayonnement, 11 rue Pierre et Marie Curie, 75231 Paris Cedex 05, France.

³ CNRS, UMR 7614, LCPMR F-75005 Paris, France.

A strong laser field may tunnel ionize a molecule from several orbitals simultaneously, forming an attosecond electron-hole wave-packet. Both temporal and spatial information on this wavepacket can be obtained through the coherent soft X-ray emission resulting from the laser-driven recollision of the liberated electron with the core. By characterizing the emission from aligned N₂ molecules, we evidence the attosecond contributions of the two highest occupied molecular orbitals. We determine conditions where they are disentangled in the real and imaginary parts of the emission dipole moment. This allows us to perform a tomographic reconstruction of both orbitals with Ångström spatial resolution. Their coherent superposition provides experimental images of the attosecond wavepacket created in the ionization process. Our results open the perspective of imaging ultrafast intra-molecular dynamics combining attosecond and Ångström resolutions.

The recent development of attosecond sources of coherent soft X-rays has opened the perspective of observing and controlling the fastest electronic processes in matter. In this rapidly evolving field, the attosecond processes explored up to now may be grouped in two categories. The first one encompasses the dynamics driven by a strong laser field in atoms and molecules. The laser period being a few femtoseconds, the timescale of sub-cycle electron dynamics is attosecond, as in tunnelling ionization^{1,2} and continuum dynamics³⁻⁷. The second category deals with ‘intrinsic’ (laser-free) dynamics that is characteristic of the system: conduction band dynamics⁸ or bound-state dynamics related to ultrashort lived transient states⁹⁻¹¹. Attosecond ‘intrinsic’ dynamics could also be driven by coherent superposition of bound states. Such coherent superposition of bound states determines, e.g., intra-molecular electron transfer via non-adiabatic transitions in chemical reactions¹². Theoretical studies investigated for instance electron-electron correlation^{13,14} or charge migration in small peptides¹⁵, and only recently both theoretical and experimental work has been performed in the context of tunnel ionization^{16,17}.

Imaging such coherent wavepackets localized in time and space would allow a better understanding of their dynamics. High-order harmonic generation (HHG) can be an efficient tool for such purpose. HHG occurs when a strong laser pulse, of frequency ω_L , tunnel-ionizes a gas target, creating an electron wave-packet (EWP) that is subsequently accelerated and driven back to the core where it recombines, emitting an attosecond burst of coherent soft X-rays¹⁸⁻²⁰. Advanced characterization of the latter gives extremely precise information on both the structure and the dynamics of the radiating system. As the EWP associated with the observed photon emission has a duration at recollision of a few hundred attoseconds, it allows probing ultrafast dynamics in the excited molecular system (ion and correlated continuum electron) such as ultrafast nuclear motion^{21,22}, or attosecond electron dynamics in the recombination process²³. As the EWP de Broglie wavelength λ_{dB} is of the order of molecular internuclear distances (~ 1 Å), it allows observing quantum interferences in the recombination process²³⁻²⁷. It may also lead to a tomographic reconstruction of the radiating orbital with Å resolution, as first proposed by Itatani et al²⁸. This fascinating possibility of spatially imaging the wave function of a quantum object in

amplitude and phase attracted much attention. However both the assumptions made in the theoretical treatment and the incomplete experimental data raised intense discussions²⁹⁻³⁴ on the feasibility of the technique that is still to be demonstrated.

Here we study an attosecond wavepacket created in aligned nitrogen molecules by tunnel ionization from both the highest occupied molecular orbital (HOMO), and the lower-lying orbital (referred to as HOMO-1). The HHG emission resulting from the freed EWP recollision is characterized in amplitude and phase. In our generation conditions, the signatures of the two orbitals can be disentangled, allowing their tomographic reconstruction. Exploiting further the measured relative phase of their contributions allows us to reconstruct the dynamic superposition of the orbitals left empty after tunnel ionization (so called “hole”), which evolves on the attosecond time-scale before recombination. This hole can be seen as a “negative” image of the ion left in a coherent superposition of the ground (X) and excited (A) states.

Creating and probing a bound attosecond wavepacket

Recent experimental and theoretical studies^{16,17,35} have revealed that molecules interacting with a strong laser field could be tunnel ionized from several valence orbitals simultaneously due to their small energy separations and different geometries. This was observed in the resulting HHG emission, where the different orbitals lead to interfering contributions in the q th harmonic total dipole moment $\vec{D}(\theta, q\omega_L)$, where θ is the angle between the laser polarization and the molecular axis. In the strong field approximation (SFA), when only the HOMO, ψ^{HOMO} , and HOMO-1, $\psi^{\text{HOMO-1}}$, contribute without coupling, $\vec{D}(\theta, q\omega_L)$ reads^{28,36}:

$$\begin{aligned} \vec{D}(\theta, q\omega_L) &= a_1(\theta, k_q) \int [\psi^{\text{HOMO}}(\vec{r})]^* \vec{r} e^{i\vec{k}_q \cdot \vec{r}} d\vec{r} + a_2(\theta, k_q) \int [\psi^{\text{HOMO-1}}(\vec{r})]^* \vec{r} e^{i\vec{k}_q \cdot \vec{r}} d\vec{r} \\ &\equiv a_1(\theta, k_q) \vec{d}^{\text{HOMO}}(\theta, k_q) + a_2(\theta, k_q) \vec{d}^{\text{HOMO-1}}(\theta, k_q) \end{aligned} \quad (1)$$

where the bound wave functions are expressed in the Koopmans approximation³⁷ and the scattering state in the plane-wave approximation, with $q\omega_L = k_q^2/2$ (discussed later, atomic units are used throughout). The complex wave packet amplitude $a_{1/2}$ of each contribution results from the tunnel-ionization and continuum excursion steps. The angle θ determines the ratio of the orbital contributions in both the ionization amplitude and the recombination dipole moment^{16,17}. The HHG emission thus contains rich structural and dynamical information on the complex ionic system but this information is not accessible through measurement of the harmonic intensity only.

Our experimental setup achieves laser-driven non-adiabatic molecular alignment, subsequent attosecond pulse generation and characterization in the spectral domain in amplitude and phase of the HHG polarization component parallel to the driving laser (see Methods). The temporal intensity profile of the attosecond emission from N_2 molecules is shown in Fig. 1a for different θ . The pulse shape hardly varies but the peak timing presents a gradual shift by -50 as when θ increases from 0° to 90° .

Understanding the origin of this temporal shift and its relation to multi-orbital contributions requires a detailed analysis of the effective recombination dipole $d^{\text{exp}}(\theta, q)$ extracted from the measured spectra. To this end, one has to remove the complex amplitude accumulated by the EWP prior to recombination, which induces a chirp in the attosecond emission⁵, i.e., $d^{\text{exp}}(\theta, q) = D^{\text{exp}}(\theta, q)/a_1$. This is achieved by normalizing the measured XUV spectrum (amplitude and phase) for nitrogen by the spectrum for argon (same ionization potential I_p) obtained under the same experimental conditions, and multiplying this ratio by the theoretical recombination dipole $d_{\text{Ar}}(q)$ for argon^{23,28}.

The obtained normalized amplitude (Fig. 2a) reproduces the results of ref. 28 with a spectral minimum at harmonic 25 at all alignment angles. However, the assumption made in ref. 28 of a π phase jump associated to structural interferences (expected to be θ -dependent²⁴) is not confirmed here. Our measured phase difference (Fig. 2b) presents a more complex behaviour with two identified jumps.

In the following, we show that this non-trivial phase is driven by not only structural interferences but also multi-orbital effects favoured by both energy and geometry criteria.

Disentangling the orbital contributions to HHG

In N_2 , the HOMO (σ_g symmetry) and HOMO-1 (π_u symmetry) are separated by only³⁸ $\Delta\varepsilon \approx -1.4$ eV. The differences in symmetry and geometry result in a strong angular dependence of the ratio of their ionization probabilities^{39,40}, that is maximum at $\theta = 90^\circ$. They also lead to a larger plane-wave recombination dipole moment for the HOMO-1 at high energy, and consequently an overall significant contribution to the high-harmonic emission at 90° . Our analysis, focused on the dipole *phase*, follows the chronology of the SFA model: we address for each contribution the phase $\phi_d = \phi_c + \phi_r$, with (i) the phase $\phi_c = \arg(a_{1/2})$ acquired by the ionic system during the continuum excursion and (ii) the phase $\phi_r = \arg(d^{\text{HOMO/HOMO-1}})$ added by recombination.

The dipole normalization procedure removed the phase ϕ_c , *but only for the HOMO contribution*. The HOMO-1 contribution is left, after calibration, with a phase equal to⁴¹ $\Delta\phi_c(q\omega_L) = \arg(a_2/a_1) = \phi_c^{\text{HOMO-1}}(q\omega_L) - \phi_c^{\text{HOMO}}(q\omega_L) \approx \Delta\varepsilon \tau_q$ (see Supplementary Information), where τ_q is the electron excursion time associated with harmonic order q . The difference $\Delta\phi_c(q\omega_L)$ is plotted in Fig.3a for our experimental conditions. It evolves slowly around $-\pi$, value reached in the middle of the experimental spectral range, at H25.

The recombination dipole expressed in the plane-wave (PW) approximation (appearing in Eq. (1)) turns out to be the Fourier transform of the bound wave-function times the dipole operator^{28,36} \vec{r} . Due to the symmetry properties of the orbitals and of the dipole operator (antisymmetric) on the one hand, and of the Fourier transform on the other hand, the recombination dipole is purely *imaginary-valued* for the HOMO (σ_g) and purely *real-valued* for the HOMO-1 (π_u), resulting in $\Delta\phi_r = \pi/2$. At this stage, the accumulated phase difference $\Delta\phi_d = \Delta\phi_c + \Delta\phi_r$ is close to $-\pi/2$: the HOMO and HOMO-1 contributions to the normalized dipole $d^{\text{exp}}(\theta, q)$ are *practically* disentangled in the imaginary and real part, respectively. The measured phase variation around H25 at $\theta = 90^\circ$ could be a signature of a significant contribution of HOMO-1 coming into play for the high harmonics.

However, the PW approximation assumes the recolliding electron to be free, although it is accelerated by the parent ionic core, inducing a distortion of the EWP, which may cancel out the disentanglement of the HOMO and HOMO-1 contributions. Computing exact values of molecular recombination dipoles requires a precise knowledge of the continuum states, which is by no means a simple task in such multi-electron multi-center systems^{30,42}. Nevertheless, valuable insight can be gained through a relatively simple model, that uses Coulomb waves³⁷ (CWs) for the continuum. This approach is motivated by the fact that the ionic core acts asymptotically as an effective point charge $Z^* = 1$. Figure 3b,c presents the phase variation of the dipole against the electron momentum k computed for the HOMO within the CW approximation, for three illustrative θ values. Two representative cases are considered: the plane wave limit $Z^* = 0$ (Fig. 3b) and $Z^* = 1$ corresponding to the effective N_2^+ charge (Fig. 3c). As expected from the symmetry criteria mentioned before, in the case of PWs, the phase is an odd multiple of $\pi/2$, the sudden jumps being a manifestation of structural sign changes in the purely imaginary dipole. For $Z^* = 1$ and $k > 0.5$ a.u., the evolution tends to follow the variations observed for $Z^* = 0$, with the following differences: (i) besides being smoothed, the π -jumps are translated towards lower k by an amount $\delta k \approx 0.4$ a.u. and (ii) the phases are vertically shifted by a global term which decays smoothly as k increases. By assigning to each harmonic frequency $q\omega_L$ an asymptotic momentum k_q using³⁶ $k_q^2/2 = q\omega_L - I_p$, one finds that our measurements were performed in the window $0.9 \text{ a.u.} < k < 1.54 \text{ a.u.}$ In this range, the phase variations are dominantly governed by the structural jumps also observed in the PW approximation, with a global phase shift $\delta\phi_r \approx \pi/4$. We performed the same study for the HOMO-1, and obtained similar conclusions both on the jump translation and on the global phase shift. Therefore we conclude that (i) we can base our interpretation on the PW approximation, provided a proper translation is made on the electron momentum scale, and (ii) we can still consider the HOMO and HOMO-1 contributions to be disentangled in the imaginary and real parts of $d^{\text{exp}}(\theta, q)$ respectively, provided a $-\delta\phi_r$ rotation in the complex plane. Within the experimental k -range, the momentum

translation in (i) corresponds to a kinetic energy translation of ≈ 15 eV. This is consistent with the heuristic relation $k_q^2/2 = q\omega_L$ generally used in the SFA interpretation of molecular harmonic spectra²⁴. The removal of I_p from the energy conservation law is interpreted as a compensation for the absence of electron acceleration close to the core in the PW treatment. In (ii), performing a global phase shift assumes that the *exact* scattering phase shift is practically independent of energy in the studied spectral range, molecular alignment, and ionized orbital – as suggested by the CW model. This is consistent with numerical experiments³¹ based on the time-dependent Schrödinger equation for a single contributing orbital, where such an overall dipole rotation allowed quasi-suppression of the imaginary part of the reconstructed orbital. The physical origin of this rotation was, however, not identified in ref. 31. The global phase shift, $\delta\phi_r$, for *exact* N₂ scattering states is probably different from the CW based prediction, we thus empirically chose the phase origin that provided the most consistent reconstructions (see Fig.2 and Supplementary Information).

Tomographic imaging of the dynamic hole

Our understanding of the complex dipole structure allows us to exploit the measured data and (i) to simulate the temporal profiles of the attosecond emission, (ii) to reconstruct the involved orbitals by a tomographic procedure, and, merging the temporal and structural aspects, (iii) to image, at the instant of recombination, the dynamic “hole” formed by the coherent ionization channels.

Combining the predicted phases ϕ_d and experimental harmonic amplitudes, we simulated the temporal intensity profile of the attosecond emission as a function of the relative weight $|a_2|:|a_1|$ of both contributions. Figure 1b reproduces very well the experimental negative temporal shift of the attosecond pulse peak when a significant HOMO-1 contribution is gradually added to the HOMO contribution as the angle is increased from 0° to 90°. This regular evolution is consistent with the phase difference close to $-\pi/2$ that minimizes the interference of the two contributions. Different experimental conditions (laser intensity and wavelength, selection of long trajectories) can lead to stronger interferences and much more distorted temporal profiles, as illustrated by the simulations presented in Fig.1c where $\Delta\phi_r=\pi/2$ was omitted leading to a total phase difference centered around $-\pi$.

Following the tomographic procedure suggested by Itatani *et al.*²⁸, we now define the 2D reconstructed functions:

$$f_\alpha(x, y) = \frac{1}{\alpha} \sum_q \sum_j 2\omega_L \Delta\theta \left[d_\alpha^{\text{exp}}(\theta_j, k_q) \right]^* \exp[ik_q(x \cos \theta_j + y \sin \theta_j)] \quad (\alpha = x, y), \quad (2)$$

where q and j span the harmonic and angular samplings respectively, $\Delta\theta$ is the angular step (10°), $[d_\alpha^{\text{exp}}]^*$ is the complex-conjugated α -component of the normalized dipole and the discretized inverse Fourier transform is restricted to the (x, y) plane. If the transform were performed exactly, both f_x and f_y would be equal to the wavefunction contributing to the dipole, integrated over the transverse direction z .

We present in Fig.4a,b the 2D orbitals reconstructed from our data shown in Fig.2, taken as the half sum of f_x and f_y in order to average the errors due to the discrete sampling. The measurements were done for angles between 0° and 90°. The tomographic procedure requires the experimental dipole to be extrapolated up to 360°, by imposing the assumed symmetry associated with the orbital to be imaged. Note that new methods are currently developed to detect experimentally the orbital symmetries by controlling the EWP trajectory^{43,44}. The disentanglement of the multi-orbital contributions in the experimental dipole allows us to reconstruct both the HOMO (from its imaginary part when selecting the σ_g symmetry), and the HOMO-1 (from its real part when selecting the π_u symmetry). As seen in Fig. 4a, our reconstructed σ_g orbital possesses the main characteristics of the nitrogen HOMO (Fig. 4e), namely three main lobes with alternating signs, separated by two nodal surfaces passing through each nucleus. The visual aspect of the HOMO-1 reconstruction (Fig. 4b) is dominated by the imposed symmetry and possesses little particular structure.

We performed simulated reconstructions for the HOMO and HOMO-1 in the PW approximation, based on orbitals calculated with GAMESS⁴⁵. To mimic the experimental conditions, we computed

the dipoles over the span corresponding to the harmonic and orientation samplings using the relation $k_q^2/2 = q\omega\lambda$, restricting the dipoles to the laser polarization orientation. The simulated HOMO reconstruction, shown in Fig. 4c, is strikingly similar to the experimental one (Fig. 4a): both present very similar distorted lobes, with extrema and nodes at the same locations. For the HOMO-1, the experimental and simulated reconstructions (Fig. 4b,d) both present a main central lobe, but with notably different sizes. We relate this to the fact that the HOMO-1 reconstructions had to be done using the velocity-form of the dipole operator, in order to avoid numerical singularities appearing when reconstructing π orbitals in the length gauge. This was confirmed by very similar discrepancies obtained when reconstructing the HOMO in the velocity gauge (see Supplementary Information).

The main distortions and extra oscillations in our reconstructions, compared to *exact* Hartree-Fock orbitals (shown in Fig. 4e,f), thus result essentially from the restricted harmonic span. Our analysis cannot account for the remaining deviations, in particular the HOMO:HOMO-1 contrasts (the ratio of the maximum amplitudes is 1:10 in the experiment, while 3:10 in the simulations). Our simulations do not take into account the different ionization yields of the two orbitals and possibly different continuum wavepacket spreading. Deviations may also be related to approximations inherent to the SFA, such as neglecting bound- and continuum-state distortions by the strong external field^{46,47}. For systems with little relaxation, such as N₂, the Dyson orbital (which is the orbital to be considered in a rigorous treatment) does not differ significantly from the ionized Hartree-Fock orbital and the exchange terms^{48,49}, the magnitude of which is considerably overestimated in the plane-wave approximation, are negligible. Distortions may also result from properties of the *exact* dipole absent in our model^{30,42}, though we expect relatively long-lived resonances to have little impact on the HHG recombination dipole due to the sub-cycle time-scale of the electron excursion.

The HOMO and HOMO-1 experimental reconstructions, $\psi_{\text{exp}}^{\text{HOMO}}$ and $\psi_{\text{exp}}^{\text{HOMO-1}}$ (Fig. 4a,b), provide snapshots of the orbitals at the recombination instant $\tau \approx 1.5$ fs after tunnel-ionization, *i.e.* they contain the relative phase $\Delta\phi_c$ accumulated during the EWP excursion. These images are averaged over $\Delta\tau \approx 600$ as, as given by the electron excursion times spanned by the harmonics (cf. Fig. 3a). The coherent superposition of $\psi_{\text{exp}}^{\text{HOMO}}$ and $\psi_{\text{exp}}^{\text{HOMO-1}}$ provides time-resolved experimental images of the wave-packet left empty after coherent tunnel ionization from both orbitals^{16,17}. Figure 5a shows $\psi_{\text{exp}}^{\text{HOMO}} + \psi_{\text{exp}}^{\text{HOMO-1}}$, *i.e.* the ‘hole’ at the recombination time. The same wave-packet taken at the tunnel-ionization instant ($\tau = 0$), reconstructed by removing from the HOMO-1 the phase difference $\Delta\phi_c = -\pi$ acquired until recombination, *i.e.* as $\psi_{\text{exp}}^{\text{HOMO}} - \psi_{\text{exp}}^{\text{HOMO-1}}$, is shown in Fig. 5b. Since the value of τ coincides approximately with one half-period $\pi/|\Delta\varepsilon|$ of the HOMO-HOMO-1 beating, we observe the motion of the ‘hole’ from one side of the molecule to the other.

Intra-molecular time-resolved imaging

Varying the generation parameters (laser intensity and wavelength, selection of the long trajectories) provides different ways for controlling the EWP recombination time, and thus makes it possible to probe the hole at different instants. Combining various phase measurement techniques^{5,16,23,27} (RABITT, 2-source interferometry, gas mixing) with the driving-field polarization control^{43,44} will allow lifting the assumptions made in the tomographic reconstructions, in particular *a priori* knowledge of the orbital symmetry. This imaging of a dynamic hole wave-packet serves as a test bench for intra-molecular time-resolved imaging. This is a general technique that can be applied to follow the ‘frontier’ orbital of a system during, e.g., a photo-excited process in a conventional pump-probe scheme. Our progress towards time-resolved tomography thus opens the perspective of imaging ultrafast dynamics of valence electrons and light nuclei at various stages of chemical reactions.

Methods

We use the ‘Laser UltraCourt Accordable’ (LUCA) of the ‘Saclay Laser Matter Interaction Center’ (SLIC), delivering pulses centered around 795 nm with up to 30 mJ energy and ≈ 55 fs duration at a repetition rate of 20 Hz.

Our setup is based on a Mach-Zehnder type interferometer for the ‘Reconstruction of Attosecond Beating by Interference of Two-photon Transitions’ (RABITT) measurement (see Supplementary Information). Drilled mirrors (8 mm hole diameter) separate the annular generating beam (outer diameter cut to 17 mm by an iris), which contains most of the energy (≈ 1 mJ), and the weak central part (≈ 50 μ J, diameter ≈ 4 mm). The latter can be delayed by a piezoelectric translation stage with interferometric stability (~ 10 nm). In both arms, combinations of half-wave plate and polarizer allow to finely control the pulse energy. The two beams are then collinearly focused by the same lens of 1 m focal length ($F_{\#} \approx 60$ for the generating beam and $F_{\#} \approx 250$ for the probe beam). The beam focus is placed ≈ 5 mm before the HHG gas jet, thus selecting the short trajectory contribution⁵⁰. An iris of ≈ 4 mm diameter blocks the annular generating beam in the far field. The source point of the XUV emission together with the on-axis probe beam is then imaged by a broadband gold-coated toroidal mirror into the detection volume of a magnetic bottle electron spectrometer (MBES).

This toroidal mirror together with a flat mirror cause two grazing-incidence (11.5°) reflections of the HHG radiation on Au-surfaces, preferentially transmitting the s-polarized component into the electron spectrometer (with a 2:1 contrast). The generating laser is kept s-polarized while the molecular alignment axis is rotated in order to predominantly detect the HHG polarization component parallel to the driving laser.

In the spectrometer interaction volume, the neon target gas, injected by a permanent leak, is photoionized by the high harmonics. With the HHG and detection gas jet running, the pressure is $\sim 10^{-3}$ - 10^{-2} mbar in the HHG chamber, $\sim 10^{-5}$ mbar in the toroidal mirror chamber, $\sim 10^{-4}$ mbar in the MBES interaction volume and $\sim 10^{-6}$ mbar in the MBES flight tube.

To align molecules in the HHG gas jet, a third laser pulse with controllable delay, polarization and intensity is needed. To this end, a larger interferometer, based on amplitude beam splitters, is set up around the compact RABITT interferometer. One fifth of the incoming pulse energy is transmitted into the arm for the aligning beam and passes a motorized delay stage. Here, the stability requirements are much less severe than for the RABITT interferometer, since the variation of the angular distribution of the molecules varies on a ~ 10 fs timescale. The central part (≈ 4 mm diameter) of this beam is blocked so as to limit the amount of its energy passing into the MBES and thus prevent above-threshold ionization. The polarization direction of the aligning beam is set by a motorized half-wave plate, thus controlling directly the alignment angle of the molecular ensemble with respect to the HHG driving laser polarization direction at the half-revival delay. The pulse energy in the aligning beam is limited by a diaphragm (cutting the beam to typically 12 mm diameter), thereby limiting the aligning beam intensity to $\approx 5 \cdot 10^{13}$ Wcm⁻² in the HHG gas jet. This also ensures that the aligning beam focal spot is larger than that of the generating beam.

The HHG gas jet has an orifice of 300 μ m diameter backed with 3 bar pressure. This leads to an estimated 90 K rotational temperature of the nitrogen molecules at ≈ 1 mm distance from the orifice, where the generating beam is focused. This estimate is obtained by Fourier transforming the revival trace (dependence of the total harmonic yield on the aligning beam – generating beam delay), and comparing to the Fourier transform of calculated $\langle \cos^2\theta \rangle$ -traces.

Acknowledgements:

We thank O. Smirnova, M. Ivanov and Y. Mairesse for fruitful discussions. Financial support from the LASERLAB2 program and from the ANR ATTO-WAVE is acknowledged. Parts of the computations have been performed at the Institut du Développement et des Ressources en Informatique Scientifique IDRIS.

Author Contributions :

P.S. with B.C. planned the project. W.B., P.B. B.C. and P.S. designed and installed the experiment. S.H. with assistance of W.B. P.B. and P.S. performed the measurements. S.H. and J.C. with assistance from W.B., T.R., Z.D. and P.S. analyzed the data. J.C., C.G.-T., T.A., A.M. and R.T. performed the calculations. All authors discussed the results and contributed to the final manuscript.

Competing financial interests :

The authors declare that they have no competing financial interests.

References:

1. Uiberacker, M. *et al.* Attosecond real-time observation of electron tunnelling in atoms. *Nature* **446**, 627-632 (2007).
2. Eckle, P. *et al.* Attosecond ionization and tunnelling delay time measurements in Helium. *Science* **322**, 1525-1529 (2008).
3. Niikura, H. *et al.* Probing molecular dynamics with attosecond resolution using correlated wave packet pairs. *Nature* **421**, 826-829 (2003).
4. Mauritsson, J. *et al.* Coherent Electron Scattering Captured by an Attosecond Quantum Stroboscope. *Phys. Rev. Lett.* **100**, 073003 (2008).
5. Mairesse, Y. *et al.* Attosecond synchronization of high harmonic soft X-ray. *Science* **302**, 1540-1543 (2003).
6. Sola, I. *et al.* Controlling attosecond electron dynamics by phase-stabilized polarization gating. *Nature Phys.* **2**, 319-322 (2006).
7. Dudovich, N. L. *et al.* Measuring and controlling the birth of attosecond XUV pulses. *Nature Phys.* **2**, 781-786 (2006).
8. Cavallieri, A. *et al.* Attosecond spectroscopy in condensed matter. *Nature* **449**, 1029-1032 (2007).
9. Drescher, M. *et al.* Time-resolved atomic inner-shell spectroscopy. *Nature* **419**, 803-807 (2002).
10. Fohlisch, A. *et al.* Direct observation of electron dynamics in the attosecond domain. *Nature* **436**, 373-376 (2005).
11. Haessler *et al.* Phase-resolved attosecond near-threshold photoionization of molecular nitrogen. *Phys. Rev. A* **80**, 011404 (2009).
12. H. Nakamura. *Nonadiabatic Transitions. Concepts, Basic Theories and Applications.* (World Scientific Publishing, Singapore, 2002).
13. Breidbach, J. & Cederbaum, L. S. Universal Attosecond Response to the Removal of an Electron. *Phys. Rev. Lett.* **94**, 033901 (2005).
14. Hu, S. X. & Collins, L. A. Attosecond Pump Probe: Exploring Ultrafast Electron Motion inside an Atom. *Phys. Rev. Lett.* **96**, 073004 (2006).
15. Remacle, F. & Levine, R. D. An electronic time scale in chemistry. *PNAS* **103**, 6793-6798 (2006).
16. Smirnova, O. *et al.* High harmonic interferometry of multi-electron dynamics in molecules. *Nature* **460**, 972-977 (2009).
17. Smirnova, O. Patchkovskii, S., Mairesse, Y., Dudovich, N. & Ivanov, M. Yu Strong-field control and spectroscopy of attosecond electron-hole dynamics in molecules. *PNAS USA* **106**, 16556-16561 (2009).
18. Schafer, K. J., Yang, B., DiMauro, L. F. & Kulander K. C. Above threshold ionization beyond the high harmonic cutoff. *Phys. Rev. Lett.* **70**, 1599-1602 (1993).
19. Corkum, P. B. Plasma perspective on strong field multiphoton ionization. *Phys. Rev. Lett.* **71**, 1994-1997 (1993).
20. Krausz, F. & Ivanov M. Yu. Attosecond physics. *Rev. Mod. Phys.* **81**, 163-245 (2009).
21. Baker S. *et al.* Dynamic two-center interference in high-order harmonic generation from molecules with attosecond nuclear motion. *Phys. Rev. Lett.* **101**, 053901 (2008).
22. Li, W. *et al.*, Time-resolved dynamics in N₂O₄ probed using high harmonic generation. *Science* **322**, 1207-1211 (2008).
23. Boutu, W. *et al.* Coherent control of attosecond emission from aligned molecules. *Nature Phys.* **4**, 545-549 (2008).
24. Lein, M. Molecular imaging using recolliding electrons. *J. Phys. B* **40**, R135-R173 (2007).
25. Kanai, T., Minemoto, S. & Sakai, H. Quantum interference during high-order harmonic generation from aligned molecules. *Nature* **435**, 470-474 (2005).

26. Vozzi, C. *et al.* Controlling two-center interference in molecular high harmonic generation. *Phys. Rev. Lett.* **95**, 153902 (2005).
27. Wagner, N. *et al.* Extracting the phase of high-order harmonic emission from a molecule using transient alignment in mixed samples. *Phys. Rev. A* **73**, 061403 (2007).
28. Itatani, J. *et al.* Tomographic imaging of molecular orbitals. *Nature* **432**, 867-871 (2004).
29. Schwarz, W. H. E. Measuring Orbitals: Provocation or Reality? *Angewandte Chemie* **45**, 1508-1517 (2006).
30. Walters, Z. B., Tonzani, S. & Greene, C. H. Limits of the plane wave approximation in the measurement of molecular properties. *J. Phys. Chem.* **112** 9439-9447 (2008).
31. van der Zwan, E., Chirila, C. C. & Lein, M. Molecular orbital tomography using short laser pulses. *Phys. Rev. A* **78**, 033410 (2008).
32. Le, V.-H., Le, A.-T., Xie, R.-H. & Lin, C. D. Theoretical analysis of dynamic chemical imaging with lasers using high-order harmonic generation. *Phys. Rev. A* **76** 013413 (2007).
33. Torres, R. & Marangos, J. P. Mapping of orbital structure from high harmonic generation through the molecular dipole moment. *J. Mod. Opt.* **54**, 1883-1899 (2007).
34. Gibson, G. N. & Biegert, J. Influence of orbital symmetry on high-order-harmonic generation and quantum tomography. *Phys. Rev. A* **78**, 033423 (2008).
35. McFarland, B. K., Farrell, J. P., Bucksbaum, P. H. & Gühr, M. High harmonic generation from multiple orbitals in N₂. *Science* **322**, 1232-1235 (2008).
36. Lewenstein, M., Balcou, Ph., Ivanov, M. Yu, L'Huillier, A. & Corkum, P. B. Theory of high harmonic generation by low-frequency laser fields. *Phys. Rev. A* **49**, 2117-2132 (1994).
37. Bransden, B. H. & Joachain, C. J. *Physics of Atoms and Molecules* (Pearson Education, Harlow, 2003).
38. Lofthus, A. & Krupenie, P.H. Spectrum of molecular nitrogen. *J. Phys. Chem. Ref. Data* **6**, 113-307 (1977).
39. Tong, X. M., Zhao, Z. X. & Lin, C. D. Theory of molecular tunneling ionization. *Phys. Rev. A* **66**, 033402 (2002).
40. Pavicic, D., Lee, K., Rayner, D. M., Corkum, P. B. & Villeneuve, D. M. Direct Measurement of the Angular Dependence of Ionization for N₂, O₂, and CO₂ in Intense Laser Fields. *Phys. Rev. Lett.* **98**, 243001 (2007).
41. Kanai, T., Takahashi, E. J., Nabekawa, Y. & Midorikawa, K. Destructive interference during high harmonic generation in mixed gases. *Phys. Rev. Lett.* **98**, 153904 (2007).
42. Le, A.T., Lucchese, R. R., Tonzani, S., Morishita, T. & Lin C. D. Quantitative rescattering theory for high-order harmonic generation from molecules. *Phys. Rev. A* **80**, 013401 (2009).
43. Shafir, D., Mairesse, Y., Villeneuve, D. M., Corkum, P. B. & Dudovitch, N. Atomic wavefunctions probed through strong-field light-matter interaction. *Nature Phys.* **5**, 412-416 (2009).
44. Mairesse, Y. *et al.* Electron wavepacket control with elliptically polarized laser light in high harmonic generation from aligned molecules. *New J. Phys.* **10**, 025015 (2008).
45. Schmidt, M. W. *et al.* General atomic and molecular electronic-structure system. *J. Comput. Chem.* **14**, 1347- 1363 (1993).
46. Smirnova, O. A., Moritzen, S., Patchkovskii, S. & Ivanov, M. Yu. Coulomb-laser coupling in laser-assisted photoionization and molecular tomography *J. Phys. B* **40**, F197-F206 (2007).
47. Jordan, G. & Scrinzi, A. Core-polarization effects in molecular high harmonic generation. *New J. Phys.* **10**, 025035 (2008).
48. Patchkovskii, S., Zhao, Z., Brabec, T. & Villeneuve, D. M. High Harmonic Generation and Molecular Orbital Tomography in Multielectron Systems: Beyond the Single Active Electron Approximation. *Phys. Rev. Lett.* **97**, 123003 (2006).
49. Santra, R. & Gordon, A. Three-Step Model for High-Harmonic Generation in Many-Electron Systems. *Phys. Rev. Lett.* **96**, 073906 (2006).
50. Balcou, P., Salières, P., L'Huillier, A. & Lewenstein, M. Generalized phase-matching conditions for high harmonics: The role of field-gradient forces. *Phys. Rev. A* **55**, 3204-3210 (1997).

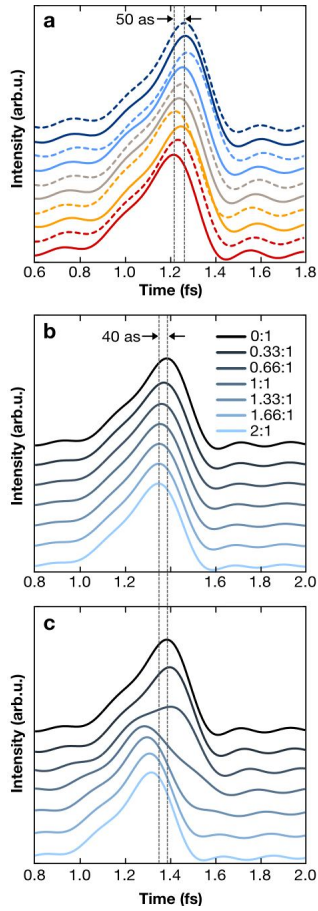


Figure 1. Attosecond emission of aligned N_2 molecules. (a): Temporal intensity profile of an average pulse in the attosecond pulse train emitted by N_2 molecules aligned at angles $\theta=0^\circ$ to 90° , reconstructed from a series of RABITT measurements, taking into account harmonics 17 to 27. Line colours correspond to alignment angles as indicated in Fig. 2. Relative timing calibration was ensured by setting the group delay for the lowest harmonic (H17) to the same value for all angles (see Supplementary Information). The observed evolution thus results from the phase variations within the considered spectral range. While close to our experimental sensitivity limit (± 20 as for the pulse peak positions, see Supplementary Information), the 50-as shift is reliable in view of its regular, almost monotonic (except for the fluctuation at $\theta = 60^\circ$) evolution in the 10 independent measurements. (b), (c) Simulated intensity profiles resulting from a coherent superposition of two contributions whose relative weight ($|a_2|:|a_1|$) is varied from 0:1 to 2:1 for all harmonics 17 to 27. The continuum spectral phases are computed as in Fig. 3a. For the spectral amplitudes (not a sensitive parameter), we used an experimental spectrum (N_2 at $\theta=0^\circ$) for all curves. In (b), $\Delta\phi_c = \pi/2$ is taken into account by correspondingly shifting the spectral phase for the HOMO contribution, whereas this additional phase is omitted in (c). The ≈ 150 as overall time-shift between the measured (a) and simulated (b) pulse profiles is presumably due to macroscopic effects (dispersion during propagation), not accounted for in our simulations.

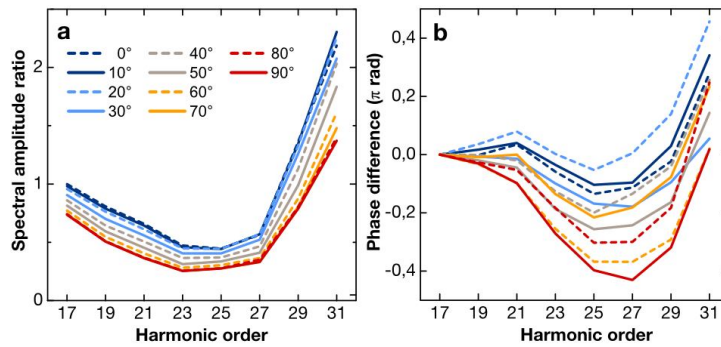


Figure 2. Experimental recombination dipole for N_2 molecules. (a): Amplitude and (b) phase of the complex XUV field for N_2 at various alignment angles normalized by that for argon. For perpendicular alignment ($\theta = 90^\circ$), the phase decreases by $\pi/2$ between harmonic 17 and 27. This jump gradually disappears when rotating the molecules towards parallel alignment ($\theta = 0^\circ$). For all angles, the phase increases by $\pi/2$ from harmonic 27 on, which might be the beginning of a larger jump not completely contained in our spectral range. The phase difference is set to 0 at the lowest harmonic order 17; see Supplementary Information for details on the data analysis.

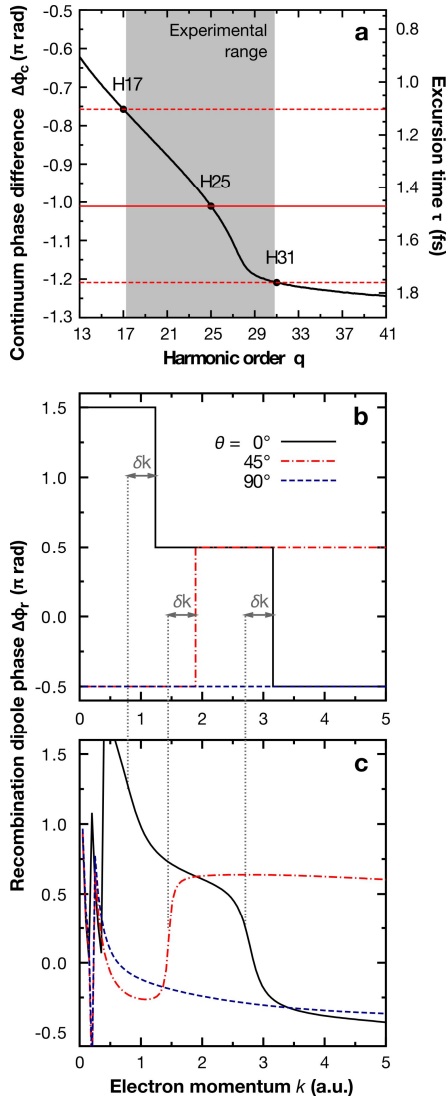


Figure 3. Phase of the harmonic emission. (a): Continuum phase difference $\Delta\phi_c(q\omega_L)$ computed within SFA for an 800 nm laser field with intensity $1.2 \cdot 10^{14} \text{ Wcm}^{-2}$ and binding energies $\varepsilon_1 = -15.58 \text{ eV}$ and $\varepsilon_2 = -17.00 \text{ eV}$, corresponding to the HOMO and HOMO-1 contributions (short trajectories are considered). Horizontal lines indicate the phase differences and excursion times for the first (H17), middle (H25) and last (H31) harmonics of the experimental range (grey area). (b, c): Phases of the HOMO recombination dipole computed with Coulomb-waves, at 3 different orientations θ , vs. electron momentum k . For computational purposes, the orbital was expressed as a combination of single-center Slater functions. Two values of the effective charge are considered for the Coulomb waves: (b) $Z^* = 0$, corresponding to plane waves, and (c) $Z^* = 1$, corresponding to the asymptotic charge of N_2^+ . For $k > 0.5 \text{ a.u.}$, both series of curves show similar patterns, up to a k -dependent global phase shift and a translation $\delta k \approx 0.4 \text{ a.u.}$ on the momentum scale. For $k < 0.5 \text{ a.u.}$, the fast oscillations in (c) are a direct imprint left by the Coulomb-waves, as can be seen from their partial wave-expansion³⁷, where each angular momentum l contributes with a phase $\eta_l(Z^*, k) = \arg[\Gamma(l+1+iZ^*/k)]$.

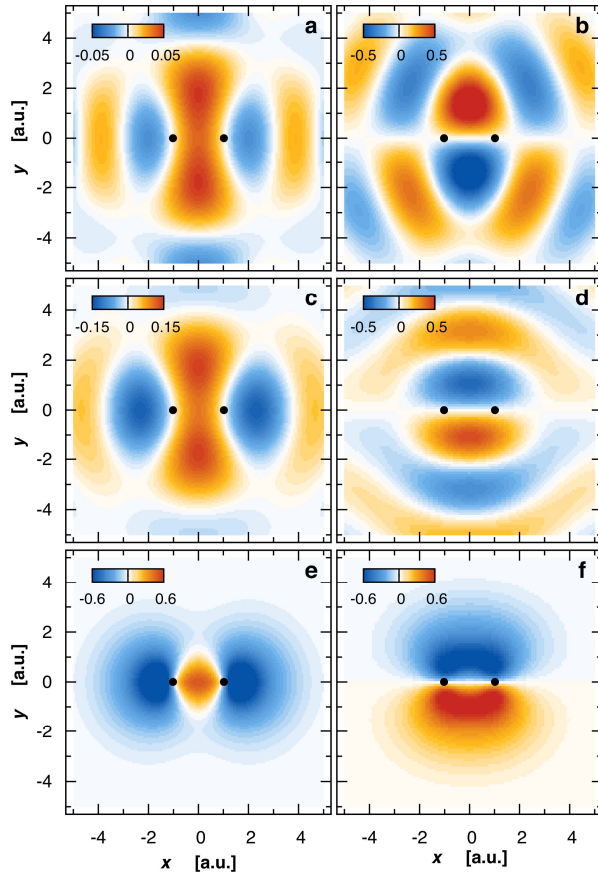


Figure 4. Orbital tomographic reconstructions. (a): from the imaginary part of the experimental dipole imposing σ_g -symmetry; (b) : from the real part of the experimental dipole imposing π_u -symmetry; (c) : simulated reconstruction with the HOMO PW-dipole; (d) : simulated reconstruction with the HOMO-1 PW-dipole. For the sake of comparison, simulations were done with the experimental sampling (harmonics and angles, see Fig. 2), using the dispersion relation $k_q^2/2 = q\alpha_L$, and by restricting the theoretical dipole to its component along the laser polarization. Black dots indicate the nuclei position at equilibrium distance. Reconstructions in (b,d), are based on the ‘velocity-form’ of the dipole to avoid division by x/y in real space and thus numerical problems with the orbital nodes at $y=0$. (e): Hartree-Fock HOMO and (f): HOMO-1, calculated with GAMESS⁴⁵.

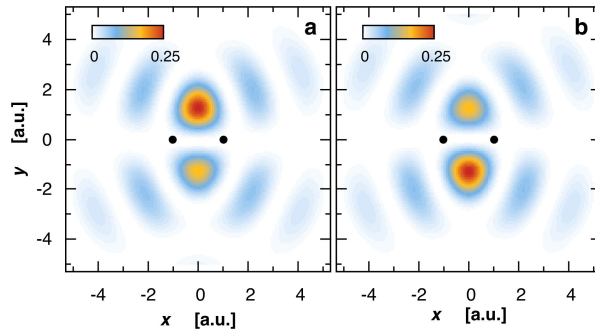
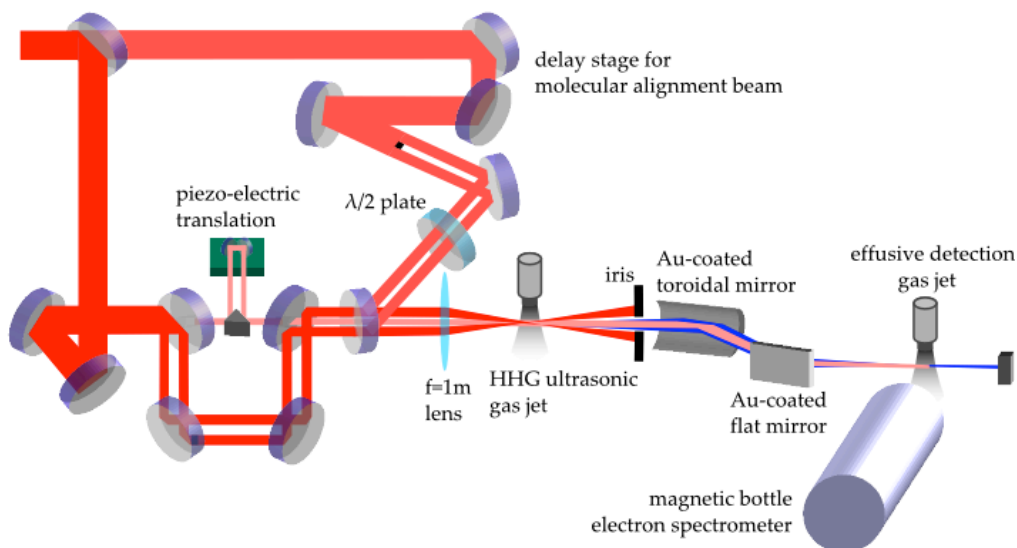


Figure 5. Reconstructions of the dynamic hole. (a): Squared sum and (b): squared difference of the wavefunctions shown in Figure 4a,b. These can be interpreted as the hole-density in the ion at the recollision / tunnel-ionization instants (see text) for a relative weight of the HOMO:HOMO-1 contributions corresponding to the relative amplitudes of the wavefunctions in Figure 4a,b. Although we have access to *wave-packets*, we plot the corresponding densities so as to visually emphasize their asymmetries.

Supplementary Information to the article “Attosecond imaging of molecular electronic wave-packets”

Experimental setup



Supplementary Figure 1: Schematic of the experimental setup. The laser beam enters at the upper left of the scheme. The part transmitted through the first beam splitter is the beam producing nonadiabatic alignment¹ of the molecules in the HHG gas jet. In the lower left part of the figure, the drilled mirror based interferometer for the RABITT measurement is depicted. Here, the large annular beam is the harmonic generating beam, whereas the small central part is the probe beam for RABITT. From the focusing lens on, the setup is placed under vacuum.

The RABITT method

We detect the harmonic emission with photon energies larger than $I_p^{\text{Ne}} = 21.6$ eV by photoionizing neon atoms and detecting the released photoelectrons with a magnetic bottle electron spectrometer. Intensity spectra, corrected for the energy-dependent ionization cross-section of neon, readily yield the XUV spectral intensities.

The spectral phase $\varphi(\omega)$ of the harmonics is measured with the RABITT technique²⁻⁵. It is based on the analysis of sidebands, created in the photoelectron spectrum by absorption of one harmonic photon and simultaneous absorption or stimulated emission of one infrared (IR) photon from a weak probe beam, which is also present in the detection volume. This probe beam having the same frequency ω_L as the generating beam, this leads to the interference of two quantum paths “absorption of harmonic q and absorption of 1 IR photon” and “absorption of harmonic $q+2$ and stimulated emission of 1 IR photon” at the same photoelectron energy, $(q+1)\omega_L - I_p^{\text{Ne}}$. Varying the phase of the IR probe field by varying its delay τ relative to the generating beam and thus the harmonic beam leads to a modulation of the sideband intensity $S_{q+1}(\tau)$ as

$$S_{q+1}(\tau) \propto \cos(2\omega_L\tau + \varphi_{q+2} - \varphi_q - \Delta\phi^{\text{at}}), \quad (\text{S1})$$

where φ_{q+2} and φ_q are the spectral phases of harmonics $q+2$ and q , respectively, and $\Delta\phi^{\text{at}}$ is a small phase correction, characteristic of the target gas, which can be calculated for rare gas atoms^{3,4}. Extracting the phase of the oscillating sidebands via a Fourier transform thus yields the relative phase of neighbouring harmonic orders q and $q+2$, and thus the group delay, also called emission time

$$t_e(q+1) = (\partial\varphi/\partial\omega)|_{q+1} \approx (\varphi_{q+2} - \varphi_q)/(2\omega_L). \quad (\text{S2})$$

The RABITT method can be complemented by using the interference of the probe beam with the generating beam in the HHG medium, that leads to a small modulation of the total harmonic yield $\propto \cos(\omega_L \tau + \alpha)$. The phase of this modulation serves as a reference for the sideband phases in our measurements^{3,6} leading to the determination of a ‘time reference’ for the group delay values, modulo π/ω_L , on a scale where $t=0$ is located at an extremum of the generating IR field.

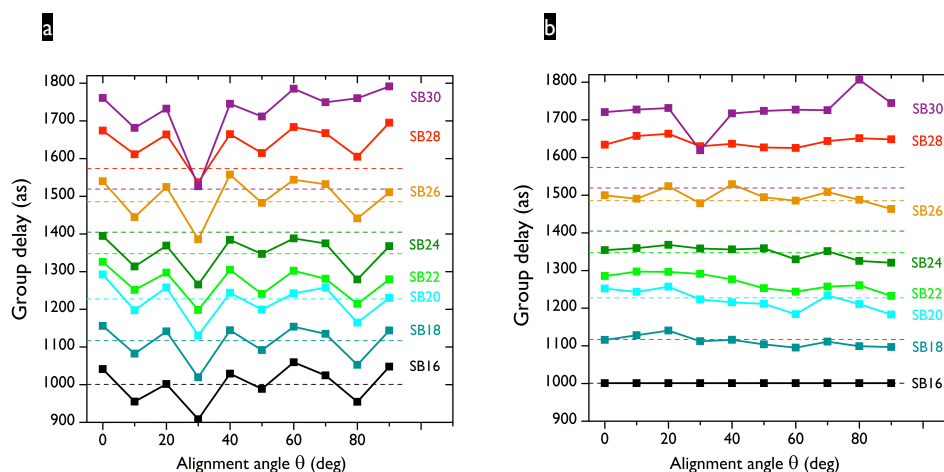
The experimental observable is thus the derivative of the spectral phase $\phi(\omega)$ with respect to frequency and $\phi(\omega)$ is obtained by concatenating the measured relative phases. The spectral phase is thus determined up to an integration constant ϕ_0 .

Details on the phase data analysis

In a series of RABITT scans where the molecule alignment angle is varied and experimental conditions otherwise remain the same, the ‘time reference’ fluctuates over a narrow range (typically ± 50 as), see Supplementary Fig. 2a. For instance, at 30° and 80° , almost all group delays are shifted downwards, indicating a modification of the ‘time reference’. We have never observed a *systematic* shift of the ‘time reference’ with the angle: in another series of measurements, such shifts occur at different angles. Therefore, the observed shifts are probably a measurement error rather than a real single-molecule effect. Albeit being small, these fluctuations induce rather large errors in the integration performed to obtain the spectral phases. This is the reason why we usually remove them.

To this end, we choose a sideband order where we suppose that the group delay does not vary with the angle – in general the lowest order: sideband 16 – and normalize all curves in the series to the average value for this sideband. The chosen value for the ‘time reference’ is thus not arbitrary but an average over random fluctuations. The result is shown in Supplementary Fig. 2b. These data are then integrated to obtain the spectral phases for each alignment angle. Note that the same integration constant is used for all angles.

For the argon reference scan (shown in the Supplementary Fig. 3), it turns out that the group delay at sideband 16 is almost the *same* (+2.7 as) as the average value for sideband 16 obtained from the different N_2 curves. In the integration of the group delay to obtain the spectra phase, the integration constant is set to the same value as in N_2 .



Supplementary Figure 2: Fluctuation of the ‘time reference’ for the group delays. In both panels, dashed lines mark the group delays measured for the argon reference, with the line colors corresponding to the sideband order. (a) ‘Raw’ group delays extracted for each sideband in a series of RABITT scans for N_2 for alignment angles from 0° to 90° . Clearly, the dominating variation of the group delay with angle is irregular and reproduced by every sideband. It is due to fluctuations of the ‘time reference’. (b) Group delays after the values for each individual angle were shifted such that the group delay at sideband 16 is the same and equal to the average value of the fluctuating data. Integrating these data (i.e. concatenating the group delays of subsequent sidebands for each individual alignment angle) yields the spectral phases for nitrogen at the individual alignment angles and for the argon reference. The *difference* between the two is then the sought-for dipole phase, shown in Fig. 2b of the main paper.

In summary: (i) the recombination dipole phase, obtained as the *difference* between the spectral phases for the molecule and the reference atom, is *set to* zero at harmonic 15 for all angles (by always using the same integration constant). (ii) The linear slope between harmonics 15 and 17 of the recombination dipole phase is also *set to* zero for all alignment angles (by setting the same group delay at sideband 16 for all scans).

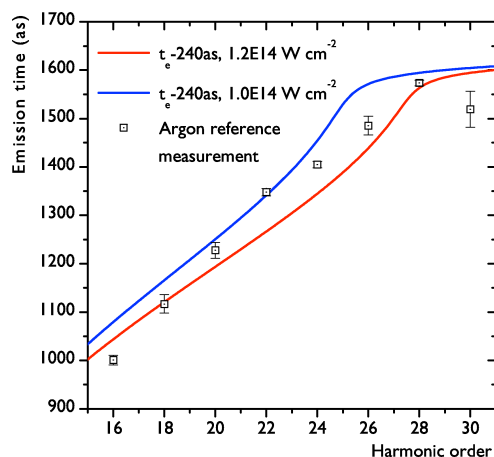
Point (i) concerns two issues. First, it contains the ‘absolute’ phase difference between the H15 emissions from N₂ and argon as a function of alignment angle. In our experiments, we do not measure it but it could be accessed through the gas mixing method⁷⁻⁹. We assume an angle-independent H15 phase, which is supported by recent interferometric experiments¹⁰ demonstrating a very weak angular dependence of the phase of low harmonics in N₂. Second, it also implicitly includes any constant phase such as the theoretical correction $-\delta\phi_r$, which removes the scattering phase shift and allows a plane-wave tomographic reconstruction. Since the latter correction is not known, the H15 phase difference is an adjustable parameter which is chosen in order to get the most consistent tomographic reconstructions. Obviously, a global phase shift transfers amplitude from the real to the imaginary part and vice versa, i.e. if it has the ‘wrong’ value, the separation into HOMO and HOMO-1 is lost.

In point (ii), we decide to dismiss the ‘angle-dependent time reference’ information that can in principle be extracted from RABITT measurements, because we are convinced that in our data, this information is dominated by noise. Note that the group delay variation is obtained from the interference of two-photon transitions *in the detection gas*, visible on the sidebands (see paragraph ‘The RABITT method’), whereas the ‘time reference’ is obtained from the interference of the IR generating and probe beams *in the HHG medium* – so the two pieces of information really stem from different processes occurring at different parts of the setup. Setting the *same* ‘time reference’ for all angles due to the limited precision of its measurement simply means that we neglect a possible (small) angle-dependent linear component of the dipole phase.

The phases resulting from the above procedure is shown in Fig. 2b) and used for the reconstructions presented in Fig. 4.

Intensity calibration

The effective harmonic generation intensity for the measurements reported here is determined via both the experimentally observed cut-off position and the ‘attochirp’, i.e. the slope of the measured group delay vs. harmonic order. For rare gas atoms, it has been shown that the harmonic group delay, also called emission time, agrees with recombination instants calculated with the SFA model³. The slope of



Supplementary Figure 3: Determination of the effective experimental intensity. The red and blue lines show recombination times for argon ($I_p=15.76$ eV), calculated by solving the saddle-point equations of the SFA model for an intensity of $1.2 \cdot 10^{14}$ W cm⁻² and $1.0 \cdot 10^{14}$ W cm⁻², respectively. Only the points for the short trajectory contribution are shown. They have been shifted by -240 as in order to facilitate direct comparison with the experimental group delay of the argon reference measurement (squares), used for the study presented in this paper.

3.3 Control of the Two Orbital Contributions

At first sight, the presence of multiple orbital contributions in HHG seems to be a rather bothering phenomenon for tomographic orbital reconstruction. As discussed above, one may find special conditions, where the "image" of the two orbitals are disentangled into the real and imaginary parts of the measured dipole. But in general, one may have even more orbitals contributing to the harmonic signal, like in (Smirnova et al. [147]), chasing away all our hope for tomography. In this part of the thesis we will show that not all the hopes are gone and tomography still may be feasible through understanding and control over the multiple orbital contributions.

At second sight, one does not want always to reconstruct static orbitals. One of the main goals of attosecond science is to localize spatially and temporally an electronic excitation in a molecule and to control the intra-molecular ultrafast charge transfer. Therefore, here we investigate how the control over the driving laser intensity affect the interplay between the two ionization channels in N_2 .

3.3.1 Experimental results

As presented earlier the behavior of multi-orbital dynamics is controlled by the phase difference between the two orbital contributions that is accumulated during the excursion of the electron in the continuum $\Delta\varphi_{con}(q, I_L) = -\Delta I_p \tau_q(I_L)$. The excursion time is governed by the driving laser, hence the interference between the two ionization channels can be controlled through I_L . By measuring the spectral intensity and phase of the emitted harmonics from aligned N_2 molecules and from Ar with different I_L , we have studied the dynamics of the two competing channels.

The experimental setup and conditions for generating high harmonics are exactly the same as presented in sections 2.1, 2.2.1 and 2.2.2, except for the varying laser intensity. The molecules were aligned at the half-revival parallel ($\vartheta = 0^\circ$) and perpendicular ($\vartheta = 90^\circ$) to the driving laser polarization. This way, in principle we can study two extreme cases, when mainly one orbital is contributing (parallel case) and when multiple orbitals are present (perpendicular case).

Figures 3.2 a,b,c show the measured group delays (GD) for different I_L in Ar, N_2 aligned parallel and perpendicular to the driving laser field, respectively. The data for different laser intensities were not collected on the same day, because the repetition rate of the laser is 20 Hz and we could perform at most 10 RABBIT scans per day. However, for a given intensity, it was very important to perform the measurements in Ar and N_2 ($\vartheta = 0^\circ, 90^\circ$) in a row, i.e. in the same conditions to eliminate, thanks to the calibration, any errors coming from the different setup alignment, focusing, laser beam profile that may change from day to day. To determine the generating laser intensity in the gas jet, we apply the method described in section 1.4.5. After determining the slope Δt_e of the plateau region in Ar, we search the corresponding laser intensities in figure 1.12. In principle, each group delay curve has its own absolute timing, τ_0 . But as discussed earlier, in section 2.2.2, our system do not provide precise absolute timing determination. Within one day in the same experimental conditions, τ_0 varied of about 200 as. Therefore we normalized all curves at side band 16 to a typical absolute timing of Ar. This corresponds to a global vertical shift.

It is interesting to compare the 3 plots in figure 3.2. The slope of Ar (a) is quite linear, as expected because it reflects the intrinsic attochirp of HHG and the phase of its RDM is quite flat. While in the same generating conditions N_2 is supposed to have the same attochirp, since $I_p(N_2) \approx I_p(Ar)$, there are clear deviations from that, at both alignment angles. A group delay "dip" is present in the plateau region, that is increasing with the laser intensity and is always larger for perpendicular alignment than for the parallel case. There are three

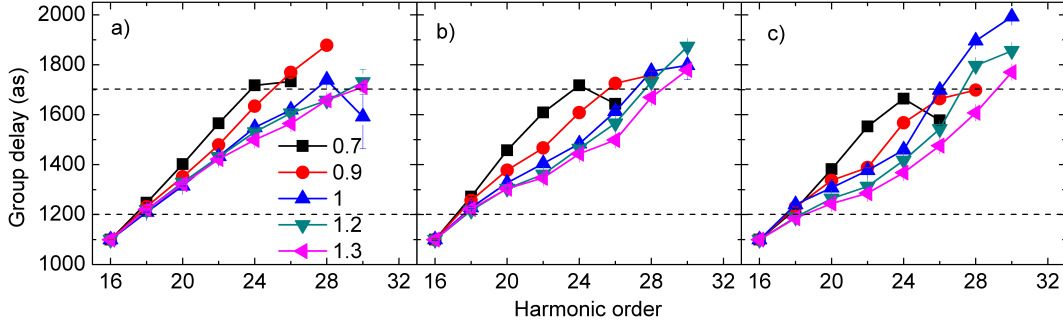


Figure 3.2: Measured group delays of Ar (a), N_2 ($\theta = 0^\circ$) (b) and N_2 ($\theta = 90^\circ$) (c). The code of the symbols and the corresponding I_L values (in units of 10^{14} W/cm^2) are given in (a). Horizontal dashed lines are put to 1200 as and to 1700 as to make easier the comparison between the plots.

remarkable observations concerning the measured group delays, detailed below.

(i) Since the dip evolves with the intensity around the spectral region of harmonic 25, it cannot be simply a structural effect of N_2 . As we already know from the previous section, the multi-orbital contributions are sensitive to for the laser intensity. The dip also changes with the alignment of the molecules. The dip is more pronounced when the molecules are perpendicular to the driving laser and that is the condition when the HOMO-1 is contributing the most probably to the HHG. Since the alignment of the molecule is not perfect, in the case of parallel alignment, there has to be already some influence of HOMO-1 causing the evolution of the dip with the intensity.

(ii) Surprisingly, the GD dip is not present at $I_L = 0.7 \times 10^{14} \text{ W/cm}^2$. The three GD curves in figures 3.2 a,b,c for this intensity are quite similar to each other, as seen in figure 3.3 a. This suggests first that there is no contribution of HOMO-1, it is mainly the attochirp (Δt_e) that determines the behavior of the GD curve while the RDM does not add any chirp. To verify this statement we recall that the total phase constructs from the three steps of the HHG: $\varphi_{tot}(\omega) = \varphi_{ion}(\omega) + \varphi_{con}(\omega) + \varphi_{rec}(\omega)$, where we assume that the ionization phase is zero. The group delay then is obtained by deriving the total phase with the frequency:

$$GD(\omega) = \frac{\partial \varphi_{tot}(\omega)}{\partial \omega} = \frac{\partial \varphi_{con}(\omega)}{\partial \omega} + \frac{\partial \varphi_{rec}(\omega)}{\partial \omega}$$

$$GD(\omega) \sim \Delta t_e \omega + \frac{\partial \varphi_{rec}(\omega)}{\partial \omega} \quad (3.20)$$

For plane wave RDM the last term in eq. 3.20 is zero, since the phase of the RDM of Ar in our spectral range is flat, similarly to N_2 when considering only the contribution of HOMO orbital at $\theta = 0^\circ$ and $\theta = 90^\circ$. Therefore, the group delay in all three cases is described by the attochirp. We verified this idea also with scattering wave RDMs, presented in figure 3.3 b, and found the same tendency (all curves were shifted vertically to 1100 as at side band 16). The second conclusion is that the tunnel ionization rate is an exponential function of the laser field and of the ionization potential of the orbital, see eq. 1.42. Because of this non-linear behavior of tunnel ionization, at low intensity, the potential barrier of N_2 is not bent enough to achieve tunnel ionization from HOMO-1. Therefore the contribution from HOMO-1 is suppressed while HOMO still produces harmonics.

However, there is a clear difference between measurements and calculations in figure 3.3. In theory, reaching the cut-off harmonics, the group delay saturates, but it is not the case for the experiment. This is not due to the propagation effect, since the laser intensity is very low. Nevertheless, we have several sets of group delays obtained using approximately the

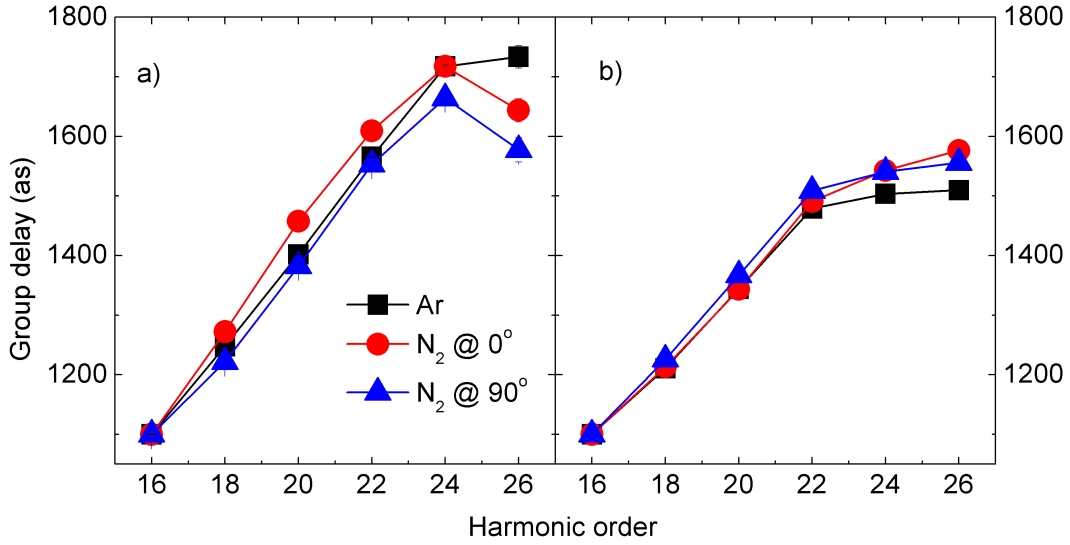


Figure 3.3: Direct group delay comparison for $I_L = 0.7 \times 10^{14} \text{ W/cm}^2$ of Ar (black square), N₂ parallel (red circle) and perpendicular (blue triangle) alignment measured experimentally (a) and calculated (b) using saddle-point approximation, to obtain the attochirp, and scattering wave based RDMs. For N₂ the RDM is retrieved from figure 1.9, while for Ar we used the scattering-wave data presented in (Jin et al. [59]).

same I_L and all of them behave similarly. For the moment, the origin of this difference is still a mystery for us.

(iii) At high I_L , towards the cut-off energies for side bands 26-30 in figures 3.2 b and c, the GD steeply increases for $\vartheta = 0^\circ$ and even more for $\vartheta = 90^\circ$. Such an increase is absent in the case of Ar, which rather shows the sign of saturation comparing to the cut-off harmonics. During the modeling of our experiments, we found that something similar can be achieved by including the nuclear dynamics during HHG, see section 3.3.2.

All the effects discussed in (i-iii) are transferred to the calibrated phase of N₂ by the calibration with Ar, figures 3.4 a,b. The GD dip (i) corresponds to a phase decrease around harmonics 23-27 and there is a phase increase (iii) at high orders 27-31. At the lowest intensity the phase seems to be similar for both alignments (ii). At $\vartheta = 0^\circ$ (fig 3.4 a), there is little variation with I_L : all curves are grouped together. In contrast, at $\vartheta = 90^\circ$ (fig 3.4 b), there is a strong variation when I_L reaches $1.1 \times 10^{14} \text{ W/cm}^2$. In figures 3.4 a and b, the angular relation of the calibrated phases are imposed by hand, since as it was explained in section 2.2.2, RABBIT detects only the spectral phase but it is not able to observe phase variation with the alignment angle. We imposed this, (1) the phase of harmonic 15 is the same as in Ar for both parallel and perpendicular alignments and for all intensities; and (2) the same for harmonic 17 (which is a consequence of (1) plus the normalization at side band 16). By doing (1) we add or remove a constant, order independent phase term $\varphi_0(\theta)$. Hence it does not change the characteristics of the dipole. Performing (2) is imposed by the instability in absolute timing. It results in the removal or addition of a linear phase as a function of harmonic order that is characteristic for each laser intensity and alignment angle (see eq. 2.20). Therefore, the characteristics of the total dipole phase are modified by a linear term.

Figures 3.4 c and d show the corresponding calibrated intensity of the total dipole. What is very surprising is that at all intensities and both alignments there is a clear minimum in the spectra. When aligned parallel to the driving laser this minimum is more shallow. We recall that in figure 2 a of PAPER I a similar minimum is shown, as a function of the alignment angle at $I_L = 1.2 \times 10^{14} \text{ W/cm}^2$.

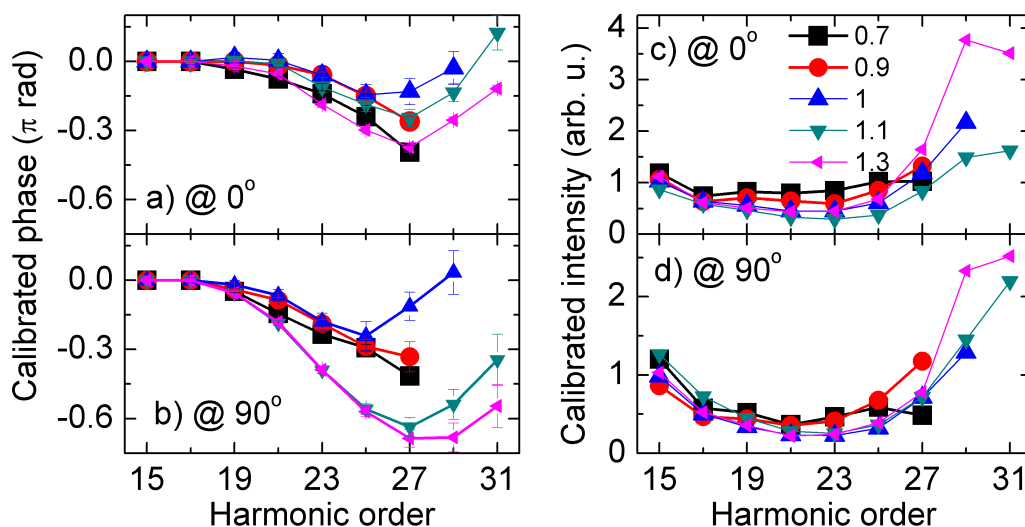


Figure 3.4: Calibrated harmonic phases (left side) and intensities (right side) for N_2 molecules aligned parallel (a,c) and perpendicular (b,d) to the driving laser. Note that in c and d the vertical scales are not covering the same range. The plotted phases are an average over several calibrated phase curves with the same I_L . The color code and the corresponding intensity range are the same as in figure 3.2.

Contradiction between spectral intensity and phase measurements

From the group delay measurements we infer that in N_2 the HOMO and HOMO-1 are both contributing to HHG. When these two contributions are dephased by π , this results in a dynamical minimum in the spectrum that moves as the laser intensity changes. This is not the case in our observations. Another interpretation would be a structural minimum, e.g. resulting from two-center interference, but it does not move with the alignment angle neither. In summary, the observed spectral minimum seems to be angle and intensity independent, although the dipole phase varies considerably with these parameters.

Other groups have studied aligned N_2 molecules with HHG, but they looked mainly at the harmonic spectra. They did observe this minimum by using different driving laser intensities, wavelengths and molecular alignments (Mairesse et al. [100], McFarland et al. [104], Torres et al. [159], Wörner *et al.* [179]), but the minimum seemed to be located firmly, even though the different groups found it in slightly different positions within a 5 eV range. Up to our knowledge only (Farrell et al. [30]) could observe a slightly moving minimum in the spectrum between H23 and H27 by changing both the intensity and the molecular alignment. While relating it to multi-orbital contributions, they recognized that a "field-free static model of the molecule is insufficient to explain the observations". (Mairesse et al. [100]) attributed it tentatively to multi-electron effects. The only published simulation recovering a spectral minimum (at 45 eV) was reported by (Jin et al. [59]) who claim that they explain the results shown in (Wörner *et al.* [179]) using only the HOMO orbital and including macroscopic effects. The minimum would result from a change of sign of the scattering-wave RDM at 50 eV for $\theta = 0^\circ$ that is shifted to lower energy by the macroscopic response. This does not explain however, why the minimum is still present at $\theta = 90^\circ$, since in this condition the RDM at $\theta = 0^\circ$ does not contribute much to the macroscopic response. Another interpretation was proposed by O. Smirnova (unpublished): the spectral minimum would originate from the temporal filtering of the recombination dipole moment. This would mean that the radiative electron recombination in HHG and the single photon

ionization are not reverse processes. It was suggested that the shape resonance occurring in N_2 around 30 eV could result in a spectral minimum at a higher energy when filtered on an attosecond time scale. But up to now there are no decisive conclusions on this in the scientific community.

The uncertainty in the understanding of the experimental results shows the need for more observables. Since our phase and intensity observations seem rather contradictory they may be the result of two different effects. We still claim (and show by modeling) that at high enough intensities, multi-orbitals are playing an important role in N_2 . Based on (i) and (ii) it seems that the spectral phase is sensitive to the passage between single and multi-orbital contributions. Our homemade model presented below, did not answer the whole problem, in particular the origin of the spectral minimum, but clarified the measured phase evolution.

3.3.2 Model construction

To simulate the experimental results, we construct a QRS like model (Le et al. [79]), where the three steps of the HHG are well separated and calculated one by one. Our starting point is equation 3.19 and according to the self-probing scheme we calibrate with the signal measured in Ar (we discuss only parallel components of length form in the LF):

$$\begin{aligned} \epsilon_{cal}(q, I_L, \theta) &= \frac{\epsilon_{XUV}(q, I_L, \theta)}{\epsilon_{XUV}^{Ar}(q, I_L)} = \\ &= \frac{\gamma_X(q, I_L, \theta)}{\gamma_{Ar}(q, I_L)} \frac{a_X(q, I_L)}{a_{Ar}(q, I_L)} \frac{d_X(q, \theta)}{d_{Ar}(q)} + \frac{\gamma_A(q, I_L, \theta)}{\gamma_{Ar}(q, I_L)} \frac{a_A(q, I_L)}{a_{Ar}(q, I_L)} \frac{d_A(q, \theta)}{d_{Ar}(q)}, \end{aligned} \quad (3.21)$$

where $d_i = \langle \psi_i(\mathbf{r}) | \mathbf{r} | \psi_c(\mathbf{r}) \rangle$ is the complex recombination dipole moment, γ_i is the square root of the ionization rate while a_i is the complex term representing the spreading of the EWP and the accumulated phase during the excursion in the continuum for $i = X, A, Ar$ and q denotes the harmonic order. We are only interested in the phase behavior of $\epsilon_{cal}(q, I_L, \theta)$. We use plane wave approximation to describe the RDM and our study is restricted to $\theta = 90^\circ$. The reason for that is discussed later. To identify which term affects the most the final result, we investigate each ratio separately.

Tunnel ionization

The square roots of tunnel ionization rates for the HOMO and HOMO-1 of N_2 when the molecule is aligned perpendicular to the driving laser, are plotted in figure 3.5 calculated with a numeric code called PYMOLION, developed by R. Murray [113]. It is visible that in this configuration the rates are of the same order of magnitude. We have to mention that the calculation of ionization rates is extremely difficult and requires numerous approximations. Different models predict different rates that are more or less in agreement with experimental results. Our model seems to underestimate the rates of HOMO-1 at $\theta = 0^\circ$.

Tunnel ionization of Ar is angle independent and since $I_p(Ar) \approx I_p(X)$ we assume that $\gamma_{Ar}(q, I_L) = \gamma_X(q, I_L, \theta = 0^\circ)$. Therefore we introduce the normalized rates: $\gamma_X^N(q, I_L, \theta) = \gamma_X(q, I_L, \theta) / \gamma_X(q, I_L, \theta = 0^\circ)$ and $\gamma_A^N(q, I_L, \theta) = \gamma_A(q, I_L, \theta) / \gamma_X(q, I_L, \theta = 0^\circ)$. The important parameter is $\gamma_A^N(q, I_L, \theta)$ that determines the competition between the X and A channels. It is plotted in figure 2 a of PAPER II for $\theta = 90^\circ$. The sudden ruptures in the plot are due to the transition between the plateau and the cut-off region. We can conclude that this parameter barely varies as a function of harmonic order in the plateau region. But as a function of intensity the ratio may vary almost by a factor of 2. Therefore the increase of I_L does affect the multi-orbital contributions in favor of HOMO-1.

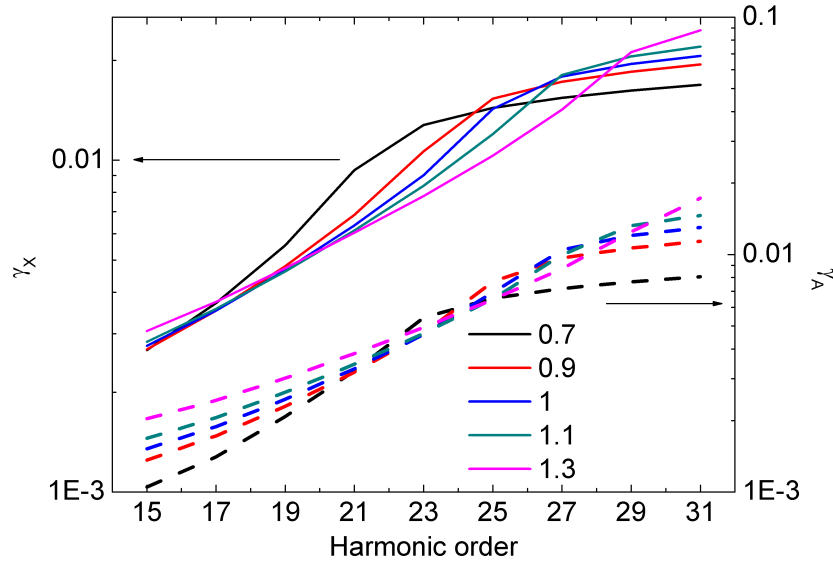


Figure 3.5: The square root of tunnel ionization rates calculated for HOMO (γ_X , full lines) and for HOMO-1 (γ_A , dashed lines). Colors define the laser intensity in units of 10^{14} W/cm 2 .

Continuum acceleration

In the same generating conditions $a_X(q, I_L) = a_{Ar}(q, I_L)$ while this is not true for the A channel. The second term on the right-hand side of eq. 3.21 will involve the ratio of the EWP spreading for the two ionization channels $|a_A(q, I_L)/a_X(q, I_L)|$ and the difference in the gathered phase during the excursion $\Delta\varphi_{con}(q, I_L) = -\Delta I_p \tau_q(I_L)$. These quantities are presented in figure 2b of PAPER II. Considering the spreading of the wavepacket, in the plateau region there is almost no harmonic order dependence and no difference between different laser intensities. In contrast, in the cut off region, HOMO-1 becomes more important, because its cut-off limit is shifted towards higher photon energies, due to its larger I_p . Meanwhile, $\Delta\varphi_{con}(q, I_L)$ varies approximately by $\pi/2$ over our spectral range, depending on I_L .

In conclusion, $\Delta\varphi_{con}(q, I_L)$ will affect the phase of $\epsilon_{cal}(q, I_L, \theta)$ with a weight defined by the wavepackets' spreading.

Recombination

The RDM is a crucial point since it encodes the structural effects. The PWA do not reproduce well the molecular structure, but here, we are rather interested in the ratio of the HOMO-1 and HOMO dipoles. Figure 3.6a shows the RDM amplitude ratios and phase differences calibrated for both the plane and scattering waves at $\theta = 90^\circ$ (a) and $\theta = 3^\circ$ (b) (at $\theta = 0^\circ$ the dipole of HOMO-1 is zero). The plotted values do not agree exactly, but the tendency is similar for both (a) and (b). At $\theta = 90^\circ$ there are no structural effects neither in the plane nor in the scattering wave dipoles. At $\theta = 3^\circ$ a clear deviation in the tendency between the two dipole simulations appear at low orders due to a shape resonance in the scattering-wave RDM of HOMO. Therefore, by using plane wave RDMs we qualitatively include the trends of the scattering-wave RDMs in our calculation.

With the PWA, the phase difference is constant as a function of harmonic order and the amplitude ratio shows that HOMO-1 becomes more and more important as the harmonic order increases (as was already pointed out for each step of HHG).

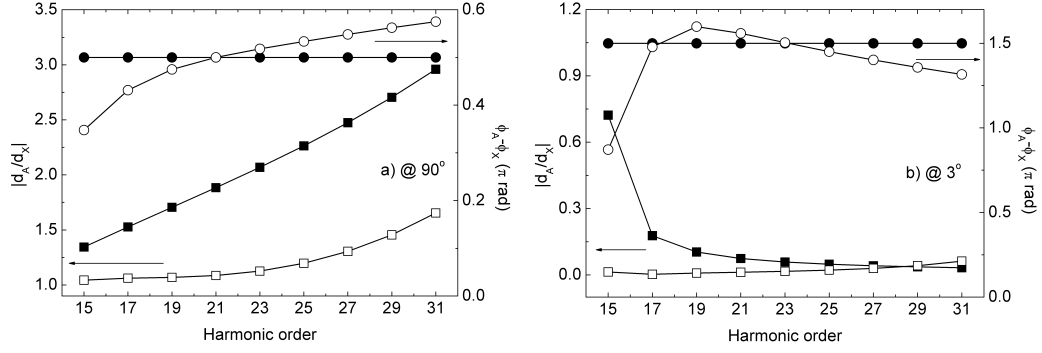


Figure 3.6: Comparison of the plane wave (full symbols) and scattering wave (open symbols) dipole amplitudes $|d_A(q, \theta)/d_X(q)|$ (squares) and phases $\varphi_A^{rec}(q, \theta) - \varphi_X^{rec}(q, \theta)$ (circles) for $\theta = 90^\circ$ (a) and $\theta = 3^\circ$ (b).

Summarizing all the made assumptions, the calibrated signal is calculated as:

$$\epsilon_{cal}(q, I_L, \theta) = \gamma_X^N(q, I_L, \theta) \frac{d_X(q, \theta)}{d_{Ar}(q)} + \gamma_A^N(q, I_L, \theta) \left| \frac{a_A(q, I_L)}{a_X(q, I_L)} \right| e^{-i\Delta I_p \tau_q(I_L)} \frac{d_A(q, \theta)}{d_{Ar}(q)}. \quad (3.22)$$

The phase of $\epsilon_{cal}(q, I_L, \theta)$ is shown in figure 3 b of PAPER II, with dashed lines. To compare it with the experimental results, each curve is then shifted vertically, in order to shift the phase of harmonic 15 to zero (normalization) and a linear phase function is subtracted to make the phase of harmonic 17 equal to zero as well (rotation). The results are presented in dashed lines in fig. 3 c in the article. A clear similarity is present already here between the simulated and measured phases: the increasing intensity results in a phase decrease, especially for higher harmonic orders. This is a clear sign of multi orbital contributions. But in contrast to the measured phases, the calculated ones do not re-increase at the end of our spectral range. As we could see from the discussions presented above, this is not due to the PWA. There are additional factors missing in our model.

Nuclear dynamics

The nuclear part of the molecular wavefunction can also affect the HHG if nuclear dynamics occurs during the excursion of the tunnel ionized electron. This is described by the $C(\tau_q(I_L))$ autocorrelation function (see equation 1.68). Although for heavy nuclei this function is in general negligible concerning tunnel ionization through the X channel ($|C_X(\tau_q(I_L))| \approx 1$ and $\arg(C_X(\tau_q(I_L))) \approx 0$), this may not be the case for the A channel. The Born-Oppenheimer energy curves of the neutral ground state and the first excited state of N_2^+ are shifted horizontally with respect to each other. The induced nuclear wavepacket oscillation through the A channel decreases the efficiency of the HHG. Figure 2 c of PAPER II shows the calculated autocorrelation amplitude and phase for the A channel, as a function of harmonic order. The amplitude decreases towards higher orders due to the longer excursion time, meaning that these harmonics will contribute less to the HHG. Moreover, the nuclear dynamics induces almost 0.3π phase variation. Therefore, equation 3.22 has to be modified into:

$$\begin{aligned} \epsilon_{cal}(q, I_L, \theta) = & \gamma_X^N(q, I_L, \theta) \frac{d_X(q, \theta)}{d_{Ar}(q)} C_X(\tau_q(I_L)) + \\ & + \gamma_A^N(q, I_L, \theta) \left| \frac{a_A(q, I_L)}{a_X(q, I_L)} \right| e^{i\Delta I_p \tau_q(I_L)} \frac{d_A(q, \theta)}{d_{Ar}(q)} C_A(\tau_q(I_L)). \end{aligned} \quad (3.23)$$

The so obtained phases are presented in figure 3 b with full lines, while the phases after normalization and rotation are shown in figure 3 c, with full lines also in PAPER II. The

presence of nuclear dynamics in the A channel could thus modify the decrease of the phase and even induce a re-increase at high orders. The autocorrelation is angle independent, hence it fits well to the experimental results obtained at parallel alignment as well. However, the re-increase is not as marked as in the measured phases, suggesting that this is still not the end of the story. Maybe, including the coupling between the two channels could give more insight.

Nevertheless, besides the recent publication of (Farrell et al. [31]), this is the first time that multi-orbital nuclear dynamics are revealed and in particular the phase of the autocorrelation function. These findings are opening up brand new research directions. The fact that the autocorrelation function is alignment independent, but depends on the laser intensity as well as on its wavelength could provide more insight on the nuclear dynamics of molecules on an attosecond timescale. By properly choosing the experimental conditions to obtain long excursion times, one can reduce the influence of lower lying orbitals if needed for instance by the tomographic reconstruction.

PAPER II

Spectrally-resolved multi-channel contributions to the harmonic emission in N₂

Z. Diveki, A. Camper, S. Haessler, T. Auguste, T. Ruchon, B. Carré, P. Salières
R. Guichard, J. Caillat, A. Maquet, R. Taïeb and
Submitted (2011).

Spectrally-resolved multi-channel contributions to the harmonic emission in N₂

Z. Diveki, A. Camper, S. Haessler,* T. Auguste, T. Ruchon, B. Carré, and P. Salières†
CEA-Saclay, IRAMIS, Service des Photons, Atomes et Molécules, 91191 Gif-sur-Yvette, France

R. Guichard, J. Caillat, A. Maquet, and R. Taïeb
UPMC Université Paris 6, UMR 7614, Laboratoire de Chimie Physique-Matière et Rayonnement,
11 rue Pierre et Marie Curie, 75231 Paris Cedex 05, France and
CNRS, UMR 7614, LCPMR, Paris, France

In molecules, high-order harmonics can be emitted through different ionization channels. The coherent and ultrafast electron dynamics occurring in the ion during the emission process is directly imprinted in the harmonic spectral phase. In aligned N₂ molecules, we evidence a strong variation of this phase as a function of the driving laser intensity. Our simulations reveal that it results from a transition from a single- to a multi-channel regime. Moreover, we show that significant nuclear dynamics may occur in the A-ionization channel on an attosecond timescale, affecting both the amplitude and phase of the subsequent harmonic emission.

PACS numbers: 42.65.Ky 32.80.Rm 41.50.+h

High-order harmonic generation (HHG) in molecules results from the nonlinear interaction with a strong laser field, in which an electron is: i) liberated through tunnel ionization, ii) accelerated by the laser electric field in the continuum and finally iii) driven back to the ionic core leading to recombination and emission of coherent XUV radiation [1, 2]. The recolliding electron wavepacket combines two unique properties, *i.e.* ultrashort de Broglie wavelength and ultrashort duration, which allows probing the molecular structure and dynamics with both sub-ångström spatial and attosecond (10^{-18} s) temporal resolutions [3]. Detailed understanding of this self-probing process combined with pump-probe and molecular alignment techniques have led to a number of breakthroughs in recent years: orbital reconstruction [4–7], observation of ultrafast molecular dynamics [8–10], time-resolved study of ultrafast chemical reactions [11]...

A particularly interesting situation arises when the molecular orbitals (HOMO-1,...) lying below the highest-occupied one (HOMO) are energetically high enough to contribute to the tunneling process, leaving the molecular ion in a coherent superposition of the ground (X) and excited states (A,B...). All these ionization channels finally contribute to the harmonic emission [12, 13] which encodes the ultrafast dynamics occurring in the molecular ion during the emission process, giving access, *e.g.*, to the rearrangements occurring in the electronic shells within less than a laser cycle [14, 15]. However, retrieving this information is extremely difficult and requires unambiguous identification of the different channel contributions. Up to now, this has been done almost exclusively using harmonic intensity measurements [12, 16–20]. The variation of the harmonic yield as a function of the recollision angle gives clues for identifying the dominant contribution [12, 16]. But it is difficult to extract the relative amplitudes and phases of the different contributions since macroscopic effects like phase-matching

may affect considerably the harmonic intensity [21]. The shape of the harmonic spectrum gives additional information in the very specific case where two contributing channels have a π -phase difference and thus interfere destructively, leading to a deep minimum in the harmonic spectrum. Varying the driving laser intensity or wavelength shifts their relative phase and thus modifies the spectral position of this 'dynamical' minimum [13, 17]. In contrast, 'structural' minima that are characteristic of the recombination dipole moment of a given channel do not change position with the laser parameters [22, 23]. Interplay between the two types of minima present in the same harmonic spectrum complicate even more the retrieval of information [18–20, 24].

More advanced characterization of the harmonic emission is thus required to better identify the different channel contributions. Recent measurements of the harmonic ellipticity confronted to simulations concluded on a single efficiently-contributing channel in N₂ in their generation conditions [15, 25, 26]. Besides, the variations of the harmonic phase with the recollision angle have been used to identify the main contributing channel in CO₂ [13].

In this Letter, we show that the measurement of the harmonic *spectral phase* is a powerful tool for evidencing multi-orbital contributions and extracting information on their relative amplitude and phase. By varying the laser intensity I_L , we demonstrate a control of the relative weight of the X and A channels contributing to the HHG in N₂, up to a situation where the A channel contribution is made negligible. In our simulations, we identify two mechanisms to explain the measured non-trivial phase evolution. First, the difference in continuum dynamics of the two channels controls the harmonic phase in the cutoff region. Second, the remarkably fast nuclear dynamics occurring on an attosecond timescale in the A channel strongly modifies its contribution to HHG.

Our experimental setup performs non-adiabatic align-

ment [27] of the N_2 molecules, followed by attosecond pulse generation and characterization in amplitude and phase (details can be found in [5]). In this work, the alignment laser pulse was stretched to 120 fs, while keeping an intensity of 5×10^{13} W/cm², in order to maximize the degree of alignment at half-revival, which was estimated to be $\langle \cos^2 \theta \rangle \approx 0.6$. The 55-fs generating pulse then drives HHG at the half-revival. Care was taken to ensure detection of only the short trajectories' contribution to HHG [28, 29]: first, the gas jet was placed ≈ 3 mm after the laser focus in order to phase match only these contributions; second, an iris set 0.8 m downstream cut the outer part of the harmonic beam, where the long trajectories may contribute. Harmonic phase characterization was performed using the RABITT technique [30] that yields the group delay (GD) at the even ordered side-bands (SB): $GD_q = (\phi_{q+1} - \phi_{q-1})/2\omega_L$, where $\phi_{q\pm 1}$ are the phases of two consecutive odd harmonics and ω_L is the fundamental laser frequency.

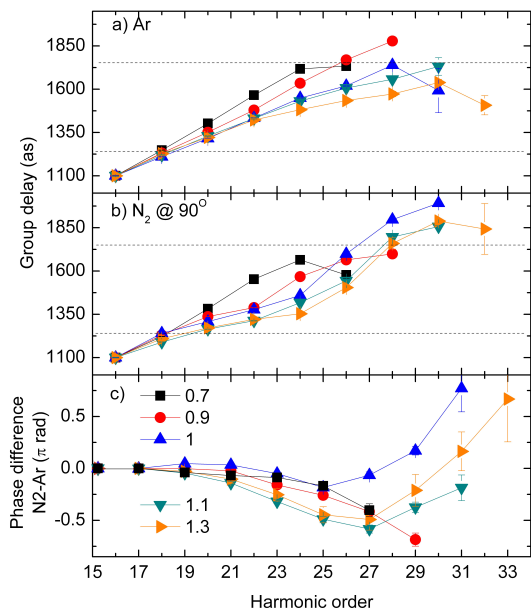


FIG. 1. Group delays measured in Ar (a) and in N_2 (b) for different driving laser intensities indicated in c) in units of 10^{14} W/cm². c) Harmonic phase difference between N_2 and Ar extracted from a) and b). The phase difference is calibrated to 0 at H15 and the GDs to 1100 as at SB16. Horizontal dashed lines are plotted in order to emphasize the difference between the GDs of Ar and N_2 .

Our procedure for evidencing multi-orbital contributions is the following. We measure the spectral phase of harmonics generated in Ar (ionization potential $I_p^{Ar}=15.7$ eV) and in N_2 ($I_p^{HOMO}=15.6$ eV) under the same experimental conditions. Argon provides a very useful reference for two reasons: first, the phase of its recombination dipole moment (RDM) (step iii) does not vary much

over our considered spectral range [31] so that the harmonic phase is determined by the continuum dynamics (step ii). The latter leads to a quadratic spectral phase and thus a linear GD in the plateau region corresponding to the recollision times of the electron trajectories [32], as shown in Fig. 1a). Second, the slope of the GD curves (atto-chirp) is inversely proportional to the driving laser intensity and provides a quite accurate estimate of the effective intensity in the generating medium [32, 33]. Fitting the data in Fig. 1a) and comparing to Strong-Field-Approximation (SFA) calculations [32, 34] gives intensities in the range: $0.7-1.3 \times 10^{14}$ W/cm². The same I_p and generation conditions ensure that the continuum dynamics for all harmonic orders is the same in Ar and N_2 provided that only the HOMO (channel X) contributes. In that case, their harmonic phase difference should contain only the phase of the HOMO RDM. It has been shown that the influence of the laser on the recombination step is negligible [23, 31]. Therefore, any distortion of the harmonic phase difference when varying the laser intensity I_L can be attributed unambiguously to lower-lying orbitals. This technique is very general and applies whatever the value of the relative phase between the different contributing channels.

We show in Fig. 1b) the GD measured in N_2 for a recollision angle of 90° (the generating beam polarization was orthogonal to that of the alignment beam). This angle is expected to maximize the contribution of the HOMO-1 (channel A, $I_p^{HOMO-1} \approx 17$ eV) due to its symmetry [12]. Yet, at low intensity ($I_L = 0.7 \times 10^{14}$ W/cm²), the measured GD is very linear in the plateau region, similar to the one measured in Ar. This translates into an almost constant phase difference in this region, as shown in Fig. 1c). Two conclusions can be drawn from this result: i) at this low intensity, the channel A contribution is negligible; ii) the phase of the HOMO RDM does not vary much over this spectral range, as predicted in [31]. Indeed, the shape resonance occurring around H17-21 affects the RDM mostly at small recollision angles and vanishes at larger angles around 90° . At higher intensities, increasingly distorted GD curves are obtained with values smaller than in Ar below SB26 and larger above. The resulting phase differences show an increasingly deep minimum at H27, peaking at $-\pi/2$ rad, and a fast rise at high orders. This behavior is a clear signature of a growing contribution from channel A. A striking fact is that, when calibrating the harmonic intensity spectra measured in N_2 by that measured in Ar, we find a broad minimum around H23-25 that *does not* depend on intensity. In previous work, this led to the conclusion that a single orbital contributes in this spectral region [17]. Our measurements show that phases are much more sensitive to multi-orbital dynamics than the harmonic intensity spectra.

To interpret the observed phase behavior and spectrally resolve the multichannel contributions to the mea-

sured data, we have developed a SFA-based model aimed at a qualitative interpretation. The radiative molecular dipole \vec{D}_{N_2} is expressed as a sum over the complex amplitudes for the uncoupled X and A channels. Each amplitude is a product of factors issued from the three-step model [31]. In the following, we study for each step the factors governing the relative amplitude of channels X and A.

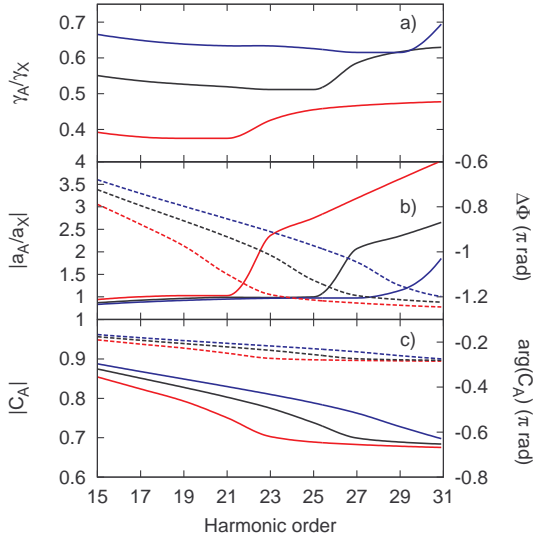


FIG. 2. Variation of the relative amplitudes of the X and A channels as a function of the harmonic order at different intensities: a) Square-root of tunneling rate ratio γ_A/γ_X at $\theta = 90^\circ$, b) Modulus (solid) and phase $\Delta\Phi$ (dash) of the continuum amplitude ratio a_A/a_X , c) Modulus (solid) and phase (dash) of the autocorrelation function C_A ; the corresponding axes are left and right for modulus and phases respectively. $I_L = 0.7$ (red), 1 (black) and 1.3 (blue) $\times 10^{14}$ W/cm 2 .

We show in Fig. 2a) the ratio of the square-root of the tunnel ionization rates $\gamma_{X,A}(\theta = 90^\circ, q)$, relative to step i). They are computed with a method recently developed by R. Murray *et al.* [35]. For each harmonic order q , we used the instantaneous field strength at the ionization time corresponding to the short trajectories. It turns out that the ratio of the ionization rates slowly varies with the order q but strongly depends on I_L : the higher the intensity, the larger the weight of the A channel.

In Fig. 2 b), the modulus and phase $\Delta\Phi(q) = \Phi_A(q) - \Phi_X(q)$ of the continuum amplitude ratio a_A/a_X are shown. These complex amplitudes account for both the spreading and the accumulated phase of the electron wave packet during its excursion in the continuum (step ii) in each ionizing channel. These quantities and all the requested timings are evaluated using “atomic” SFA calculations [34] with I_p ’s adjusted to the ones of the HOMO and HOMO-1 of N_2 . In analyses based on single channel descriptions [4, 24, 31], the continuum amplitude $a_X(q)$ is expected to disappear when calibrating the dipole by a

reference atom. However, in our multichannel formalism, calibration with Ar removes this amplitude only in the channel X, leaving a ratio $a_A/a_{Ar} \simeq a_A/a_X$ in the channel A. We found that the modulus of this ratio, close to unity for lower harmonics, displays a sudden jump at a definite order depending on I_L . These jumps occur between the different cutoff locations of the channels X and A, and strongly increase the weight of the latter. The relative phase $\Delta\Phi$ decreases almost linearly towards the channel A cutoff and then remains constant. This is reminiscent of the evolution with harmonic order of the short trajectory duration τ_q since $\Delta\Phi \approx \Delta I_p \tau_q$ [5]. This phase also characterizes the coherent superposition of the X and A states as it evolved until recombination time.

To model the recombination step iii) in molecules, one must in principle take into account both electronic and nuclear parts of the total molecular wavefunction [36, 37]. The latter is important when fast nuclear motion occurs during the electron excursion in the continuum. This is accounted for in a given channel by the autocorrelation function $C(q) = \langle \chi_+(\tau_q) | \chi_0 \rangle$, where $|\chi_0\rangle$ represents the fundamental vibrational state of N_2 and $|\chi_+(\tau_q)\rangle$ represents the nuclear wave packet as it evolved on the ionic energy surface during the electron excursion time τ_q [36]. While this is known to insignificantly affect HHG through channel X in N_2 ($C_X \approx 1$) [37], we found that its impact is far from negligible for channel A. The corresponding autocorrelation function $|C_A|$, displayed in Fig. 2 c) decreases significantly until the cutoff region where it remains constant; there, it lowers the contribution of channel A by a factor larger than 2 in intensity. Interestingly, $C_A(q)$ also introduces an additional phase close to -0.3π that slowly varies with the order q . Such a phase, not taken into account in previous studies, is large enough to significantly modify the interference between the two channels.

The electronic recombination is described by the RDMS $d_{X,A,Ar}$, calculated from field-free atomic or molecular orbitals given by GAMESS [38] and continuum plane waves (PW). We checked that the dipole ratios d_A/d_X evaluated with PWs or using accurate scattering waves [31] are remarkably close to each other for $\theta = 90^\circ$.

All these contributions can finally be gathered under an expression of the dipole \vec{D}_{N_2} calibrated by Ar and projected onto the θ direction

$$\begin{aligned} \frac{D_{N_2}(\theta)}{D_{Ar}} &= \frac{D_X(\theta)}{D_{Ar}} + \frac{D_A(\theta)}{D_{Ar}} = \frac{\gamma_X(\theta)}{\gamma_{Ar}} \frac{d_X(\theta)}{d_{Ar}} C_X \\ &+ \frac{\gamma_A(\theta)}{\gamma_{Ar}} \left| \frac{a_A}{a_X} \right| \exp[i\Delta\Phi] \frac{d_A(\theta)}{d_{Ar}} C_A. \end{aligned} \quad (1)$$

Note that all factors are q - and I_L -dependent except $d_{X,A,Ar}$, that depend on q only.

The total amplitude ratio $|D_A/D_X|$, shown in Fig. 3 a) for $\theta=90^\circ$, exhibits a transition from a main channel X contribution at low harmonic orders to a dominant

channel A at high orders. The observed jumps are clear imprints of the continuum amplitude ratio (cf. Fig. 2 b). Inclusion of the autocorrelation functions decreases the A contribution as expected from the above analysis.

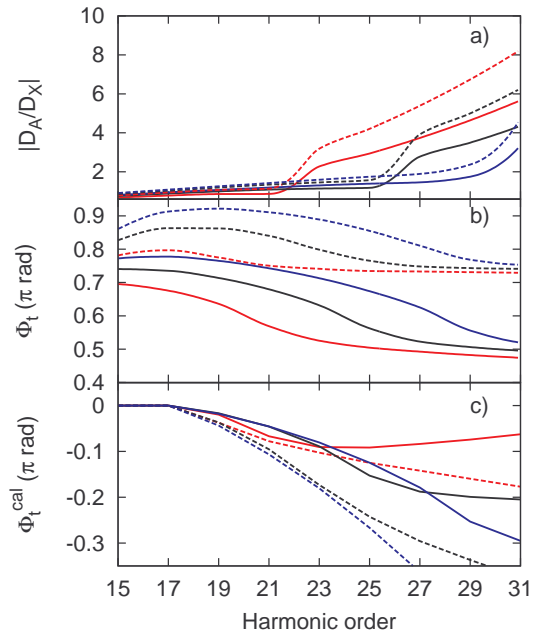


FIG. 3. Variation with harmonic order at $\theta=90^\circ$ for different intensities of: a) $|D_A/D_X|$, b) $\Phi_t = \arg(D_{N_2}/D_{Ar})$, c) Φ_t^{cal} , *i.e.* Φ_t calibrated. Simulations are performed with (solid) and without (dash) autocorrelation functions; same color keys as in Fig. 2.

Fig. 3 b) shows the phase evolution of the normalized D_{N_2} dipole, Φ_t . At low orders, it converges to the phase of D_X , mainly given by the phase of the HOMO RDM d_X . At high orders, it is governed by the phase of D_A and thus by the phase of the HOMO-1 RDM d_A , the continuum phase $\Delta\Phi$ and the phase of C_A that shifts all curves by $\approx -\pi/4$. At intermediate orders, the relative amplitude of the two channels determines the phase transition between the two regimes. The intensity dependence of Φ_t comes directly from that of the continuum phase $\Delta\Phi$, dampened by the amplitude factors. In order to compare to the experimental trend shown in Fig. 1 c), we calibrated both the phases at H15 and the GDs at SB16, according to the experimental procedure. A qualitative agreement of Φ_t^{cal} with experimental results is found, with an increasingly faster decrease of the phase with intensity. The phase increase measured at high orders is retrieved when taking into account the autocorrelation functions that significantly modify the general trend. We checked that averaging over the experimental angular distribution leads to the same conclusions. Finally, other factors not included in our theory could also lead to spectral phase distortions, like couplings be-

tween different ionization channels [15]. This emphasizes the need for a thorough characterization of the harmonic signal in order to identify and separate the nuclear and electronic ultrafast dynamics.

In conclusion, we found that the relative contributions of different ionization channels to HHG can be controlled through a fine tuning of the laser intensity. More precisely in N_2 , we attribute the non-trivial HHG phase behavior over the spectral range to variations of the X- and A-channel relative amplitudes and phases. This opens manifold perspectives. First, this should benefit to the selection of single channels in order to better resolve structural and dynamical effects in HHG. Second, a control over the weight of ionization channels should provide insight into the electron dynamics taking place during tunnel ionization. Third, the uncovered channel-dependent nuclear dynamics opens the possibility of interferometric measurement of the phase of the autocorrelation function, that could be explored over longer timescales using long trajectories or mid-IR laser fields. This also extends the field of HHG-based ultra-fast measurements to the study of correlated vibronic motion possibly launched by non-Frank-Condon transitions.

We thank R. Murray and P. Breger for their help in the simulations and the experiments, respectively. We acknowledge financial support from the EU-FP7-ATTOFEL and ANR-09-BLAN-0031-01.

* Present address: Photonics Institute, Vienna University of Technology, Gusshausstraße 27/387, 1040, Vienna, Austria

† pascal.salieres@cea.fr

- [1] P. B. Corkum, Phys. Rev. Lett. 71, 1994 (1993).
- [2] K. J. Schafer et al., Phys. Rev. Lett. 70, 1599 (1993).
- [3] F. Krausz et al., Rev. Mod. Phys. 81, 163 (2009).
- [4] J. Itatani et al., Nature 432, 867 (2004).
- [5] S. Haessler et al., Nature Physics 6, 200 (2010).
- [6] C. Vozzi, et al., Nature Physics, doi:10.1038/nphys2029 (2011).
- [7] D. Shafir et al., Nature Physics 5, 412 (2009).
- [8] S. Baker et al., Science 312, 424 (2006).
- [9] S. Haessler et al., J. Phys. B 42, 134002 (2009).
- [10] W. Li, et al., Science 322, 1207 (2008).
- [11] H. J. Wörner et al., Nature 466, 604 (2010).
- [12] B. K. McFarland et al., Science 322, 1232 (2008).
- [13] O. Smirnova et al., Nature 460, 972 (2009).
- [14] O. Smirnova et al., PNAS 106, 16556 (2009).
- [15] Y. Mairesse et al., Phys. Rev. Lett. 104, 213601 (2010).
- [16] A.-T. Le et al., J. Phys. B 42 (2009).
- [17] H. J. Wörner et al., Phys. Rev. Lett. 104, 233904 (2010).
- [18] R. Torres et al., Phys. Rev. A 81, 051802 (2010).
- [19] T. Kanai et al., Nature 435, 470 (2005).
- [20] C. Vozzi et al., Phys. Rev. Lett. 95, 153902 (2005).
- [21] B. A. Sickmiller et al., Phys. Rev. A 80, 031802 (2009).
- [22] M. Lein et al., Phys. Rev. Lett. 88, 183903 (2002).
- [23] E. van der Zwan et al., Phys. Rev. A 82, 033405 (2010).
- [24] W. Boutu et al., Nature Physics 4, 545 (2008).

- [25] X. Zhou et al., *Phys. Rev. Lett.* 102, 073902 (2009).
- [26] A.-T. Le et al., *Phys. Rev. A* 82, 023814 (2010).
- [27] F. Rosca-Pruna et al., *Phys. Rev. Lett.* 87, 153902 (2001).
- [28] M. Gaarde et al., *Phys. Rev. A* 59, 1367 (1999).
- [29] P. Salières et al., *Science* 292, 902 (2001).
- [30] P. M. Paul et al., *Science* 292, 1689 (2001).
- [31] A.-T. Le et al., *Phys. Rev. A* 80, 013401 (2009).
- [32] Y. Mairesse et al., *Science* 302, 1540 (2003).
- [33] V. Varjú et al., *Phys. Rev. Lett.* 95, 243901 (2005).
- [34] M. Lewenstein et al., *Phys. Rev. A* 49, 2117 (1994) G. Sansone et al., *Phys. Rev. A* 70, 013411 (2004).
- [35] R. Murray et al., *Phys. Rev. Lett.* 106, 173001 (2011).
- [36] M. Lein, *Phys. Rev. Lett.* 94, 053004 (2005).
- [37] S. Patchkovskii, *Phys. Rev. Lett.* 102, 253602 (2009).
- [38] M. Schmidt et al., *J. Comput. Chem.* 14, 1347 (1993).

3.4 Effect of the Molecular Distribution

When aligning a molecular ensemble, one does not align all the molecules in one single direction (as they were treated until now), but creates a distribution of alignment (see section 2.1.1). If any structural or dynamical information encoded in the XUV emission is angle dependent, there is a great chance to wash it out by having low quality molecular alignment. Therefore, it is very important to achieve high degree of alignment, in order to decrease the size of the distribution cone ($\alpha/2$), defined by the angle between the molecules most extremely aligned and the polarization of the aligning beam. In our case $\alpha \approx 30^\circ$. From the results presented in PAPER I, we may see that considerable amplitude and phase change may occur over 30° distribution. Despite this fact, a lot of studies concentrated on the amplitude change and neglected the phases (Torres et al. [157]).

In principle, molecular orbital tomography requires decomposing the macroscopic response from the distribution of the molecules in order to get the single molecule response (SMR). In this section, macroscopic response refers to the averaging over the molecular alignment and not on the averaging due to propagation effects. To that aim the "absolute" harmonic phase has to be measured, both as a function of harmonic order and alignment angle. Then, eq. 2.8 can be written in a matrix form (note that only parallel components are treated):

$$E_{\text{XUV}}^{\parallel}(q, \theta) = \mathbf{D}(\theta, \vartheta) e^{\text{SMR}}(q, \theta), \quad (3.24)$$

where $\mathbf{D}(\theta, \vartheta)$ is a real valued matrix corresponding to the matrix of the probability of finding a molecule aligned to θ if the molecular ensemble is in ϑ distribution. $E_{\text{XUV}}^{\parallel}(q, \theta)$ and $e^{\text{SMR}}(q, \theta)$ are the macroscopic and single molecule responses, respectively. The SMR is obtained by inverting $\mathbf{D}(\theta, \vartheta)$, if it is possible. $\mathbf{D}(\theta, \vartheta)$ is calculated theoretically.

However, up to now, no one could perform the full characterization of the harmonic phase. So, researchers concentrated on investigating eq. 3.24 for each harmonic order separately from the measurement of the angular dependence of the macroscopic response. Different approaches were used. The article of (Wagner et al. [173]) belongs to the rare studies where spectral intensity and phase measurements resolved in angle were performed using the gas mixing technique of Kr and CO₂. Their method relies on measuring the macroscopic signal in aligned molecules and expressing the SMR as a sum of Legendre-polynomials, as it was presented by (Faisal et al. [28]): $e^{\text{SMR}}(q, I_L, \theta) = c_0 + c_1 \cos^2 \theta + c_2 \sin^2 2\theta$. By applying a least square fitting procedure, they could find back the complex coefficients c_i and thus retrieve the angular dependence of the amplitude and phase of the SMR for each harmonics order. A recent study by (Yoshii et al. [180]) applies more or less the same technique, but without phase measurements. Despite this deficiency, they claim to be able to deconvolve the SMR of N₂ by assuming that its phase changes slowly with the angle. We think, based on our simulations, that this approximation is not true in general, except if one can achieve extremely good alignment. (Vozzi et al. [172]) overcome the problem of the angular phase measurement by applying a phase retrieval algorithm to find both the angular phase of the macroscopic signal and the complex valued SMR. They applied their technique on CO₂ with success. However, the phase retrieval procedure recovers the harmonic phase variation with angle, but gives no link between two harmonics. They imposed an a priori link between the phases of consecutive harmonic orders at one particular alignment distribution, based on theoretical calculations and on earlier experimental results. They could perform molecular orbital tomography as well, from the retrieved SMR.

By using RABBIT technique in N₂ we showed that the spectral phase changes considerably in different alignment distributions. But as mentioned earlier, RABBIT cannot relate different alignment measurements. So we normalize the phases at harmonics 15 and rotate them at harmonic 17. These assumptions introduce a twist in the analysis and may be the

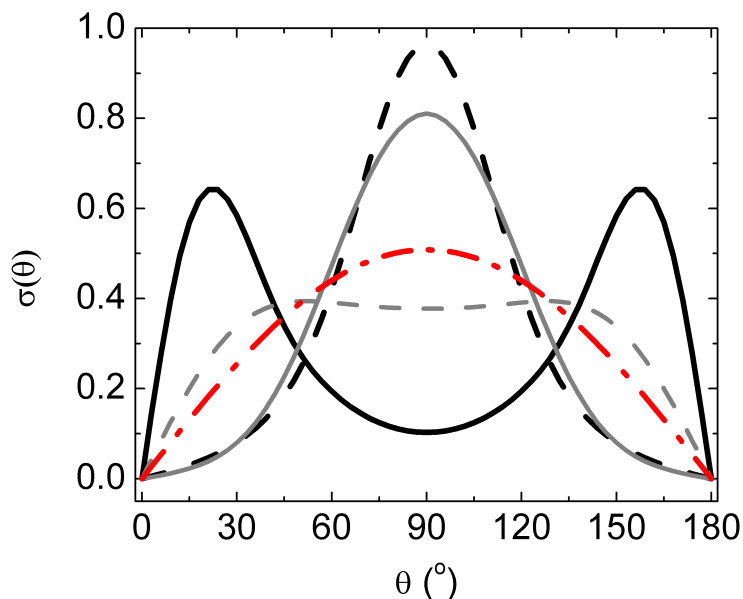


Figure 3.7: The probability of finding a molecule aligned at θ having alignment distributions at half-revival parallel (black full line), perpendicular (black dashed line) to the driving laser; at anti-revival parallel (gray full line) and perpendicular (gray dashed line) to the driving laser; and without alignment, isotropic distribution (red dashed dot line). The parameters for this set of alignment distributions are described in section 2.1.1.

reason why we did not succeed to decompose the SMR. Instead, we applied the developed models to evaluate how the angular distribution affects the multi-orbital contributions.

3.4.1 Experimental results

In our experiments we studied 5 different alignment distributions (see figure 3.7), obtained by setting the delay between the aligning and the generating laser pulse to: $\Delta t = 4.235$ ps corresponding to the half-revival (HR), aligned parallel (HR@ 0°) and perpendicular (HR@ 90°) to the driving field; $\Delta t = 4.425$ ps corresponding to the anti-revival (AR), aligned parallel (AR@ 0°) and perpendicular (AR@ 90°) to the driving field and finally we omitted the aligning beam to obtain isotropic distribution of molecules. Interestingly, HR@ 0° peaks around $\theta \approx 20^\circ$, meaning that the molecular characteristics at this angle will be most pronounced in the macroscopic response. Furthermore, HR@ 90° and AR@ 0° are almost identical, although the former peaks higher giving better conditions to study molecules aligned perpendicular to the driving laser field. AR@ 90° and the isotropic distributions are also quite similar. Similar distributions are expected to result in similar macroscopic harmonic response.

The HHG setup, the used techniques and the experimental conditions are exactly the same as in the earlier studies, except for the intensity of the generating laser. It is held constant at $I_L = 1.2 \times 10^{14}$ W/cm². In this study, it is still assumed that the XUV emission is only polarized parallel to the driving laser. Figures 3.8 a and b present the calibrated harmonic intensity and phase, respectively. On one hand, the famous spectral minimum in N₂ is present in each alignment distribution even in the isotropic case. This shows that one has to be careful when using the non-aligned molecular ensemble as a reference and calibrate other measurements with it. (Torres et al. [158]) calibrated the measured harmonic intensities at the half-revival of N₂ with the signal of the non-aligned molecular ensemble, that already contained a huge minimum at 39 eV. Of course, the minimum disappeared after the

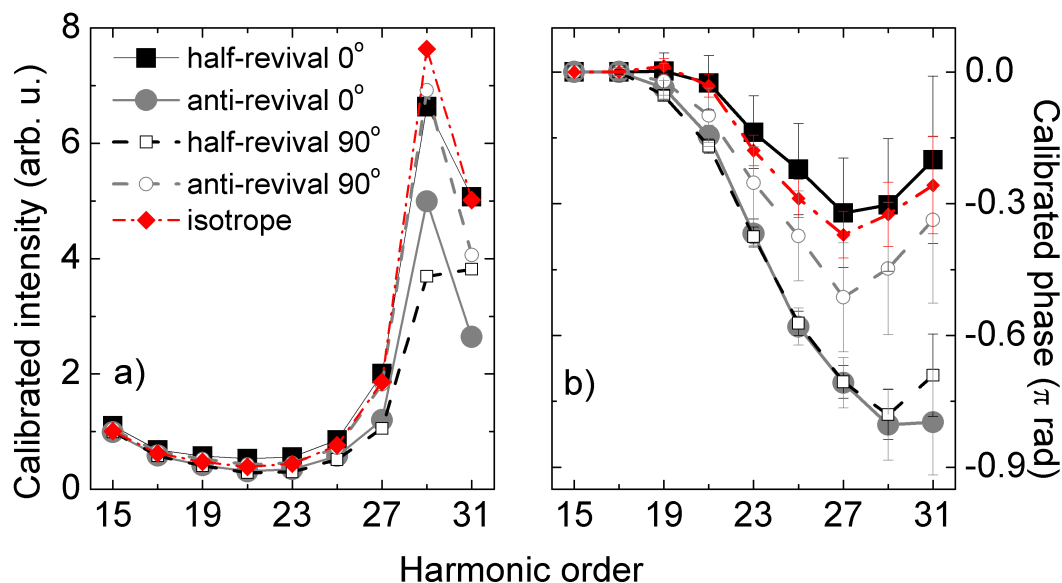


Figure 3.8: Measured harmonic intensity (a) and phase (b) of N_2 after calibration with Ar.

calibration. On the other hand, the calibrated spectral phase shows similar characteristics as it was already presented in PAPER I and II. In figure 3.8 b, HR@ 0° and HR@ 90° show the different depth minimum at harmonic 27, while AR@ 0° is almost identical to the latter, as expected. Also AR@ 90° is considerably different from HR@ 0° . However, the calibrated phase obtained from the isotropic distribution is closer to HR@ 0° than to AR@ 90° . We guess that this is rather due to subtle changes in the generating conditions and it should be rather closer to AR@ 90° . Nevertheless, these results tell us to be careful on how to interpret the signal coming from a non aligned molecular ensemble. All the presented calibrated phases are in agreement with our earlier discussions on multi-orbital contributions concerning the alignment dependent phase decrease and re-increase. Even the isotropic alignment cannot wash out the signs of it. Therefore, experiments like the two source technique, that uses non aligned molecules as the reference (Lock et al. [95], Smirnova et al. [147], Zhou et al. [183]), are exposed to a calibration with a not structureless signal. This does not question the measurement of the angular dependence of the harmonic phase but it prevents from getting absolute values of course. In such type of experiments it is impossible to use a structureless noble gas atom as an absolute reference.

3.4.2 Simple model

To show our reasoning explicitly, we construct a very simple model that imitates the multi orbital behavior in N_2 . We assume that the SMR behaves as it is presented in figures 3.9 a and b representing the intensity and the phase, respectively. We assumed that the largest harmonic signal is emitted when the molecule is parallel to the driving laser ($\theta = 0^\circ$) and the smallest (3 times smaller) when it is perpendicularly aligned ($\theta = 90^\circ$). We assume also that the amplitude of the SMR is constant with the harmonic order for a given alignment angle. The phase of the SMR is constructed in order to reflect the slowly evolving $\pi/2$ phase jump from $\theta = 0^\circ$ to $\theta = 90^\circ$ around harmonic 25. This would correspond to the effect of the multi-orbital contributions.

Figure 3.10 is the macroscopic response of the constructed model, obtained by using eq. 2.8. The model shows that a drop in the macroscopic intensity is expected to occur due to the angle varying phase above harmonic 23. Both the intensity and phase results are

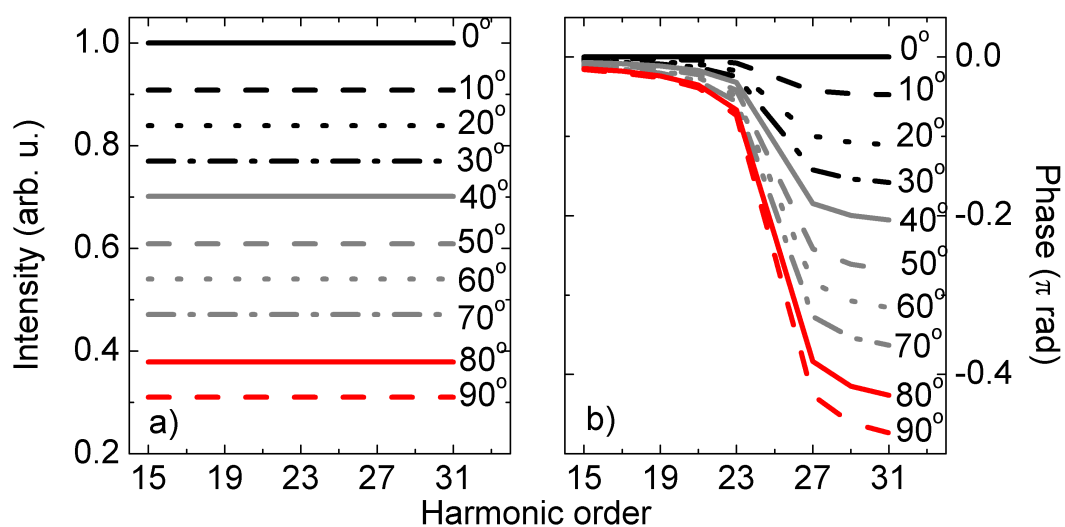


Figure 3.9: Intensity (a) and phase (b) of the single molecule response as a function of harmonic order. The numbers on the side represent the alignment angle of the molecule with respect to the generating laser.

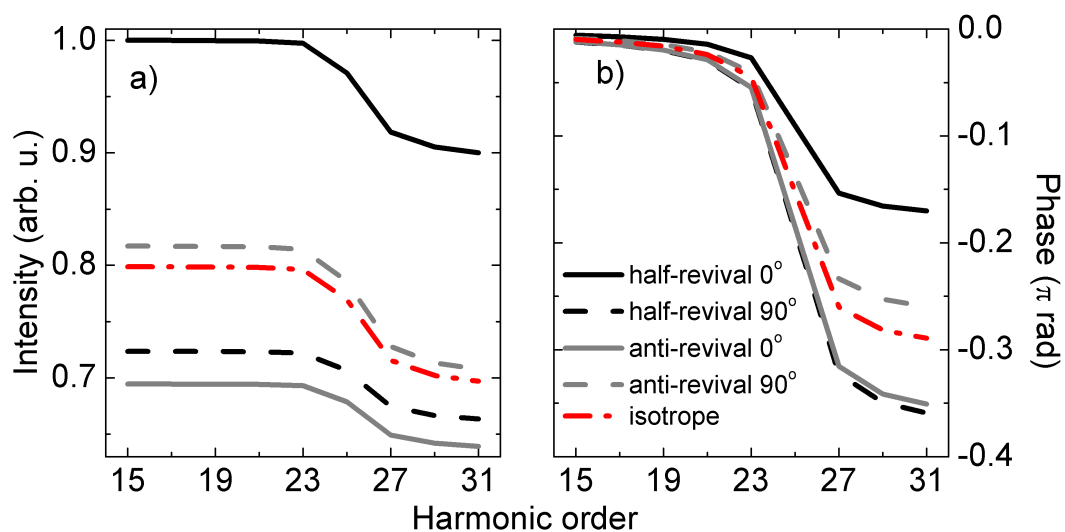


Figure 3.10: Intensity (a) and phase (b) of the macroscopic response as a function of harmonic order, after averaging the SMR over the angular distributions.

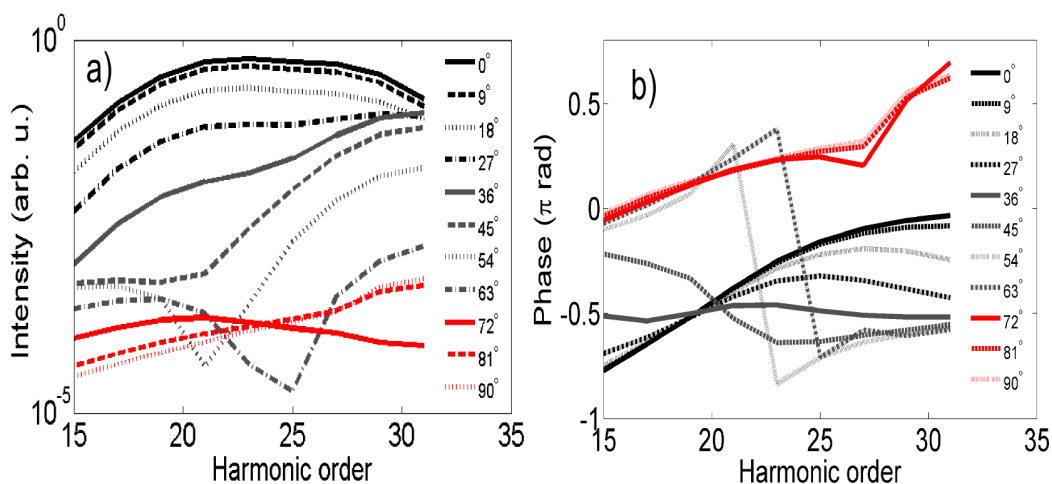


Figure 3.11: Intensity (a) and phase (b) of the single molecule response constructed with equation 3.23, as a function of harmonic order. The scale of the vertical axis in a) is logarithmic.

in good agreement with our conclusions deduced from the analysis of the angular distributions. Except for the phase at isotropic distribution, the other phase curves are in good agreement with our measurements. The results are emphasizing the importance of choosing the right reference target, since it can easily affect the final conclusions. Therefore, Ar is a better choice than unaligned N_2 , despite the small difference in geometry and ionization potential, because Ar's harmonic signal is structureless. There is the presence of a Cooper-minimum in the Ar spectra, (Higuete et al. [48]) but it is just outside our experimental spectral range, at around 52 eV.

3.4.3 QRS like model

In section 3.3 we developed an HHG model, where we relied on the plane wave RDMs. Soon after that study, we established a collaboration with Robert Lucchese who provided us with single photon ionization matrix elements including the exact continuum electronic states, shown in figures 1.8 and 1.9. Substituting them into eq. 3.23 and including all the findings on multichannel tunnel ionization, continuum and nuclear dynamics, one ends up with the SMR given in figure 3.11. The results are not as easy to interpret as in the PW case. Based on calculations not presented here, the fingerprints of HOMO are dominating both the intensity and phase, especially at angles $\theta < 60^\circ$. The π phase jump (and the corresponding minimum in the SMR) at $\theta \approx 60^\circ$ for harmonic 25 comes from the phase of the HOMO dipole. At larger angles, the tunnel ionization rate of HOMO-1 slowly becomes comparable to the HOMO one and starts to influence the SMR. The additional autocorrelation function in the A channel is important also at larger angles and especially for high energy harmonics. It tends to decrease the influence of HOMO-1 at these harmonics. In total, the influence of the A channel is only visible at larger angles and in the middle of the harmonic spectral range.

Figure 3.12 presents the macroscopic intensity (a) and phase (b) after averaging over the molecular distributions. The presented intensities are quite different from the ones we measured except at HR@ 90° . Interestingly a small minimum appears around harmonic 25 at the distribution HR@ 90° . The minimum in the dipole clearly survived the averaging. When comparing the calculated and measured phases one finds the same general trend of a decrease at high harmonics, but the order of the curves is wrong. For the distribution

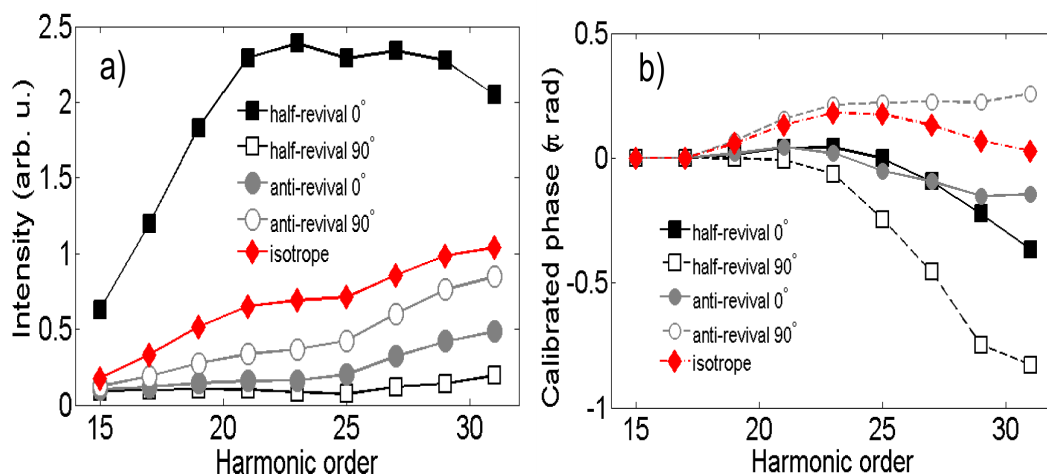


Figure 3.12: Intensity (a) and phase (b) of the macroscopic response as the function of harmonic order, after averaging the SMR over the angular distributions.

HR@90°, the phase drops qualitatively as in the experiments and the small rupture between harmonic 27 and 31 is coming from the presence of the A channel, involving the nuclear dynamics (relying on the same simulations performed using only (i) HOMO and (ii) both orbitals without nuclear dynamics). To our opinion, the disagreement between these phase simulations and the experimental results are originating from the shape resonance in the HOMO single photon ionization dipole matrix elements. At small θ angles and H17-21 orders the shape resonance "captures" the recombining electrons for more than a half laser cycle. Hence, it should be strongly affected by the attosecond filtering of the HHF process. Since these low harmonic orders are used for the normalization and rotation of the phase, this influence on the general behavior of the phase curves is dramatic.

In conclusion, our simulations show that there are characteristic features of the dipole that are surviving the averaging over the angular distribution, if the degree of alignment is high enough. This suggests that both molecular orbital tomography and multi-channel dynamics studies are possible using the macroscopic signal.

3.5 Study of the harmonic polarization

Complete characterization of the harmonic emission requires polarization studies. In the recent few years, several polarization experiments were performed, mainly based on the idea introduced by (Levesque et al. [92]), presented in section 2.2.3. Interestingly, they found that by generating harmonics in aligned molecules (N_2 , CO_2 and O_2) using linearly polarized driving laser, the harmonics' electric field may present an orthogonal component to the laser polarization. They did not observe elliptically polarized harmonics, but they found connection between the symmetry of the active molecular orbital and the polarization state of the harmonics. (Hijano et al. [50]) simulated these findings and explained them with both PWA and numerical 2D TDSE calculations. Meanwhile, (Lee et al. [85]) worked out a new technique, based on the two source interferometry, to measure the offset angle of the emitted harmonics when they are linearly polarized. By claiming better alignment conditions ($\langle \cos^2 \theta \rangle \approx 0.65$), (Zhou et al. [184]) measured elliptically polarized harmonics, from aligned ensemble of N_2 molecules and (Le et al. [80]) simulated these results with a single orbital treatment using exact photoionization dipole moments for HOMO. (Mairesse et al. [101]) observed harmonic ellipticity in N_2 that slightly changes with the intensity of the driving

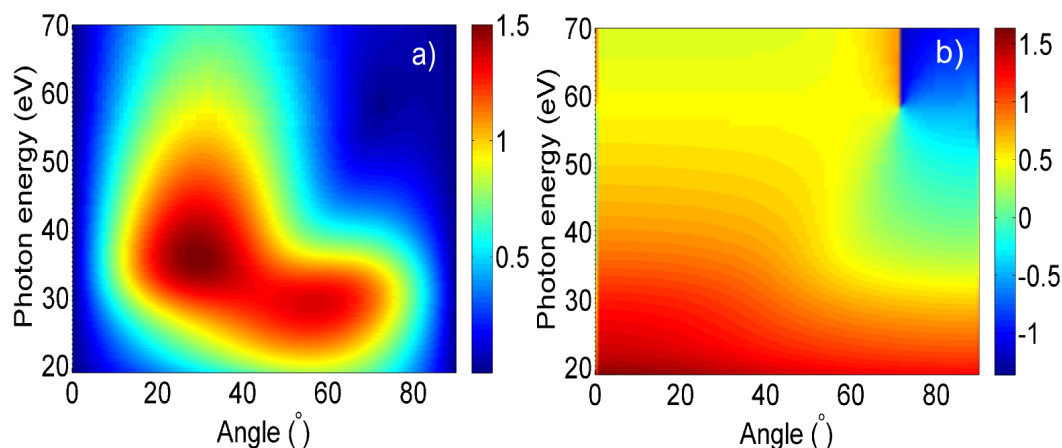


Figure 3.13: Amplitude (in a.u.) (a) and phase (in π rad) (b) of the perpendicular component of the scattering-wave HOMO photoionization dipole moment in the LF calculated in the length form. The angle is defined between the molecular axis and the polarization of the driving laser. The color code is not the same as for the parallel component of the dipole in figure 1.8.

laser for the first time. Their simulations included scattering-wave dipoles, HOMO and HOMO-1 contributions and the coupling between the two channels.

In the followings we compare the ellipticities obtained by different models concentrating on the influence of multi-orbital contributions. We investigate what kind of additional information could be retrieved from the ellipticity and offset angle measurements, with respect to the structure and dynamics already accessible from the measurement of one harmonic field component. In the end, using purely experimental characterization of the harmonics' intensity, phase and polarization, we perform the first Vectorial Orbital Tomography (VOT) along the axis of the molecule and perpendicular to it.

3.5.1 Origin of ellipticity and offset angle

HHG with linearly polarized driving laser does not result in elliptically polarized XUV light in isotropically distributed gas phase atoms and molecules, due to symmetry considerations. The generation of elliptically polarized harmonics requires aligned molecular distributions not having cylindrical symmetry with respect to the polarization of the generating laser. These are purely macroscopic requirements.

On the single molecule level, for orbitals with spherical symmetry, elliptically polarized harmonics cannot be produced. Orbitals with non-spherical symmetry can in principle generate elliptically polarized light. The tunnel ionization and the continuum acceleration of the EWP do not contribute to the ellipticity, since their direction is determined by the polarization of the driving laser (van der Zwan and Lein [165]). The recombination dipole moment may have components both along the molecular axis and orthogonal to it, but to have elliptically polarized harmonics, the two components have to be shifted in phase. The orthogonal components of plane wave dipoles are not shifted in phase (Levesque et al. [92]), while the exact RDMs may be so (Le et al. [80]). Using a modified SFA model, (Etches et al. [27]) showed that plane wave treatment still can produce elliptically polarized light, if the electron is ionized from one of the atomic centers and recombines to the other, although it results in very small ellipticities, $\epsilon < 0.03$. Including multi-orbital contributions to the PWA can be another source of harmonic ellipticity. In this study we will investigate the effect of exact RDMs.

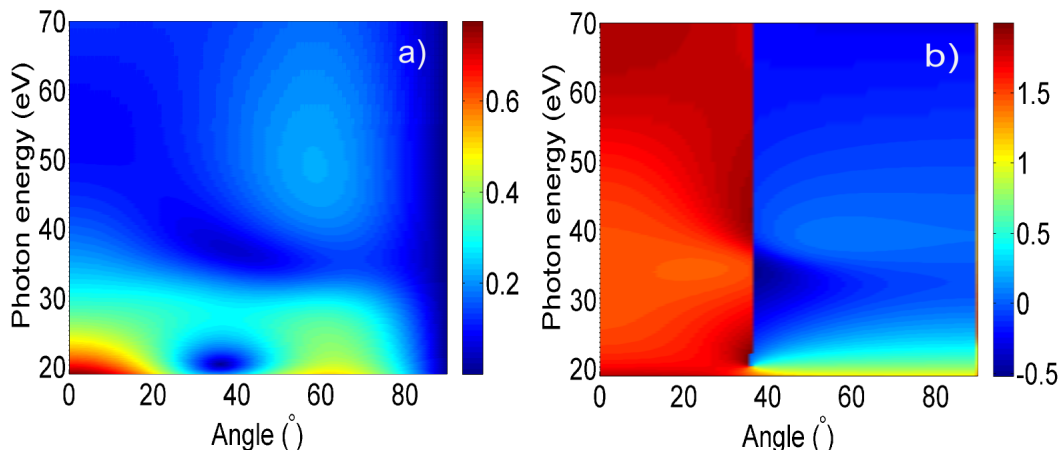


Figure 3.14: Amplitude (in a.u.) (a) and phase (in π rad) (b) of the perpendicular component of the scattering-wave HOMO-1 photoionization dipole moment in the LF calculated in the length form. The angle is defined between the molecular axis and the polarization of the driving laser.

Figure 3.13 shows $d_{\perp}^{\hat{r},L}(q, \theta)$, the perpendicular component (with respect to the polarization of the driving laser, in the LF calculated in the length form) of the HOMO dipole. The amplitude of this component reaches its maximum at $20^{\circ} < \theta < 60^{\circ}$ and in this region the phase is shifted with respect to $d_{\parallel}^{\hat{r},L}(q, \theta)$, the parallel component, see figure 1.9. Therefore we are expecting high ellipticity values in this region. The perpendicular component of HOMO-1 is presented in figure 3.14 and it is visible that its amplitude is about twice smaller than the one of HOMO, suggesting small influence on the ellipticity.

We will construct two models to compare the influence of single and multi-orbital contributions to the ellipticity and offset angle. From now on, we do not denote the form of the dipole because it will be described exclusively in the length form. In the first model, (i) the SMR in the LF, $\epsilon_{\parallel, \perp}^L(q, \theta)$, is described by the HOMO orbital contribution alone while in the second model (ii) HOMO and HOMO-1 are both contributing with the autocorrelation function involved. The parallel component, still in the LF, of the macroscopic signal $E_{\parallel}^L(q, \vartheta)$ of a molecular distribution ϑ , is given by eq. 2.8, while the perpendicular component $E_{\perp}^L(q, \vartheta)$ is calculated with eq. 2.9. The experimental ellipticity and the offset angle are given in the HHF, see figure 2.12, therefore all the calculated components are expressed in that frame.

Figure 3.15 a presents the harmonic ellipticities measured as explained in section 2.2.3. We obtained quite high values $\epsilon \approx 0.4$, for $\vartheta \sim 40^{\circ}$ - 70° and harmonic orders above 21. (Zhou et al. [184]) and (Mairesse et al. [101]) report similar values of ellipticity. Their origin is still not well understood. Using only the RDM of HOMO to simulate the harmonic signal (Le et al. [80]) obtained $\epsilon \approx 0.4$, while (Mairesse et al. [101]) got $\epsilon \approx 0.7$. The latter propose to include X and A channels plus a coupling between the two channels, since the energy difference between the channels approximately corresponds to one IR photon energy. Doing so, they are able to obtain $\epsilon \approx 0.4$ in the region of interest. Our calculations using only HOMO are presented in figure 3.15 b and they are rather similar to the results of (Mairesse et al. [101]). The simulated ellipticity is almost the double of the measured one, meaning that in the experiments there is something that decreases the influence of the HOMO orbital.

Figure 3.16 a shows the measured offset angle. There are two well separated regions indicating that above the harmonic order 21 the polarization ellipse of the harmonics is tilted on the left side with respect to the polarization of the driving laser field (the main

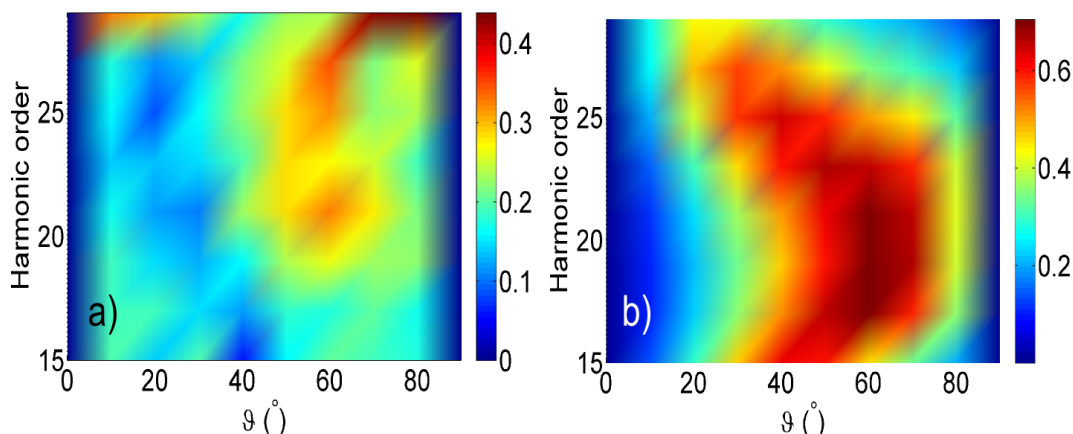


Figure 3.15: Measured (a) and simulated (b) ellipticity. Only HOMO contribution was used for the simulation. The color codes are not the same.

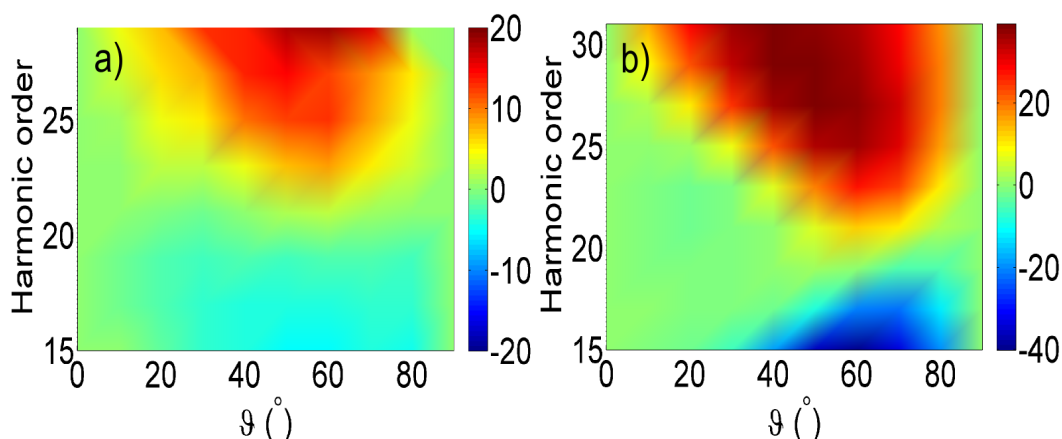


Figure 3.16: Measured (a) and simulated (b) offset angle in units of degrees. Only HOMO contribution was used for the simulation. The color codes are not the same.

axis is getting closer to the molecular axis), while below harmonic 21 they are tilted to the right side. This observation fits well the results presented in (Levesque et al. [92], Zhou et al. [184]), although there are slight differences in the maximum values. According to (Ramakrishna et al. [126]) this is due to different alignment conditions in the experiments and indeed, having low quality alignment, the offset angle is smaller than in the case of good quality alignment. However, our simulations in figure 3.16b show two times larger offset angles than measured which cannot be simply explained by the quality of alignment. This supports our previous conclusion that in our experimental conditions, HOMO is not enough to explain both the ellipticity and the low offset angle.

For that reason, we include the A channel into our simulations as described by the equation 3.23. We do not discuss the effect of channel coupling because we have not yet developed the technique to simulate it. In figure 3.17 a we present the comparison of calculated ellipticities taking into account single (full line) and multiple (dashed line) orbital contributions for three different harmonic orders. Figure 3.17 b shows the same comparison for the offset angle. The results do not show large differences between the two simulations. As expected the HOMO-1 contribution influences the results for $\vartheta > 50^\circ$. More surprisingly, its influence for H27 is small in contrast to the phase measurements and simulations reported in the preceding sections. These results confirm our suspicion that either the tunnel ion-

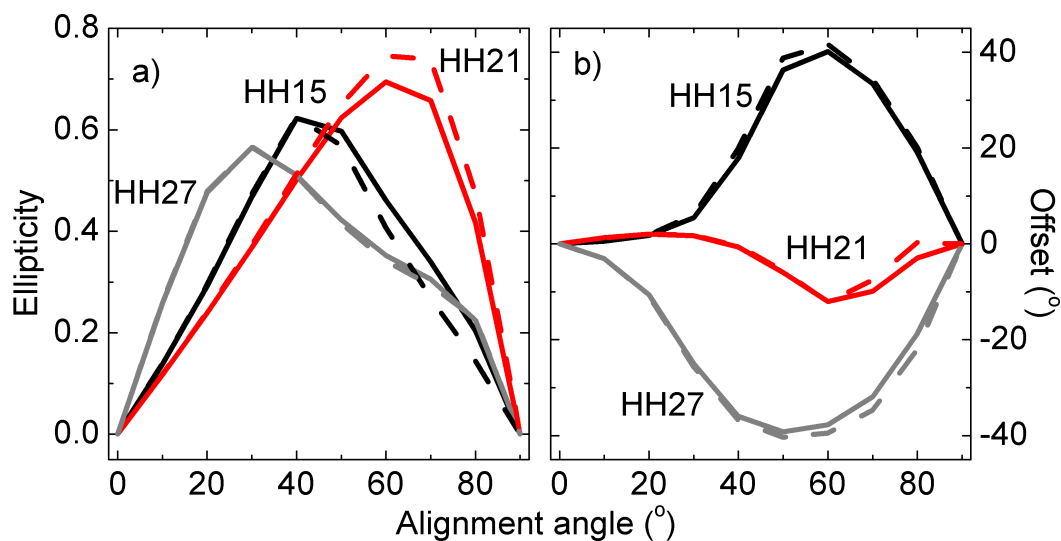


Figure 3.17: Comparison of ellipticities (a) and offset angles (b) as a function of alignment angle, calculated with only HOMO orbital contribution (full line) and with multi orbital contributions including nuclear dynamics (dashed line). Harmonic 15 corresponds to the black color, 21 to the red and 27 to the gray.

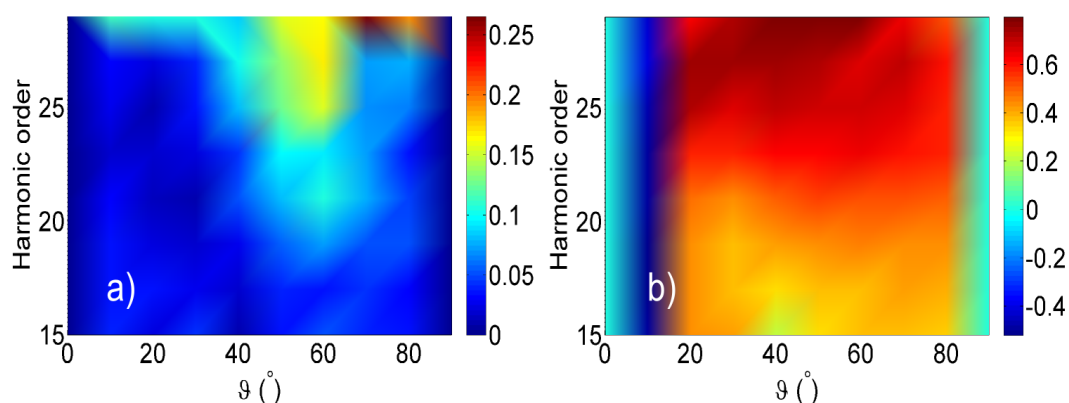


Figure 3.18: Experimentally retrieved ratio of intensities $|\mathbf{E}_{\perp}^L/\mathbf{E}_{\parallel}^L|$ (a) and phase difference (in units of π rad) between the components $\delta^L = \varphi_{\perp}^L - \varphi_{\parallel}^L$ as a function of alignment angle.

ization rates are underestimated for the HOMO-1 or there is still an additional effect (like coupling between the channels) that has to be taken into account.

As defined by the equations 2.24 and 2.25, the measured ellipticity and offset angle relate the parallel and perpendicular components in the LF. Figures 3.18 a and b show the intensity ratio and the phase difference between the perpendicular and parallel components, respectively. The intensity ratio clearly reflects the characteristics of both ellipticity and offset angle. It shows that the perpendicular component remains much smaller than the parallel one. The phase difference reflects a passage through $\pi/2$ at harmonic 21 exactly where the offset angle changes sign.

These quantities will be used to retrieve the perpendicular component of the harmonics in intensity and phase from the measurement of these two parameters for the parallel component. We remark already that the harmonic ellipticity and the δ^L phase shift indicate that the parallel and the perpendicular components in the LF are not in phase. This could be a problem for molecular orbital tomography since it assumes plane wave dipoles, for which

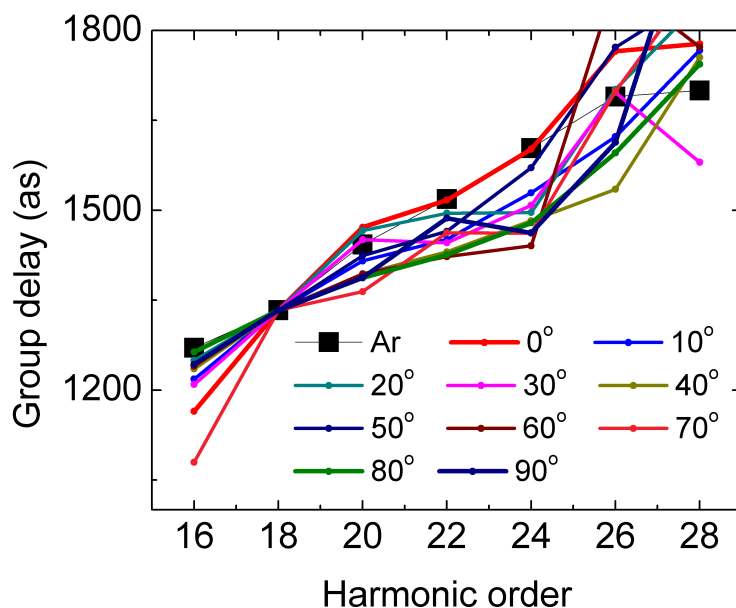


Figure 3.19: Measured group delays of harmonics generated from Ar (black square) and N_2 (see the color code). All the curves are shifted vertically in order to make SB18 overlap for each curve at $GD_{q=18}(Ar)$.

the two components are intrinsically in phase.

3.5.2 Spectral amplitudes and phases measured for the parallel component

After performing the characterization of the harmonics' polarization, we perform RABBIT type phase characterization at the maximum point of the Malus oscillations that corresponds to the parallel component of the harmonics in the LF. Due to the polarizer inserted in the harmonic line the harmonic signal is severely decreased, therefore the side band oscillation of the RABBIT measurement becomes extremely difficult to detect. In principle, one could perform the same measurement at the minimum of the Malus oscillation, targeting the perpendicular component of the harmonic field, but the signal was not large enough to perform a complete tomography scan from $\vartheta = 0^\circ, \dots, 90^\circ$ in these conditions.

In figure 3.19 we present the measured group delays for Ar (black square) and for the first quadrant of the Fourier space for N_2 in the same experimental conditions. After comparing the GD curve of Ar with other Ar GD curves in approximately the same experimental conditions, we found out that the GD at SB16 is at least 50 as larger than it is normally. Therefore, for the sake of presentation we normalized all curves at the GD of SB18 in Ar, instead of doing it for SB16. It is clearly visible that except for the GD curve of N_2 aligned at 0° , all other curves are below the curve of Ar in the plateau region, with a minimum value around SB24. This confirms that we are approximately in the same conditions as in PAPER I. We then apply our calibration method developed in PAPER I to the measured intensities and phases.

The result of the calibration procedure is presented in figure 3.20. On one hand, the calibrated intensity (a) still contains the so far mysterious minimum around HH23,25. On the other hand, the calibrated phase (b) at low harmonic orders is slightly shifted towards positive values. This is due to the slightly wrongly positioned argon GD at SB16 and to our calibration process. However, all the calibrated phases are affected similarly by this fact, the negative and positive phase jumps presented in PAPER I are recognizable.

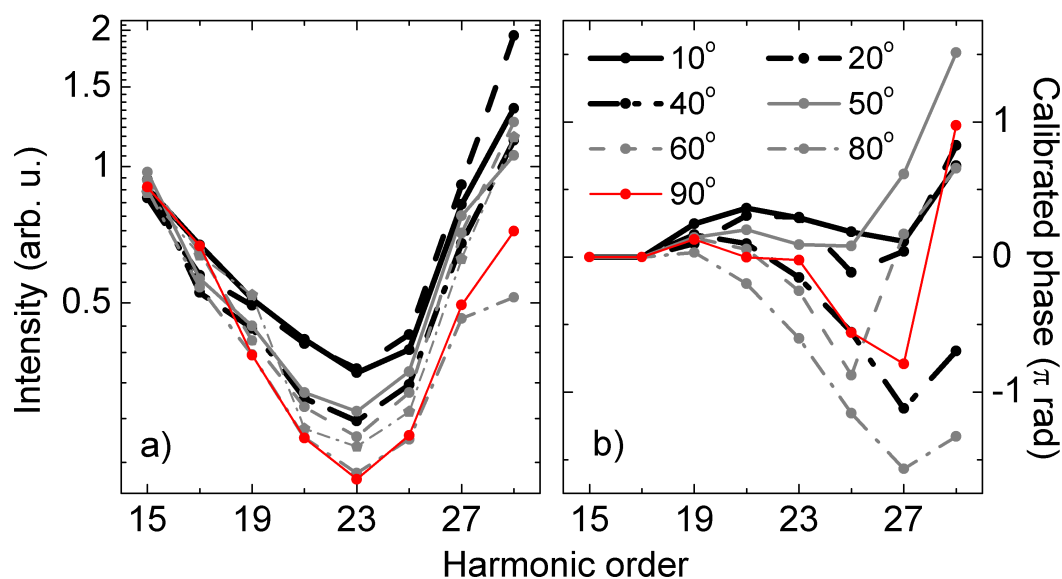


Figure 3.20: Experimentally calibrated intensity (a) and phase (b) in π rad units, for the parallel component of the harmonic field as a function of alignment angle and harmonic order. For the sake of clarity we do not present the results at all alignment angles.

Because of the reasons explained earlier, we use the relations between the two components given in figure 3.18 and the measured parameters for the parallel component in order to extract the intensity and phase parameters of the perpendicular component. This gives us a complete characterization of the RDM (except for the angular phase dependence that is imposed by the normalization procedure).

3.5.3 Vectorial Orbital Tomography (VOT)

Molecular orbital tomography is performed in the molecular frame. Therefore, the previously described calibrated dipole components have to be projected from the laboratory frame onto the molecular frame. Then, applying eq. 3.7 we can reconstruct the HOMO orbital along the molecular axis and orthogonal to it, as plotted in figure 3.21 a and b, respectively. The three lobe structure of the HOMO orbital is already visible in these reconstructions, although in (a) the central lobe is more emphasized while in (b) the side lobes are. The origin of this behavior is not exactly clear, but as already mentioned, the reconstructions along the two axes are in general not the same due to the discrete sampling and the assumptions made. Other distorting effects could be multi-orbital contributions.

Averaging the two reconstructions can wash out the distortions as presented in figure 3.22 b. The theoretical reconstruction (a) and the reconstruction after averaging the experimental results (b) show remarkable resemblance. (c) presents the reconstruction obtained by taking into account only the parallel component of the dipole in the LF and applying eqs. 3.8 and 3.9. The lobe structure is present but the form of the lobes are slightly different. This comparison clearly shows that the experimental characterization of both dipole components surely leads to better quality reconstructions. As already presented in PAPER I, the phase characteristics are much more crucial than the intensity. Despite the fact that in this set of measurements we did not get exactly the same phases as in PAPER I, the principle characteristics are still encoded, resulting in a proper reconstruction. We could destroy the good shape of the reconstruction only if the calibrated phases at several alignment angles for the whole spectral range were affected manually, e.g. by replacing them with a constant

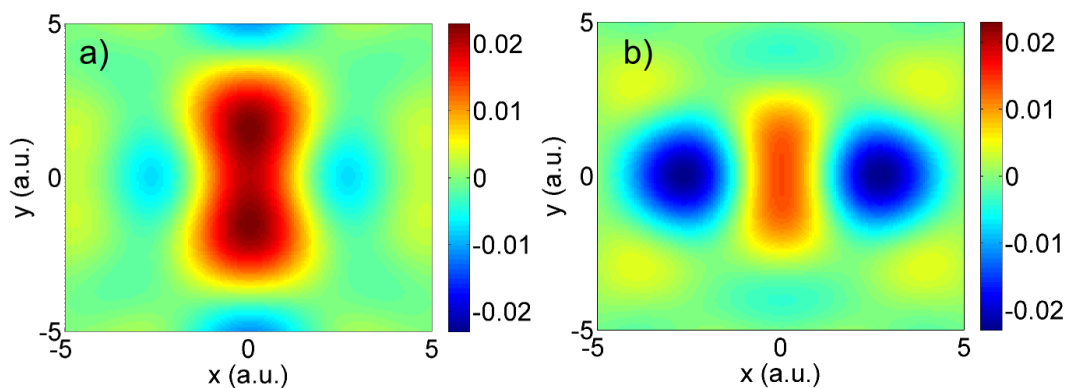


Figure 3.21: Experimental vectorial orbital reconstruction along the main axis of the molecule (a) and perpendicular to it (b). The spectral range from harmonic 17 to 29 was used and the HOMO symmetry was assumed. Only the first quadrant of the Fourier space (from 0° to 90°) was characterized.

zero phase. Note however that the reconstruction of the HOMO-1 orbital performed using the real part of the RDM, did not show a good agreement with the theoretical simulation.

Despite the success in the reconstruction of the HOMO orbital, there are several unanswered questions that have to be examined in the future. The PWA of the orbital tomography assumes no phase shift between the components of the dipole. Despite the phase shifts measured in our experiments, we can still obtain a good reconstruction. One possible explanation could be that the perpendicular component E_\perp^L is non negligible in only a small range ($50^\circ < \theta < 70^\circ$ and $25 < q < 29$, see figure 3.18 a), so that the phase shift has a limited impact on the reconstruction. It needs to be find out what are the principle characteristics of the measured intensity and phase needed to obtain a good reconstruction and in which conditions these principles are broken.

3.6 Conclusion

In conclusion, we have found that in our usual experimental conditions multi-orbitals are contributing to the HHG. Nevertheless, we could show that by decreasing the intensity of the generating laser, the contributions from the lower lying orbitals are dramatically decreased, therefore in these conditions, molecular orbital tomography should not be blurred by other orbitals. We have also found special experimental conditions where the contributions of HOMO and HOMO-1 can be separated in the imaginary and real parts, respectively of the measured dipole, allowing the reconstruction of both orbitals. We showed that the spectral phase is more sensitive to the multi-orbital effects than the spectral amplitude. Due to that we found signs of nuclear vibration dynamics related to the lower lying orbitals. The study of the effect of the molecular alignment showed that there are characteristic features of the dipole that are surviving the averaging over the angular distribution, if the degree of alignment is high enough. This suggests that both molecular orbital tomography and multi-channel dynamics studies are possible using the macroscopic signal. However, a deconvolution from the angular distribution is necessary for recovering the precise RDM. In a recent experiment we have performed characterization of the harmonic spectral amplitude, phase and polarization in the same experimental conditions and applied the results to perform vectorial orbital tomography. The polarization measurement also showed that the harmonics are elliptically polarized. We investigated the origin of the ellipticity with our multi orbital model, using scattering wave dipole moments. We found only qualita-

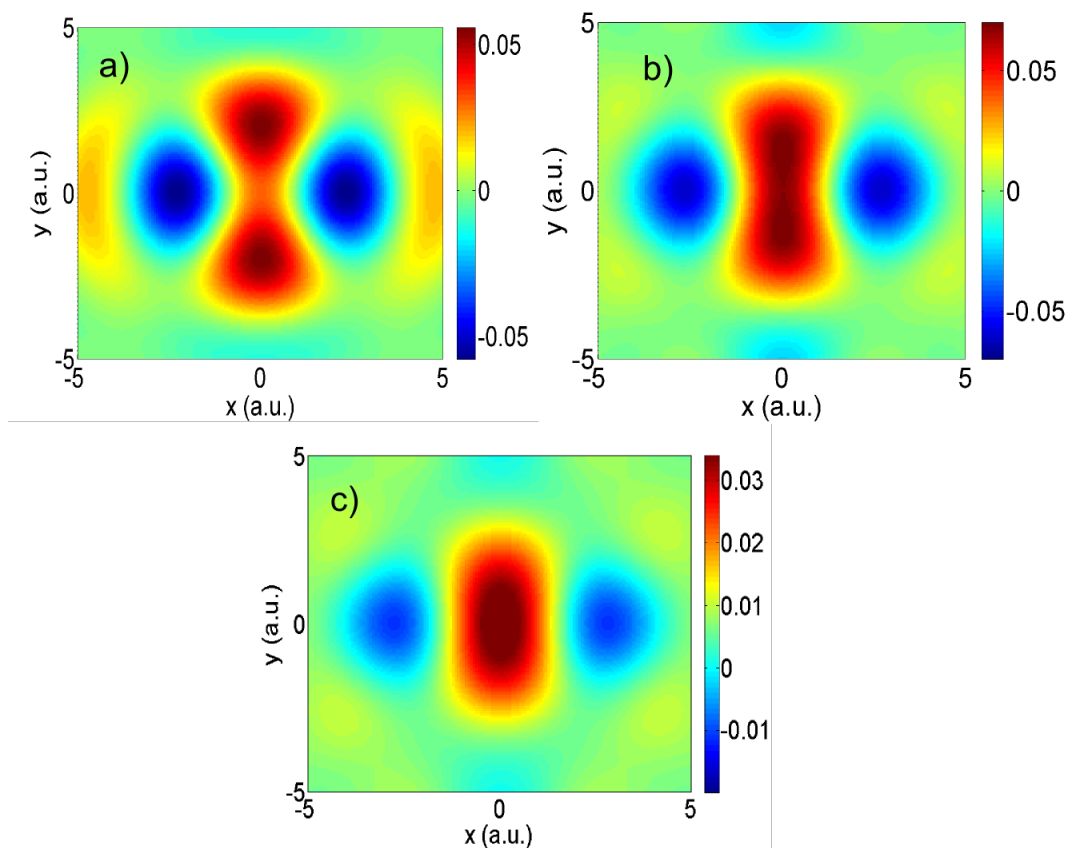


Figure 3.22: (a) Theoretical reconstruction of the HOMO orbital using plane wave dipoles with Hartree-Fock molecular orbitals filtered for the experimental spectral range; (b) Sum of the experimental reconstructions along the two axes of the molecule shown in figure 3.21. (c) Experimental reconstruction taking into account only the parallel dipole component in the LF and projected into MF by the eqs. 3.8 and 3.9. The amplitude and phase characteristics of the parallel component of the dipole are shown in figure 3.20.

tive agreement, the measured ellipticities being two times smaller than the calculated ones. Therefore, our model has to be refined to include additional processes such as channel coupling.

CHIRPED XUV MULTILAYER MIRRORS

One of the future aims of attosecond research is to perform as-pump as-probe measurements, alike what is done in the femtosecond domain. It requires high fluxes and precise control over the temporal and spatial profile of the pulses, which is not straightforward in the as regime. To achieve such controls, two main approaches exist: (i) adjustment of the experimental conditions of HHG, like the laser parameters, selection of the generating gas and adjustment of the position of the gas jet; or (ii) post generation control techniques.

In this chapter we investigate the latter approach aiming at a control over the temporal profile of the as pulses. It requires the introduction of some material in the beam line, like metallic foils, gas phase atoms, mirrors etc. The material has to affect coherently the spectral phase and to be highly reflective or transmissive over a large spectral range (several tens of eVs). In the XUV spectral range almost all materials are absorbing and show positive GDD. However, our collaborators from Laboratoire Charles Fabry at Institut d'Optique, managed to develop aperiodic large bandwidth multilayer mirrors using three materials, Si, Mo and B₄C that provide a fairly high reflectivity and versatile phase control when set at 45°.

In the unpublished manuscript PAPER III, we describe in details the process of manufacturing such mirrors and the experimental techniques used for their characterization. Three mirrors were produced with three different characteristics. We measured the reflectivity and the group delay of: a "transmissive" mirror, that do not change the pulse's chirp in the 35-55 eV spectral range; a mirror that compensates a GDD of 4200 as²/rad and a mirror compensating a GDD of 8500 as²/rad. By placing a theoretical filter on the measured spectrum, we proved that these mirrors are capable of producing both positively and negatively chirped pulses or to cancel them out. We also report the evidence of higher order dispersions in the attosecond pulses, like third order dispersion.

In PAPER IV, we first focus on the physical interpretation of the evolution of the mirrors' GDD layer by layer. We show the reconstructed temporal profile of the attosecond pulses reflected off the manufactured mirrors and a reference one and prove that the designed multilayer mirrors are capable of correcting and even over correcting the initial attochirp of the harmonic emission. Relying on the good agreement between simulated and measured GDs and reflectivities, we propose theoretically a versatile attosecond pulse shaper using two of the mirrors and an aluminum filter. Adjusting the angle of incidence on the mirrors, one is able to achieve double or single pulses.

RÉSUMÉ DU CHAPITRE

L'un des objectifs de la recherche attoseconde – à l'instar de ce qui se fait dans le domaine femtoseconde, est d'effectuer des mesures pompe/sonde tout attoseconde. Ceci requiert des flux élevés et un contrôle précis des profils temporel et spatial des impulsions, ce qui reste délicat dans le régime attoseconde. Il existe essentiellement deux approches pour réaliser ces contrôles: (i) l'ajustement des paramètres expérimentaux, comme les caractéristiques du laser, le choix du gaz de génération ou l'ajustement de la position du jet de gaz et (ii) les techniques de contrôle a posteriori.

Dans ce chapitre, nous étudions la seconde approche avec une ambition de contrôler le profil temporel des impulsions. Elle requiert l'introduction de matériaux dans le faisceau, comme des feuilles métalliques, des gaz atomiques, des miroirs etc. . . Le matériaux introduit doit affecter la phase spectrale de façon cohérente et avoir une transmission ou réflectivité élevée sur large gamme spectrale (plusieurs dizaines d'eV). Dans le domaine spectral UVX presque tous les matériaux sont absorbants et présentent une dispersion de vitesse de groupe (DVG) positive. Nos collaborateurs du Laboratoire Charles Fabry à l'Institut d'Optique, ont néanmoins réussi à développer des miroirs aperiodiques multicouches large bande en utilisant trois types de matériaux, Si, Mo et B₄C qui ont des réflectivités élevées et introduisent des DVG ajustables en signe et amplitude.

Dans l'article non publié ARTICLE III, nous décrivons en détail la procédure de fabrication de tels miroirs et les techniques expérimentales utilisées pour leur caractérisation. Trois miroirs ont été fabriqués avec trois caractéristiques différentes. Nous avons ainsi mesuré la réflectivité et le délai de groupe: d'un miroir transmissif, qui ne change pas la dérive de fréquence de l'impulsion dans la gamme spectrale 35-55 eV, d'un miroir qui compense une DVG de 4200 as²/rad et enfin d'un miroir introduisant une DVG également négative de 8500 as²/rad. En plaçant théoriquement un filtre sur la gamme d'harmoniques mesurées, nous avons montré que ces miroirs peuvent au choix produire des impulsions à dérive de fréquence positive, négative ou nulle. Nous identifions également des termes de dispersion d'ordre supérieur dans les impulsions attosecondes, comme la dispersion de troisième ordre.

Dans l'ARTICLE IV, nous nous concentrons d'abord sur l'interprétation physique de l'évolution de la DVG des miroirs couche par couche. Nous reconstruisons le profil temporel des impulsions attosecondes réfléchies sur les miroirs multicouches ainsi que sur un miroir de référence, démontrant que nos miroirs multicouches sont capable de corriger – et même sur corriger – la dérive de fréquence attoseconde initiale de l'émission harmonique. S'appuyant sur le bon accord entre les DVG et réflectivités simulées et mesurées, nous proposons théoriquement un façonneur d'impulsions attosecondes qui utilise le combinaison de deux miroirs avec un filtre d'aluminium. En ajustant l'angle d'incidence sur les miroirs, on passe rapidement d'impulsions simples à double ou encore multiples.

PAPER III

Theoretical and experimental studies of extreme broadband phase-controlled attosecond mirrors

Z. Diveki, C. Bourassin-Bouchet, E. English, E. Meltchakov, O. Gobert, D. Guenot, B. Carré, P. Salières, T. Ruchon, S. de Rossi and F. Delmotte

Unpublished

Theoretical and experimental studies of extreme broadband phase-controlled attosecond mirrors

Contents

1	Introduction:	3
2	Mirror design	4
2.1	Objectives	4
2.2	Design	6
2.3	Fabrication and control	7
3	Characterization of the mirrors	8
3.1	Method of characterization	8
3.2	Experimental setup	9
3.3	Results of phase measurements	11
3.4	Results of reflectivity measurements	13
4	Spectro-temporal analysis of the phase and pulse-shaping	15
4.1	Higher order phase terms and GD dips	15

References

- [1] M. Nisoli and G. Sansone, “New frontiers in attosecond science,” *Progress in Quantum Electronics* **33**, 17 – 59 (2009).
- [2] K. Midorikawa, Y. Nabekawa, and A. Suda, “Xuv multiphoton processes with intense high-order harmonics,” *Progress In Quantum Electronics* **32**, 43–88 (2008).
- [3] M. F. Kling and M. J. J. Vrakking, “Attosecond Electron Dynamics,” *Annual Review of Physical Chemistry* **59**, 463–492 (2008).
- [4] C. Froehly, B. Colombeau, and M. Vampouille, “Shaping and analysis of picosecond light pulses,” *Progress in Optics* **33**, 65–153 (1983).
- [5] P. Tournois, “Acousto-optic programmable dispersive filter for adaptive compensation of group delay time dispersion in laser systems,” *Optics Communications* **140**, 245–249 (1997).
- [6] M. Ferray, A. L’Huillier, X. F. Li, G. Mainfray, and C. Manus, “Multiple-harmonic conversion of 1064 nm radiation in rare gases,” *J. Phys. B* **21**, L31 (1988).
- [7] A. McPherson, G. Gibson, H. Jara, U. Johann, T. S. Luk, I. A. McIntyre, K. Boyer, and C. K. Rhodes, “Studies of multiphoton production of vacuum-ultraviolet radiation in the rare gases,” *J. Opt. Soc. Am. B* **4**, 595 (1987).
- [8] Y. Mairesse, A. de Bohan, L. J. Frasinski, H. Merdji, L. C. Dinu, P. Monchicourt, P. Breger, M. Kovačev, R. Taïeb, B. Carré, H. G. Muller, P. Agostini, and P. Salières, “Attosecond Synchronization of High-Harmonic Soft X-rays,” *Science* **302**, 1540–1543 (2003).
- [9] K. Varjú, Y. Mairesse, P. Agostini, P. Breger, B. Carré, L. J. Frasinski, E. Gustafsson, P. Johnsson, J. Mauritsson, H. Merdji, P. Monchicourt, A. L’Huillier, and P. Salières, “Reconstruction of

- Attosecond Pulse Trains Using an Adiabatic Phase Expansion,” *Phys. Rev. Lett.* **95**, 243901 (2005).
- [10] J. Tate, T. Augustine, H. G. Muller, P. Salières, P. Agostini, and L. F. DiMauro, “Scaling of wavepacket dynamics in an intense midinfrared field,” *Phys. Rev. Lett.* **98**, 013901 (2007).
- [11] W. Boutu, S. Haessler, H. Merdji, P. Breger, G. Waters, M. Stankiewicz, L. J. Frasinski, R. Taieb, J. Caillat, A. Maquet, P. Monchicourt, B. Carre, and P. Salieres, “Coherent control of attosecond emission from aligned molecules,” *Nat Phys* **4**, 545–549 (2008).
- [12] X. Zhou, R. Lock, W. Li, N. Wagner, M. M. Murnane, and H. C. Kapteyn, “Molecular recollision interferometry in high harmonic generation,” *PHYSICAL REVIEW LETTERS* **100** (2008).
- [13] T. Ruchon, C. P. Hauri, K. Varjú, E. Mansten, M. Swoboda, R. López-Martens, and A. L’Huillier, “Macroscopic effects in attosecond pulse generation,” *New Journal of Physics* **10**, 025027 (10pp) (2008).
- [14] K. T. Kim, C. M. Kim, M.-G. Baik, G. Umesh, and C. H. Nam, “Single sub-50-attosecond pulse generation from chirp-compensated harmonic radiation using material dispersion,” *Phys. Rev. A* **69**, 051805 (2004).
- [15] R. López-Martens, K. Varjú, P. Johnsson, J. Mauritsson, Y. Mairesse, P. Salières, M. B. Gaarde, K. J. Schafer, A. Persson, S. Svanberg, C.-G. Wahlström, and A. L’Huillier, “Amplitude and Phase Control of Attosecond Light Pulses,” *Physical Review Letters* **94**, 033001–+ (2005).
- [16] E. Gustafsson, T. Ruchon, M. Swoboda, T. Remetter, E. Pourtal, R. López-Martens, P. Balcou, and A. L’Huillier, “Broadband attosecond pulse shaping,” *Opt. Lett.* **32**, 1353–1355 (2007).
- [17] D. H. Ko, K. T. Kim, J. Park, J. hwan Lee, and C. H. Nam, “Attosecond chirp compensation over broadband high-order harmonics to generate near transform-limited 63 as pulses,” *New J. Phys.* **12**, 063008 (2010).
- [18] A. Wonisch, T. Westerwalbesloh, W. Hachmann, N. Kabachnik, U. Kleineberg, and U. Heinzmann, “Aperiodic nanometer multilayer systems as optical key components for attosecond electron spectroscopy,” *Thin Solid Films* **464-465**, 473–477 (2004).
- [19] A.-S. Morlens, P. Balcou, P. Zeitoun, C. Valentin, V. Laude, and S. Kazamias, “Compression of attosecond harmonic pulses by extreme-ultraviolet chirped mirrors,” *Opt. Lett.* **30**, 1554–1556 (2005).
- [20] A.-S. Morlens, R. López-Martens, O. Boyko, P. Zeitoun, P. Balcou, K. Varjú, E. Gustafsson, T. Remetter, A. L’Huillier, S. Kazamias, J. Gautier, F. Delmotte, and M.-F. Ravet, “Design and characterization of extreme-ultraviolet broadband mirrors for attosecond science,” *Opt. Lett.* **31**, 1558 (2006).
- [21] C. Bourassin-Bouchet, Z. Diveki, S. de Rossi, E. English, E. Meltchakov, O. Gobert, D. Guénot, B. Carré, F. Delmotte, P. Salières, and T. Ruchon, “Control of the attosecond synchronization of xuv radiation with phase-optimized mirrors,” *Opt. Express* **19**, 3809–3817 (2011).
- [22] E. Goulielmakis, M. Schultze, M. Hofstetter, V. S. Yakovlev, J. Gagnon, M. Uiberacker, A. L. Aquila, E. M. Gullikson, D. T. Attwood, R. Kienberger, F. Krausz, and U. Kleineberg, “Single-Cycle Nonlinear Optics,” *Science* **320**, 1614–1617 (2008).
- [23] M. Suman, G. Monaco, M.-G. Pelizzo, D. L. Windt, and P. Nicolosi, “Realization and characterization of an xuvmultilayer coating for attosecond pulses,” *Opt. Express* **17**, 7922–7932 (2009).
- [24] J. Gautier, F. Delmotte, M. Roulliay, F. Bridou, M.-F. Ravet, and A. Jérôme, “Study of normal incidence of three-component multilayer mirrors in the range 20-40 nm,” *Appl. Opt.* **44**, 384–390 (2005).
- [25] H. Takenaka, H. Ito, T. Haga, and T. Kawamura, “Design and fabrication of highly heat-resistant Mo/Si multilayer soft X-ray mirrors with interleaved barrier layers,” *Journal of Synchrotron Radiation* **5**, 708–710 (1998).
- [26] S. Bajt, J. B. Alameda, T. W. Barbee, W. M. Clift, J. A. Folta, B. B. Kaufmann, and E. A. Spiller, “Improved reflectance and stability of Mo/Si multilayers,” *Optical Engineering* **41**, 1797–1804 (2002).

- [27] H. Maury, P. Jonnard, J. Andre, J. Gautier, M. Roulliay, F. Bridou, F. Delmotte, M. Ravet, A. Jerome, and P. Holliger, “Non-destructive X-ray study of the interphases in Mo/Si and Mo/B₄C/Si/B₄C multilayers,” *Thin Solid Films* **514**, 278–286 (2006).
- [28] F. Delmotte, J. Gautier, M. Roulliay, M. F. Ravet, F. Bridou, and A. Jerome, “B₄C/Mo/Si multilayers for 20-40 nm wavelengths: application to broadband mirrors,” in “Society of Photo-Optical Instrumentation Engineers (SPIE) Conference Series,” , vol. 5963 of *Society of Photo-Optical Instrumentation Engineers (SPIE) Conference Series*, C. Amra, N. Kaiser, & H. A. Macleod, ed. (2005), vol. 5963 of *Society of Photo-Optical Instrumentation Engineers (SPIE) Conference Series*, pp. 539–546.
- [29] Y. Ménesguen, S. de Rossi, E. Meltchakov, and F. Delmotte, “Aperiodic multilayer mirrors for efficient broadband reflection in the extreme ultraviolet,” *Applied Physics A: Materials Science & Processing* **98**, 305–309 (2010).
- [30] Y. Mairese, A. de Bohan, L. J. Frasinski, H. Merdji, L. C. Dinu, P. Monchicourt, P. Breger, M. Kovacev, T. Auguste, B. Carré, H. Muller, P. Agostini, and P. Salieres, “Optimization of Attosecond Pulse Generation,” *Phys. Rev. Lett.* **93**, 163901 (2004).

1. Introduction:

The demand for convenient and tunable attosecond sources is increasing ever since their first demonstration in the early 2000’s. Either one wants to get them intense to achieve two photons XUV-transitions, to tune their central wavelength to target photoionization channels of specific species, or to change their temporal profile to perform XUV-coherent excitation of a target [1, 2, 3]. All these aims require the shaping in amplitude and phase of a given spectrally broad and coherent XUV source, which is by no way trivial. Indeed, attosecond sources are necessarily in the XUV domain or beyond: the Fourier transform of a 100 as-long gaussian pulse (full width at half maximum, FWHM) is a gaussian spectrum having a bandwidth of 18 eV (FWHM). Such a broad spectrum only fits in the XUV spectral range or beyond. Moreover, in the XUV range, virtually any material is highly absorbent. Consequently for temporal shaping, the difficulty of precisely controlling the phase over a very large bandwidth adds up to the challenge of preserving the flux using an appropriate combination of materials.

In the IR-femtosecond pulses domain, quasi-universal pulse shaping devices are available, such as 4-f zero dispersion delay lines [4] or acousto-optic programmable dispersive filters [5]. On the contrary, no ubiquitous device is available for attosecond pulses. Instead a series of techniques has been derived. So far, they all start from a High Harmonic Generation (HHG) source using a gaseous medium as a non linear medium [6, 7]. More precisely, an intense femtosecond laser pulse is usually focused to intensities in the 10^{14} W/cm² range in a noble gas where a non linear process takes place. Using pulses in the 10-100 fs range, a comb of odd harmonics of the fundamental laser frequency is generated. Importantly, these harmonics are spectrally coherent: if one selects the central part of the beam in the far-field, their relative spectral phase is purely quadratic as a first approximation [8, 9, 10]. However, the medium itself might alter this behavior, introducing jumps or linear offsets due to its internal structure, [11, 12], or due to phase matching [13]. Besides, after the generation stage, spectral manipulations can be undertaken downstream, using dispersive media, such as metallic

foils [14, 15, 16], plasmas [8] or atomic gases [17]. Nevertheless, all these controls are limited, being unable to cover the full spectral range and to provide higher-order phase profiles adjustable in both amplitude and sign. Therefore, they require to adjust a spectrum to one given material, whereas one would like to proceed the other way around, so as to target specific atomic or molecular processes.

Building on what exists in the IR domain, it was early proposed to designed reflective multilayer optics that would introduce a fully controlled phase on the harmonic radiation [18, 19, 20]. Although introduced in 2005, these devices have not become ubiquitous thus far, certainly due to their poor reflectivity and fairly narrow band of phase control. In a recent publication [21], we reexamined this proposition, showing that significant progress could be achieved by a careful analysis of the phase behavior in XUV multilayer mirrors. First, we showed that the properties of such mirrors could be perfectly predicted. Second, they can be used to perform on-line pulse shaping in the attosecond regime, using not only second order dispersion, but also higher order phase terms. The present paper is a follow-up of ref. [21], intended to present in more details the design procedure and the experimental results. It is organized as follows: in section 2, the design and fabrication process is detailed, section 3 is dedicated to the characterization of the mirrors' reflectivities in amplitude and phase with an HHG beamline, section 4 presents an analysis of the attosecond shapes achievable with the mirrors.

2. Mirror design

2.1. Objectives

The main objective is to design, produce and characterize mirrors with high reflectivity on a broad spectral band with a well controlled spectral phase in order to finally allow an extended XUV-pulse shaping. We decided to focus our study on mirrors to be used with an HHG source in argon gas, driven by a Ti:sapphire laser with an 800 nm wavelength and 50 fs duration. This offers a good compromise between the achievable bandwidth and the conversion efficiency about the 40-50 eV range. Such a source has its cut-off around 55 eV, which was therefore chosen as the upper bound for the optimization range of the mirrors. On the low energy side, we limited ourselves to 35 eV due to the lack of reliable optical constants for most of the materials used in multilayer mirrors at lower energy. Thus, in this study, the spectral domain for the mirror optimization is fixed to 35 eV-55 eV.

In these generating conditions, over the major part of the spectrum, the phase of the harmonics, denoted $\varphi(\omega)$ is quadratic with the photon energy. The group delay ($\text{GD}(\omega)$), and the dispersion of the group delay ($\text{GDD}(\omega)$, also called attochirp), which are respectively defined as the first and second derivative of $\varphi(\omega)$ against ω , are therefore respectively linear and constant [8]. Moreover, $\text{GDD}(\omega)$ scales with a $1/I$ law, where I is the IR-intensity. For exemple, close to the saturation intensity in argon, and using

a Ti:Sapphire laser, $GDD(\omega) \simeq 20000 \text{ as}^2/\text{rad}$. To get a complete control range with an argon-based source, we designed three mirrors aimed respectively at a full compensation of this chirp (M_3), at a compensation of half of it (M_2) and finally at no modification of it (M_1). Their complex reflectivity versus the angular frequency of XUV light, denoted ω , is throughout the article denoted $\sqrt{R_n(\omega, \theta)} e^{i\psi_n(\omega, \theta)}$ where $n=1,2$ or 3 is the reference number for one of the mirror type and θ the angle of incidence.

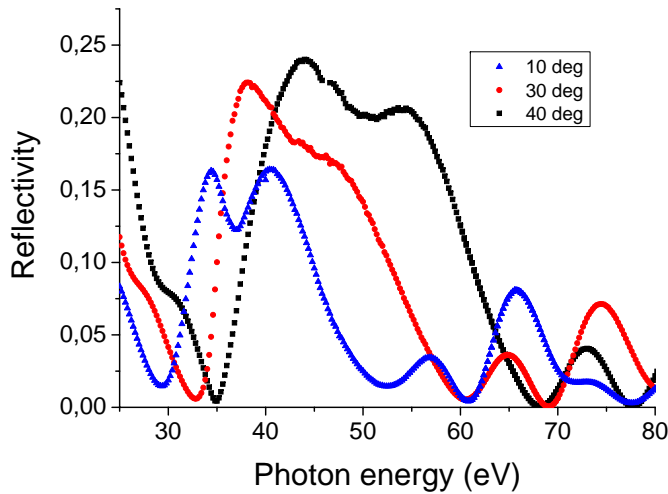


Figure 1. Experimental reflectivity measured for an angle of incidence of 10° (blue uptriangles), 30° (red circles) and 40° (black squares) with a 80% S polarized beam.

Up to now, most of multilayer mirrors for attosecond sources have been designed to work at near normal incidence [18, 20, 22, 23]. However, as HHG sources are linearly polarized, it is in principle possible to increase the reflectivity by increasing the angle of incidence. This is illustrated in Fig. 1 where we plotted the reflectivity of a typical multilayer mirror measured on synchrotron radiation source at different incidence angles. The mirror coating consists of a stack of two boron carbide/molybdenum/silicon (B4C/Mo/Si) periodic multilayers (two periods each). The increase of the averaged reflectivity with the incidence angle goes from 15% at 10° up to 20% at 40° . Moreover, the relative bandwidth ($\Delta E/E$) of this multilayer mirror increases significantly as well with the angle of incidence, from 0.36 at 10° up to 0.47 at 40° . For these reasons, added to the fact that it allows a convenient beam steering, we have chosen to design mirrors working at 45° of incidence.

2.2. Design

The simplest way to produce a broadband mirror is to use a periodic stack of two materials, with a very low number of periods. In this case, the bandpass is broad but the reflectivity is limited to a few percent in normal incidence configuration and the

spectral phase is almost linear in the bandpass [22]. A typical example of this case is shown in Figure 2(b). As exemplified in Figure 2(b), increasing the number of layers

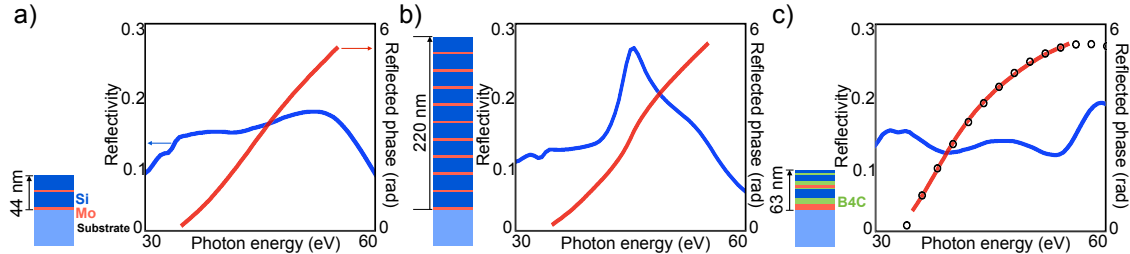


Figure 2. Comparison of three multilayer structures and their corresponding theoretical reflectivity (blue curve) and phase (red curve). Periodic Mo/Si multilayer structure made of a) two or b) ten Mo/Si periods (Mo: 4 nm, Si: 18 nm). The thicknesses are chosen to get the Bragg’s peak at 45 eV for an incidence angle of 45°. c) M_3 aperiodic three-materials multilayer mirror. The targeted phase response is also reported (open black circles).

does not help as for the phase and just increases the reflectivity over a narrow band around a Bragg peak. To overcome these limitations, a first step is the use of a three component multilayer stack, such as B4C, Mo and Si instead of only two. We have shown theoretically and experimentally that the reflectivity gets higher and the bandpass larger than for a conventional two component multilayers. Moreover, in the case of periodical stacks, the reflectivity increases much more rapidly with the number of period [24]. It has also been demonstrated that the addition of thin B4C “barrier” layers in Mo/Si multilayers reduces the formation of molybdenum silicides, and produces more ideal interfaces [25, 26, 27]. In our optimization procedure, we decided to set the minimum thickness of each B4C layer to 0.3 nm in order to take advantage of this “barrier” layer effect.

As a second step to improve the bandwidth and reflectivity, some years ago, we proposed to use a multiperiodic stack, *i.e.* a superposition of several periodic multilayers, in order to achieve high normal incidence reflectivities (about 20%) over broad spectral ranges [28]. However, we showed that such a broadband mirror presents a relatively linear spectral phase within the bandpass [20]. To overcome this final limitation and control the Group Delay Dispersion of the mirror, it is necessary to add even more degrees of freedom in the stack during the optimization procedure. We chose to allow for a totally aperiodic structure determined by a simulated annealing algorithm. The merit function MF of the algorithm was chosen to optimize both the GDD and the reflectivity R of the mirror on the 35-55 eV range. It reads

$$MF = W_R \cdot \left[\sum_{\Delta E} (R(E) - R_{target})^2 \right] + W_{GDD} \cdot (GDD_{\Delta E} - GDD_{target})^2, \quad (1)$$

where R_{target} and GDD_{target} are the targeted values, and W_R and W_{GDD} their corresponding weights. The latter two and R_{target} were refined empirically during the

	Number of layers	GDD	Reflectivity
M_1	8	$42 \text{ as}^2/\text{rad}$	17 – 27 %
M_2	7	$-5150 \text{ as}^2/\text{rad}$	10 – 20 %
M_3	9	$-8579 \text{ as}^2/\text{rad}$	10 – 15 %

Table 1. Parameters of the optimized aperiodic structures. The reported GDD is averaged over the 35 – 55 eV, and the reflectivities are the peak-to-valley variations on the same range.

process. In the optimization procedure, the angle of incidence was not allowed to vary and set at $\theta=45^\circ$. To simplify the notations, this parameter is therefore discarded in $R(E)$. Finally, $GDD_{\Delta E}$ is the slope of the linear fit of $\partial\psi_n(\omega)/\partial\omega$ for a potential stack. In this study, we optimized three different stacks setting respectively $GDD_{target} = 0 \text{ as}^2/\text{rad}$ (M_1), $-4200 \text{ as}^2/\text{rad}$ (M_2) and $-8500 \text{ as}^2/\text{rad}$ (M_3). The results of the coating optimization are detailed in Table 1 and in Fig. 2 for M_3 , taken as a typical case. Also displayed is the parabolic targeted phase. At variance with the other regular structures which do not show any phase alteration, it is remarkable that the phase of the optimized structure nicely matches the parabola, corresponding to the constant targeted GDD.

2.3. Fabrication and control

The deposition of aperiodic structures requires a precise control and metrology of each individual layer thickness. All multilayers have been deposited using a magnetron sputtering (MS) system equipped with four cathodes [24]. The 80 mm \times 200 mm rectangular targets are mounted at the bottom of the chamber with chimneys that limit the deposition region to the area directly above them. A background pressure of 2.7×10^{-6} Pa is obtained with a cryogenic pump. Successive layers are deposited by scanning the substrate above the target at a distance of 10 cm. The thickness of each layer is controlled by the rotation velocity of the substrate on the target box. The typical velocity is adjusted from 0.2°/s to 2°/s. The substrate is rotating around its axis of symmetry at 50 rpm in order to obtain a good uniformity. During the process, we use a 0.27 Pa argon pressure in the deposition chamber. The plasma discharges are established with a RF power of 150 W for B4C and Si targets and a DC current of 0.06 A for the Mo target. Multilayers are deposited onto 1" silica superpolished wafers with roughness lower than 0.2 nm. The multilayer structure is controlled by grazing-incidence X-ray reflectometry at 0.154 nm (GIXR). Fitting the experimental data, we can deduce the thicknesses of the different layers, the averaged interfacial roughnesses and the material complex index at 0.154 nm. An example of GIXR measurement and fit is shown in Fig. 3 for the aperiodic mirror M_2 . The interfacial roughness stays in the range 0.1 to 0.4 nm for all interfaces, which is an excellent match. The fitted thicknesses are very close to the targeted values for each layer (within ± 0.2 nm), which will allow reliable comparison of the experimental and predicted properties.

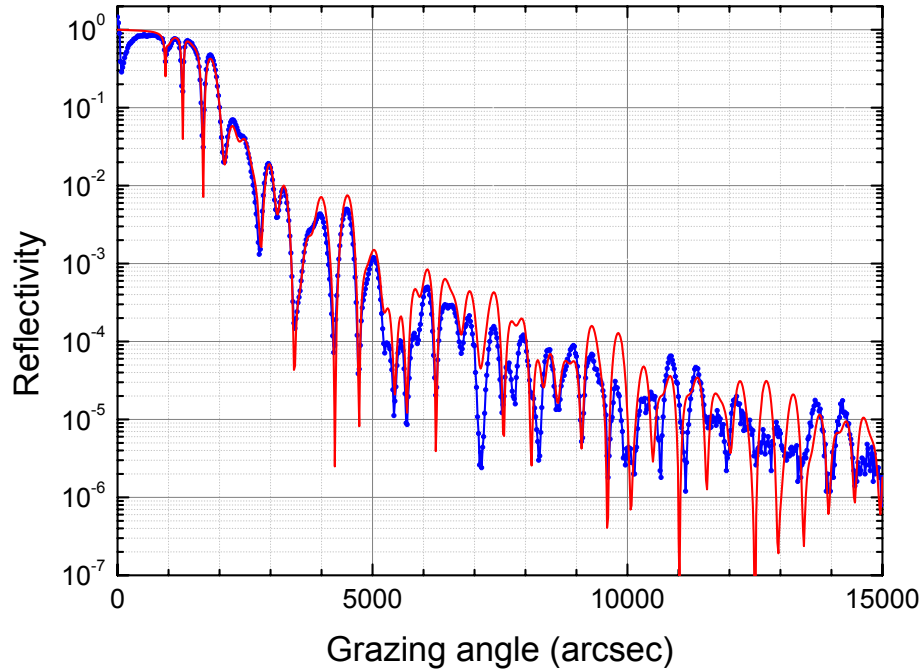


Figure 3. Reflectivity (red curve) of mirror M_2 measured at 0.154 nm with respect to the grazing angle, along with the fitted curve (blue dotted line).

3. Characterization of the mirrors

3.1. Method of characterization

Let us consider a broadband electromagnetic radiation in the XUV range which electric field spectrum reads $E^{in}(\omega)\exp(i\varphi^{in}(\omega))$ where the spatial variations have been disregarded. When impinging onto a mirror labeled n , the reflected electric field reads

$$E_n^{out}(\omega)\exp(i\varphi_n^{out}(\omega)) = E^{in}(\omega)\exp(i\varphi^{in}(\omega))\sqrt{R_n(\omega)}\exp(i\psi_n(\omega)). \quad (2)$$

where $E^{out}(\omega)$, $E^{in}(\omega)$, $\varphi^{out}(\omega)$, $\varphi^{in}(\omega)$ are all real functions. The use of this equation to measure the complex reflectivity requires the full characterization (amplitude and phase) of both incoming and outgoing broadband XUV radiations generated through HHG. Two steps are taken to characterize our HHG source. First, with all optics on the way but the mirror to be characterized, the source was carefully calibrated after reflection off an Au-coated grating at grazing incidence. Since at grazing incidence the electromagnetic field does not penetrate in the medium and the reflectivity is fairly flat, we assumed that the measurement gave an image of the radiation of the source. We hereafter call these measurements “direct measurements”. Second, before and after each characterization of a multilayer mirror, it was replaced by a silver mirror

at the same incidence angle, and a measurement of the outgoing radiation, denoted $E_{ref}^{out}(\omega)exp(i\varphi_{ref}^{out}(\omega))$ was recorded. This additional silver mirror has a tabulated complex reflectivity denoted $\sqrt{R_{ref}(\omega)}exp(i\psi_{ref}(\omega))$. It is supposed to reflect high harmonics up to 70 eV with more than 4% efficiency and to have a tiny GD of less than 10^{-5} as/rad. It thus appeared to be well suited to serve as a reference. Using the data from this reference mirror, Equation (2) could be rewritten as:

$$\sqrt{R_n(\omega)}exp(i\psi_n(\omega)) = \frac{E_n^{out}(\omega)}{E_{ref}^{out}(\omega)}exp(i(\varphi_n^{out}(\omega) - \varphi_{ref}^{out}(\omega) + \psi_{ref}(\omega)))\sqrt{R_{ref}(\omega)}.(3)$$

Carrying out measurements of the phase and amplitude of the field outgoing the setup with each mirror, and knowing the values of reflectivity for the reference mirror, this equation gives the full characterization of the ML mirror.

In the context of controlling the temporal pulse shapes, the values of importance in this equation are the amplitude on the one hand and on the other hand, the spectral derivatives of the phases above second order. Indeed, the 0th (resp. 1st) order term of the Taylor expansion of the phase vs. ω , gives the absolute phase (resp. absolute delay) of the pulse, which are of no significance here and will therefore be disregarded. Taking the modulus and the phase terms separately in Equation (3) we are eventually left with the study of the evolution of:

$$R_n(\omega) = \frac{I_n^{out}(\omega)}{I_{ref}^{out}(\omega)}R_{ref}(\omega) \quad (4)$$

$$GD_n(\omega) = GD_n^{out}(\omega) - GD_{ref}^{out}(\omega) + GD_{ref}(\omega) \quad (5)$$

where $GD_n(\omega)$ equals $\frac{\partial\phi_n(\omega)}{\partial\omega}$ and $I_n^{out}(\omega)$ (resp. $I_{ref}^{out}(\omega)$) corresponds to $(E_n^{out}(\omega))^2$ (resp. $(E_{ref}^{out}(\omega))^2$).

3.2. Experimental setup

Physical description. The characterization of the multilayer mirrors was performed on an attosecond beamline in CEA-Saclay using the RABITT technique for the measurements of the outgoing spectral phases. The pump laser was the ‘‘LUCA’’ Ti:sapph laser delivering pulses of 50 mJ energy, 792 nm central wavelength, and 50 fs pulse duration and operated at a 20 Hz repetition rate. The laser beam was split in two parts using a drilled mirror with a 8 mm hole set at 45° , in order to form a generating beam used to produce high order harmonics and a well-synchronized dressing beam required to perform the RABITT measurements (Figure 4). The two beams were delayed one with respect to the other using a delay line equipped with a piezoelectric transducer. They were subsequently recombined using a second drilled mirror at 45° , exact copy of the first one. The two beams were made co-propagative, the most intense one being annular and carrying up to 4.1 mJ, the less intense carrying about $35 \mu\text{J}$. A 1 m focal length lens was used to focus them in a piezoelectric-driven gas jet with 2.5 bar backing pressure where high order harmonics were generated. We alternatively used

Ar and Ne as a gas target to either probe the low or high energy parts of the mirrors' reflectivities. The calibration of the setup, in agreement with the results of Ref. [8], showed a very linear GD for harmonics above the ionization potential of the generating gas, with a slope inversely proportional to the generating intensity.

80 cm downstream the gas jet, an iris cut out the remaining of the annular generating beam and let through the high order harmonics and the dressing beam. Both beams were then reflected off the multilayer mirror under investigation (or the reference mirror) positioned in the beamline at 42° angle of incidence (due to geometrical constraints on our vacuum chambers it turned out to be impossible to set them exactly at 45°). Finally, both the high order harmonics and the dressing beams were reflected off a toroidal mirror which focused them in the sensitive region of a magnetic bottle electron spectrometer. The target gas for the detection was chosen to be Ar or Ne depending on the targeted spectral range.

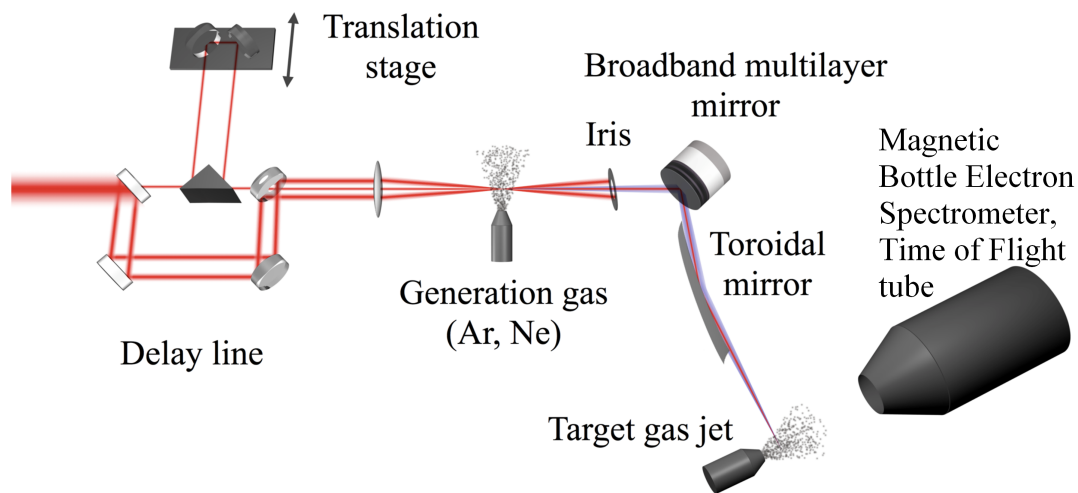


Figure 4. Schematic of the experimental setup (see the text for a precise description). The laser is coming from the left and propagates to the right. The dimensions of the optical part is 60×80 cm, making the interferometer compact and steady.

Amplitude measurements. The absorption of the harmonics by the target gas frees electrons which carry discrete kinetic energies. It maps the energy distribution of the harmonics multiplied by the cross sections of the target gas and convoluted by the response of the detector. The cross sections are tabulated data for noble gases and can easily be coped with to retrieve the intensities of the harmonics. As for the response of the detector, it has a 15 meV width for the lowest energies but dramatically enlarges with the energy detected, with a $E^{3/2}/L$ power law where E is the energy of the electron and the length L of the time of flight tube equals 1.5 m. Experimentally, it was impossible to resolve more than 13 harmonics at once. However, we could use a

retarding potential to slow down the most energetic electrons and bring them down into the high resolution spectral range of the detector. For each mirror, four experiments with four retarding potentials allowed us to detect the whole range of harmonics reflected off the mirrors with a significant overlap between them. This technique allowed to get a sufficient spectral resolution over 60 eV and to mutually calibrate the different spectra recorded. In the regions of overlap, the final results were simply averaged.

Phase measurements. The dressing beam overlapping with the harmonics in the target gas induces additional absorption or emission of photons, creating side bands between the discrete harmonics peaks. Their intensity is proportional to $\cos(2\omega_0(\tau + \tau_0) + (\phi_{q+1} - \phi_{q-1}) + \phi_{at})$, where ω_0 is the laser frequency, τ is the delay between the dressing and the XUV beam, τ_0 is the absolute timing, *i.e.* the delay between the dressing and the generating beam, $\phi_{q\pm 1}$ are the phases of the $q \pm 1$ harmonics and ϕ_{at} is the dipole phase which is negligible in our spectral range. Scanning τ over several periods of the dressing electric field and recording the corresponding oscillations of the sidebands, one can obtain the phase difference between consecutive harmonics. This technique requires an interferometric stability between the two beams, which is achieved by keeping the interferometer compact. It should be noted however that this scheme, which uses co-propagative XUV and IR beams, prevents the use of filters on the HHG beam for they would also block the IR beam needed for the measurement.

3.3. Results of phase measurements

In this section, we successively discuss the dispersion of the reference and multilayer mirrors. In the investigated spectral range the reference silver mirror is not supposed to have any dispersion thus presumably allowing to set $GD_{ref}(\omega)$ to 0 in Equation (5). We could double-check this assumption by comparing the measurements done in the actual configuration depicted in Figure 4 and the “direct measurements”, keeping the same generating conditions. The results obtained using argon as a generating gas, together with the linear fits of the GD over the 25–42 eV spectral range, are reported in Figure 5. Surprisingly, the slopes of the group delays are significantly different: the reflection off the reference mirror introduces an extra GDD of 5200 as²/rad. We speculate that this is due to an hydrocarbon layer that got deposited on our reference mirror after evaporation from the vacuum pumps of the harmonic line. This assumption is supported by i) measurements made using Ne as a generating gas which showed the same offset on the GD slope compared to usual values at an identical intensity (Figure 5) and ii) the quicker than expected drop of the reflectivity compared to tabulated values (Figure 7(e)). On the contrary, we calculated the effect of oxyde layers up to 100 nm and observed that neither for the reflectivity, nor for the chirp, the changes could be reproduced, ruling out this hypothesis. The rapid drop of the reflectivity of the silver mirror prevented any calibration of the GD above 62.5 eV. In agreement with direct measurements and Ref. [8], we thus extrapolated the experimental data assuming a linear slope given by

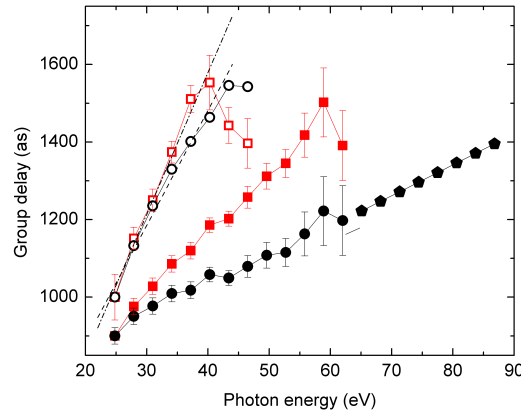


Figure 5. Measured group delays in argon (open symbols) and in neon (full symbols). Open red squares and open black circles correspond to GD measurements using silver mirror and grating at grazing incidence, respectively. The dash and dash dot lines are linear fits over the 25 – 42 eV spectral range. Full red squares corresponds to GDs in neon and full black circles to dispersion corrected GDs. Full black pentagonals are the extrapolated group delays. The group delay origin has been arbitrarily shifted to 1000 as for the first harmonic measured in argon, which is a typical value.

the actual measurement minus the contribution of 5200 as²/rad due to the hydrocarbon layer (Figure 5) in the 62.5 eV-90 eV range.

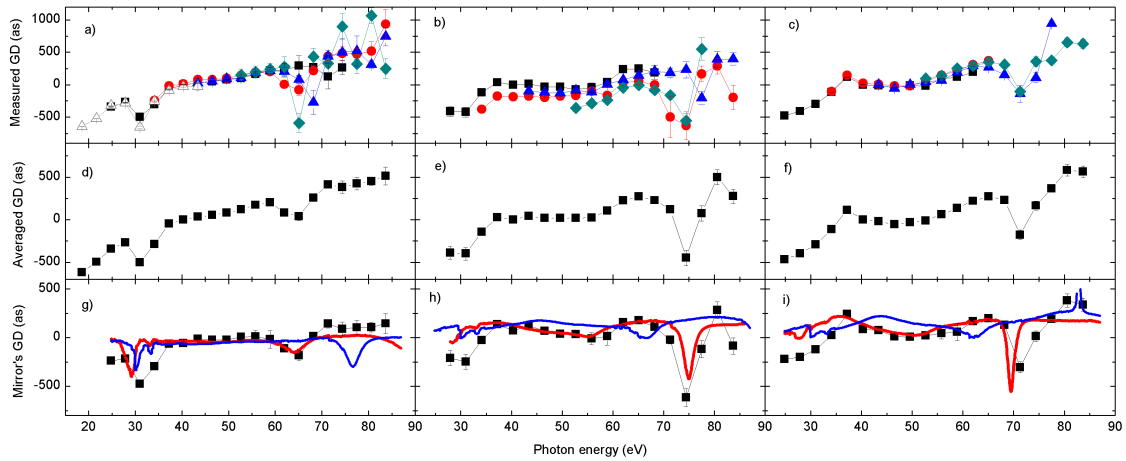


Figure 6. Measurement of the mirrors' group delays. (Top line) Raw GD measured for M₁(a), M₂(b) and M₃(c) with the RABITT technique using a retarding potential of 0 V (black squares), 9 V (red circles), 18 V (blue uptriangles) and 27 V (gray diamonds). (Middle line) Averaged GDs of the radiation using M₁(d), M₂(e) and M₃(f) (see text for the averaging procedure). (Bottom line) GD's introduced by M₁(g), M₂(h) and M₃(i) deduced using Equation (5) (Black squares) and theoretical calculations for angles of incidence of 42° (red line) and 52.5° (blue line).

The measurements of the GD of the electric field after reflection off the multilayer

mirrors are reported in Figure 6(a-c) for four retarding potentials. Due to the differences of reflectivities of the mirrors, the region of overlap of all four measurements slightly differed, being $52.7 - 74.4 \text{ eV}$, $52.7 - 68.2 \text{ eV}$ and $52.7 - 62 \text{ eV}$ for M_1 , M_2 and M_3 respectively. We merged the measurements together in two steps: first each curve corresponding to one retarding potential but 0 V is shifted to minimize its distance to the one with 0 V retarding potential, second the data are averaged with a weight inversely proportional to their square error bar. In this procedure the distance between two series of points is chosen to be the least square one. The results are reported in Figure 6(d-f). Eventually, the dispersion of the multilayer mirrors is obtained applying Equation (5) to the data sets with $GDD_{ref}(\omega) = -5200 \text{ as}^2/\text{rad}$ (Figure 6(g-i)). Also displayed in Figure 6(g-i) are the theoretical predictions for 42° and 52.5° angle of incidence. The latter two were shifted vertically so that their distances to the experimental curves over the optimized region of the mirror are minimized. The agreement between the theoretical points at 42° and the experiment is remarkable. In particular, M_2 and M_3 introduce negative GDDs in their optimized range while M_1 maintains the GDD of the source, as expected from the design. It is also remarkable that a slight change of the angle of incidence significantly changes the phase profile, essentially introducing an horizontal shift of the curves. This provides us with an adjustment knob to shape the attosecond pulses.

3.4. Results of reflectivity measurements

The standard way to determine an XUV mirror reflectivity is to use a synchrotron beamline. We indeed performed such a measurement at ELETTRA over the $30 - 74 \text{ eV}$ spectral range. The results are displayed in Figure 7(f-h) and show an excellent agreement with the theoretical predictions above $35/40 \text{ eV}$. The reason for the slightly worse agreement on the lowest part of the spectrum is certainly the lack of precision on the optical indices of the deposited materials at these wavelengths [29].

Otherwise, Equation (4) predicts that such a result should be achievable with the combined measurements of the outgoing intensities of an HHG-based source reflected off a reference mirror and off the mirror to be characterized. Such an achievement would provide a full characterization (amplitude and phase) of the mirror on the same spot and at the same time, without risking any pollution through venting chambers and transporting mirrors from one setup to the other or avoiding any aging of the multilayers. In the remaining of this paragraph we address this question of measuring reflectivities on a harmonic line.

The use of Equation (4) to determine the reflectivity of a multilayer mirror requires the knowledge of the reflectivity of a reference mirror, which is itself determined by an equation analogous to Equation (2), where the intensity of the source comes into play. Again, the whole difficulty is to characterize the amplitude of the HHG source, which requires well calibrated reflective optics. To get out of this vicious circle we proceeded in two steps, resorting to the synchrotron measurements. First, we measured the intensity

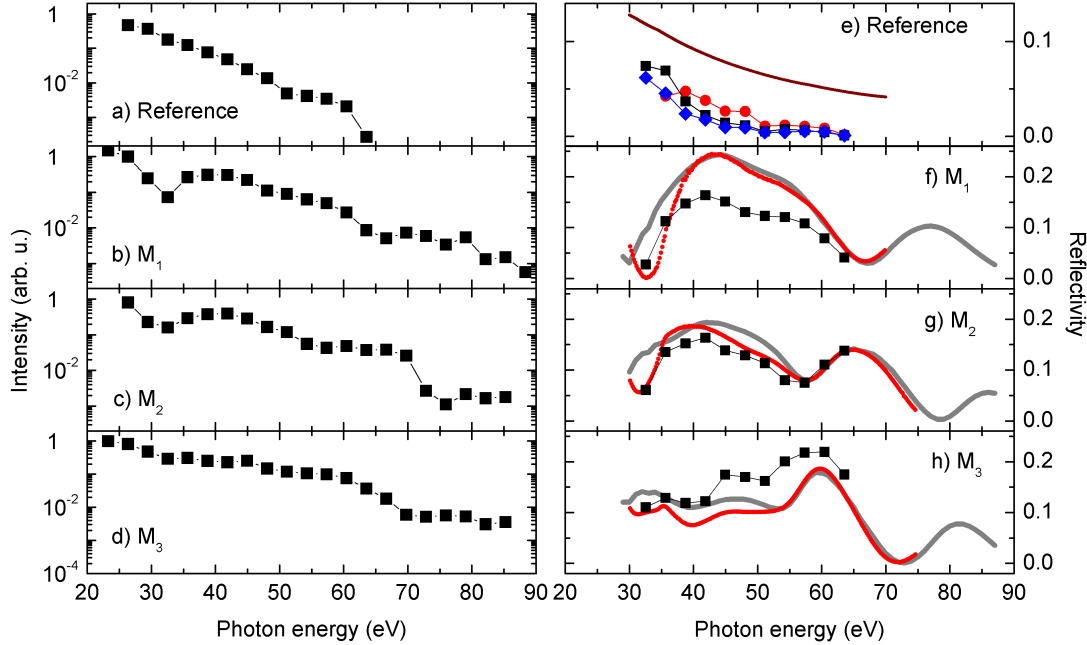


Figure 7. (Left column) Harmonic intensity measured with the photoelectron spectrometer after reflection off a silver mirror (a), M_1 (b), M_2 (c) and M_3 (d). The intensities are normalized to 1 for the first detected harmonic. (Right column, top) Reflectivities of the silver mirror as tabulated in the CXRO database (brown line) and deduced using Equation (4) with $I_n^{out}(\omega)$ measured with the silver mirror, $I_{ref}^{out}(\omega)$ and R_{ref} measured respectively on the harmonic and synchrotron lines using M_1 (red circles), M_2 (black squares) and M_3 (blue diamond). Reflectivities of the multilayer mirrors predicted (gray lines), measured on the synchrotron line (full red circles) and measured on the harmonic line (full black squares) for M_1 (f), M_2 (g) and M_3 (h).

of the outgoing harmonic field after reflection off all four mirrors (Figure 7 (a-d)). Based on the excellent agreement between the theoretical predictions and the measurements carried out at ELETTRA on the multilayer mirrors, we temporarily exchanged the roles of the reference and multilayer mirrors. Taking the ratio of the curve in Figure 7(a) and one of the three displayed in Figure 7(b-d), we could calculate three tentative reflectivities for the silver mirror, using each of the multilayer mirrors reflectivities determined with the synchrotron source as a reference in Equation (4). The results are displayed in Figure 7(e) along with the data taken from the CXRO database. The abscissa limits are given, for the lowest by the spectral range accessible at ELETTRA, and for the highest by the detection limit of HHG after reflection off the silver mirror. Although the results showed a degraded reflectivity of the silver mirror as compared to the CXRO database – which supports again the presence of an hydrocarbon layer deposited on the surface – the overall shape of the reflectivity is retrieved for all three “references”, showing a pattern very similar to the tabulated one.

As a second step, to calculate the reflectivity of one given multilayer mirror, we used again Equation (4). Here we took as a reference the average of the reflectivities of the silver mirror obtained using the two other multilayers mirrors, thus avoiding any self-referencing. The results are displayed in Figure 7 (f-h). The measurements on the attosecond beamline and the theoretical predictions have the same shapes: they clearly display – at the right locations – the dips and humps which are not present in the reference mirror reflectivities, but are stringent in the theoretical predictions about the multilayer mirrors. This observation supports the validity of the protocol and make further use of these silver calibration data sounded for the characterization of new multilayer mirrors. The agreement for the amplitudes is fairly good as well for M_2 and M_3 . The case of M_1 is more questioning, showing a discrepancy of a factor of almost two for the reflectivity all through the central range. The reason for this discrepancy in amplitude remains unclear, but we suspect it to be related to a slight miscontrol of the IR-intensity of the source while collecting one reference data. However, since all three references mainly disagreed by the amplitude and not so much by their shape as above mentioned, the disagreement on the multilayer reflectivity almost solely appear on the amplitude, not on the structure of the curve.

As a conclusion, a well control HHG-based source is therefore a promising alternative to synchrotron lines for measuring the reflectivity of XUV mirrors, and is very well suited for determining their phase behavior. The latter is almost perfectly reproduced, while the former shows the right pattern though with an amplitude disagreement that could certainly be fixed by controlling more precisely the generating conditions. Using HHG-based characterization beamlines thus offers a unique combined measurement of both parts of the complex reflectivity of reflective optics at once.

4. Spectro-temporal analysis of the phase and pulse-shaping

4.1. Higher order phase terms and GD dips

In agreement with the calculations, the multilayer mirrors experimentally showed unprecedented features, especially on the phase, such as linear phase, positive and negative GDDs, GD dips or third order dispersion (TOD) defined as $\frac{dGDD(\omega)}{d\omega}$. This opens the door for a full range of pulse shaping functions in the temporal domain. To investigate the new possibilities offered, we focus in this section on filtering out numerically a given portion of the spectrum with a square-shape filter introducing no-phase. We used the measured harmonic GDs (Fig. 6 (d-f)) and intensities (Fig. 7 (b-d)) as input parameters, and propagated them through a square-shape filter which limits were adjusted to highlight specific features. It is worth noting that the latter filter is the only non experimental data.

First, the protocol is applied to exemplify the effect of a GD dip such as the ones that appear in M_1 's profile about 31 eV and 64 eV. Selecting either the first GD dip or not, we observe that a double pulse is progressively turned into a single pulse (Figure 8

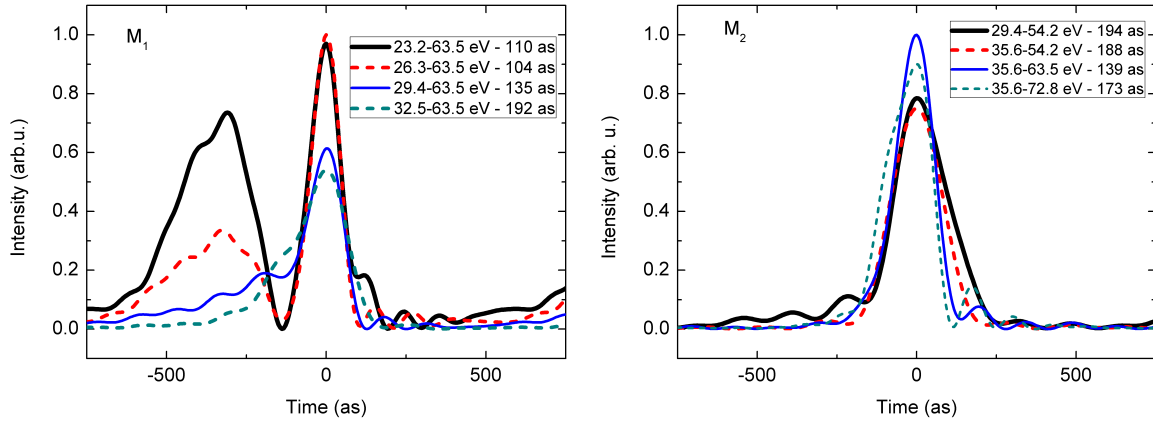


Figure 8. Temporal profiles reconstructed after the selection of a given portion of the spectrum of the harmonic source by a square amplitude filter after reflection off M_1 (left) and M_2 (right).

(left)). The relative weights of the two pulses is a consequence of the relative intensity of the involved harmonics. It should be noted as well that the spectral content of both pulses is different. In this specific case of M_1 , the pulse remaining after the exclusion of the dip shows a shoulder that is the well-known consequence of a remaining GD (see e.g. Ref. [15] [30]). As a counter example, when selecting a flat portion of the GD curve after reflection off M_2 , a Fourier-transform pulse is obtained (Figure 8 (right, red)).

Second, the case of M_2 also nicely illustrates the effect of a TOD. The two selections (29.4 eV-54.2 eV) and (35.6 eV-63.5 eV) correspond to two zones of opposite curvature (TOD) of the GD curves. It is not surprising, just like in the femtosecond case, some secondary bounds are observed on either side of the main pulse, depending on the sign of the TOD (Figure 8 (right)). Finally, the last case (35.6 eV-72.8 eV) corresponds to a fourth-order phase, showing both bounces and widening.

This analysis shows the greater than ever deal of functions that may be achieved by such mirrors. Moreover, as shown in Figure 6, the phase properties are highly dependent on the mirror orientation. Based on the reliable theoretical predictions shown above, in the following we build upon this statement to assess the feasibility of a temporal XUV pulse shaper.

PAPER IV

Control of the attosecond synchronization of XUV radiation with phase-optimized mirrors

C. Bourassin-Bouchet, Z. Diveki, S. de Rossi, E. English, E. Meltchakov, O. Gobert, D. Guenot, B. Carré, F. Delmotte, P. Salières, and T. Ruchon
Optics Express **19**, 4 (2010).

Control of the attosecond synchronization of XUV radiation with phase-optimized mirrors

C. Bourassin-Bouchet,^{1,*} Z. Diveki,² S. de Rossi,¹ E. English,² E. Meltchakov,¹ O. Gobert,² D. Guénot,² B. Carré,² F. Delmotte,¹ P. Salières,² and T. Ruchon²

¹Laboratoire Charles Fabry, Institut d'Optique, Université Paris-Sud, CNRS, 2 Avenue Augustin Fresnel, 91127 Palaiseau, France

²CEA-Saclay, IRAMIS, Service des Photons, Atomes et Molécules, 91191 Gif-sur-Yvette, France

*charles.bourassin-bouchet@institutoptique.fr

Abstract: We report on the advanced amplitude and phase control of attosecond radiation allowed by specifically-designed multilayer XUV mirrors. We first demonstrate that such mirrors can compensate for the intrinsic chirp of the attosecond emission over a large bandwidth of more than 20 eV. We then show that their combination with metallic foils introduces a third-order dispersion that is adjustable through the mirror's incidence angle. This results in a controllable beating allowing the radiation to be shaped from a single to a series of sub-100 as pulses.

© 2011 Optical Society of America

OCIS codes: (120.5050) Phase measurement; (230.4170) Multilayers; (320.5540) Pulse shaping; (340.7480) X-rays, soft x-rays, extreme ultraviolet (EUV).

References and links

1. F. Krausz and M. Ivanov, "Attosecond physics," *Rev. Mod. Phys.* **81**, 163–234 (2009).
2. C. Froehly, B. Colombeau, and M. Vampouille, "Shaping and analysis of picosecond light pulses," *Prog. Opt.* **33**, 65–153 (1983).
3. P. Tournois, "Acousto-optic programmable dispersive filter for adaptive compensation of group delay time dispersion in laser systems," *Opt. Commun.* **140**, 245–249 (1997).
4. M. Ferray, A. L'Huillier, X. F. Li, L. A. Lompre, G. Mainfray, and C. Manus, "Multiple-harmonic conversion of 1064 nm radiation in rare gases," *J. Phys. B* **21**, L31–L35 (1988).
5. A. McPherson, G. Gibson, H. Jara, U. Johann, T. S. Luk, I. A. McIntyre, K. Boyer, and C. K. Rhodes, "Studies of multiphoton production of vacuum-ultraviolet radiation in the rare gases," *J. Opt. Soc. Am. B* **4**, 595–601 (1987).
6. Y. Mairesse, A. de Bohan, L. J. Frasinski, H. Merdji, L. C. Dinu, P. Monchicourt, P. Breger, M. Kovacev, R. Taïeb, B. Carré, H. G. Muller, P. Agostini, and P. Salières, "Attosecond synchronization of high-harmonic soft x-rays," *Science* **302**, 1540–1543 (2003).
7. K. Varjú, Y. Mairesse, P. Agostini, P. Breger, B. Carré, L. J. Frasinski, E. Gustafsson, P. Johnsson, J. Mauritsson, H. Merdji, P. Monchicourt, A. L'Huillier, and P. Salières, "Reconstruction of attosecond pulse trains using an adiabatic phase expansion," *Phys. Rev. Lett.* **95**, 243901 (2005).
8. K. Varjú, Y. Mairesse, B. Carré, M. B. Gaarde, P. Johnsson, S. Kazamias, R. López-Martens, J. Mauritsson, K. J. Schafer, Ph. Balcou, A. L'Huillier, and P. Salières, "Frequency chirp of harmonic and attosecond pulses," *J. Mod. Opt.* **52**, 379 (2005).
9. J. Tate, T. Augustine, H. G. Muller, P. Salières, P. Agostini, and L. F. DiMauro, "Scaling of wave-packet dynamics in an intense midinfrared field," *Phys. Rev. Lett.* **98**, 013901 (2007).
10. W. Boutou, S. Haessler, H. Merdji, P. Breger, G. Waters, M. Stankiewicz, L. J. Frasinski, R. Taïeb, J. Caillat, A. Maquet, P. Monchicourt, B. Carré, and P. Salières, "Coherent control of attosecond emission from aligned molecules," *Nat. Phys.* **4**, 545–549 (2008).

11. X. Zhou, R. Lock, W. Li, N. Wagner, M. M. Murnane, and H. C. Kapteyn, "Molecular recollision interferometry in high harmonic generation," *Phys. Rev. Lett.* **100**, 073902 (2008).
12. T. Ruchon, C. P. Hauri, K. Varjú, E. Mansten, M. Swoboda, R. López-Martens, and A. L'Huillier, "Macroscopic effects in attosecond pulse generation," *New J. Phys.* **10**, 025027 (2008).
13. K. T. Kim, C. M. Kim, M.-G. Baik, G. Umesh, and C. H. Nam, "Single sub-50-attosecond pulse generation from chirp-compensated harmonic radiation using material dispersion," *Phys. Rev. A* **69**, 051805 (2004).
14. R. López-Martens, K. Varjú, P. Johnsson, J. Mauritsson, Y. Mairesse, P. Salières, M. B. Gaarde, K. J. Schafer, A. Persson, S. Svanberg, C.-G. Wahlström, and A. L'Huillier, "Amplitude and phase control of attosecond light pulses," *Phys. Rev. Lett.* **94**, 033001 (2005).
15. E. Gustafsson, T. Ruchon, M. Swoboda, T. Remetter, E. Pourtal, R. López-Martens, Ph. Balcou, and A. L'Huillier, "Broadband attosecond pulse shaping," *Opt. Lett.* **32**, 1353–1355 (2007).
16. D. H. Ko, K. T. Kim, J. Park, J. Lee, and C. H. Nam, "Attosecond chirp compensation over broadband high-order harmonics to generate near transform-limited 63 as pulses," *New J. Phys.* **12**, 063008 (2010).
17. R. Szipocs, K. Ferencz, C. Spielmann, and F. Krausz, "Chirped multilayer coatings for broadband dispersion control in femtosecond lasers," *Opt. Lett.* **19**, 201–203 (1994).
18. A. Wonisch, T. Westerwalbesloh, W. Hachmann, N. Kabachnik, U. Kleineberg, and U. Heinzmann, "Aperiodic nanometer multilayer systems as optical key components for attosecond electron spectroscopy," *Thin Solid Films* **464-465**, 473–477 (2004).
19. A.-S. Morlens, Ph. Balcou, Ph. Zeitoun, C. Valentin, V. Laude, and S. Kazamias, "Compression of attosecond harmonic pulses by extreme-ultraviolet chirped mirrors," *Opt. Lett.* **30**, 1554–1556 (2005).
20. A.-S. Morlens, R. López-Martens, O. Boyko, Ph. Zeitoun, Ph. Balcou, K. Varjú, E. Gustafsson, T. Remetter, A. L'Huillier, S. Kazamias, J. Gautier, F. Delmotte, and M.-F. Ravet, "Design and characterization of extreme-ultraviolet broadband mirrors for attosecond science," *Opt. Lett.* **31**, 1558–1560 (2006).
21. E. Goulielmakis, M. Schultze, M. Hofstetter, V. S. Yakovlev, J. Gagnon, M. Uiberacker, A. L. Aquila, E. M. Gullikson, D. T. Attwood, R. Kienberger, F. Krausz, and U. Kleineberg, "Single-cycle nonlinear optics," *Science* **320**, 1614–1617 (2008).
22. S. Kirkpatrick, C. D. Gelatt, and M. P. Vecchi, "Optimization by simulated annealing," *Science* **220**, 671–680 (1983).
23. M. Yamamoto and T. Namioka, "Layer-by-layer design method for soft-x-ray multi layers," *Appl. Opt.* **31**, 1622–1630 (1992).
24. J. Gautier, F. Delmotte, M. Rouillay, F. Bridou, M.-F. Ravet, and A. Jérôme, "Study of normal incidence of three-component multilayer mirrors in the range 20–40 nm," *Appl. Opt.* **44**, 384–390 (2005).
25. A. Aquila, F. Salmassi, and E. Gullikson, "Metrologies for the phase characterization of attosecond extreme ultraviolet optics," *Opt. Lett.* **33**, 455–457 (2008).
26. M. Suman, G. Monaco, M.-G. Pelizzo, D. L. Windt, and P. Nicolosi, "Realization and characterization of an XUV multilayer coating for attosecond pulses," *Opt. Express* **17**, 7922–7932 (2009).
27. S. Haessler, B. Fabre, J. Higuier, J. Caillat, T. Ruchon, P. Breger, B. Carré, E. Constant, A. Maquet, E. Mével, P. Salières, R. Taïeb, and Y. Mairesse, "Phase-resolved attosecond near-threshold photoionization of molecular nitrogen," *Phys. Rev. A* **80**, 011404 (2009).
28. S. Haessler, J. Caillat, W. Boutou, C. Giovanetti-Teixeira, T. Ruchon, T. Auguste, Z. Diveki, P. Breger, A. Maquet, B. Carré, R. Taïeb, and P. Salières, "Attosecond imaging of molecular electronic wavepackets," *Nat. Phys.* **6**, 200–206 (2010).
29. S. Zamith, J. Degert, S. Stock, B. de Beauvoir, V. Blanchet, M. A. Bouchene, and B. Girard, "Observation of coherent transients in ultrashort chirped excitation of an undamped two-level system," *Phys. Rev. Lett.* **87**, 033001 (2001).

1. Introduction

The advent of attosecond sources in the early 2000's has triggered a great deal of interest in many scientific communities ranging from atomic and molecular physics to surface science and chemistry [1]. However, although the demand is high, the generalization of these sources has been hampered by the difficulty to manipulate and control such ultrashort pulses. Indeed, this combines two difficulties: first, the pulses are centered in the XUV spectral range where absorption of most materials is high; second, they cover a huge spectral range (20 eV are needed to sustain 100 as pulses) making them very sensitive to any dispersive element that would distort the spectral phase and consequently the attosecond structure. It thus remains a challenge to control this radiation, shape it in the temporal and spectral domains, propagate it and deliver it on target without losing too much flux.

Current femtosecond infrared (IR) pulse shaping techniques, which are based either on a 4-f

zero dispersion optical delay line [2] or on an acousto-optic programmable dispersive filter [3], cannot be directly transposed in the XUV because of absorption. Therefore, the attosecond pulse control possibilities have been very limited so far. At the source, one may tailor their generation conditions, *i.e.* control the nonlinear interaction of the strong laser field with the gas target that results in High-order Harmonic Generation (HHG) [4,5]. The laser parameters (intensity, wavelength) can be used to control the value of the intrinsic Group Delay Dispersion (GDD) and thus the chirp of the attosecond emission [6–9], but only in a limited range and without the possibility of introducing higher-order phase terms. The generating medium may also introduce spectral phase features, such as jumps or linear offsets, either on the molecular [10, 11] or macroscopic [12] levels, but with limited control over their position, amplitude and shape. Downstream, a post-control can be performed using dispersive media, such as metallic foils [13–15], plasmas [6] or atomic gases [16]. However, all these techniques suffer from a lack of versatility: they all depend on matching a spectrum to a given material. A more versatile control could be allowed by multiple interference effects as was performed in the IR region with chirped mirrors over sub-1 eV bandwidths [17]. Some steps have already been taken in that direction, through the design of XUV multilayer mirrors [18–20]. However no phase control over bandwidths of tens of eV has been demonstrated thus far, and chirped mirrors have not entered the attosecond realm. In this article, we report on the design and characterization of a toolset of mirrors that fulfill the four-fold objective: high reflectivity (10-20%) and phase control over 20-30 eV bandwidth, central energy of 50 eV where intense attosecond pulses can be generated, and 45° incidence to steer the beam. We show that such mirrors allow compensation for the intrinsic harmonic GDD, and thus compression of the attosecond pulses. Furthermore, their combination with standard metallic filters introduces third order dispersion opening new phase control opportunities. This allows for instance shaping the XUV pulse in the form of multi sub-100 as pulses. This attosecond beating is controllable through the mirrors' incidence angle.

2. Design of multilayer mirrors

The multiple beam interference effect occurring in the mirror structure provides a great deal of controls: one can adjust the alternating materials, thereby setting the Fresnel coefficients at each interface, the layer thicknesses, thereby setting the phase and group delays (GD), and the number of layers. Clearly, the greater the number of layers, the more comprehensive the control of the reflected field. However, the absorption of the materials in the 30-60 eV range limits the overall thickness of the stack to about 100 nm with approximately 10 layers (compared to up to 100 layers in the visible range). The first desirable function of a pulse shaper is the compensation of the intrinsic atto-chirp [6] in order to get Fourier-transform limited pulses. The second function would be to tailor the phase up to third order so as to design attosecond pulse shapes on demand, such as double or multiple pulses. All this, added to the targeted broad bandwidth, led us to include some extra liberty in the optimization process through the use of three materials, molybdenum, silicon and boron carbide, instead of the standard combination of two [21]. The optimization process used a metaheuristic, namely a simulated annealing algorithm [22] which took into account the behavior of the layers when they are stacked, such as their inter-diffusion and roughness. The evolution of the complex reflectivity of one optimized stack as one progresses through the mirror from the substrate is reported in Fig. 1 using the Yamamoto spiral [23].

The spiral actually turns around the Fresnel coefficients of the successive materials with an angular length and a variable radius determined by the layer thickness. In other words, the propagation through a layer modifies the accumulated phase and reflectivity at a given depth. It should be noted that Mo's reflectivity point is i) far away from the other materials' points, and

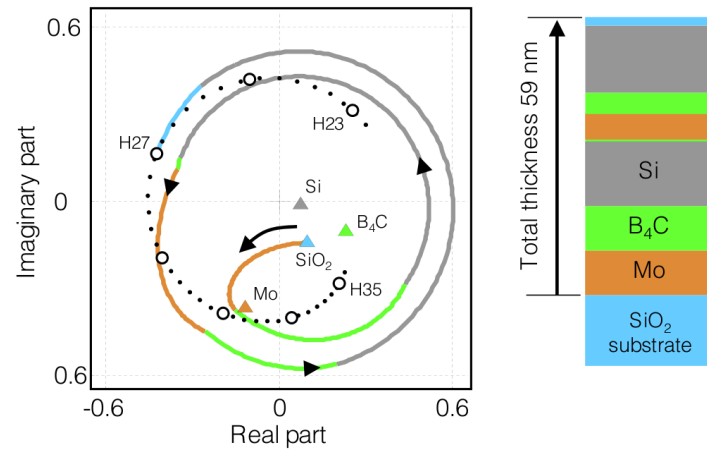


Fig. 1. Evolution of the complex reflectivity at an energy of 42 eV of the M_2 multilayer structure (shown on the right) as it is grown on the substrate (thick line colored depending on the layer). The Fresnel coefficients for the vacuum-material interfaces are shown in triangles. The end points of the spiral are displayed for 0.5 eV-spaced energies (dots) and for odd harmonic orders of an 800 nm laser (open circles).

ii) shifted along the imaginary axis due to high absorption. It thus plays a crucial role in shaping the phase and reflectivity of the stack. This representation also highlights the compromise that has to be made between the GDD and the reflectivity. Indeed when increasing the final silicon layer, the reflectivity becomes greater than 30% but the thickness of the layer is further increased to get the desired phase at this energy, even though it decreases the reflectivity to 20%. The spiral end points for harmonics 23-35 (36-54 eV) are reported in Fig. 1. The angular interval between two consecutive harmonics decreases with respect to the order, indicating a negative GDD of the mirror, as targeted in this case. Moreover the reflectivity remains high in this spectral range and does not vary much. It should be noted as well that the main effect is due to the mirror structure, *i.e.* interference effect, and not so much to the dispersion that slightly changes the position of the Fresnel coefficient points in Fig. 1 as the energy is varied. These simulations thus show that 3-material aperiodic mirrors have the capability to achieve our goal, *i.e.* broadband high reflectivity with controlled phase. To this aim, we optimized three mirrors on the 35-55 eV spectral range to get a constant GDD (M_1), with a theoretical reflectivity between 17% and 26%, or alternatively a $-4200 \text{ as}^2/\text{rad}$ (M_2) or a $-8500 \text{ as}^2/\text{rad}$ (M_3) GDD, with reflectivities greater than 11% on the optimized range. Their expected GDs calculated during the optimization are reported in Fig. 2 (Gray Lines). The mirrors coatings were deposited in a magnetron sputtering machine [24]. In order to guarantee a precision on the thicknesses better than 0.3 nm, we calibrated the deposition process with a grazing-incidence Cu-K α reflectometer.

3. Setup and experimental results

The mirrors' reflectivity was characterized using the BEAR beamline at the ELETTRA synchrotron. For all three mirrors, the measured reflectivity was close to the calculated one, as exemplified in Fig. 2(d) for mirror M_2 . The measurement of the mirrors' group delay is a much more difficult task that has become possible only recently, using either an indirect [25, 26] or

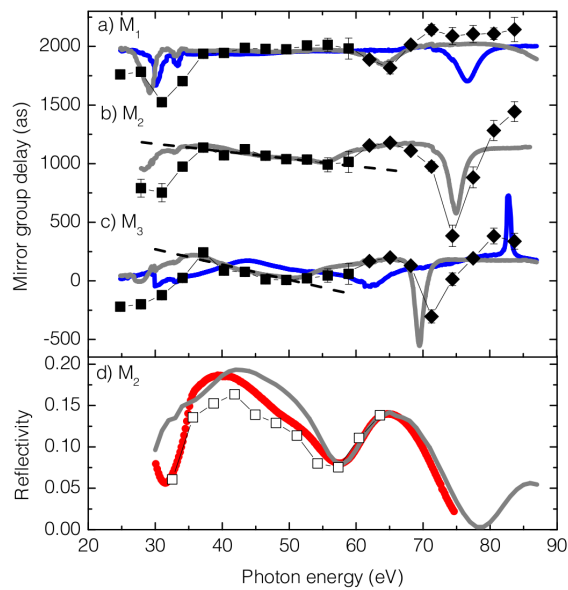


Fig. 2. Group delay (a-c) and reflectivity (d) of designed multilayer mirrors. In (a-c), the simulated GDs are plotted for 42° incidence (gray lines) and also for 52.5° in the case of M₁ and M₃ (blue lines). The GDs measured at 42° are reported in black squares (diamonds) when the experimental (extrapolated) reference was used. Dashed lines show linear fits performed over the optimized 35-55 eV range. The curves were vertically shifted for visibility; the GD absolute values were not measured in the experiment. In (d), the reflectivity of M₂ is plotted as a typical case: simulated (gray line), and measured reflectivity using HHG (open squares) and synchrotron radiation (red dots).

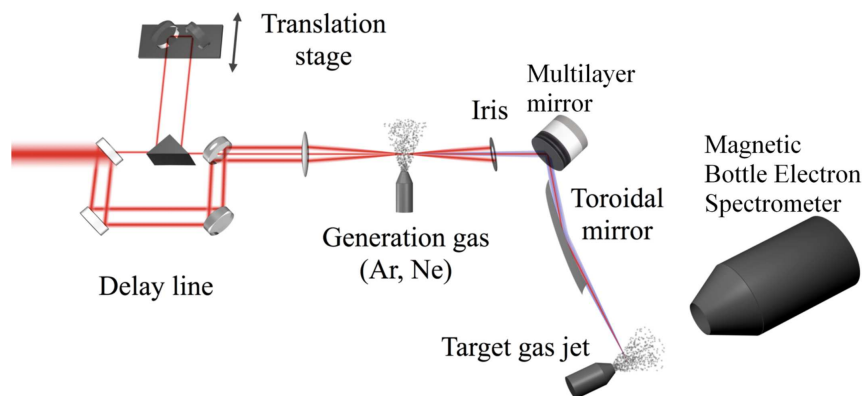


Fig. 3. Experimental setup on the attosecond beamline for the mirrors group delay characterization.

a direct [20] technique. The latter is very demanding since it requires both a broadband coherent XUV source and a group delay characterization setup. To do so, we used the attosecond beamline in CEA-Saclay, as described in Fig. 3. The 20 Hz, 50 fs, 800 nm LUCA laser beam first goes through a drilled-mirror-based interferometer which produces two beams of complementary shapes: one is ring-shaped and performs the high harmonic generation while the other, of much lower energy, is plain and provides the dressing beam for the RABITT measurement. Their relative delay can be finely adjusted by a piezoelectric delay stage. From the focusing lens on, the setup is placed under vacuum. The harmonics are generated in Ar or Ne gas jets which come out of a nozzle controlled by a piezoelectric crystal. To get rid of the intense generating beam, an iris is set after the gas jet. Its opening size is small enough to cut out the annular generating beam but large enough to let through the XUV radiation and the dressing beam. Both beams are then reflected off either the multilayer mirror or a reference silver mirror set at 42° and finally focused by a toroidal mirror at grazing incidence angle in the target gas (Ne). The electrons produced through two-photon XUV+IR photoionization are detected in a time-of-flight magnetic bottle electron spectrometer. The compactness of the setup results in a high stability but excludes placing any full metallic foil (like an aluminum filter for spectral selection) that would also block the infrared dressing beam used for the RABITT measurement. The RABITT temporal characterization technique [20], as opposed to the photocurrent technique [25,26], is very effective in this spectral range at this incidence angle and has proven to be extremely sensitive to phase jumps [27,28]. We first calibrated the reference mirror by comparison with “direct” measurements involving only grazing incidence reflections: it induces a $+5300 \text{ as}^2/\text{rad}$ GDD that adds to the intrinsic $+6300 \text{ as}^2/\text{rad}$ GDD of the neon attosecond emission. This was attributed to a hydrocarbon layer adsorbed on the mirror. Then, comparing the GDs measured on a beam reflected off a given multilayer mirror and off the reference silver mirror, we obtained the GDs reported in Fig. 2(a-c). The overall agreement with the simulations is excellent for the three mirrors: in the optimized 35-55 eV range, the XUV light can be reflected either with no phase distortion (M_1), or alternatively with a $-4200 \text{ as}^2/\text{rad}$ (M_2) or a $-8500 \text{ as}^2/\text{rad}$ (M_3) GDD. To illustrate this point, we plot in Fig. 4 the amplitudes and group delays of the harmonics reflected off M_2 and off the silver mirror. As expected, M_2 efficiently compensates for the intrinsic GDD of the harmonics, giving a flat GD in the 35-55 eV range.

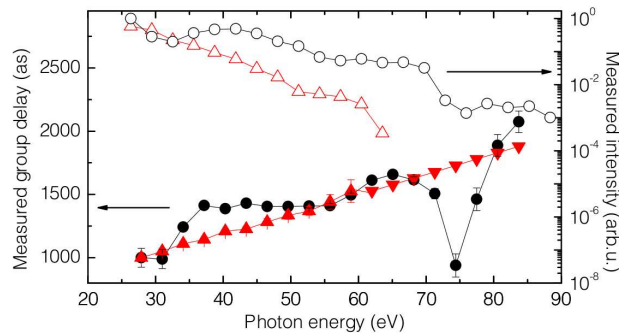


Fig. 4. Spectral intensity (open symbols) and GD (filled symbols) measured in the detection region after reflection off the Ag reference mirror (up triangles) and off M_2 (circles). The Ag low reflectivity above 65 eV prevented measurement of the GD. It was thus linearly extrapolated following [6] (down triangles): indeed the intrinsic harmonic GD was shown to vary linearly with harmonic order in the plateau region. Both GD curves are shifted to get the GD of sideband 18 (28 eV) at 1000 as.

4. Temporal reconstruction and discussion

As explained in the setup description, the RABITT version used in our measurements allows a broadband spectral characterization of the XUV radiation but is not compatible with spectral filtering. However, using i) tabulated values for the complex transmission of metallic foils, and ii) the measured spectral amplitudes and group delays, we can reconstruct reliably by Fourier transform the shape of the resulting attosecond pulses. First, in order to evidence the different effects generated by the mirrors on the attosecond pulse structure, we introduced numerically an amplitude filter. It was chosen to have a square shape, encompassing the common spectral range of measurements of all mirrors, namely 32.5-63.5 eV. The results are displayed in Fig. 5(a). The 135 and 123 as-long pulses obtained after reflection off M_2 and M_3 respectively are twice as short, and five times more intense than the one reflected off the reference mirror. As expected, mirror M_1 which does not compensate for the intrinsic chirp, gives a significantly different pulse shape and duration mainly due to the remaining GD of the radiation. This enlightens the crucial effect of the phase control achieved with M_2 and M_3 . Note that for M_2 (resp. M_3), by adding a few harmonic orders on both sides of the optimized 35-55 eV range where the GD smoothly deviates from the constant value, a pulse duration close to the Fourier transform limit of 124 as (resp. 115 as) is still obtained.

Second, Fig. 5(b) shows the pulse profiles that would be obtained in a realistic attosecond experiment where the harmonic radiation would be spectrally filtered using a standard 250 nm-thick aluminum filter. Its complex transmission is calculated from tabulated indices. The full band pass of the Al filter is considered, from its cut-on at 17 eV to its cut-off at 73 eV. Due to the lack of experimental data near the cut-on of the filter, the theoretical GDs and reflectivities of the mirrors were used below 20 eV. Above 30 eV, only measured data were used. In the intermediate range the two were averaged to achieve continuity. In the three cases, the pulse durations are reduced resulting in sub-100 as pulses. The reason for such a pulse shortening is that the negative GDD of Al below 35 eV compensates for the intrinsic GDD of the harmonic emission in this spectral range. To be more specific, the combination of the filter and mirrors M_2 or M_3 allows a phase compensation over a large spectral bandwidth that shortens the attosecond pulse down to 85 as, close to the Fourier limit of 74 as. As for M_1 , the main peak is followed by replicas of decreasing amplitudes. Identifying the source of such a beating and controlling it through the introduction of a new degree of freedom, namely the angle of incidence on the mirror, make it possible to achieve attosecond pulseshaping, as described below.

5. Controlling sub-100 as beating

By modifying the angle of incidence θ , one controls the spectral phase of the mirror, as exemplified in Fig. 2(a,c). Indeed the accumulated phase through the layers varies as $\cos\theta$, *i.e.* the mirror's response will be highly sensitive around $\theta \simeq 45^\circ$. This turns into a great advantage of these mirrors: when paired together, they form a pulse shaper that may be adjusted simply by turning a rotation stage (inset in Fig. 6(a)). This allows fine control of the GDD above 35 eV. The aluminum filter introduces an important GDD below 35 eV (Fig. 6(b)). By combining the filter and the mirrors, the GDD control can be extended over a larger bandwidth, resulting in shorter attosecond pulses. Alternatively, one can design conditions where the two spectral regions have opposite GDDs, resulting in third-order dispersion (TOD) and attosecond beating, as will be shown below.

Taking as an incoming radiation the harmonic spectrum and GD deduced at the source from "direct" measurements, and using tabulated values for the Al filter response, we calculated the temporal profiles of the pulses outgoing the pulse shaper (Fig. 6(a,c)). In the first configuration, M_1 and M_3 are combined. The pulse reconstructed for $\theta = 42^\circ$ consists of a main 85 as pulse followed by two weak replicas (Fig. 6(a)). Since the experimental results of Fig. 2 showed a

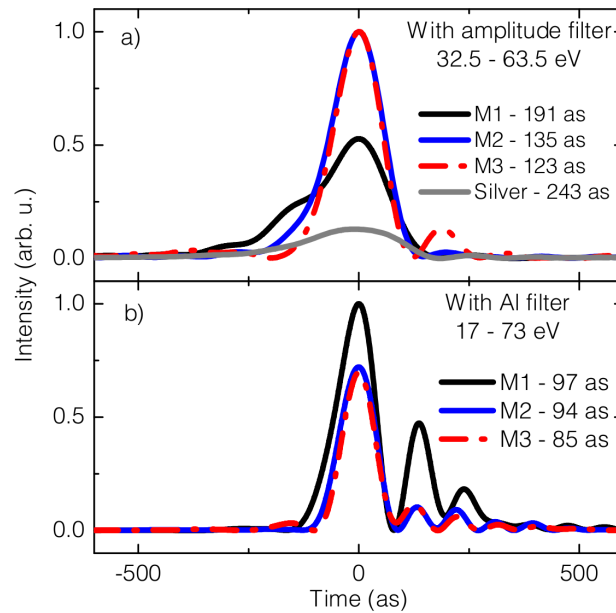


Fig. 5. Temporal reconstruction of attosecond pulses after reflection off the mirrors using the data displayed in Fig. 4 and the corresponding ones for M_1 , M_3 and the reference mirror when considering (a) only the 32.5 - 63.5 eV range, or (b) the transmission through a 250 nm-thick aluminum filter. The full width at half maximum is indicated for each pulse.

good agreement with theoretical predictions, we can reliably simulate the behavior of the mirrors for higher incidence angles. Increasing θ makes double sub-100 as pulses appear with variable relative intensities, as reported in Fig. 6(a). Now changing the M_3 mirror for a second M_1 -type mirror (2nd configuration), we can extend the tunability to get multiple sub-100 as pulses as exemplified in Fig. 6(c) for $\theta = 52.5^\circ$.

The reason for the observed attosecond beating lies in the phase profiles of the outgoing radiation (Fig. 6(b)). In the 15-35 eV range, which lies close to the onset of the Al transmission, the initial positive GDD is overcompensated by the dispersion of the filter and either brought back towards zero by M_3 or slightly affected by M_1 . In the 35-73 eV range, the initial GDD is barely affected by the filter and M_1 , but is decreased by M_3 , depending on θ . Altogether, the final group delay may then be approximated by two linear zones with slopes of opposite signs and is fitted by a second order polynomial. The highest order corresponds to third-order dispersion (TOD). The TOD value can be adjusted from $3.1 \times 10^5 \text{ as}^3/\text{rad}^2$ to $5.7 \times 10^5 \text{ as}^3/\text{rad}^2$ by varying the incidence angle and the mirrors. Further insight can be gained in the temporal domain: Fig. 6(c) shows the temporal profiles and instantaneous frequencies, calculated for the two aforementioned spectral ranges in the second configuration. The chirps of the two pulses have opposite signs, following those of the GDDs. The difference in instantaneous frequencies increases with time from $\delta\omega \simeq 15 \text{ eV}$ to $\delta\omega \simeq 42 \text{ eV}$. It leads to a beating of the coherent sum of the two pulses with a period $T = 2\pi/\delta\omega$ decreasing from 260 as to 100 as. The resulting pulse durations ($\simeq T/2$) nicely match the values in Fig. 6(c). By precisely tailoring the chirp in the different spectral regions, we can thus finely control the attosecond beating.

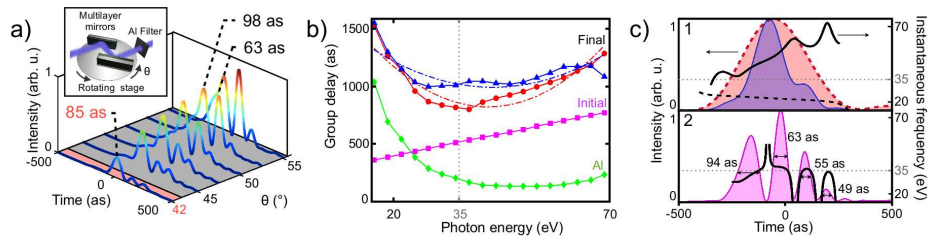


Fig. 6. Attosecond pulse shaping using a tunable pulse shaper based on a rotating pair of multilayer mirrors and an aluminum filter (inset): (a) Temporal profiles obtained using M_1 and M_3 for different angles of incidence θ . The reported durations are the full widths at half maximum. (b) GD curves of the HHG source (purple squares), the Al filter (green losanges), the outgoing radiation from the pulse shaper in the 1st configuration at 42° (blue triangles), in the 2nd configuration at 52.5° (red circles), and the corresponding second order fits for the latter two (dashed-dotted lines) (c) Study of the 52.5° case in (b): temporal profile (shaded curves) and instantaneous frequency (lines) for (1) the 15-35 eV spectral range (dotted lines), and the 35-73 eV range (solid lines), (2) the pulse corresponding to the coherent superposition of the previous pulses.

6. Conclusion

In conclusion, we have manufactured broadband aperiodic multilayer chirped XUV mirrors using a combination of three materials (Mo, Si, B_4C). Utilized with metallic filters, these mirrors allow unprecedented control of the phase and amplitude in a broad XUV spectral range; this results in a variety of attosecond pulse-shaping functions, such as pulse compression and attosecond beating (related to second and third order dispersion), that can be controlled by changing the incidence angle on the mirrors. This opens manifold perspectives. First it may allow the production of much shorter attosecond pulses than currently available. Indeed, the harmonic plateau extends over hundreds of eV and could sustain pulses much shorter than the atomic unit of time if the intrinsic atto-chirp were properly compensated for. Our phase-controlled mirrors, when combined with the currently used compensation techniques, will allow a phase control over larger bandwidths. Second, the demonstrated pulse shaping opens the possibility of extending coherent quantum control to the extreme ultraviolet and attosecond domains. For instance, coherent transient enhancements of a resonant transition [29] could be induced by adjusting the chirp of the XUV pulse. Finally, a new type of attosecond pump-probe experiments would be made possible by finely controlling the delays between the peaks in the multipulse.

Acknowledgments

We thank S. Nannarone, N. Mahne and A. Giglia for assistance at Elettra Sincrotrone Trieste, T. Auguste and P. Breger for their help on the CEA experiment. We acknowledge financial support from the EU-FP7-ATTOFEL, ANR-09-BLAN-0031-01 and RTRA-Triangle-2008-045T.

4.1 Conclusion

We have presented the spectral characterization of chirped XUV multilayer mirrors which provide high throughput ($\approx 20\%$) in the XUV domain and application-specific phase control over large bandwidths (≥ 20 eV). We could demonstrate their capability of controlling the spectral phase of the incoming pulse up to high order dispersion terms. In the optimized spectral range we presented i) the compensation of the attochirp, ii) the appearance of double peaked pulses and iii) of multiple peaks, due to TOD. Finally we proposed a novel attosecond pulse shaper based on the combination of a pair of these mirrors with an Al filter installed on a rotational stage. Our simulations showed that by changing the angle of incidence, this pulse shaper changes its dispersion characteristics and may provide easily controllable single or multiple peaked attosecond pulses.

CONCLUSIONS AND PERSPECTIVES

This thesis relies on the results obtained by generating and characterizing high order harmonics from gas phase atoms and molecules. We had two main objectives: a) To study molecular structures and intra-molecular charge rearrangements with Ångström-spatial and as-temporal resolution using the self-probing scheme; b) To develop pulse shaping techniques on the attosecond timescale using chirped XUV multilayer mirrors. Here, we give a general summary of the presented experimental and theoretical results and discuss the perspectives that they offer.

Self-probing scheme

The central subject of Chapter 3 is the self-probing technique and its application to retrieve the complex recombination dipole moment of N₂ molecule and identify multi-orbital contributions to HHG. We used molecular orbital tomography to reconstruct the molecular orbitals from the measured recombination dipole moments. There are several technical and theoretical requirements that have to be met in order to perform proper molecular orbital tomography:

(i) The high-order harmonic emission induced by an intense laser beam can be used as a molecular benchmark. The characteristics of the recombination dipole are imprinted in the harmonic spectral intensity and phase of both parallel and perpendicular components to the driving laser field. Complete characterization of the harmonic emission thus gives access to the complex recombination dipole in the molecular frame. In section 3.5, we presented the first experimental realization of such kind of harmonic characterization.

(ii) The extraction of the orbitals' RDM from the harmonic signal requires the calibration of the tunnel ionization and the continuum acceleration steps. A reference atom with known RDM and with an ionization potential equal to the ionization potential of the molecule fits well this task. It eliminates the problem of characterizing the spectral response of the detector as well. But, in general there are no reference atoms for all molecules, hence theoretically constructed references are needed. Furthermore, any structural features, like Cooper minima or resonances (Shiner et al. [145]), may spoil the orbital reconstruction if the reference RDM is not precisely calculated. In general, these effects have to be taken into account during the calibration, but by choosing the observed spectral range properly, they can be avoided. Finally, real reference atoms do not account for the angular dependence of the tunnel ionization rate of molecules, that has to be retrieved either theoretically or by measurements.

(iii) The detected harmonic signal is the result of an averaging process of the single molecular response over the imperfect alignment distribution of the molecules. Unless having high alignment degrees, one has to deconvolve the macroscopic signal to obtain the angular dependence of the single molecule radiating dipole. The techniques listed in section 3.4 make this all possible.

(iv) For symmetric molecules the reconstruction of a molecular orbital requires knowledge of the orbital symmetry. In a general case, it would be unknown, hence this is an experimental issue. It requires control over the trajectory of the tunnel ionized electron in HHG, to transfer the information on a possible sign change between the lobes of the orbital into the harmonics' phase or polarization. It is probable that an additional second order harmonic laser beam with controllable delay with respect to the driving laser and polarized perpendicular to it meets the requirements (Shafir et al. [142]). Another approach for the symmetry determination is based on the a priori knowledge of the relation between the orbital symmetry and the polarization map of the harmonics, as proposed by (Hijano et al. [50]). For asymmetric molecules, one needs to perform orientation and to probe the molecules only from one side (e.g. by breaking the symmetry of the laser field thanks to addition of second harmonic) (van der Zwan et al. [166]). Then the complete characterization of the Fourier space is required, $\theta = 0^\circ, \dots, 360^\circ$.

(v) The idea of molecular orbital reconstruction is brilliant, but the main assumption of PWA cannot be generalized. Therefore, improvement on the orbital reconstruction from the recombination dipole moment is inevitable. The first step of such an improvement was developed by (Vozzi et al. [172]) and presented in section 3.2.3.

(vi) If more than two orbitals are contributing to the harmonic generation, orbital reconstruction becomes impossible. When two orbitals are playing a role, one has to find proper experimental conditions where their contributions are disentangled into the real and imaginary parts of the measured calibrated dipole. Nevertheless, by decreasing the intensity of the generating laser pulse, one may end up with single contributing orbital, due to the exponential behavior of the tunnel ionization (as we showed it in section 3.3). Another and possibly more suitable approach is to generate harmonics with longer wavelength lasers (in the mid infra red region). Their advantage is that they can produce large harmonic spectra even with low intensities, but the price to pay is the low harmonic signal. Probably, these lasers are the future path for molecular orbital tomography.

(vii) Even though the precision of the reconstructed orbitals is limited by the above-mentioned problems, we believe that tomographic reconstruction has a big potential for measuring temporal evolution of an orbital during for example a chemical reaction. Observing the ultrafast distortions on the attosecond/femtosecond time scale would be a big step forward, even with a limited spatial resolution. Alternatively, chemical imaging with iterative techniques has been proposed theoretically by (Le et al. [81]) to investigate, e.g., the isomerization of acetylene into vinylidene.

Besides time resolved and static orbital reconstructions, the self-probing scheme is perfect to investigate the dynamics of the intra-molecular charge redistribution. As we proposed in PAPER I, multi-orbital contributions enable the detection of electronic hole dynamics on the attosecond time scale. Unfortunately, the very basic principles of physics tell us that both high spatial and temporal resolutions cannot be achieved simultaneously. Large spectral bandwidths provide unprecedented spatial resolutions, but due to the time-energy mapping of harmonics it provides large exposition times as well. However, we demonstrate that a compromise can be found to reach \AA spatial and 600 as temporal resolution.

Besides the induced electronic dynamics, multi-orbital contributions may involve wide range of vibrational effects. As discussed in PAPER II, in the case of "heavy" molecules,

the different ionization channels have different nuclear dynamics that can be read out from the phase of the harmonics.

Based on the discussion above, we may conclude that the self-probing scheme and the molecular orbital tomography are still in their infancy having plenty room for developments. It is a huge challenge to fulfill the above mentioned requirements, but they may provide high reward in return.

Pulse shaping on the attosecond time scale

The applications of ultra-short pulses are many-fold and sometimes require predefined temporal and spatial profile. This thesis discussed the control of the temporal profile on the attosecond time scale.

There are several obstacles that have to be overcome in order to perform a versatile control over the temporal profile of attosecond pulses. First, attosecond pulse generation requires the generation of large (at least several eVs) spectrum with synchronized phase. Up to now attosecond pulses are obtained through HHG and the central frequency was located in the XUV spectral range. Second, pulse shaping requires control of the spectral amplitude and phase over this large spectral range. It can be achieved through several approaches: i) by controlling the HHG conditions through the generating laser intensity and by choosing different target media; ii) by inserting different materials into the XUV beam line after HHG that affect the spectral features of the pulse, like metallic foils or noble gas cells. Unfortunately, all the optical materials are highly absorbing in the XUV domain.

Our approach consisted in developing (in collaboration with Institut d'Optique) broadband XUV multilayer mirrors with a controlled dispersion. 3 different chirped mirrors were designed for different spectral responses in an optimized spectral range between 35 eV and 55 eV. The use of three different materials, Si, Mo and B₄C, to construct the mirror layers, provided more than 20% reflectivity in the optimized range when installed at 45° angle of incidence. Concerning their dispersion, the first one was designed to be flat, to barely affect the incident beam, the second to compensate a GDD of 4200 as²/rad and the third to compensate a GDD of 8500 as²/rad in the optimized range. These properties were confirmed by our characterization experiments using the MBES+TOF and RABBIT.

Our experimental setup did not allow the use of filters to measure exactly the pulse durations. Therefore we performed numerical spectral filtering on the measured data. We showed that these mirrors are indeed affecting the temporal profile of the generated XUV pulses and are able to control the spectral phase even up to the third order dispersion factors. Our simulations showed that both the spectral amplitude and phase can be controlled over a large spectral range by changing the incidence angle. Therefore, we proposed a novel attosecond pulse shaper based on a rotational stage equipped with two chirped XUV multilayer mirrors plus an Al filter. By changing the incidence angle, the temporal profile of the outgoing pulse can be changed from a single peak to double or multiple peaks.

Perspectives - Future experiments

Molecular orbital tomography is a promising tool to determine molecular structures. Its pure experimental realization is still a big challenge. In section 3.5 we presented the most complete recombination dipole moment characterization, up to now, in intensity, spectral phase and polarization state. The angular phase still needs to be measured. Fortunately, the techniques to do this are already developed. The latter phase can be observed with the two source technique (Smirnova et al. [147]) or with mixed gases (McFarland et al. [104]). The only and very severe criterion of the RDM characterization is to be completed in the same experimental conditions.

N_2O could be the next target to perform molecular orbital tomography because of several reasons. It is quite easy to handle experimentally and (Lock et al. [95]) showed with the two source technique, that structural phase jump can be observed around 51 eV. The structural phase jump is related to the lobe structure of the molecule, and is essential for the tomographic reconstruction. N_2O is a slightly asymmetric molecule, therefore molecular orientation is in principle needed (see point (iv) above). It also provides an opportunity to perform time dependent molecular orbital tomography because by irradiating it with a photon of energy $E \geq 3.5$ eV photodissociation can be induced: $\text{N}_2\text{O} \rightarrow \text{N}_2 + \text{O}$. By changing the delay between the photoionizing beam and the generating beam, in principle one could follow the evolution of the non dissociated orbital structure into the dissociated one. However, one of the great difficulties is to separate the harmonic signal coming exclusively from the N_2O , N_2 and O components. (Wörner *et al.* [178]) showed that by using transient grating techniques to induce dissociation of Br_2 molecules the problem of harmonic signal separation can be resolved.

A major technical issue for performing time-resolved tomography is the long acquisition time. A single orbital reconstruction as performed in sections 3.1 and 3.5 on the 20 Hz LUCA laser took more than 2 hours (10 alignment angles RABBIT measurements lasting 15 minutes each). It is thus necessary to transfer all these techniques to a laser system with higher repetition rate. The new beam line in Saclay called 'Plate-forme Lasers Femtosecondes Accordables' (PLFA) with its 13 mJ energy per pulse, 35 fs pulse duration and 1 kHz repetition rate is a promising setup to perform molecular orbital tomography with full experimental characterization. A reliable RABBIT scan can be obtained in 1 minute with PLFA in contrast to the 15 minutes with LUCA. Moreover, the post-compression of the generating pulse to sub-10 fs will allow to decrease the harmonic emission potentially to a single laser half-cycle providing optimum temporal resolution for time-resolved tomography. The FROG-CRAB technique will be needed to characterize such pulses. Finally the CEP stabilization will provide the laser field symmetry breaking allowing the study of asymmetric molecules.

To our opinion, the path of the future orbital tomography should follow the MIR laser technology. The advantages of this technology are many-fold. i) Using MIR lasers, larger spectral range of harmonics can be generated than with IR lasers at the same intensity. Higher energy EWPs can be created in HHG leading to shorter de Broglie wavelengths allowing higher than ever spatial resolution of the tomographic procedure. ii) By decreasing the laser intensity, one can favor the HHG from only the HOMO orbital while increasing it, the multi-orbital contributions can be investigated. iii) Due to the large excursion time of the EWP trajectories with MIR lasers, intra-molecular electron hole dynamics can be studied from the as to the fs time scale. Furthermore, the channel dependent nuclear vibration dynamics can be enlarged from the as to the femtosecond time scale. iv) The coupling between different ionization channels (Mairesse et al. [101], Walters and Smirnova [175]) is still barely investigated. These lasers could help to probe the population transfer between different ionization channels during HHG on a "larger" time scale.

Concerning the attosecond pulse shaping, real pulse duration measurements are the first task to do. It requires the insertion of a filter that provides us with a well determined spectral range of harmonics in the detection chamber. On the PLFA attosecond beamline the harmonic phase characterization does not require collinear propagation of the generating and the dressing beam, therefore a filter could be installed. Up to now, we characterized APTs, but with the developments on PLFA, single attosecond pulses could be characterized, too. The proposed attosecond pulse shaper has to be built and tested. The group of Franck Delmotte is already developing new mirrors combined with filters that could provide us with "high intensity" and controllable sub-80 as pulses.

ATOMIC UNITS

To simplify our life when dealing with quantum mechanics, atomic units are introduced because they transform the equations into a much clearer form and make the calculations faster. In atomic units, the four fundamental quantities *electron rest mass*, m_e , *elementary charge*, e , the *reduced Planck's constant*, \hbar , and *Coulomb's constant*, $1/4\pi\epsilon_0$, are set to unity:

$$m_e = e = \hbar = 4\pi\epsilon_0 = 1.$$

This means, that one atomic unit, (a.u.), of the following quantities correspond in SI units to:

Angular momentum, Action	\hbar	=	$1.054 \times 10^{-34} \text{ J s}$
Mass	m_e	=	$9.109 \times 10^{-31} \text{ kg}$
Charge	e	=	$1.602 \times 10^{-19} \text{ C}$
Length	$a_0 = \frac{4\pi\epsilon_0\hbar^2}{m_e e^2}$	=	$5.291 \times 10^{-11} \text{ m} = 0.53 \text{ \AA}$
Velocity	$v_B = \frac{e^2}{4\pi\epsilon_0\hbar}$	\approx	$2.187 \times 10^6 \text{ m s}^{-1}$
Momentum	$m_e v_B$	=	$1.992 \times 10^{-24} \text{ kg m s}^{-1}$
Time	$\tau_0 = \frac{a_0}{v_B}$	=	$2.418 \times 10^{-17} \text{ s} = 24.2 \text{ as}$
Frequency	τ_0^{-1}	\approx	$4.134 \times 10^{16} \text{ Hz}$
Energy	$E_h = \frac{m_e e^4}{(4\pi\epsilon_0)^2 \hbar^2}$	=	$4.359 \times 10^{-18} \text{ J} = 27.2 \text{ eV}$
Electric field	$\mathcal{E}_0 = \frac{e}{4\pi\epsilon_0 a_0^2}$	=	$5.142 \times 10^{11} \text{ V m}^{-1}$
Intensity	$\frac{1}{2} \epsilon_0 c \mathcal{E}_0^2$	=	$3.509 \times 10^{16} \text{ W cm}^{-2}$

SYMMETRY PROPERTIES OF THE FOURIER TRANSFORM

The Fourier transformation¹, \mathcal{F} , between a complex valued function $f(\mathbf{r})$ in real space with the Cartesian coordinates $\mathbf{r} = (x, y, z)$ and the function $F(\mathbf{k})$ in frequency space of wave vectors $\mathbf{k} = (k_x, k_y, k_z)$ is defined as

$$F(\mathbf{k}) = \mathcal{F}_{\mathbf{r} \rightarrow \mathbf{k}}[f(\mathbf{r})] = \frac{1}{\sqrt{2\pi}} \int_{-\infty}^{\infty} d\mathbf{r} f(\mathbf{r}) e^{-i\mathbf{k} \cdot \mathbf{r}}, \quad (\text{B.1})$$

$$f(\mathbf{r}) = \mathcal{F}_{\mathbf{k} \rightarrow \mathbf{r}}[F(\mathbf{k})] = \frac{1}{\sqrt{2\pi}} \int_{-\infty}^{\infty} d\mathbf{k} F(\mathbf{k}) e^{i\mathbf{k} \cdot \mathbf{r}}. \quad (\text{B.2})$$

It will be sufficient to discuss properties of a one-dimensional case since \mathcal{F} in a higher dimensional space can simply be written as a series of one-dimensional transforms, e.g.

$$F(\mathbf{k}) = \frac{1}{\sqrt{2\pi}} \int_{-\infty}^{\infty} dz \left\{ \int_{-\infty}^{\infty} dy \left[\int_{-\infty}^{\infty} dx f(x, y, z) e^{-ik_x x} \right] e^{-ik_y y} \right\} e^{-ik_z z}. \quad (\text{B.3})$$

Splitting $f(x)$ in its real and imaginary part:

$$f(x) = a(x) + ib(x) \quad : \quad a(x), b(x) \in \mathbb{R} \quad \forall x, \quad (\text{B.4})$$

and using the Euler's formula $e^{\pm i\phi} = \cos \phi \pm i \sin \phi$, equation B.1 writes:

$$F(k_x) = \frac{1}{\sqrt{2\pi}} \int_{-\infty}^{\infty} dx [a(x) \cos(k_x x) + b(x) \sin(k_x x)] \\ + \frac{i}{\sqrt{2\pi}} \left\{ \int_{-\infty}^{\infty} dx [b(x) \cos(k_x x) - a(x) \sin(k_x x)] \right\}. \quad (\text{B.5})$$

Taking a close look at equation B.5 and bearing in mind that the integrals vanish for integrands odd in x , one is readily convinced of the following handy symmetry properties of

¹This appendix is copied from (Haessler [41]).

the Fourier transform:

$f(x) \dots$		$F(k_x) \dots$
real valued and even in x	\Leftrightarrow	is real valued and even in k_x
real valued and odd in x	\Leftrightarrow	is imaginary valued and odd in k_x
imaginary valued and even in x	\Leftrightarrow	is imaginary valued and even in k_x
imaginary valued and odd in x	\Leftrightarrow	is real valued and odd in k_x
real valued	\Leftrightarrow	has an even real part and an odd imaginary part
imaginary valued	\Leftrightarrow	has an odd real part and an even imaginary part

ACKNOWLEDGMENTS

In the last days of my studies at the university I only knew that I wanted to study attosecond physics. I did not know much about it neither about how to work in a laboratory nor how to present scientific results. I consider myself lucky because this small but hard working and efficient group of dr. Pascal Salières guided me through the first steps of my journey in the jungle of science.

It is my pleasure to thank Valerie Blanchet and Pierre Agostini that they sacrificed their time to review my thesis. I am also grateful to Danielle Dowek, Katalin Varjú and Mauro Nisoli for being members of my jury.

My deepest admiration and gratitude goes to Pascal Salières who took the responsibility over me and addressed me with his time, advice and knowledge. I appreciate that his was available whenever needed. During scientific discussions he was explaining with patience and enthusiasm, listened to our ideas and criticized constructively. He always gave me the possibility to improve myself and taught me constantly how to present our results in front of an audience, in a project application or in articles. He is an excellent example how to be a supervisor.

I am also grateful to Bertrand Carré for being the kindest chef of the group who is working to maintain the existence of the group. I look at him as my French "father" who was always interested in my well-being. His general knowledge on physics and his wise remarks always amazed me. Despite of being overwhelmed with work, he also could find time to stand in the infinite long queue with me at the Prefecture.

Thierry Ruchon gave me optimism day after day in the lab with his jokes, taught me how to align a toroidal mirror and thanks to him I learned if the laser beam is misaligned we will not be afraid to re-align the whole system, even if it is 7'o clock at night. I am grateful for his advices on programming, problem solving, article writing and for teaching me swear words in French.

I express my gratitude to:

Stefan Haessler (Herr Doktor), the master of molecular orbital tomography, who showed me the way how to see molecular orbitals; Antoine Camper and Nan Lin who helped me to rediscover the principles of HHG and for the help with their remarks and data analysis, for the late night calls to return to CEA because the TOF is working and for the delicious chicken in cola sauce; Bastian Manschwetus who always has good news for everyone; Elizabeth English for being the kindest person in our office; Morganne Briand and Diego Guénot for struggling through the experiments with me; Marie Géléoc, Christian Cornaglia and Thierry Auguste for their kindness and help in my work;

the group of Coherent Diffraction Imaging (CDI), Hamed Merdji, Monsieur CDI David Gauthier, Xunyou Ge, Willem Boutu, Ana Borta, Fan Wang, Mathieu Ducouso and Aura Inés Gonzalez for insisting on going to the Restaurant 3 and for providing company, bringing life to the lab and for their interest on my work;

Pierre Breger the youngest member of the group who knows every tiny detail of all our

experiments and solves any technical problems with Marc Billon; Without the experience of Gilles, Didier and André we would not have any working equipments.

Thanks to Jacqueline and Véronique for their incredible ability to solve all our administrative problems and for their constant work on smoothing the functioning of the service.

Special thanks for the SLIC team for their fantastic job to provide us with laser day by day, especially Olivier who was kind to stay until late hours to we us to finish in the lab.

I would like to thank Franck Delmotte, Sébastien de Rossi and Charles Bourassin-Bouchet from Laboratoire Charles Fabry, Institut dOptique for their lessons on optics. It is always a great experience to discuss with them.

Without our theorist friends this thesis would not be published. Thanks to Richard Taïeb, Alfred Maquet, Jérémie Caillat, Roland Guichard and Cecilia Giovanetti-Teixeira for the fruitful discussions and for your incredible ideas to interpret our experimental results. I will never forget the never ending meetings in the Perrin office, where the spirit of a Nobel laureate was inspiring us.

I am deeply grateful for Amelle Zaïr and Roland Guichard for the exciting and inspiring scientific discussions both in Paris and in London. You showed me strength without boarders and told me hundreds of thousands of stories about cultures, cheese and wine and how to be a good person in this world.

It is hard to leave your own country to start a new life abroad, but Niki and Vangelis made it easy to me. They offered me shelter from the very first day of my stay. Thank you for the many excursions, plays, Greek and Hungarian food and habits. Thank you for the joy what I can share with you.

Although I have left my friends physically in Serbia and Hungary, they were always there for me when needed. Lajesz, Mózes, Szebi, Sziszi, Andris, Emil, Kornél, Bozsóki, Lipi, etc. you always provided me support and true friendship. Thank you for the unforgettable parties we had together.

Szeretném kifejezni őszinte hálámat és szeretetemet szüleimnek, testvéremnek és családjának akik nélkül most nem lennék itt. Azt a rengeteg önzetlen segítséget és támogatást is köszönöm amit nekem nyújtottak. Remélem egyszer képes leszek arra, hogy mindezt viszonzni tudjam.

Végül Kedves Páromnak, Krisztának szeretném megköszönni, hogy megtöltöd szívem étellel és ragyogással, hogy kitartasz mellettem, hiszel bennem és támogatsz a távolság és a hibáim ellenére is.

Thank you all.

Zsolt

REFERENCES

- [1] URL http://www.bipm.org/en/si/si_brochure/chapter2/2-1/second.html.
- [2] Abramowitz M and Stegun I. *Handbook of mathematical functions with formulas, graphs, and mathematical tables*. Number v. 55, no. 1972 in Applied mathematics series. U.S. Govt. Print. Off. (1964). ISBN 9780486612720.
- [3] Ammosov MV, Delone NB, and Krainov VP. *Tunnel ionization of complex atoms and of atomic ions in an alternating electromagnetic field*. Sov. Phys. - JETP **64**, 1191–1194 (1986).
- [4] Antoine P, L’Huillier A, and Lewenstein M. *Attosecond pulse trains using high-order harmonics*. Phys. Rev. Lett. **77**, 1234–1237 (1996).
- [5] Atkins P and Friedman R. *Molecular Quantum Mechanics*. Oxford University Press (2005).
- [6] Baggesen J and Madsen L. *On the dipole, velocity and acceleration forms in high-order harmonic generation from a single atom or molecule*. J. Phys. B **44**, 115601 (2011).
- [7] Baker S, Robinson JS, Haworth CA, Teng H, Smith RA, Chirilă CC, Lein M, Tisch JWG, and Marangos JP. *Probing proton dynamics in molecules on an attosecond time scale*. Science **312**, 424–427 (2006).
- [8] Baker S, Robinson J, Haworth C, Chirilă C, Lein M, Tisch J, and Marangos J. *Probing fast nuclear wavepackets in light molecules: monitoring structural rearrangement on an attosecond timescale*. J. Mod. Opt. **54**, 1011–1017 (2007).
- [9] Baker S, Robinson JS, Lein M, Chirilă CC, Torres R, Bandulet HC, Comtois D, Kieffer JC, Villeneuve DM, Tisch JWG, and Marangos JP. *Dynamic two-center interference in high-order harmonic generation from molecules with attosecond nuclear motion*. Phys. Rev. Lett. **101**, 053901 (2008).
- [10] Balcou P, Salières P, L’Huillier A, and Lewenstein M. *Generalized phase-matching conditions for high harmonics: The role of field-gradient forces*. Phys. Rev. A **55**, 3204–3210 (1997).
- [11] Bandrauk AD, Chelkowski S, Diestler DJ, Manz J, and Yuan KJ. *Quantum simulation of high-order harmonic spectra of the hydrogen atom*. Phys. Rev. A **79**, 023403 (2009).
- [12] Born M, Wolf E, Bhatia A, Clemmow P, Gabor D, Stokes A, Taylor A, Wayman P, and Wilcock W. *Principles of Optics: Electromagnetic Theory of Propagation, Interference and Diffraction of Light*. Cambridge University Press (2000). ISBN 9780521784498.
- [13] Boutu W, Haessler S, Merdji H, Breger P, Waters G, Stankiewicz M, Frasinski L, Taïeb R, Caillat J, Maquet A, Monchicourt P, Carré B, and Salières P. *Coherent control of attosecond emission from aligned molecules*. Nature Physics **4**, 545–549 (2008).
- [14] Boys S. *Electronic wave functions. i. a general method of calculation for the stationary states of any molecular system*. Proc. R. Soc. A **200**, 542554 (1950).
- [15] Brabec T and Krausz F. *Intense few-cycle laser fields: Frontiers of nonlinear optics*. Rev. Mod. Phys. **72**, 545 (2000).
- [16] Burnham D. "gottfried wilhelm leibniz (16461716) metaphysics 7. space, time, and indiscernibles", (2005). URL <http://www.iep.utm.edu/leib-met/#H7>.
- [17] Caillat J, Maquet A, Haessler S, Fabre B, Ruchon T, Salières P, Mairesse Y, and Taïeb R. *Attosecond resolved electron release in two-color near-threshold photoionization of n2*. Phys. Rev. Lett. **106**, 093002 (2011).
- [18] Chan WF, Cooper G, and Brion CE. *Absolute optical oscillator strengths for the electronic excitation of atoms at high resolution: Experimental methods and measurements for helium*. Phys. Rev. A **44**, 186–204 (1991).
- [19] Chirilă C and Lein M. *Assessing different forms of the strong-field approximation for harmonic generation in molecules*. J. Mod. Opt. **54**, 1039–1045 (2007).
- [20] Cohen-Tannoudji C, Diu B, and Laloë F. *Mécanique Quantique, tomes I et II*. Hermann, Paris, France (1986).
- [21] Corkum PB. *Plasma perspective on strong field multiphoton ionization*. Phys. Rev. Lett. **71**, 1994–1997 (1993).

- [22] Corsi C, Pirri A, Sali E, Tortora A, and Bellini M. *Direct interferometric measurement of the atomic dipole phase in high-order harmonic generation*. Phys. Rev. Lett. **97**, 023901 (2006).
- [23] Drescher M, Hentschel M, Kienberger R, Uiberacker M, Yakovlev V, Scrinzi A, Westerwalbesloh T, Kleineberg U, Heinzmann U, and Krausz F. *Time-resolved atomic inner-shell spectroscopy*. Nature **419**, 803–807 (2002).
- [24] Dudovich N, Smirnova O, Levesque J, Mairesse Y, Ivanov, Villeneuve D, and Corkum P. *Measuring and controlling the birth of attosecond xuv pulses*. Nature Physics **advanced online publication**, 781–786 (2006).
- [25] Einstein A. *Zur elektrodynamik bewegter krper*. Annalen der Physik **17**, 891 (1905).
- [26] Eppink ATJB and Parker DH. *Velocity map imaging of ions and electrons using electrostatic lenses: Application in photoelectron and photofragment ion imaging of molecular oxygen*. Rev. Sci. Instrum. **68**, 3477 (1997).
- [27] Etches A, Madsen CB, and Madsen LB. *Inducing elliptically polarized high-order harmonics from aligned molecules with linearly polarized femtosecond pulses*. Phys. Rev. A **81**, 013409 (2010).
- [28] Faisal FHM, Abdurrouf A, Miyazaki K, and Miyaji G. *Origin of anomalous spectra of dynamic alignments observed in n₂ and o₂*. Phys. Rev. Lett. **98**, 143001 (2007).
- [29] Farkas G and Toth C. *Proposal for attosecond light pulse generation using laser induced multiple-harmonic conversion processes in rare gases*. Physics Letters A **168**, 447–450 (1992).
- [30] Farrell J, McFarland BK, Gühr M, and Bucksbaum P. *Relation of high harmonic spectra to electronic structure in n₂*. Chemical Physics **366**, 15–21 (2009).
- [31] Farrell JP, Petretti S, Förster J, McFarland BK, Spector LS, Vanne YV, Decleva P, Bucksbaum PH, Saenz A, and Gühr M. *Strong field ionization to multiple electronic states in water*. Phys. Rev. Lett. **107**, 083001 (2011).
- [32] Farrell JP, Spector LS, McFarland BK, Bucksbaum PH, Gühr M, Gaarde MB, and Schafer KJ. *Influence of phase matching on the cooper minimum in ar high-order harmonic spectra*. Phys. Rev. A **83**, 023420 (2011).
- [33] Ferray M, L’Huillier A, Li X, Lompre L, Mainfray G, and Manus C. *Multiple-harmonic conversion of 1064 nm radiation in rare gases*. J. Phys. B **21**, L31–L35 (1988).
- [34] Flettner A, König J, Mason MB, Pfeifer T, Weichmann U, Düren R, and Gerber G. *Ellipticity dependence of atomic and molecular high harmonic generation*. Eur. Phys. J. D **21**, 115–119 (2002).
- [35] Franken *et al.* P. *Generation of optical harmonics*. Phys. Rev. Lett. **7**, 118 (1962).
- [36] Friedrich B and Herschbach D. *Alignment and trapping of molecules in intense laser fields*. Phys. Rev. Lett. **74**, 4623 (1995).
- [37] Gauthier D, Guizar-Sicairos M, Ge X, Boutu W, Carré B, Fienup JR, and Merdji H. *Single-shot femtosecond x-ray holography using extended references*. Phys. Rev. Lett. **105**, 093901 (2010).
- [38] Gibson GN and Biegert J. *Influence of orbital symmetry on high-order-harmonic generation and quantum tomography*. Phys. Rev. A **78**, 033423 (2008).
- [39] Gordon A and Kärtner F. *Quantitative modeling of single atom high harmonic generation*. Phys. Rev. Lett. **95**, 223901 (2005).
- [40] Goulielmakis E, Uiberacker M, Kienberger R, Baltuska A, Yakovlev V, Scrinzi A, Westerwalbesloh T, Kleineberg U, Heinzmann U, Drescher M, and Krausz F. *Direct measurement of light waves*. Science **305**, 1267–1269 (2004).
- [41] Haessler S. *Generation of Attosecond Pulses in Atoms and Molecules*. PhD thesis, L’Universite Paris-Sud XI and Services des Photons, Atoms et Molecules, IRAMIS, DSM, Commissariat a l’Energie Atomique, Saclay, (2009).
- [42] Haessler S, Fabre B, Higuët J, Caillat J, Ruchon T, Breger P, Carré B, Constant E, Maquet A, Mével E, Salières P, Taïeb R, and Mairesse Y. *Phase-resolved attosecond near-threshold photoionization of molecular nitrogen*. Phys. Rev. A **80**, 011404 (2009).
- [43] Haessler S, Caillat J, and Salières P. *Self-probing of molecules with high harmonic generation*. Journal of Physics B: Atomic, Molecular and Optical Physics **44**, 203001 (2011).
- [44] Haessler *et al.* S. *Attosecond chirp-encoded dynamics of light nuclei*. J. Phys. B **42**, 134002 (2009).
- [45] Han YC and Madsen LB. *Comparison between length and velocity gauges in quantum simulations of high-order harmonic generation*. Phys. Rev. A **81**, 063430 (2010).
- [46] Hecht E. *Optics*. Addison-Wesley (2002). ISBN 9780805385663.
- [47] Hentschel M, Kienberger R, Spielmann C, Reider G, Milosevic N, Brabec T, Corkum P, Heinzmann U, Drescher M, and Krausz F. *Attosecond metrology*. Nature **414**, 509–513 (2001).

- [48] Higuët J, Ruf H, Thiré N, Cireasa R, Constant E, Cormier E, Descamps D, Mével E, Petit S, Pons B, Mairesse Y, and Fabre B. *High-order harmonic spectroscopy of the cooper minimum in argon: Experimental and theoretical study*. Phys. Rev. A **83**, 053401 (2011).
- [49] Higuët *et al.* J. *High-order harmonic spectroscopy of the cooper minimum in argon: Experimental and theoretical study*. Phys. Rev. A **83**, 053401 (2011).
- [50] Hijano E, Serrat C, Gibson G, and Biegert J. *Orbital geometry determined by orthogonal high-order harmonic polarization components*. Phys. Rev. A **81**, 041401 (2010).
- [51] Hockett P, Bisgaard CZ, Clarkin OJ, and Stolow A. *Time-resolved imaging of purely valence-electron dynamics during a chemical reaction*. Nature Physics **7**, 612615 (2011).
- [52] Holmegaard L, Hansen J, Kalhj L, Kragh S, Stapelfeldt H, Filsinger F, Kpper J, Meijer G, Dimitrovski D, Abu-samha M, Martiny C, and Madsen L. *Photoelectron angular distributions from strong-field ionization of oriented molecules*. Nature Physics **6**, 428–432 (2010).
- [53] Iaconis C and Walmsley I. *Spectral phase interferometry for direct electric-field reconstruction of ultrashort optical pulses*. Opt. Lett. **23**, 792–794 (1998).
- [54] Itatani J, Levesque J, Zeidler D, Niiikura H, Pepin H, Kieffer JC, Corkum PB, and Villeneuve DM. *Tomographic imaging of molecular orbitals*. Nature **432**, 867–871 (2004).
- [55] Itatani J, Zeidler D, Levesque J, Spanner M, Villeneuve DM, and Corkum PB. *Controlling high harmonic generation with molecular wave packets*. Phys. Rev. Lett. **94**, 123902 (2005).
- [56] Ivanov MY, Brabec T, and Burnett N. *Coulomb corrections and polarization effects in high-intensity high-harmonic emission*. Phys. Rev. A **54**, 742–745 (1996).
- [57] Jarosik *et al.* N. *Seven-year wilkinson microwave anisotropy probe (wmap) observations: Sky maps, systematic errors, and basic results*. The Astrophysical Journal Supplement Series **192**, 14 (2010).
- [58] Jin C, Le AT, and Lin CD. *Retrieval of target photorecombination cross sections from high-order harmonics generated in a macroscopic medium*. Phys. Rev. A **79**, 053413 (2009).
- [59] Jin C, Le AT, and Lin CD. *Medium propagation effects in high-order harmonic generation of ar and n₂*. Phys. Rev. A **83**, 023411 (2011).
- [60] Jin C, Le AT, and Lin CD. *Analysis of effects of macroscopic propagation and multiple molecular orbitals on the minimum in high-order harmonic generation of aligned co₂*. Phys. Rev. A **83**, 053409 (2011).
- [61] Jin C, Wrner HJ, Tosa V, Le AT, Bertrand JB, Lucchese RR, Corkum PB, Villeneuve DM, and Lin CD. *Separation of target structure and medium propagation effects in high-harmonic generation*. Journal of Physics B: Atomic, Molecular and Optical Physics **44**, 095601 (2011).
- [62] Kajumba N, Torres R, Underwood J, Robinson J, Baker S, Tisch J, de Nalda R, Velotta R, Altucci C, Procino I, Turcu I, and Marangos J. *Measurement of electronic structure from high harmonic generation in non-adiabatically aligned polyatomic molecules*. New J. Phys. **10**, 025008 (2008).
- [63] Kanai T, Minemoto S, and Sakai H. *Quantum interference during high-order harmonic generation from aligned molecules*. Nature **435**, 470–474 (2005).
- [64] Kanai T, Takahashi EJ, Nabekawa Y, and Midorikawa K. *Destructive interference during high harmonic generation in mixed gases*. Phys. Rev. Lett. **98**, 153904 (2007).
- [65] Kanai T, Takahashi E, Nabekawa Y, and Midorikawa K. *Observing the attosecond dynamics of nuclear wavepackets in molecules by using high harmonic generation in mixed gases*. New J. Phys. **10**, 025036 (2008).
- [66] Kanai T, Takahashi EJ, Nabekawa Y, and Midorikawa K. *Observing molecular structures by using high-order harmonic generation in mixed gases*. Phys. Rev. A **77**, 041402 (2008).
- [67] Keldysh LV. *Ionization in the field of a strong electromagnetic wave*. Sov. Phys. JETP **20**, 1307–1314 (1965).
- [68] Kim K, Ko D, Park J, Tosa V, and Nam C. *Complete temporal reconstruction of attosecond high-harmonic pulse trains*. New J. Phys. **12**, 083019 (2010).
- [69] Kjeldsen TK and Madsen LB. *Strong-field ionization of n 2 : length and velocity gauge strong-field approximation and tunnelling theory*. Journal of Physics B: Atomic, Molecular and Optical Physics **37**, 2033 (2004).
- [70] Kling MF, Siedschlag C, Verhoef AJ, Khan JI, Schultze M, Uphues T, Ni Y, Uiberacker M, Drescher M, Krausz F, and Vrakking MJJ. *Control of electron localization in molecular dissociation*. Science **312**, 246–248 (2006).
- [71] Klünder K, Dahlström JM, Gisselbrecht M, Fordell T, Swoboda M, Guénot D, Johnsson P, Caillat J, Mauritsson J, Maquet A, Taïeb R, and L’Huillier A. *Probing single-photon ionization on the attosecond time scale*. Phys. Rev. Lett. **106**, 143002 (2011).

- [72] Koopmans T. *Über die zuordnung von wellenfunktionen und eigenwerten zu den einzelnen elektronen eines atoms*. Physica **1**, 104–113 (1934).
- [73] Krause JL, Schafer KJ, and Kulander KC. *High-order harmonic generation from atoms and ions in the high intensity regime*. Phys. Rev. Lett. **68**, 3535–3538 (1992).
- [74] Krausz F and Ivanov MY. *Attosecond physics*. Rev. Mod. Phys. **81**, 163 (2009).
- [75] Kruit P and Read FH. *Magnetic field paralleliser for 2π ; electron-spectrometer and electron-image magnifier*. J. Phys. E **16**, 313–324 (1983).
- [76] Kruse JE, Tzallas P, Skantzakis E, Kalpouzou C, Tsakiris GD, and Charalambidis D. *Inconsistencies between two attosecond pulse metrology methods: A comparative study*. Phys. Rev. A **82**, 021402 (2010).
- [77] Lambert G, Hara T, Garzella D, Tanikawa T, Labat M, Carré B, Kitamura H, Shintake T, Bougeard M, Inoue S, Tanaka Y, Salières P, Merdji H, Chubar O, Gobert O, Tahara K, and Couprie ME. *Injection of harmonics generated in gas in a free-electron laser providing intense and coherent extreme-ultraviolet light*. Nature Physics **4**, 296–300 (2008).
- [78] Lambert G, Hara T, Labat M, Tanikawa T, Tanaka Y, Yabashi M, Garzella D, Carré B, and Couprie ME. *Seed level requirement for improving the temporal coherence of a free-electron laser*. EuroPhysics Letters **88**, 54002 (2009).
- [79] Le AT, Lucchese RR, Tonzani S, Morishita T, and Lin CD. *Quantitative rescattering theory for high-order harmonic generation from molecules*. Phys. Rev. A **80**, 013401 (2009).
- [80] Le AT, Lucchese RR, and Lin CD. *Polarization and ellipticity of high-order harmonics from aligned molecules generated by linearly polarized intense laser pulses*. Phys. Rev. A **82**, 023814 (2010).
- [81] Le VH, Le AT, Xie RH, and Lin CD. *Theoretical analysis of dynamic chemical imaging with lasers using high-order harmonic generation*. Phys. Rev. A **76**, 013413 (2007).
- [82] Le et al. AT. *Polarization and ellipticity of high-order harmonics from aligned molecules generated by linearly polarized intense laser pulses*. Phys. Rev. A **82**, 023814 (2010).
- [83] Lebech M, Houver JC, Lafosse A, Doweck D, Alcaraz C, Nahon L, and Lucchese RR. *Complete description of linear molecule photoionization achieved by vector correlations using the light of a single circular polarization*. J. Chem. Phys. **118**, 9653–9663 (2003).
- [84] Lebech M, Houver JC, Doweck D, and Lucchese RR. *Molecular frame photoelectron emission in the presence of autoionizing resonances*. Phys. Rev. Lett. **96**, 073001 (2006).
- [85] Lee G, Kim I, Park S, Kim T, and Nam C. *Measurement of the polarization of high-order harmonics from aligned n_2 molecules by spatial interferometry*. Optics Letters **33**, 18 (2008).
- [86] Lein M. *Attosecond probing of vibrational dynamics with high-harmonic generation*. Phys. Rev. Lett. **94**, 053004 (2005).
- [87] Lein M. *Molecular imaging using recolliding electrons*. Journal of Physics B: Atomic, Molecular and Optical Physics **40**, R135 (2007).
- [88] Lein M, Hay N, Velotta R, Marangos JP, and Knight PL. *Interference effects in high-order harmonic generation with molecules*. Phys. Rev. A **66**, 023805 (2002).
- [89] Lein M, Hay N, Velotta R, Marangos JP, and Knight PL. *Role of the intramolecular phase in high-harmonic generation*. Phys. Rev. Lett. **88**, 183903 (2002).
- [90] Lennard-Jones JE. *The electronic structure of some diatomic molecules*. Trans. Faraday Soc. **25**, 668–686 (1929).
- [91] Leslie M. The man who stopped time, (2001). URL <http://www.stanfordalumni.org/news/magazine/2001/mayjun/features/muybridge.html>.
- [92] Levesque J, Mairesse Y, Dudovich N, Pepin H, Kieffer J, Corkum PB, and Villeneuve DM. *Polarization state of high-order harmonic emission from aligned molecules*. Phys. Rev. Lett. **99**, 243001 (2007).
- [93] Lewenstein M, Balcou P, Ivanov MY, L’Huillier A, and Corkum PB. *Theory of high-harmonic generation by low-frequency laser fields*. Phys. Rev. A **49**, 2117–2132 (1994).
- [94] L’Huillier A, Schafer KJ, and Kulander KC. *Theoretical aspects of intense field harmonic generation*. J. Phys. B **24**, 3315–3341 (1991).
- [95] Lock R, Zhou X, Li W, Murnane M, and Kapteyn H. *Measuring the intensity and phase of high-order harmonic emission from aligned molecules*. Chemical Physics **366**, 2232 (2009).
- [96] Lucchese RR, Raseev G, and Mckoy V. *Studies of differential and total photoionization cross sections of molecular nitrogen*. Phys. Rev. A **25**, 2572–2587 (1982).
- [97] Maiman T. *Stimulated optical radiation in ruby*. Nature **187**, 493 (1960).

- [98] Mairesse Y and Quéré F. *Frequency-resolved optical gating for complete reconstruction of attosecond bursts*. Phys. Rev. A **71** (2005).
- [99] Mairesse Y, de Bohan A, Frasninski L, Merdji H, Dinu L, Monchicourt P, Breger P, Kovacev M, Taïeb R, Carré B, Muller H, Agostini P, and Salières P. *Attosecond synchronization of high-harmonic soft x-rays*. Science **302**, 1540–1543 (2003).
- [100] Mairesse Y, Levesque J, Dudovich N, Corkum P, and Villeneuve D. *High harmonic generation from aligned molecules: amplitude and polarization*. Journal of Modern Optics **55**, 2591–2602 (2008).
- [101] Mairesse Y, Higuët J, Dudovich N, Shafir D, Fabre B, Mével E, Constant E, Patchkovskii S, Walters Z, Ivanov MY, and Smirnova O. *High harmonic spectroscopy of multichannel dynamics in strong-field ionization*. Phys. Rev. Lett. **104**, 213601 (2010).
- [102] McCormick M. Immanuel kant (17241804) metaphysics: 4. kant’s transcendental idealism, (2005). URL <http://www.iep.utm.edu/kantmeta/#H4>.
- [103] McFarland BK, Farrell JP, Bucksbaum PH, and Gühr M. *High harmonic generation from multiple orbitals in n₂*. Science **322**, 1232–1235 (2008).
- [104] McFarland BK, Farrell JP, Bucksbaum PH, and Gühr M. *High-order harmonic phase in molecular nitrogen*. Phys. Rev. A **80**, 033412 (2009).
- [105] McPherson A, Gibson G, Jara H, Johann U, Luk TS, McIntyre IA, Boyer K, and Rhodes CK. *Studies of multiphoton production of vacuum-ultraviolet radiation in the rare gases*. J. Opt. Soc. Am. B **4**, 595–601 (1987).
- [106] Meckel M, Comtois D, Zeidler D, Staudte A, Pavicic D, Bandulet HC, Pepin H, Kieffer JC, Dörner R, Villeneuve DM, and Corkum PB. *Laser-induced electron tunneling and diffraction*. Science **320**, 1478–1482 (2008).
- [107] Messiah A. *Quantum mechanics Volume 1*. North Holland (1961).
- [108] Milošević DB. *Strong-field approximation for ionization of a diatomic molecule by a strong laser field*. Phys. Rev. A **74**, 063404 (2006).
- [109] Morlens AS, Gautier J, Rey G, Zeitoun P, Caumes JP, Kos-Rosset M, Merdji H, Kazamias S, Cassou K, and Fajardo M. *Submicrometer digital in-line holographic microscopy at 32 nm with high-order harmonics*. Opt. Lett. **31**, 3095–3097 (2006).
- [110] Muller HG. *Numerical simulation of high-order above-threshold-ionization enhancement in argon*. Phys. Rev. A **60**, 1341–1350 (1999).
- [111] Murray R. *Tunnel Ionization in Strong Fields in Atoms and Molecules and its application*. PhD thesis, University of Waterloo, (2011).
- [112] Murray R, Liu WK, and Ivanov MY. *Partial fourier-transform approach to tunnel ionization: Atomic systems*. Phys. Rev. A **81**, 023413 (2010).
- [113] Murray R, Spanner M, Patchkovskii S, and Ivanov MY. *Tunnel ionization of molecules and orbital imaging*. Phys. Rev. Lett. **106**, 173001 (2011).
- [114] Muth-Böhm J, Becker A, and Faisal FHM. *Suppressed molecular ionization for a class of diatomics in intense femtosecond laser fields*. Phys. Rev. Lett. **85**, 2280–2283 (2000).
- [115] Nabekawa Y, Shimizu T, Okino T, Furusawa K, Hasegawa H, Yamanouchi K, and Midorikawa K. *Interferometric autocorrelation of an attosecond pulse train in the single-cycle regime*. Phys. Rev. Lett. **97**, 153904 (2006).
- [116] Ng Y, Christiansen W, and van Dam H. *Probing planck-scale physics with extragalactic sources?* Astrophysical Journal Letters **591**, L87 (2003).
- [117] Niikura H, Légaré F, Hasbani R, Bandrauk A, Ivanov MY, Villeneuve D, and Corkum P. *Sub-laser-cycle electron pulses for probing molecular dynamics*. Nature **417**, 917–922 (2002).
- [118] Papadogiannis NA, Nikolopoulos LAA, Charalambidis D, Tsakiris GD, Tzallas P, and Witte K. *Two-photon ionization of He through a superposition of higher harmonics*. Phys. Rev. Lett. **90**, 133902 (2003).
- [119] Patchkovskii S. *Nuclear dynamics in polyatomic molecules and high-order harmonic generation*. Phys. Rev. Lett. **102**, 253602 (2009).
- [120] Patchkovskii S, Zhao Z, Brabec T, and Villeneuve DM. *High harmonic generation and molecular orbital tomography in multielectron systems: Beyond the single active electron approximation*. Phys. Rev. Lett. **97**, 123003–123004 (2006).
- [121] Patchkovskii S, Zhao Z, Brabec T, and Villeneuve DM. *High harmonic generation and molecular orbital tomography in multielectron systems*. J. Chem. Phys. **126**, 114306 (2007).
- [122] Paul PM, Toma ES, Breger P, Mullot G, Auge F, Balcou P, Muller HG, and Agostini P. *Observation of a train of attosecond pulses from high harmonic generation*. Science **292**, 1689–1692 (2001).

- [123] Popmintchev T, Chen MC, Bahabad A, Gerrity M, Sidorenko P, Cohen O, Christov I, Murnane M, and Kapteyn H. *Phase matching of high harmonic generation in the soft and hard x-ray regions of the spectrum*. Proc. Natl Acad. Sci. USA **106**, 1051610521 (2009).
- [124] Popmintchev T, Chen MC, Arpin P, Murnane M, and Kapteyn H. *The attosecond nonlinear optics of bright coherent x-ray generation*. Nature Photonics **4**, 822832 (2010).
- [125] Ramakrishna S and Seideman T. *Information content of high harmonics generated from aligned molecules*. Phys. Rev. Lett. **99**, 113901 (2007).
- [126] Ramakrishna S, Sherratt P, Dutoi A, and Seideman T. *Origin and implication of ellipticity in high-order harmonic generation from aligned molecules*. Phys. Rev. A (Rapid Communication) **81**, 021802 (2010).
- [127] Ravasio A, Gauthier D, Maia FRNC, Billon M, Caumes JP, Garzella D, Géléoc M, Gobert O, Hergott JF, Pena AM, Perez H, Carré B, Bourhis E, Gierak J, Madouri A, Maily D, Schiedt B, Fajardo M, Gautier J, Zeitoun P, Bucksbaum PH, Hajdu J, and Merdji H. *Single-shot diffractive imaging with a table-top femtosecond soft x-ray laser-harmonics source*. Phys. Rev. Lett. **103**, 028104 (2009).
- [128] Reiss HR. *Effect of an intense electromagnetic field on a weakly bound system*. Phys. Rev. A **22**, 1786–1813 (1980).
- [129] Rosca-Pruna F and Vrakking MJJ. *Experimental observation of revival structures in picosecond laser-induced alignment of i_2* . Phys. Rev. Lett. **87**, 153902 (2001).
- [130] Ruchon T, Hauri CP, Varjú K, Mansten E, Swoboda M, Lopez-Martens R, and L’Huillier A. *Macroscopic effects in attosecond pulse generation*. New J. Phys. **10**, 025027 (2008).
- [131] Rudenko A, Zrost K, Feuerstein B, de Jesus VLB, Schröter CD, Moshhammer R, and Ullrich J. *Correlated multielectron dynamics in ultrafast laser pulse interactions with atoms*. Phys. Rev. Lett. **93**, 253001 (2004).
- [132] Rynasiewicz R. Newton’s views on space, time, and motion, (2004). URL <http://plato.stanford.edu/entries/newton-stm/>.
- [133] Salières P, L’Huillier A, and Lewenstein M. *Coherence control of high-order harmonics*. Phys. Rev. Lett. **74**, 3776 (1995).
- [134] Salières P, Carre B, Le Deroff L, Grasbon F, Paulus GG, Walther H, Kopold R, Becker W, Milošević DB, Sanpera A, and Lewenstein M. *Feynman’s path-integral approach for intense-laser-atom interactions*. Science **292**, 902–905 (2001).
- [135] Sandberg RL, Paul A, Raymondson DA, Hädrich S, Gaudiosi DM, Holtsnider J, Tobey RI, Cohen O, Murnane MM, Kapteyn HC, Song C, Miao J, Liu Y, and Salmassi F. *Lensless diffractive imaging using tabletop coherent high-harmonic soft-x-ray beams*. Phys. Rev. Lett. **99**, 098103 (2007).
- [136] Sansone G, Vozzi C, Stagira S, and Nisoli M. *Nonadiabatic quantum path analysis of high-order harmonic generation: Role of the carrier-envelope phase on short and long paths*. Phys. Rev. A **70**, 013411 (2004).
- [137] Santra R and Gordon A. *Three-step model for high-harmonic generation in many-electron systems*. Phys. Rev. Lett. **96**, 073906 (2006).
- [138] Schafer KJ, Yang B, Dimauro LF, and Kulander KC. *Above threshold ionization beyond the high harmonic cutoff*. Phys. Rev. Lett. **70**, 1599–1602 (1993).
- [139] Schmidt MW, Baldrige KK, Boatz JA, Elbert ST, Gordon MS, Jensen JH, Koseki S, Matsunaga N, Nguyen KA, Su S, Windus TL, Dupuis M, and Montgomery JA. *General atomic and molecular electronic structure system*. J. Comput. Chem. **14**, 1347–1363 (1993).
- [140] Schwarz WHE. *Measuring orbitals: Provocation or reality?* Angew. Chem. Int. Ed. **45**, 1508–1517 (2006).
- [141] Seideman T. *Revival structure of aligned rotational wave packets*. Phys. Rev. Lett. **83**, 4971–4974 (1999).
- [142] Shafir D, Mairesse Y, Villeneuve DM, Corkum PB, and Dudovich N. *Atomic wavefunctions probed through strong-field light-matter interaction*. Nature Phys. **5**, 412–416 (2009).
- [143] Shan B, Tong XM, Zhao Z, Chang Z, and Lin CD. *High-order harmonic cutoff extension of the O_2 molecule due to ionization suppression*. Phys. Rev. A **66**, 061401 (2002).
- [144] Sherratt P, Ramakrishna S, and Seideman T. *Signatures of the molecular potential in the ellipticity of high-order harmonics from aligned molecules*. Phys. Rev. A **83**, 053425 (2011).
- [145] Shiner AD, Schmidt BE, Trallero-Herrero C, Wörner HJ, Patchkovskii S, Corkum PB, Kieffer JC, Légaré F, and Villeneuve DM. *Probing collective multi-electron dynamics in xenon with high-harmonic spectroscopy*. Nature Physics **7**, 464467 (2011).
- [146] Smirnova O, Spanner M, and Ivanov M. *Analytical solutions for strong field-driven atomic and molecular one- and two-electron continua and applications to strong-field problems*. Phys. Rev. A **77**, 033407 (2008).

- [147] Smirnova O, Mairesse Y, Patchkovskii S, Dudovich N, Villeneuve D, Corkum P, and Ivanov MY. *High harmonic interferometry of multi-electron dynamics in molecules*. Nature **460**, 972–977 (2009).
- [148] Smirnova O, Patchkovskii S, Mairesse Y, Dudovich N, and Ivanov MY. *Strong-field control and spectroscopy of attosecond electron-hole dynamics in molecules*. PNAS USA (2009).
- [149] Spanner M, Smirnova O, Corkum P, and Ivanov M. *Reading diffraction images in strong field ionization of diatomic molecules*. J. Phys. B: At. Mol. Opt. Phys. **37**, L243 (2004).
- [150] Srivastava SJ and Jain AK. *Thermodynamics: a core course*. Prentice Hall of India Private Limited (2005).
- [151] Stanbaugh J. *Religion and Time*. Brill Academic Publisher (1992).
- [152] Stapelfeldt H and Seideman T. *Colloquium: Aligning molecules with strong laser pulses*. Rev. Mod. Phys. **75**, 543+ (2003).
- [153] Swoboda M, Dahlström M, Ruchon T, Johnsson P, Mauritsson J, L’Huillier A, and Schafer KJ. *Intensity dependence of laser-assisted attosecond photoionization spectra*. Laser Physics, **19**, 1591–1599 (2009).
- [154] Tate J, Auguste T, Muller HG, Salières P, Agostini P, and DiMauro LF. *Scaling of wave-packet dynamics in an intense midinfrared field*. Phys. Rev. Lett. **98**, 013901 (2007).
- [155] Toma ES and Muller HG. *Calculation of matrix elements for mixed extreme-ultraviolet & infrared two-photon above-threshold ionization of argon*. J. Phys. B **35**, 3435–3442 (2002).
- [156] Tong XM, Zhao ZX, and Lin CD. *Theory of molecular tunneling ionization*. Phys. Rev. A **66**, 033402 (2002).
- [157] Torres R, Kajumba N, Underwood J, Robinson J, Baker S, Tisch J, Nalda DR, Bryan W, Velotta R, Altucci C, Turcu I, and Marangos J. *Probing orbital structure of polyatomic molecules by high-order harmonic generation*. Phys. Rev. Lett. **98**, 203007 (2007).
- [158] Torres R, Siegel T, Brugnera L, Procino I, Underwood JG, Altucci C, Velotta R, Springate E, Froud C, Turcu ICE, Ivanov MY, Smirnova O, and Marangos JP. *Extension of high harmonic spectroscopy in molecules by a 1300 nm laser field*. Opt. Express **18**, 3174–3180 (2010).
- [159] Torres R, Siegel T, Brugnera L, Procino I, Underwood JG, Altucci C, Velotta R, Springate E, Froud C, Turcu ICE, Patchkovskii S, Ivanov MY, Smirnova O, and Marangos JP. *Revealing molecular structure and dynamics through high-order harmonic generation driven by mid-ir fields*. Phys. Rev. A **81**, 051802 (2010).
- [160] Trebino R, editor. *Frequency-Resolved Optical Gating: The Measurement of Ultrashort Laser Pulses*. Kluwer Academic Publishers, Dordrecht, The Netherlands (2002).
- [161] Tzallas P, Charalambidis D, Papadogiannis NA, Witte K, and Tsakiris GD. *Direct observation of attosecond light bunching*. Nature **426**, 267–271 (2003).
- [162] Tzallas P, Skantzakis E, Nikolopoulos LAA, D. TG, and Charalambidis D. *Extreme-ultraviolet pumpprobe studies of one-femtosecond-scale electron dynamics*. Nature Phys. page DOI: 10.1038/NPHYS2033 (2011).
- [163] Ullrich J, Moshhammer R, Dorn A, Dörner R, Schmidt L, and Schmidt-Böcking H. *Recoil-ion and electron momentum spectroscopy: reaction-microscopes*. Rep. Prog. Phys. **66**, 1463 (2003).
- [164] van der Zwan E. *Molecular Imaging using Strong-Field Processes*. PhD thesis, Fachbereich Naturwissenschaften der Universität Kassel, (2010).
- [165] van der Zwan EV and Lein M. *Two-center interference and ellipticity in high-order harmonic generation from h_2^+* . Phys. Rev. A **82**, 033405 (2010).
- [166] van der Zwan EV, Chirilă CC, and Lein M. *Molecular orbital tomography using short laser pulses*. Phys. Rev. A **78**, 033410 (2008).
- [167] Varjú K, Johnsson P, Lpez-Martens R, Remetter T, Gustafsson E, Mauritsson J, Gaarde M, Schafer K, Erny C, Sola I, Zaïr A, Constant E, Cormier E, Mével E, and L’Huillier A. *Experimental studies of attosecond pulse trains*. Laser Physics **15**, 888–898 (2005).
- [168] Varjú K, Mairesse Y, Carré B, Gaarde MB, Johnsson P, Kazamias S, López-Martens R, Mauritsson J, Schafer KJ, Balcou P, L’Huillier A, and Salières P. *Frequency chirp of harmonic and attosecond pulses*. J. Mod. Opt. **52**, 379–394 (2005).
- [169] Velotta R, Hay N, Mason MB, Castillejo M, and Marangos JP. *High-order harmonic generation in aligned molecules*. Phys. Rev. Lett. **87**, 183901 (2001).
- [170] Vénier V, Taïeb R, and Maquet A. *Phase dependence of $(N+1)$ -color $(N>1)$ ir-uv photoionization of atoms with higher harmonics*. Phys. Rev. A **54**, 721–728 (1996).
- [171] Vozzi C, Calegari F, Benedetti E, Caumes JP, Sansone G, Stagira S, Nisoli M, Torres R, Heesel E, Kajumba N, Marangos JP, Altucci C, and Velotta R. *Controlling two-center interference in molecular high harmonic generation*. Phys. Rev. Lett. **95**, 153902–153904 (2005).

- [172] Vozzi C, Negro M, Calegari F, Sansone G, Nisoli M, De Silvestri S, and Stagira S. *Generalized molecular orbital tomography*. Nature Physics page doi:10.1038/nphys2029 (2011).
- [173] Wagner N, Zhou X, Lock R, Li W, Wuest A, Murnane M, and Kapteyn H. *Extracting the phase of high-order harmonic emission from a molecule using transient alignment in mixed samples*. Phys. Rev. A **76**, 061403 (2007).
- [174] Walmsley IA and Dorrer C. *Characterization of ultrashort electromagnetic pulses*. Adv. Opt. Photon. **1**, 308–437 (2009).
- [175] Walters ZB and Smirnova O. *Attosecond correlation dynamics during electron tunnelling from molecules*. Journal of Physics B: Atomic, Molecular and Optical Physics **43**, 161002 (2010).
- [176] Walters ZB, Tonzani S, and Greene CH. *Limits of the plane wave approximation in the measurement of molecular properties*. J. Phys. Chem. A **112**, 9439–9447 (2008).
- [177] Wörner HJ, Niikura H, Bertrand JB, Corkum PB, and Villeneuve DM. *Observation of electronic structure minima in high-harmonic generation*. Phys. Rev. Lett. **102**, 103901 (2009).
- [178] Wörner *et al.* HJ. *Following a chemical reaction using high-harmonic interferometry*. Nature **466**, 604–607 (2010).
- [179] Wörner *et al.* HJ. *Controlling the interference of multiple molecular orbitals in high-harmonic generation*. Phys. Rev. Lett. **104**, 233904 (2010).
- [180] Yoshii K, Miyaji G, and Miyazaki K. *Retrieving angular distributions of high-order harmonic generation from a single molecule*. Phys. Rev. Lett. **106**, 013904 (2011).
- [181] Zerne R, Altucci C, Bellini M, Gaarde MB, Hänsch TW, L’Huillier A, Lyngå C, and Wahlström CG. *Phase-locked high-order harmonic sources*. Phys. Rev. Lett. **79**, 1006–1009 (1997).
- [182] Zewail AH. *Femtochemistry: Atomic-scale dynamics of the chemical bond†*. J. Phys. Chem. A **104**, 5660–5694 (2000).
- [183] Zhou X, Lock R, Li W, Wagner N, Murnane M, and Kapteyn H. *Molecular recollision interferometry in high harmonic generation*. Phys. Rev. Lett. **100**, 073902 (2008).
- [184] Zhou X, Lock R, Wagner N, Li W, Kapteyn HC, and Murnane MM. *Elliptically polarized high-order harmonic emission from molecules in linearly polarized laser fields*. Phys. Rev. Lett. **102** (2009).
- [185] Zimmermann B, Lein M, and Rost J. *Analysis of recombination in high-order harmonic generation in molecules*. Phys. Rev. A **71**, 033401 (2005).
- [186] Zwan EV and Lein M. *Control of recollision wave packets for molecular orbital tomography using short laser pulses*. J. Phys. B **41**, 074009 (2008).